Presented to the Higher Degree of Research, Macquarie University in fulfillment of the requirements for the degree of Doctor of Philosophy

The Evolution of the Wongwibinda High-T–Low-P Metamorphic Complex, New England Orogen, NSW, Australia

Stephen James Craven

November 2015

Author's declaration of originality

I, Stephen James Craven, declare that this is my own work and that it has not been submitted to any other institution for a higher degree.

Macquarie University
Earth and Planetary Sciences
North Ryde, Australia
steve.craven@mq.edu.au

+61 409 151 952

Acknowledgements

Acknowledgements

Funding in support of this research project was made possible through a Macquarie University Research and Development Grant to Nathan Daczko and recently by an MQRES Scholarship.

Irene Wainwright (University of New South Wales) performed XRF analyses. K. Goemann is thanked for help with the monazite geochronology at UTAS. The analytical data were obtained using instrumentation in the Geochemical Analysis Unit (GEMOC) at Macquarie, funded by DEST Systemic Infrastructure Grants, ARC LIEF, NCRIS, industry partners and Macquarie University.

The two publications composing Chapters 1 and 2 are Contributions 729 and 887 respectively from the Australian Research Council National Key Centre for the Geochemical Evolution and Metallogeny of Continents (http://www.gemoc.mq.edu.au). Critical reviews of the publications made by Simon Bodorkos, Glen Phillips and an anonymous reviewer are appreciated and improved the manuscripts.

"No man is an island entire of itself; every man is a piece of the continent, a part of the main" (Donne, 1624). I guess it was before the breakup of Pangaea and with this stanza in mind:

To my esteemed supervisor Nathan Daczko an ebullient, enthusiastic and competent researcher who, with his sidekick Luke Milan, coerced me into this field of endeavour. Thank you for the opportunity, enthusiastic support, encouragement and maturing friendship over the eight long years of part-time study, all sincerely appreciated. My thanks also to my Masters supervisor, now my current associate supervisor Dick Flood who has kept a weather eye on proceedings as they progressed and to my co-author Jacqui Halpin who performs magic with Thermocalc.

My gratitude to my very good friend and mentor Elena Belousova, hard to evaluate the contribution Elena has made in assisting me with this research. Suffice to say that her time and assistance with the TerraneChron survey, the subsequent analysis and interpretation of zircon data and endless discussions was simply, significant! Also, to Norm Pearson, manager of the Geochemical Analysis Unit at Macquarie, for his forbearance and assistance during the analytical phase of the study and his understanding, as my senior colleague at Macquarie, in the latter stages. Also, Justin Payne who rode shotgun to Norm on the LA-ICPMS.

I have been most fortunate to work and study in the Department of EPS at Macquarie. It has given me the opportunity to work with great people and develop some rather special friendships. It has been a special time and I am grateful for that and for the support I have received from many staff members and fellow students, particularly in the latter stages of this research. In particular, I thank Sue O'Reilly who gave me the opportunity to work at Macquarie, to be part of the exciting work performed by GEMOC and the CCFS centre, an opportunity that ultimately led to me to undertaking this research. Departmental HDR Directors, nurturers and supporters of post-graduate students, Simon Jackson, Tracy Rushmer, Craig O'Neill and Dorrit Jacob, I appreciate their support.

The landowners of the Wongwibinda Metamorphic Complex deserve special recognition for their enthusiastic support and friendship. In particular Edward and Sally and Simon and Sophia Wright of Wongwibinda Station, Ona and John (recently deceased) Winter-Erving of Noorilim, Don and Fay Tully of Tarengower, Clive and Margaret O'Connor of Mirragulee and Stewart Wheaton, manager of Lynoch at the time. Great people all.

In a personal vein, I ride a literal wave of support from all my close friends many of whom shake their head at this undertaking but have supported me just the same. My now adult family who has followed my progress, if not the content, of my research with great interest, has always been very supportive; they are very special people. I believe that they wish to live vicariously through their father's achievements. My dog, which is at the gate to welcome me each night no matter what the time or the weather, well most nights, and makes no bones about it.

However, it is my partner, my companion, very special friend, lover and wife, who has been my great supporter and motivator throughout a lifetime of part-time study, it is Jan who deserves my appreciation above all.

Donne, J., 1624. Meditation 17, Devotions upon Emergent Occasions. Poetry For 5th Year. Leaving Certificate Students, 1959.

Table of Contents

Abstract

Abstract

The Wongwibinda Metamorphic Complex is a high-temperature–low-pressure metamorphic complex located in the southern New England Orogen, northeastern NSW. It is characterised by a local steep metamorphic field gradient (up to ~100°C km^{-1}) in variably metamorphosed accretionary wedge turbidites of the central Tablelands Complex. The metamorphic rocks are surrounded to the north, east and south by S-type granite plutons of the Hillgrove Supersuite (Abroi Granodiorite and the Rockvale and Tobermory monzogranites) and the Wongwibinda Fault forms a major structural boundary on the east of the complex. The western boundary is considered to be ~25-30 km to the west where any boundary, possibly with the Sandon Beds is concealed by overburden including Tertiary Basalts.

A comparison of (i) detrital zircon U-Pb geochronology, (ii) Hf isotope character, and (iii) trace element composition, across variably metamorphosed rocks of the complex, demonstrates that the Wongwibinda Metamorphic Complex comprises metamorphosed Girrakool Beds, the protolith to the Wongwibinda Metamorphic Complex, exposed to the west of the complex. U-Pb geochronology identifies a maximum deposition age of c. 309 Ma for the metamorphosed equivalents of the Girrakool Beds, on the basis of the youngest grains. The majority of detrital zircon ages are c. 320–350 Ma, peaking at c. 330 Ma, with few Proterozoic and Archean grains. These data point to the western Keepit magmatic arc, exposed in the Tamworth Belt, as the likely volcanic provenance for the Girrakool Beds. The

Hf isotope data for c. 320-350 Ma detrital grains become less radiogenic over the 30 million year record, representing a short-term isotopic reversal of the overall trend common to external accretionary orogens. Volcanic activity in the Keepit Arc is inferred to decrease rapidly at c. 320 Ma based on a drop in the abundance of <320 Ma zircon grains in sedimentary detritus. This decrease is interpreted as coinciding with the onset of trench retreat and slab roll back that led to the Late Carboniferous to Early Permian period of extension, thus ending volcanic activity in the Keepit Arc.

Thermocalc P-T pseudosections are used to determine the P-T conditions of metamorphism and to derive field gradients. The metamorphic field gradient in the Wongwibinda Metamorphic Complex varies, being less than 15–23°C km^{-1} in the transition from sub-biotite grade to biotite-grade metaturbidites in the west of the complex, and increases to greater than 50°C km^{-1} and possibly over 100°C km^{-1} in amphibolite-grade cordierite-bearing rocks and garnet-bearing migmatites in the east. The km-scale zones of cordierite-bearing rocks (up to 5 km wide) exhibit a range of textures that include: (i) cordierite–K-feldspar–spotted hornfels, 570–620°C at 250 MPa (2.5 kbar); (ii) sheared cordierite–K-feldspar–augen schists, two samples with variable temperatures of 670-690°C or <600°C at 200 MPa (2 kbar), consistent with rapid cooling or variable thermal structure in the Glen Mohr Shear Zone, a major north-south trending structural feature; and (iii) migmatites with or without garnet, ~660°C at less than 330 MPa (3.3 kbar).

The shallow portion of the metamorphic field gradient is interpreted as resulting from conductive heating from the mantle through a thinning crust;

this drove widespread biotite-grade metamorphism in the shallow New England Orogen crust (as shallow as ~12 km). Higher-grade rocks are much more spatially restricted. The spatial association of quartzite units centered within two cordierite-bearing high-T domains of the Wongwibinda Metamorphic Complex and an increased abundance of quartz veins above the cordierite isograd suggests heat advection by aqueous fluid locally perturbed the broad conductive heating. On the basis of a spatial and temporal association, fluid was channeled within shear zones, such as the Glen Mohr and Wongwibinda shear zones, and locally infiltrated nearby rocks.

Electron microprobe chemical dating of metamorphic monazite in three migmatite samples (296.9±1.5 Ma) indicate that high-temperature–low-pressure metamorphism occurred about 10–12 million years after deposition of the sedimentary rocks (c. 309 Ma). The age determined for two samples of the Glen Mohr Shear Zone (291.5±1.8 Ma) is indistinguishable from ages determined for the post-metamorphic Abroi Granodiorite (290.5±1.6 Ma), indicating that the metamorphic cycle lasted c. 5-10 million years. Garnet grains in schists and migmatites commonly display a flat unzoned interior with narrow (350 nm) Mn-rich rims of variable composition. Unzoned cores are inferred to result from elemental homogenisation at peak metamorphic conditions. The narrow rims are associated with texturally resorbed grain edges that formed during retrograde conditions. The retrograde overprint is nearly pervasive across the complex and is most obvious nearer to shear zones and some intrusive rocks of the Hillgrove Supersuite.

U-Pb geochronology of five samples of the Hillgrove Supersuite that show plutonism in the complex involves two pulses: c. 300 Ma and c. 292 Ma, overlapping the age of high-T–low-P metamorphism (296.8±1.5 Ma), and also postdating it. Zircon xenocrysts (≥310 Ma) in the plutonic rocks have U-Pb-Hf isotopic character similar to the Girrakool Beds, indicating that crust similar to the country rocks is the likely source of the xenocrysts. The $^{176}Hf/^{177}Hf$ initial character for zircon for the c. 300 Ma plutons is less radiogenic than those in the c. 292 Ma plutons, illustrating an increasing mantle component in the Hillgrove Supersuite with time. These data are consistent with a rift tectonic setting, where mantle-derived magma is predicted to increasingly migrate to shallower crustal levels over time as the crust thins and becomes hotter (metamorphism), and early partial melting of the metasedimentary crust depletes the source rocks, thus reducing the S-type component in younger Hillgrove Supersuite plutons.

It is concluded that an extensional geodynamic setting around the Carboniferous–Permian boundary supports conductive heat transfer as the key driver of regional scale biotite-grade metamorphism. Advective heat transfer via hot aqueous fluids along shear zones is required to drive very local high-temperature–low-pressure metamorphism. The older ages for the Hillgrove Supersuite at c. 300 Ma suggest that some magmatic heat advection is also likely and may be important for the formation of the migmatite samples. The geology and evolution of the Wongwibinda Metamorphic Complex indicate a critical role for slab roll back and extension, evidenced by the presence of S-type granites, during the Late Carboniferous to Early Permian.

This geodynamic setting led to local high-temperature–low-pressure metamorphism, S-type granite production, and development of rift basins such as the Sydney-Gunnedah-Bowen system.

Introduction

The Evolution of the Wongwibinda HTLP Metamorphic Complex, New England Orogen, NSW, Australia'

Introduction

Topic, Scope and Significance

The Evolution of the Wongwibinda High-Temperature–Low-Pressure Metamorphic Complex, New England Orogen, NSW, Australia

Decoding the metamorphic pressure-temperature-time (*P-T-t*) history of rocks develops our understanding of both present-day and ancient geodynamic processes. Incorporating detailed studies of sedimentary and igneous processes builds our knowledge and aids in developing a deeper comprehension of the interrelationships and dependencies between tectonic processes. High-Temperature–Low-Pressure (HTLP) metamorphic complexes are defined as having formed at greater than 600°C and less than 5 kbar (0.5 GPa; Sandiford and Hand, 1998) which equates to about 12 km deep in the crust. Complexes (<1000 km^2) that have steep metamorphic field gradients can only form with advective heating mechanisms, mainly involving the migration of hot fluid (water and/or magma; Hoisch, 1987, 1991; Brady, 1988; Chamberlain and Rumble, 1988, 1989; De Yoreo et al., 1991). Exposures of HTLP metamorphic complexes provide an opportunity to study upper crustal metamorphism and the geological processes involved in their formation, leading to understanding the broader geodynamic setting.

The Wongwibinda Metamorphic Complex (WMC), of Permian age (Binns, 1966), is a small (~400 km^2) HTLP metamorphic terrane in northeastern NSW, Australia. It is located in the central Tablelands Complex

of the New England Orogen (NEO). The NEO is the youngest of three accretionary orogens that compose the Tasmanides (Glen, 2013) that make up much of eastern Australia. A rare, complete metamorphic progression is exposed at Wongwibinda involving virtually unmetamorphosed sedimentary rocks in the west that change into anchizonal grade (Farrell, 1992), then greenschist to biotite grade and finally amphibolite grade rocks in the east (Binns, 1966) over a distance of approximately 20 km. The highest-grade rocks are garnet-cordierite migmatite. Sedimentary rocks that are metamorphosed were only deposited approximately ten million years prior to HTLP metamorphism. The complex is surrounded on three sides by granite plutons of the Hillgrove Supersuite (Binns, 1966; Farrell, 1992) that are of similar age to the metamorphism (Craven et al., 2012). Four mechanisms have been proposed for the formation of HTLP metamorphism (Chapter 1) and although easily recognised in the field by petrological studies, the diagnosis of the formative mechanisms is not simple. The aim of this research is to achieve a better understanding of the heating mechanisms driving HTLP metamorphism, S-type granite anatexis and their relationship to subduction by studying the WMC. This project investigates the intimate and complex relationship between sedimentation, metamorphism and magmatism, and integrates this information to understand the evolution of the rocks' geodynamic setting.

Previous studies in this area have independently focused on field mapping, igneous and sedimentary petrology (Binns, 1966; Korsch, 1978; Farrell, 1992), metamorphic petrology (Binns, 1966; Stephenson and Hensel,

1979, 1982; Vernon and Pooley, 1981; Vernon, 1982; Farrell, 1992;) and structural geology (Binns, 1966, Korsch, 1981; Farrell, 1988, 1992; Landenberger et al., 1995). The detailed research and new data presented in this study builds on this previous work. This project integrates field mapping, metamorphic petrology and the characterisation of U-Pb-Hf isotopes in zircon to explore the interplay between sedimentation, HTLP metamorphism, partial melting and magmatism.

The scope of this investigation covers two broad topics. The first topic looks at the metamorphic geology of the WMC from microscopic to regional scale. The second topic uses the U-Pb-Hf isotope character of zircon to document the spatial and temporal relationships between the sedimentary, metamorphic and igneous units in the complex. In this study, surrounding plutonic rocks of the Hillgrove Supersuite are included in the WMC, as these are close in age to the HTLP metamorphism. The WMC is defined as the area bound by the Wongwibinda Fault in the east, the northern margin of the Tobermory Monzogranite in the north, and the southern margin of the Rockvale Monzogranite in the south. The western boundary is less simple to define as metamorphic grade gradually decreases to the west toward the poorly exposed contact between the Girrakool Beds, the protolith to the WMC, and Sandon Beds the adjacent geological unit to the west. The distinction between these two units was made based on a lithological change associated with a decrease in abundance of chert layers in the Girrakool Beds (Korsch, 1978). However, the exact nature of the contact has remained unclear. Rocks in the Sandon Beds are predominantly greywackes, cherts, jaspers, volcanics

and argillites, while the Girrakool Beds mainly consist of a thick sequence of argillites, siltstones and sandstones (Leitch, 1974; Korsch, 1977).

The exact stratigraphic relationship between the two units is unclear. Early Carboniferous radiolarians were found in chert layers of the Sandon Beds near Armidale (Aitchison, 1990). In the Girrakool Beds, detrital zircons (from the Wongwibinda Complex; Fig. 1) yield a dominant age range of ~350–310 Ma (Craven, 2010), indicating that sedimentation lasted at least until ~310 Ma. However, in the Walcha area to the south, these two similar sedimentary units are distinguishable in radiometric data (U, Th, K) (Brown, 2003; Li & Rosenbaum, 2014).

Part 1 (Chapters 1–3) focuses on the metamorphic geology of the WMC. The protolith to the WMC is not conducive to a classical mineral isograd approach to metamorphic studies. The protolith is high-silica (typically 65-75 wt% SiO_2) and true pelitic or mud rocks have not been identified. Therefore, a high-variance assemblage is produced during metamorphism. Previous petrographic analyses (Binns, 1966; Vernon, 1982; Farrell, 1992) provide an understanding of the mineral assemblages, their microstructural development and key metamorphic reactions, but the temperature and pressure conditions remained poorly constrained (Vernon, 1982). Here, detailed petrographic studies, bulk-rock composition and pseudosection construction (using THERMOCALC software) are integrated to determine the pressure-temperature evolution of the complex.

Chapter 1 focuses on these metamorphic techniques as applied to a series of samples taken from across the metamorphic field gradient. Polished

thin sections were used for petrographic analysis, to obtain electron microprobe (EMP) mineral chemistry and for EMP chemical dating of monazite to determine the age of metamorphism. Bulk rock geochemical analyses were obtained using X-Ray Fluorescence (XRF) to document the variability in rock types and for input into metamorphic pseudosection construction. Zircon U-Pb ages were determined for the Abroi Granodiorite, adjacent to the metamorphic field gradient examined. The age of metamorphism slightly predates the age of pluton crystallisation, suggesting that magmatic advective heat transfer was not the key mechanism in heating the complex. This manuscript is published in the Journal of Metamorphic Geology and 100% of it is counted towards this thesis. Coauthor Daczko supervised the project and coauthor Halpin contributed EMP monazite ages and Thermocalc phase diagrams.

Following from the first chapter, Chapter 2 presents a model involving the infiltration of high temperature (<650°C) aqueous fluids to drive the metamorphism. A discontinuous metamorphic field gradient is explained by the superposition of two metamorphic processes: (i) biotite grade regional metamorphism due to conductive heating mechanisms in an extensional tectonic setting, enhanced by (ii) local fluxing of hot aqueous fluids along shear zones and faults, driving the local amphibolite grade metamorphism. This manuscript is published in the Australian Journal of Earth Sciences and 100% of it is counted towards this thesis. Similar to chapter 1, coauthor Daczko supervised the project and coauthor Halpin contributed EMP monazite ages and Thermocalc phase diagrams.

Chapter 3 explores the retrograde history of the rocks and describes narrow Mn-rich rims on garnet grains that surround chemically homogenous low-Mn cores. A spatial association between retrograde metamorphism and shear zones is noted. Gravity data collected on an east-west traverse across the complex did not identify any substantial concealed mafic plutons that might explain the localised heating. This manuscript is published in the Australian Journal of Earth Sciences and approximately 10%, being the contribution of petrographic and EMP data and materials and tutoring assistance in the field, is counted towards this thesis, as it largely comprises the honours degree research of Cara Danis.

Part 2 (Chapters 4 and 5) presents the U-Pb-Hf characteristics of zircon from all the major rock types of the complex and interprets the relationships between the rocks.

Chapter 4 is a detailed investigation of detrital zircon in the protolith to the metasedimentary components of the WMC, the Girrakool Beds. These metasedimentary rocks comprise a thick packet of deep marine turbidites deposited in the ocean and scraped off to become part of a fore-arc accretionary wedge. The aim of the chapter is to compare the U-Pb-Hf character of zircon from metasedimentary rocks sampled across the metamorphic grades. The ability to identify the protolith to the metamorphic rocks by using a combination of zircon trace elements, U-Pb geochronology and Hf isotopes was investigated. The data demonstrate that the Girrakool Beds are the protolith for all metasedimentary rocks in the WMC. Further interrogation of the zircon data indicate the provenance of the sediment to be

dominated by the Keepit arc, within and west of the Tamworth Belt. The detrital zircon grains record a trend in the Keepit arc from more radiogenic magmatism at c. 350 Ma to less radiogenic magmatism at c. 320 Ma.

Chapter 5 investigates the three plutons of the Hillgrove Supersuite in the WMC: (i) Abroi Granodiorite, (ii) Tobermory Monzogranite and (iii) Rockvale Monzogranite. Petrography is combined with U-Pb geochronology and Hf isotope characterisation of zircon. Primary magmatic zircon grains are compared with secondary xenocrystic zircon grains to show the xenocrysts are very similar to grains examined from the Girrakool Beds (Chapter 4). Two pulses of plutonism are recognized at c. 300 Ma and c. 292 Ma, although both ages are present in what is presently seen as a single pluton (Abroi Granodiorite). The younger plutons have more radiogenic zircon compared to the older plutons. The data point to an increasing mantle component in S-type granite production with time in the Hillgrove Supersuite.

The synthesis chapter brings together the detailed information in the five chapters to build a geological evolution of the WMC from the Carboniferous to Early Permian. It places the WMC within the tectonic framework of the NEO and provides a deeper understanding of the extensional geodynamic setting pivotal in the creation of this HTLP complex. This research is significant, as it has taken an interdisciplinary approach, applying new metamorphic and zircon trace element, geochronological and Hf isotope techniques to examine plate tectonic processes through a rare glimpse into the deeper New England crust, providing important new

information about the NEO and contributing to how wider geodynamic interpretations are made.

All zircon trace element, U-Pb and Hf isotope analytical data are provided in the Digital Appendix. Appendix 1 is an extended abstracts presented at the 2010 New England Orogen conference. It contains preliminary data interpretations of material presented in chapters 4 & 5. Conference presentations were also made at the Australian Earth Science Convention (AESC, 2010) and at the Geological Society of Australia Specialist Group in Tectonics and Structural Geology (SGTSG) conference (2010). Three other publications were co-authored during the course of this PhD research and copies of the journal articles are appended (Appendix 2-4). The appended publications are unrelated to the main study but reflect my ability to carry on parallel lines of research in my role as a part-time student and staff member at Macquarie. They demonstrate my ability to organise myself and to work with other researchers. Also, there is a tacit relationship with the content of the thesis. Appendices 2 & 3 involve the application of zircon isotope and trace element studies. Appendices 3 & 4 involve provenance studies involving archaeological material. In Belousova et al. (2015), my contribution includes providing prior geological knowledge of the Coolac Serpentinite Belt, organization of two field trips, the processing of the chromitite samples and, as the Manager of the Mineral Processing Unit at Macquarie, authorship of the section on sample preparation techniques. In the two archeological papers by Kelloway et al. (2013), my contribution entailed the training and instruction of my co-author in the interpretation of petrographic thin sections and the use

of zircon geochronology as a tool for determining the provenance of pot shards.

References

Binns, R. A., 1966. Granitic intrusions and regional metamorphic rocks of Permian age from the Wongwibinda district, northeastern New South Wales. Journal of the Proceedings of the Royal Society of N.S.W., **99**, 5–36.

Brady J. D., 1988. The role of volatiles in the thermal history of metamorphic terranes. Journal of Petrology, **29**, 1187–1213.

Brown, R.E., 2003. Peel South Exploration NSW geophysics — interpretation of new data for exploration and geological investigations in the western New England area of New South Wales. Quarterly Notes, **114**, 1–27.

Chamberlain C. P. and Rumble D., 1988. Thermal anomalies in a regional metamorphic terrane: An isotopic study of the role of fluids. Journal of Petrology, **29**, 1215–1232.

Chamberlain C. P. and Rumble D., 1989. The influence of fluids on the history of a metamorphic terrane: New Hampshire, USA. In: Daly J. S., Cliff R. A. & Yardley B. W. D. eds. Evolution of Metamorphic Belts, pp. 203–213. Geological Society of London, Special Publication 43.

Craven S. J., Daczko N. R. and Halpin J. A., 2012. Thermal gradient and timing of high-T–low-P metamorphism in the Wongwibinda Metamorphic Complex, southern New England Orogen, Australia. Journal of Metamorphic Geology, **30**, 3–20.

De Yoreo J. J., Lux D. R. and Guidotti C. V., 1991. Thermal modeling in low-pressure/high-temperature metamorphic belts. Tectonophysics, **188**, 209–238.

Farrell T.R., 1988, Structural geology and tectonic development of the Wongwibinda metamorphic complex, *in* Kleeman J.D., ed., New England Orogen; Tectonics and Metallogenesis. Symposium Proceedings: Armidale, University of New England, p.117–124.

Farrell, T. R., 1992. Deformation, Metamorphism and Migmatite Genesis in the Wongwibinda Metamorphic Complex. Unpublished PhD thesis, University of Newcastle, Australia.

Hoisch. T. D., 1987. Heat transport by fluids during Late Cretaceous regional metamorphism in the Big Maria Mountains, southeastern California. Geological Society of America Bulletin, **98**, 549–553.

Hoisch. T. D., 1991. The thermal effects of pervasive and channelised fluid flow in the deep crust. Journal of Geology, **99**, 69–80.

Korsch, R. J., 1978. Stratigraphic and igneous units in the Rockvale-Coffs Harbour region, New South Wales. Journal and Proceedings, Royal Society of New South Wales, **111**, 13–17.

Korsch, R.J., 1981. Structural geology of the Rockvale Block, northern New South Wales. Journal of the Geological Society of Australia, **28**, 51–70.

Landenberger, B., Farrell, T.R., Offler, R., Collins, W.J. and Whitford, D.J., 1995. Tectonic implications of Rb–Sr biotite ages for the Hillgrove Plutonic Suite, New England Fold Belt, N.S.W. Australia. Precambrian Research, **71**, 251–263.

Li, P. and Rosenbaum, G., 2014. Does the Manning Orocline exist? New structural evidence from the inner hinge of the Manning Orocline (eastern Australia). Gondwana Research, **25**, 1599–1613.

Stephenson, N.C.N. and Hensel, H.D., 1979. Intergrown calcic and Fe–Mg amphiboles from the WMC, N.S.W., Australia. Canadian Mineralogist, **17**, 11–23.

Stephenson, N. C. N. and Hensel, H. D., 1982. Amphibolites and related rocks from the Wongwibinda metamorphic complex, northern NSW, Australia. Lithos, **15**, 59–75.

Vernon, R. H. and Pooley, G. D., 1981. SEM/microprobe study of some symplectic intergrowths replacing cordierite. Lithos, **14**, 75–82.

Vernon, R.H., 1982. Isobaric cooling of two regional metamorphic complexes related to igneous intrusions in southern Australia. Geology, **10**, 76–81.

Part 1. Metamorphic Geology of the Wongwibinda Metamorphic Complex

Chapter 1

Thermal gradient and timing of high-T–low-P metamorphism in the Wongwibinda Metamorphic Complex, southern New England Orogen, Australia

S. J . CRAVEN,[1] N. R. DACZKO[1] AND J . A. HALPIN[1,2]

[1]GEMOC ARC National Key Centre, Department of Earth and Planetary Sciences, Macquarie University, NSW 2109, Australia
[2]ARC Centre of Excellence in Ore Deposits, University of Tasmania, Private Bag 126, TAS 7001, Australia

Pages 27-44 of this thesis have been removed as they contain published material under copyright. Removed contents published as:

Craven, S.J., Daczko, N.R. and Halpin, J.A. (2012), Thermal gradient and timing of high-T–low-P metamorphism in the Wongwibinda Metamorphic Complex, southern New England Orogen, Australia. *Journal of Metamorphic Geology*, 30: 3-20. Doi. 10.1111/j.1525-1314.2011.00949.x

Chapter 2

High-T–low-P thermal anomalies superposed on biotite-grade rocks, Wongwibinda Metamorphic Complex, southern New England Orogen, Australia: heat advection by aqueous fluid?

S. J . CRAVEN,[1] N. R. DACZKO[1] AND J . A. HALPIN[1,2]

[1]GEMOC ARC National Key Centre, Department of Earth and Planetary Sciences, Macquarie University, NSW 2109, Australia
[2]ARC Centre of Excellence in Ore Deposits, University of Tasmania, Private Bag 126, TAS 7001, Australia

Australian Journal of Earth Sciences (2013)
60, 621–635, http://dx.doi.org/10.1080/08120099.2013.814590

High-*T*–low-*P* thermal anomalies superposed on biotite-grade rocks, Wongwibinda Metamorphic Complex, southern New England Orogen, Australia: heat advection by aqueous fluid?

S. J. CRAVEN[1], N. R. DACZKO[1]* AND J. A. HALPIN[1,2]

[1]*GEMOC ARC National Key Centre, Department of Earth and Planetary Sciences, Macquarie University, NSW 2109, Australia.*
[2]*ARC Centre of Excellence in Ore Deposits, University of Tasmania, Private Bag 126, TAS 7001, Australia.*

The Wongwibinda Metamorphic Complex is characterised by ~400 km^2 of biotite-grade rocks with irregular, km-scale zones of cordierite-bearing high-*T* rock ($T > 550$°C). Cordierite-bearing rocks include different textures: (i) cordierite–K-feldspar–spotted hornfels; (ii) sheared cordierite–K-feldspar–augen schists; and (iii) migmatites with or without comparatively coarse garnet poikiloblasts. Integrated petrography, mineral chemistry and mineral equilibria modelling indicate metamorphic peak conditions in samples of hornfels of approximately $P \leq 250$ MPa and $T = 570$–620°C. Two samples of sheared rock preserve peak conditions of approximately $T = 670$–690°C or $T < 600$°C and $P \leq 200$ MPa, consistent with rapid cooling or variable thermal structure in the Glen Mohr Shear Zone. Electron microprobe U–Th–Pb monazite data indicate a date of 291.5 ± 1.8 Ma for the shear zone, indistinguishable from the age of Hillgrove Plutonic Suite granitoids in the complex. Monazite ages are complex in the hornfels samples that were likely, on the basis of structural relationships, metamorphosed early in the history of the Wongwibinda Metamorphic Complex (*ca* 300 Ma). Previous monazite dating of migmatite samples (*ca* 297 Ma) suggests that the metamorphic cycle was short-lived, lasting less than *ca* 10 m.y. Metamorphic field gradients are <15–23°C km^{-1} across much of the complex but locally steep (>50–100°C km^{-1}) around the high-*T* rocks. Rejection of most heat sources leaves regional conductive heating as the most plausible explanation for the smooth, broad and shallow metamorphic field gradient in the biotite-grade rocks. Another mechanism of heat transfer is required to explain the local, steep metamorphic field gradients and development of high-*T* cordierite-bearing rocks. The spatial association of quartzite units centred within two cordierite-bearing high-*T* domains and an increased abundance of quartz veins above the cordierite isograd suggests heat advection by aqueous fluid locally perturbed the broad conductive heating. Fluid was channelled within shear zones and locally infiltrated nearby rocks. Variable fluid flux and strain have produced the range of different textures in cordierite-bearing rocks of the Wongwibinda Metamorphic Complex.

KEY WORDS: monazite, pseudosection, cordierite, meta-turbidite, migmatite, HTLP metamorphism, Wongwibinda Metamorphic Complex, New England

INTRODUCTION

High-temperature–low-pressure (HTLP) metamorphism involves significant heating of the shallow crust (<10–15 km depth), invoking the question: what mechanisms of heat transfer are responsible? Heat transfer may be conductive or advective and at many scales. Conduction through shallowing of a thermal boundary layer such as the mantle during continental extension (Wickham & Oxburgh 1985; Sandiford & Powell 1986; Bodorkos *et al.* 2002; Collins & Richards 2008; Langone *et al.* 2010) elevates the regional geothermal gradient. Conduction via incubation from increased radioactive heat production (Sandiford *et al.* 1998; McKenzie & Priestley 2008) may also elevate a geothermal gradient, but generally on a smaller scale. The advective transfer of heat by magma is commonly invoked to explain heating of the shallow crust (Thompson & England 1984; Lux *et al.* 1986; Sisson & Hollister 1988; De Yoreo *et al.* 1989; Sisson *et al.* 1989; Collins & Vernon 1991; Sandiford *et al.* 1991), although another mechanism of advective heat transfer may involve hydrothermal activity (Hoisch 1987, 1991; Brady 1988; Chamberlain & Rumble 1988, 1989; De Yoreo *et al.* 1991). Combinations of these end-member mechanisms should also be considered in complex geological settings. In this contribution a multi-disciplinary approach is used on rocks of the Wongwibinda Metamorphic Complex, southern New England Orogen, NSW, to investigate

*Corresponding author: nathan.daczko@mq.edu.au

mechanisms of heat transfer in an HTLP metamorphic complex, in order to explain the development of cordierite-bearing rocks.

Field and laboratory observations of mineral assemblages readily permit recognition of HTLP metamorphism in the Wongwibinda Metamorphic Complex (Binns 1966; Farrell 1992; Craven *et al.* 2012). Conductive heat transfer through shallowing of the mantle during extension is consistent with the late Carboniferous to early Permian tectonic setting of the New England Orogen (e.g. Jenkins *et al.* 2002; Glen 2005, 2013; Collins & Richards 2008; Kemp *et al.* 2009) and reasonably explains the regional west to east increase in metamorphic grade across the Wongwibinda Metamorphic Complex (Craven *et al.* 2012). However, the very steep (~100°C km^{-1}), local (km-scale), non-linear metamorphic field gradients documented by Craven *et al.* (2012) are inconsistent with conductive heating alone. On the basis of spatial and temporal relationships between S-type granites of the Hillgrove Plutonic Suite and the HTLP metamorphism, magmatic advective heat transfer is rejected (Craven *et al.* 2012). Here, we explore the potential for a combination of conductive heat transfer during regional extension and advective heat transfer via hydrothermal activity to produce the observed distribution of high-grade rocks.

Heat advection by hydrothermal activity requires high fluid fluxes (Oliver 1996), most easily inferred for externally derived and chemically reactive fluids. Observations that are diagnostic of heat advection by hydrothermal activity may therefore include wall-rock interaction involving metasomatism at elevated temperatures compared with rocks distal to the site of fluid flux, field evidence for the mechanism of fluid transport (e.g. shear zones, faults, veins), and a spatial association between inferred sites of fluid flux and metamorphic field gradients. Advection of heat by aqueous fluid is likely to be short-lived.

We integrate field mapping, petrography and mineral chemistry with mineral equilibria modelling and *in situ* electron microprobe chemical dating of monazite to constrain the *P*–*T*–*t* evolution of the Wongwibinda HTLP metamorphic complex. The combination of conductive heat transfer through shallowing of the mantle during extension and advection of heat by aqueous fluids is presented as the most likely mechanism of locally heating the highest-*T* rocks of the complex.

REGIONAL GEOLOGY

Three turbidite–granite orogens: Delamerian (western), Lachlan (medial) and New England (eastern) comprise the Tasmanide orogenic system in eastern Australia (see Glen 2005, 2103 for an overview). HTLP metamorphic complexes are commonly associated with discrete belts of S-type granite that comprise up to half the plutonic rocks (White & Chappell 1988). The New England Orogen comprises an ancient, deformed fore-arc basin/accretionary wedge pair, the Tamworth Belt and Tablelands Complex, respectively (Figure 1; e.g. Jenkins *et al.* 2002).

The Wongwibinda Metamorphic Complex (>400 km^2) is located within the Central Tablelands Complex of the southern New England Orogen (Figure 1). The protolith is the Girrakool Beds (Korsch 1978, 1981; Jenkins *et al.* 2002); these are an accreted package of Devonian and Carboniferous medium to fine-grained siliceous turbidites with minor quartzite and very rare metabasite and calcareous nodules.

Late Carboniferous to early Permian S-type Hillgrove Plutonic Suite granitoids intruded the Wongwibinda Metamorphic Complex; three plutons, formally defined by Binns (1966), form the southern (Rockvale Adamellite and southern part of the Abroi Granodiorite), eastern (central part of the Abroi Granodiorite) and northern (Tobermory Adamellite and northern part of the Abroi Granodiorite) boundaries of the Wongwibinda Metamorphic Complex (Figure 2). The Abroi pluton is undeformed in the west and becomes increasingly gneissic towards the Wongwibinda Fault. Although an overall increase in metamorphic grade is observed from west to east in the Wongwibinda Metamorphic Complex, some mineral isograds (e.g. cordierite-in; Figure 2) are patchy and do not follow the contact between the plutonic and metasedimentary rocks (Farrell 1992).

Peak *P*–*T* conditions in the Wongwibinda Metamorphic Complex have been determined at $P \sim 300$ MPa and $T \sim 650$°C (Stephenson & Hensel 1979; Vernon 1982; Farrell 1992; Danis *et al.* 2010; Craven *et al.* 2012). A metamorphic field gradient extends discontinuously (i.e with variable slope) for greater than 20 km from the amphibolite facies Zone of Migmatites to the biotite-in isograd in the Girrakool Beds (Figure 2).

Geochronological studies are few, and Permian biostratigraphic markers identified in the Girrakool Beds (Runnegar 1970; Binns 1966) overlap crytallisation ages for the Hillgrove Plutonic Suite (*ca* 296–289 Ma; Cawood *et al.* 2011; Craven *et al.* 2012; Rosenbaum *et al.* 2012). Metamorphic monazite ages in Wongwibinda Metamorphic Complex migmatite samples return *ca* 297 Ma (Craven *et al.* 2012). Exhumation along the Wongwibinda Fault (eastern boundary of Wongwibinda Metamorphic Complex) and rapid cooling of the Wongwibinda Metamorphic Complex were dated by biotite Rb–Sr at 266–258 Ma (Landenberger *et al.* 1995).

METHODS

Whole-rock major elements and selected trace elements (Table 1) were determined using a Philips PW2400 X-ray fluorescence (XRF) spectrometer at the University of New South Wales Analytical Centre, Sydney, Australia. Mineral major-element oxides (Table 2) were determined by a Cameca SX100 electron microprobe equipped with five wavelength-dispersive spectrometers at operating conditions of 15 kV and 20 nA at the Geochemical Analysis Unit in the Department of Earth and Planetary Sciences, Macquarie University, Sydney.

P–*T* pseudosections were constructed in the model system MnNCKFMASHTO (MnO–Na_2O–CaO–K_2O–FeO–MgO–Al_2O_3–SiO_2–H_2O–TiO_2–Fe_2O_3), using THERMOCALC (version 3.33; Powell & Holland 1988) and the v.5.5 dataset of Holland & Powell (1998, 2011; November 2003 update). Minerals (references refer to the *a*–*x* model used) included in the construction of the pseudosections

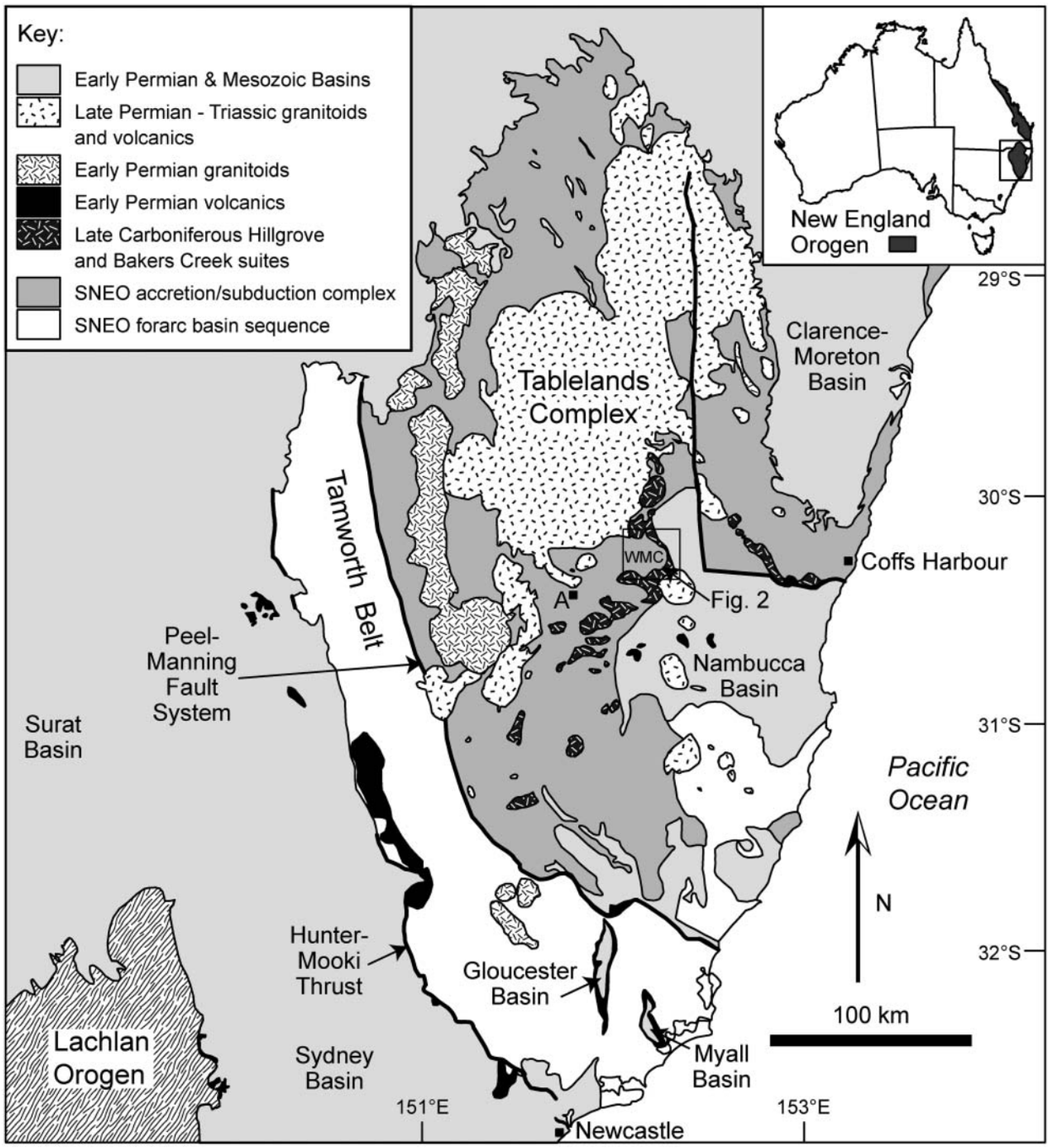

Figure 1 Regional geology of the southern New England Orogen (modified from Jenkins *et al.* 2002). WMC, Wongwibinda Metamorphic Complex; A, Armidale.

are garnet (g; White *et al.* 2005), orthopyroxene (opx; White *et al.* 2002), muscovite (mu; Coggon & Holland 2002), biotite (bi; White *et al.* 2005), chlorite (chl; combination of Mahar *et al.* 1997 and Holland *et al.* 1998), staurolite (st; combination of Mahar *et al.* 1997 and Holland & Powell 1998), cordierite (cd; combination of Mahar *et al.* 1997 and Holland & Powell 1998), epidote (ep; Holland & Powell 1998), plagioclase/potassium feldspar (pl/ksp; Holland & Powell 2003), ilmenite/hematite (ilm/hem; White *et al.* 2005), silicate melt (liq; White *et al.* 2007), aluminosilicate (ky/sill/and), quartz (q) and fluid (H_2O). Mineral average end-member proportions (Table 3) are calculated using the formulas stated in the text.

Thin-sections were examined for monazite on a scanning electron microscope utilising Mineral Liberation Analysis (MLA) software at the University of Tasmania. This MLA software independently controls the instrument for an automated quantitative mineralogical and textural analysis by matching the BSE response of monazite and other mineral phases found in the samples with a standard library, providing mineral identification and

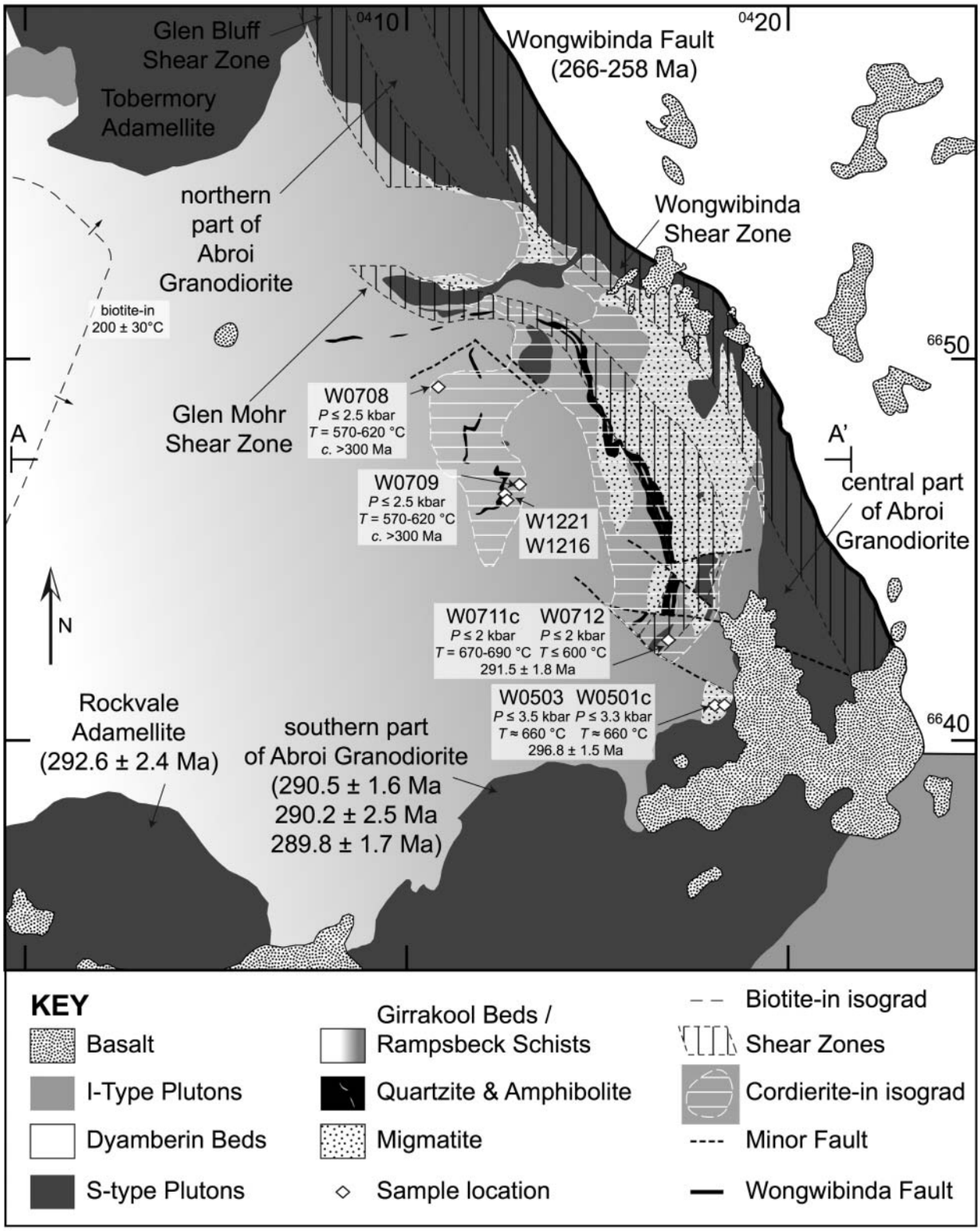

Figure 2 Geology of the Wongwibinda Metamorphic Complex, indicating locations discussed in the text (modified from Leitch 1978; Farrell 1992) and Dorrigo 1:100 000 Sheet (Leitch *et al.* 1971). Darker shading in the Girrakool Beds/Rampsbeck Schists represents increasing metamorphic grade. Age of Rockvale Adamellite and Abroi Granodiorite from Cawood *et al.* (2011). Age of Abroi Granodiorite and metamorphic ages for W0501c and W0503 from Craven *et al.* (2012). Age of faulting and uplift along the Wongwibinda Fault from Landenberger *et al.* (1996). Other metamorphic ages (this study). Section A–A' shown in Figure 8.

Table 1 Representative major-oxide and selected trace element data for pelitic samples. Easting and northing locations are UTM readings in the AGD66 datum, zone 56J.

Sample	W0708	W0709	W0711c	W0712
Easting	410821	412935	416877	416850
Northing	6649264	6646709	6642631	6642631
Type	Hornfels	Hornfels	Shear zone	Shear zone
wt%				
SiO2	66.40	65.68	62.73	65.04
TiO2	0.72	0.74	0.93	0.69
Al2O3	15.59	16.76	16.19	17.31
Fe2O3	5.77	5.94	7.63	5.93
MnO	0.09	0.07	0.26	0.10
MgO	1.88	2.23	2.49	2.26
CaO	1.21	0.84	2.08	1.02
Na2O	2.01	1.28	2.99	2.02
K2O	4.41	4.60	3.21	4.10
LOI	1.60	0.81	1.04	1.70
Total	99.66	98.95	99.55	100.17
ppm				
V	146	140	173	125
Cr	50	76	67	62
Ni	32	39	35	38
Cu	15	51	38	10
Zn	130	117	126	115
Ga	21.1	20.3	21.4	21.5
As	4.9	5.0	5.2	11.5
Rb	157	172	144	141
Sr	179	113	262	147
Y	42	43	43	41
Zr	177	199	190	228
Nb	8.2	10.0	7.3	9.5
Mo	<1.8	2.0	<1.8	<1.8
Cd	<3.0	4.5	4.7	3.1
Sn	<3.9	<3.9	<3.9	<3.9
Sb	<2.9	<2.9	<2.9	<2.9
Ba	944	711	794	1156
Ce	56	61	56	58
Pb	28.5	27.3	22.9	30.5
Th	10.0	11.8	8.6	10.9
U	6.2	6.8	4.3	6.0
Co	33.0	44.4	45.3	33.4

Loss of ignition (LOI) at 1050°C. A less than symbol (<) represents concentrations below the stated lower limit of detection.

textural context of monazite grains and surrounding minerals. Once located, monazite was analysed at the University of Tasmania *in situ* using a Cameca SX100 electron microprobe equipped with five wavelength dispersive spectrometers at operating conditions of 20 kV and 100 nA. The method for the U–Th–Pb monazite dating (including error estimation/propagation and background Pb estimation) follows Berry *et al.* (2007) and Halpin *et al.* (2008). Th, U and Pb calibration standards were analysed at the start and end of each of the three analytical sessions to correct for machine drift if necessary. Instrument calibrations were checked using standard monazite grains including RGL4B (1566 ± 3 Ma; Rubatto *et al.* 2001) and 94-222 (467 ± 8 Ma; Hand *et al.* 1999) and yielded weighted mean ages of 1571 ± 11 Ma (95% confidence, $n = 18$) and 468 ± 6 Ma (95% confidence, $n = 18$), respectively. On the basis of the multiple calibrations against international standard monazites over several years, we consider the systematic error to be <0.5%. Individual monazite ages are presented in the Supplementary Papers, and ages of monazite populations are presented as calculated tanh ages (Powell *et al.* 2002; Kelsey *et al.* 2003; Daczko *et al.* 2009) that reflect the actual data scatter, rather than assuming a Gaussian distribution. A weighted least-squares (wlsq) approach (Mikhail 1976), which does assume that the data are Gaussian-distributed, is also calculated for comparison with the tanh age (Table 4).

FIELD RELATIONSHIPS AND PETROGRAPHY

Cordierite-bearing samples in the Wongwibinda Metamorphic Complex form three textural groups: (i) cordierite–K-feldspar–spotted hornfels; (ii) sheared cordierite–K-feldspar–augen schists; and (iii) migmatites with comparatively coarse garnet poikiloblasts. The migmatites are well studied (Farrell 1992; Danis *et al.* 2010; Craven *et al.* 2012), and this study focuses on two samples of each of the other textural groups. Sample locations are shown on Figure 2. The sampled lithologies formally encompass the Rampsbeck Schists and border the Zone of Migmatites. However, field observations indicate one protolith (Girrakool Beds) and petrographic observations show the range of textural types above. Therefore, we chose not to use these formal names, as the boundaries between them are gradational and difficult to define. In this contribution, we refer to the textural groups as (i) hornfels; (ii) augen schists; and (iii) migmatites. Samples of hornfels (W0708 and W0709) and augen schists (W0711c and W0712) were collected on the basis of previous mapping of the cordierite-in isograd and regional shear zones (Figure 2; Farrell 1992).

Cordierite–K-feldspar–spotted hornfels (samples W0708 and W0709)

Samples with hornfels texture (pre-D1 spotted hornfels of Farrell 1992) are restricted to a 3 × 5 km area in the centre–northeast of the complex, centred on the western group of quartzites (Figure 2). They are characterised by cordierite poikiloblasts (up to 20 mm; Figures 3a, b, 4a, b). W0709 also contains K-feldspar poikiloblasts (up to 1 mm; Figure 3b) in both the rim domains of larger cordierite poikiloblasts and the matrix (Figure 4b). Poikiloblasts are equigranular and nodular (Figures 3b, 4a, b). Inclusions within poikiloblasts are randomly oriented and dominated by biotite and quartz. Both samples contain randomly oriented coarse muscovite grains (0.6–1.0 mm and 0.2–0.5 mm in W0708 and W0709, respectively; Figure 3a, b) that share crystal faces with K-feldspar and cordierite (Figure 3b). The matrix (grain-size up to 1.0 mm) consists of randomly oriented biotite, quartz and plagioclase. Poikiloblastic ilmenite is common in both samples (Figure 4a, b), a feature unusual for the complex where oxide minerals are rare (Craven *et al.* 2012). Cordierite in sample W0708 is partially pseudomorphed by pinnite in a thin rim with low BSE emission (<200 μm; Figure 4a). Accessory minerals include fine-grained apatite, zircon and monazite. The key features

Table 2 Representative electron microprobe analyses.

	W0708						W0709						W0711c				W0712				
	pl	**ksp**	**mu**	**bi**	**cd**	**ilm**	**pl**	**ksp**	**mu**	**bi**	**cd**	**ilm**	**g**	**pl**	**ksp**	**bi**	**pl**	**ksp**	**mu**	**bi**	**cd**
SiO_2	61.88	63.84	45.36	34.59	47.32	0.06	60.58	64.03	45.55	34.66	47.33	0.02	36.87	61.14	62.58	33.87	61.49	63.34	45.58	34.43	47.86
TiO_2	0.00	0.01	0.78	2.44	0.00	51.71	0.00	0.00	1.03	2.93	0.00	51.19	0.00	0.00	0.00	3.14	0.01	0.00	0.76	3.28	0.00
Al_2O_3	23.80	18.54	36.18	20.10	32.17	0.00	24.43	18.68	35.88	19.79	32.62	0.00	20.99	23.62	18.40	19.13	24.01	18.70	36.40	19.14	32.92
Cr_2O_3	0.01	0.00	0.00	0.05	0.00	0.03	0.00	0.03	0.07	0.08	0.00	0.01	0.00	0.01	0.01	0.02	0.00	0.00	0.03	0.05	0.00
FeO	0.02	0.06	0.70	21.13	9.65	42.57	0.27	0.13	0.86	19.95	10.08	45.86	29.20	0.14	0.34	19.48	0.00	0.08	0.73	20.57	8.40
MnO	0.00	0.00	0.04	0.25	0.92	3.19	0.04	0.03	0.00	0.14	0.31	1.14	10.29	0.02	0.00	0.35	0.00	0.00	0.00	0.29	0.79
MgO	0.00	0.00	0.41	7.48	6.84	0.12	0.00	0.01	0.47	7.54	6.86	0.17	2.48	0.01	0.01	7.76	0.00	0.00	0.47	7.77	7.69
CaO	5.17	0.00	0.00	0.00	0.03	0.02	5.95	0.01	0.00	0.01	0.02	0.01	0.82	5.17	0.00	0.00	4.98	0.00	0.00	0.01	0.01
Na_2O	9.14	1.70	0.36	0.13	0.18	0.01	8.54	1.38	0.45	0.11	0.13	0.00	0.01	9.09	1.42	0.12	8.76	1.54	0.43	0.14	0.27
K_2O	0.13	14.53	11.06	9.46	0.02	0.00	0.14	14.92	10.80	9.39	0.00	0.00	0.00	0.16	14.27	9.56	0.12	14.34	10.77	9.40	0.01
Total	100.16	98.68	94.89	95.61	97.14	97.72	99.95	99.20	95.12	94.60	97.37	98.41	100.66	99.36	97.02	93.44	99.37	98.00	95.17	95.08	97.95
O	8	8	22	22	18	3	8	8	22	22	18	3	12	8	8	22	8	8	22	22	18
Si	2.7	3.0	6.1	5.3	5.0	0.0	2.7	3.0	6.1	5.3	5.0	0.0	3.0	2.7	3.0	5.3	2.7	3.0	6.1	5.3	5.0
Ti	0.0	0.0	0.1	0.3	0.0	1.0	0.0	0.0	0.1	0.3	0.0	1.0	0.0	0.0	0.0	0.4	0.0	0.0	0.1	0.4	0.0
Al	1.2	1.0	5.7	3.6	4.0	0.0	1.3	1.0	5.6	3.6	4.0	0.0	2.0	1.2	1.0	3.5	1.3	1.0	5.7	3.5	4.0
Cr	0.0	0.0	0.0	0.0	0.0	0.0	0.0	0.0	0.0	0.0	0.0	0.0	0.0	0.0	0.0	0.0	0.0	0.0	0.0	0.0	0.0
Fe^{2+}	0.0	0.0	0.1	2.7	0.9	0.9	0.0	0.0	0.1	2.6	0.9	1.0	2.0	0.0	0.0	2.5	0.0	0.0	0.1	2.6	0.7
Mn	0.0	0.0	0.0	0.0	0.1	0.1	0.0	0.0	0.0	0.0	0.0	0.0	0.7	0.0	0.0	0.0	0.0	0.0	0.0	0.0	0.1
Mg	0.0	0.0	0.1	1.7	1.1	0.0	0.0	0.0	0.1	1.7	1.1	0.0	0.3	0.0	0.0	1.8	0.0	0.0	0.1	1.8	1.2
Ca	0.2	0.0	0.0	0.0	0.0	0.0	0.3	0.0	0.0	0.0	0.0	0.0	0.1	0.2	0.0	0.0	0.2	0.0	0.0	0.0	0.0
Na	0.8	0.2	0.1	0.0	0.0	0.0	0.7	0.1	0.1	0.0	0.0	0.0	0.0	0.8	0.1	0.0	0.8	0.1	0.1	0.0	0.1
K	0.0	0.9	1.9	1.8	0.0	0.0	0.0	0.9	1.8	1.8	0.0	0.0	0.0	0.0	0.9	1.9	0.0	0.9	1.8	1.8	0.0
Total	5.0	5.0	14.0	15.5	11.0	2.0	5.0	5.0	14.0	15.5	11.0	2.0	8.0	5.0	5.0	15.5	5.0	5.0	14.0	15.5	11.0
X_{Alm}													0.65								
X_{Prp}													0.10								
X_{Grs}													0.02								
X_{Sps}													0.23								
X_{An}	0.24						0.28							0.24			0.24				
X_{Mg}								0.88													
X_{Or}		0.85													0.87			0.86			
X_{Fe}			0.49	0.61	0.44				0.50	0.60	0.45					0.58			0.47	0.60	0.38

Fe^{2+} is total Fe.

of this group are the poikiloblasts of cordierite and randomly oriented grains. Some rock samples of 'hornfels' from near the western group of quartzites contain weakly aligned minerals, suggesting variable minor strain.

Sheared cordierite–K-feldspar–augen schists (samples W0711c and W0712)

These samples were collected from within high-strain zones of the Glen Mohr Shear Zone (Figure 2; D3 of

Table 3 Mineral end-member proportions showing the mean and standard deviation of all grains analysed.

		W0708			W0709			W0711c			W0712		
Mineral		**Mean**	**SD**	***n***	**Mean**	**SD**	***n***	**Mean**	**SD**	***n***	**Mean**	**SD**	***n***
Plagioclase	X_{An}	0.24	0.00	11	0.29	0.02	8	0.23	0.02	9	0.24	0.01	9
K-feldspar	X_{Or}	0.89	0.02	13	0.87	0.02	10	0.87	0.02		0.84	0.02	5
Biotite	X_{Fe}	0.61	0.02	8	0.61	0.01	18	0.59	0.01	22	0.60	0.00	9
Cordierite	X_{Fe}	0.44	0.01	47	0.44	0.01	12	pin.	–	–	0.38	0.01	10
Muscovite	X_{Fe}	0.52	0.04	14	0.49	0.04	10				0.50	0.04	10
	X_{Na}	0.07	0.01	14	0.07	0.02	10				0.07	0.02	10
Ilmenite	X_{Fe}	0.92	0.02	10	0.96	0.01	6						
	X_{Mn}	0.08	0.02	10	0.03	0.01	6						
Garnet	X_{Alm}							0.64	0.01	13			
	X_{Pyp}							0.10	0.01	13			
	X_{Grs}							0.02	0.00	13			
	X_{Sps}							0.24	0.01	13			

pin., cordierite is completely pseudomorphed by pinnite.

Table 4 U–Th–Pb pooled monazite tanh and Mikhail ages.

Sample	*n*	Mikhail age (Ma) (2σ error)			σ fit	σ fit limit for 95% conf.	Tanh age (Ma) (2σ error)		
Hornfels W0708	16	302.3	±	11.0	1.60	1.29	304.6	±	11.8
Hornfels W0709	23	300.4	±	8.3	1.61	1.24	311.3	±	8.4
Hornfels combined	39	301.1	±	6.6	1.58	1.19	314.6	±	6.6
Rejected >330 Ma	29/39	295.3	±	7.3	1.17	1.22	301.0	±	5.4
Rejected >340 Ma	32/39	301.3	±	7.2	1.16	1.20	307.8	±	5.6
Shear zone W0711c	36	291.4	±	5.6	0.92	1.19	291.9	±	2.8
Shear zone W0712	36	289.8	±	5.3	1.43	1.19	291.4	±	2.7
Shear zone combined	72	290.6	±	3.9	1.20	1.34	291.5	±	1.8

σ fit, goodness of fit parameter ($\sqrt{}$MSWD).

Farrell 1992). Sample W0711c contains poikiloblastic garnet (<1.6 mm; Figure 3c) and K-feldspar augen (<0.6 mm; Figure 4c) enveloped by a well-developed coarse-grained continuous schistosity (S3 of Farrell 1992), defined by quartz–plagioclase–biotite (<0.8 mm grainsize; Figure 3c). Inclusions within the poikiloblasts are dominated by fine-grained biotite and quartz (<0.04 mm). The matrix includes quartz–plagioclase–biotite. Quartz grains exhibit undulose extinction and recrystallisation textures. Accessory minerals include fine-grained apatite, zircon, monazite and pyrite.

Sample W0712 contains poikiloblastic cordierite (up to 12 mm) and K-feldspar (0.2–1 mm; Figure 3d). A well-developed coarse-grained spaced schistosity (S3 of Farrell 1992), defined by biotite (<1 mm), envelops the poikiloblasts to form augen schist. K-feldspar may be perthitic (Figure 4d). Inclusions within the poikiloblasts are dominated by fine-grained biotite and quartz (<0.03 mm). Quartz and plagioclase display recrystallisation textures and undulose extinction in the matrix. Accessory minerals include fine-grained apatite, zircon, monazite, tourmaline and pyrite.

Quartzite and nearby hornfels

Eastern quartzite rocks are associated with minor amphibolites (Figure 2; Stephenson & Hensel 1979, 1982), both largely deformed in the Glen Mohr Shear Zone (Figure 2; D3 of Farrell 1992). Poor outcrop and shearing reduce the clarity of original relationships between the quartzite, amphibolite and meta-turbidite rocks in the eastern area. All previous workers have interpreted these rocks as a metamorphosed interbedded package of turbidite, with minor impure chert and basaltic lavas (Stephenson & Hensel 1979, 1982; Farrell 1992). However, quartz veins and pegmatite within the shear zone are syn-tectonic on the basis of mutual cross cutting relationships. A link between quartz veins and the thicker quartzite outcrops makes plausible a hydrothermal metamorphic origin for the quartzite units. In this scenario, the protolith of the quartzite units is precipitated from fluid flux channelled along the shear zone, rather than being metamorphosed chert units.

Quartzite rocks in the western group are not associated with amphibolite and are not deformed by D3 shear zones (Figure 2). Field observations show good outcrop in creek sections. Key relationships include: (i) cordierite grainsize in meta-turbidite increases from <1 mm a few hundred metres from quartzite to > 20 mm within a few metres of quartzite; (ii) layers within quartzite range from pure to impure, with impure layers preserving laminations; (iii) there are local differences in strike between layering in quartzite and bedding in meta-turbidite; (iv) quartz veins in meta-turbidite increase in abundance with proximity to quartzite (Figure 3e); and (v) key metamorphic minerals are spatially associated with quartz veins in the hornfels (Figure 3f).

Field observations reveal the network of veins in meta-turbidite rocks proximal to the quartzite units to be pervasive throughout the outcrops (Stuart 2012). Sets of veins are commonly seen to be cross-cutting. Thin-sections of quartz veins reveal a complex accessory mineralogy of other silicates, oxides and sulfides (e.g. Figure 3f). The veins are divided into two groups on the basis of width. Narrow veins <5 mm are common proximal (<250 m) to the main quartzite units, and broad veins >5 mm are observed within 50 m of the quartzite units. Distal to the quartzite units, veining is much less common and less complex, being composed almost entirely of quartz. Pure quartz layers in the quartzite units (up to 1 m thick) are interpreted as metamorphosed large veins; these are too large to be derived from outcrop-scale dewatering and require open system processes and significant fluid flux.

WHOLE ROCK AND MINERAL GEOCHEMISTRY

In this section, we outline the whole-rock major and trace-element geochemistry of the four samples examined (Table 1) to explore the variation in composition between samples and to give context to the calculated phase diagrams. Representative mineral chemistry is presented in Table 2, and average end-member proportions are given in Table 3.

Three of the samples (W0708, W0709 and W0712) are very similar in composition; these have (i) high SiO_2 (65.0–66.4 wt%); (ii) moderate Al_2O_3 (15.6–17.3 wt%); and (iii) K_2O (4.1–4.6 wt%) greater than Na_2O (1.3–2.0 wt%). The other sample (W0711c) is (i) higher in MnO and (ii) lower in K_2O, and (iii) tends to have variably higher or lower contents of the other elements compared with the first three samples. All four samples plot as claystones and psammites on an Al_2O_3–CaO–[FeO+MgO]

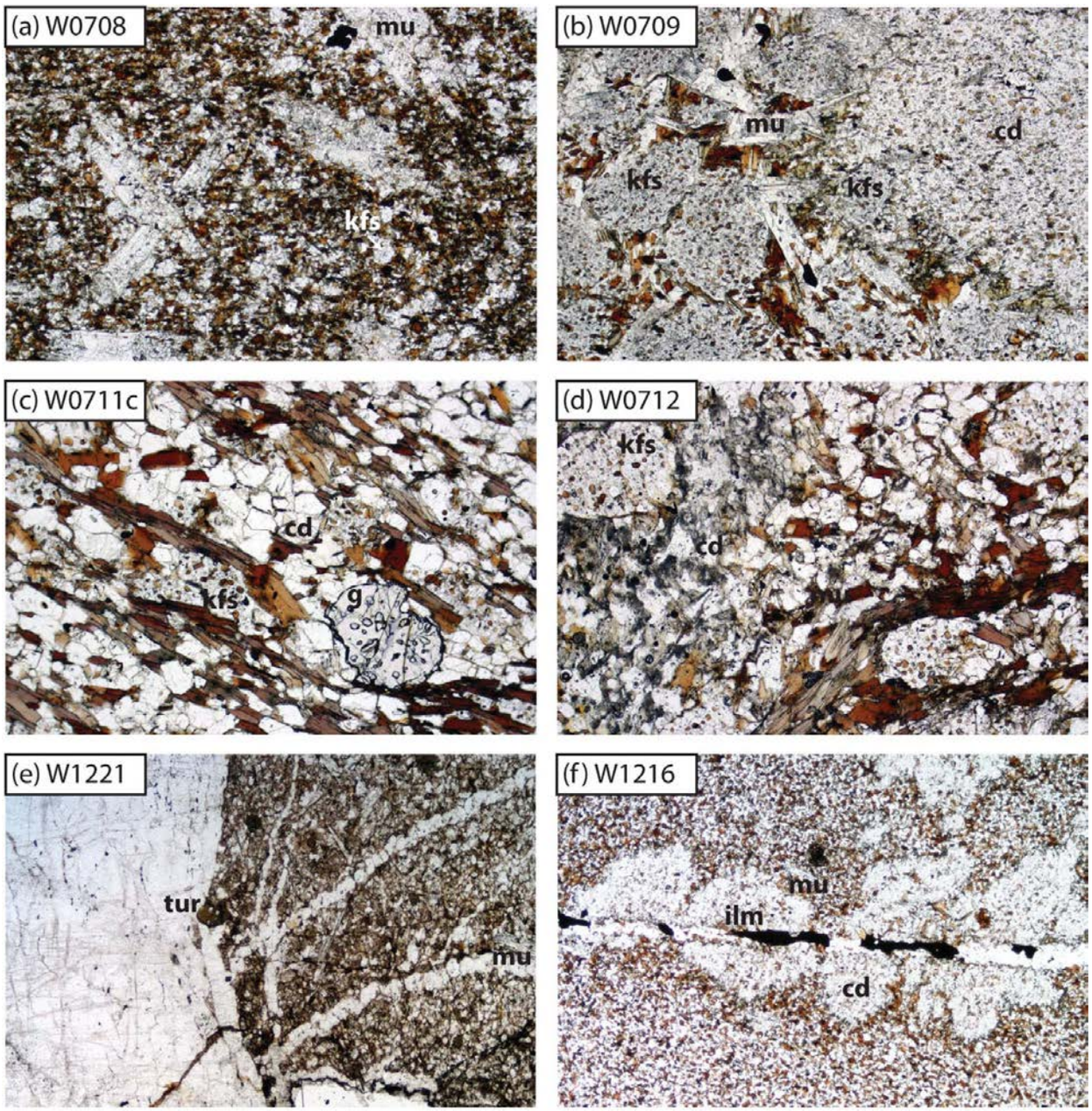

Figure 3 (a, b) Photomicrographs of cordierite–biotite–muscovite–K-feldspar–plagioclase–quartz–ilmenite hornfels (samples W0708 and W0709 respectively). Muscovite grains are randomly oriented. Cordierite and K-feldspar are poikiloblastic. (c) Photomicrograph of well-foliated garnet–cordierite–biotite–K-feldspar–plagioclase–quartz schist (sample W0711c). Garnet and K-feldspar are poikiloblastic. Cordierite is completely pseudomorphed by pinnite. (d) Photomicrograph of well-foliated cordierite–biotite–muscovite–K-feldspar–plagioclase–quartz augen schist (sample W0712). Cordierite and K-feldspar are poikiloblastic augen surrounded by shear zone fabric. (e) Photomicrograph of meta-turbidite rich in quartz veins proximal to western quartzite units. (f) Photomicrograph of quartz vein with complex accessory mineralogy including ilmenite, biotite and two feldspars. Note cordierite growth spatially associated with the vein. Field of view for all photomicrographs is 3.5 mm across.

ternary diagram (e.g. Vernon & Clarke 2008). The trace-element compositions of all four samples are broadly similar.

Neither appreciable compositional zoning nor inter-sample compositional differences were detected in plagioclase and potassium feldspar; these show a narrow compositional range with $X_{An}[Ca/(Ca+Na)] = 0.23–0.29$ and $X_{Or}[K/(K+Na)] = 0.84–0.89$, respectively, in all four samples. Plagioclase is oligoclase.

The compositions of biotite in the two hornfels samples (W0708, W0709) and the two shear zone samples (W0711c, W0712) are similar with $X_{Fe}[Fe/(Fe+Mg)] = 0.59–0.61$. Biotite has moderate Ti content in all samples with 0.2–0.5 cations of Ti per formula unit, based on 22 oxygen. Muscovite is compositionally uniform with $X_{Na}[Na/(Na+K)] = 0.07$ and $X_{Fe} = 0.49–0.52$. All muscovite grains have 3.0–3.2 Si cations per formula unit, based on 11 oxygen.

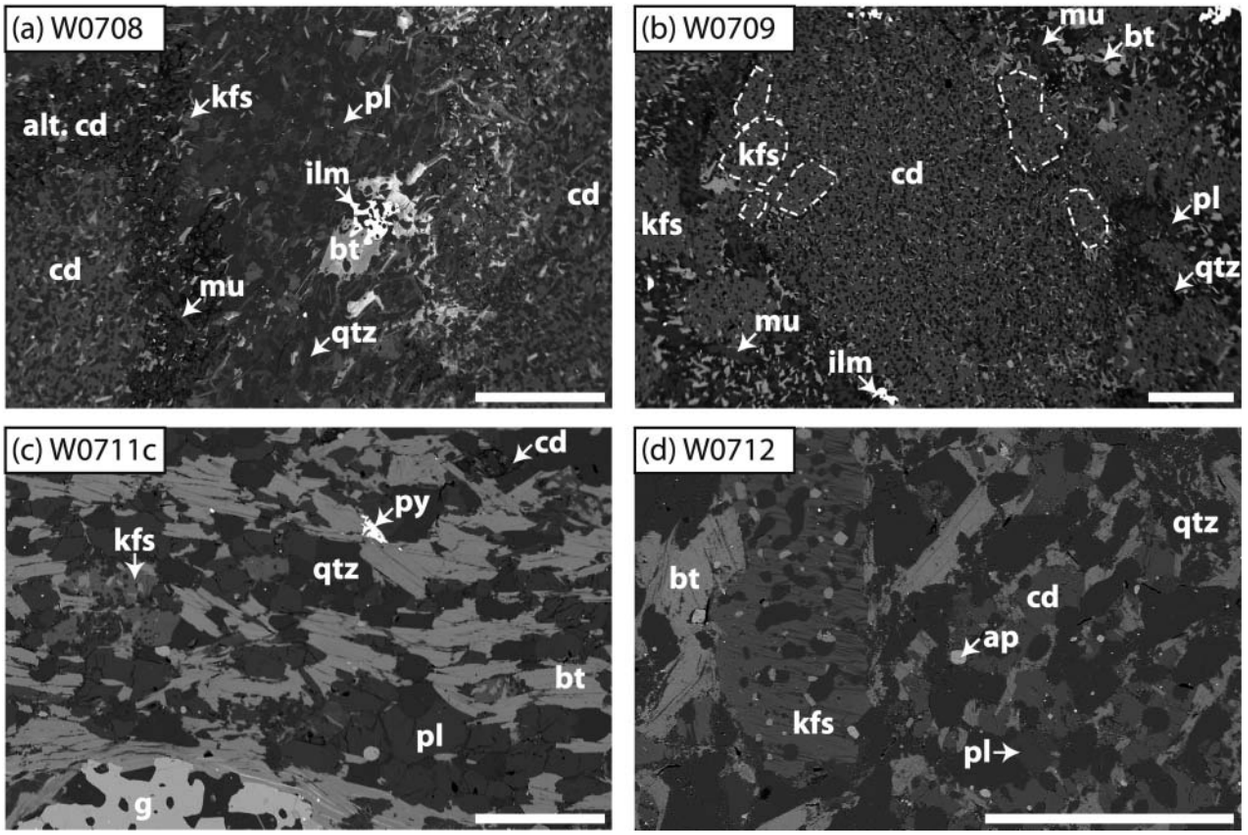

Figure 4 Back-scattered electron images. (a) Cordierite hornfels with narrow pinnite alteration on rim of cordierite. Cordierite and ilmenite are poikiloblastic. (b) Cordierite hornfels with K-feldspar inclusions in the rims of cordierite poikiloblasts. K-feldspar is also poikiloblastic. (c) Well-foliated schist with cordierite completely pseudomorphed by pinnite. (d) Well-foliated augen schist with cordierite and K-feldspar poikiloblastic augen. Note albite flames in K-feldspar. Scale bar is 0.5 mm.

Cordierite shows insignificant compositional zoning and has $X_{Fe} = 0.44$ in both hornfels samples (W0708, W0709). Cordierite is also not zoned and has $X_{Fe} = 0.38$ in one shear zone sample (W0712) and is pseudomorphed by pinnite in the second sample from the Glen Mohr Shear Zone (W0711c).

Garnet in one shear zone sample (W0711c) is spessartine-rich almandine, which displays no appreciable compositional zoning. Grains in sample W0711c have $Alm_{0.64}Prp_{0.10}Grs_{0.02}Sps_{0.24}$, where Alm = X_{Alm} = Fe/(Fe+Mg+Ca+Mn), Prp = X_{Prp} = Mg/(Fe+Mg+Ca+Mn), Grs = X_{Grs} = Ca/(Fe+Mg+Ca+Mn), and Sps = X_{Sps} = Mn/(Fe+Mg+Ca+Mn).

CALCULATED PHASE DIAGRAMS

Bulk-rock compositions were derived by XRF (Table 1) recalculated to molar percent and are shown on the diagrams (Figures 5a, b, 6a, b). Sub-solidus assemblages for each bulk-rock composition are calculated with H_2O in excess. Supra-solidus assemblages were not calculated, as none of the samples examined are migmatites. The rarity of opaque minerals in most samples suggests low bulk Fe_2O_3 contents in the modelled bulk compositions. Furthermore, the presence of altered pyrite suggests originally reduced conditions. Diener & Powell (2010) show that typical pelite compositions with low Fe^{3+} contents contain ilmenite as the opaque oxide phase; magnetite occurs at higher $X Fe^{3+}$. Given that samples contain only ilmenite and no magnetite, our estimate of 1% total Fe as Fe_2O_3 (recast as 'O' in MnNCKFMASHTO) is an upper limit. This estimated Fe^{3+} content results in trace (maximum <<1 molar oxide%) ilmenite across the pseudosections. Representative pseudosections were constructed for two hornfels samples (W0708 and W0709, Figure 5a, b) and two augen schist samples from the Glen Mohr Shear Zone (W0711c and W0712; Figure 6a, b).

The inferred peak assemblage for both the hornfels samples (W0708 and W0709) contains cordierite, biotite, muscovite, potassium feldspar, plagioclase, quartz and ilmenite. Although cordierite, muscovite and potassium feldspar form an unusual assemblage, we argue for equilibrium on the basis of a lack of reaction textures, shared crystal faces and the correlation of natural and modelled mineral chemistry of cordierite and biotite. Inferred peak P–T conditions for both samples correspond to a narrow quinivariant field (Figure 5a, b). Calculated cordierite compositional isopleths (X_{Fe}(cd)) are largely T-sensitive with a positive gradient. Calculated biotite compositional isopleths (X_{Fe}(bi)) are also T-sensitive in the narrow peak field, but then barely change once cordierite has replaced muscovite with increasing

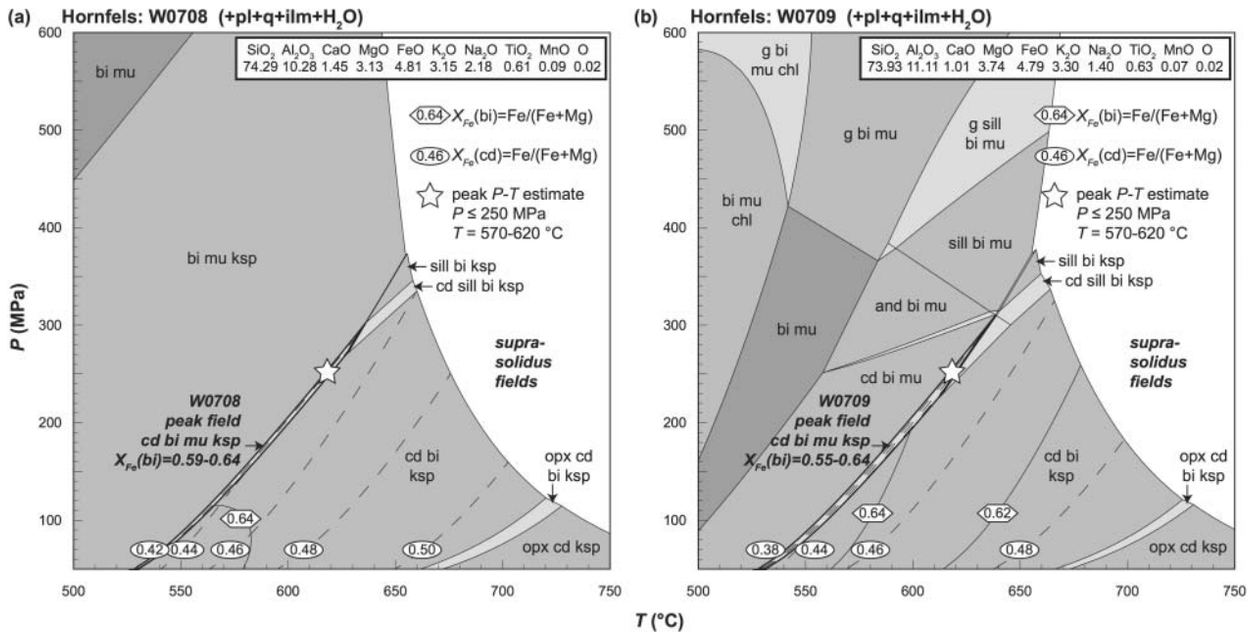

Figure 5 (a, b) *P–T* pseudosections calculated for the bulk compositions of two hornfels samples. The inferred peak assemblage fields are labelled and outlined in bold. Mineral compositional contours are shown in relevant fields. The star indicates the best peak *P–T* estimate.

temperature. The intersection of X_{Fe}(bi) and X_{Fe}(cd) for the mineral compositions from each sample (Table 3) occurs towards the high-*P* end of the peak field and indicates peak conditions of approximately $P \leq 250$ MPa and $T = 570–620°C$ (Figure 5a, b).

The inferred peak assemblage for augen schist sample W0711c from the Glen Mohr Shear Zone is best represented by the quinivariant field involving garnet, cordierite, biotite, potassium feldspar, plagioclase, quartz and ilmenite (Figure 6a). Calculated biotite and garnet compositional isopleths (X_{Fe}(bi); X_{Alm} and X_{Sps}) are largely *T*-sensitive. X_{Fe}(bi), X_{Alm} and X_{Sps} for the biotite and garnet compositions from sample W0711c (Table 3) occur towards the high-*T* end of the peak field and indicates peak conditions of approximately $P \leq 200$ MPa and $T = 670–690°C$ (Figure 6a).

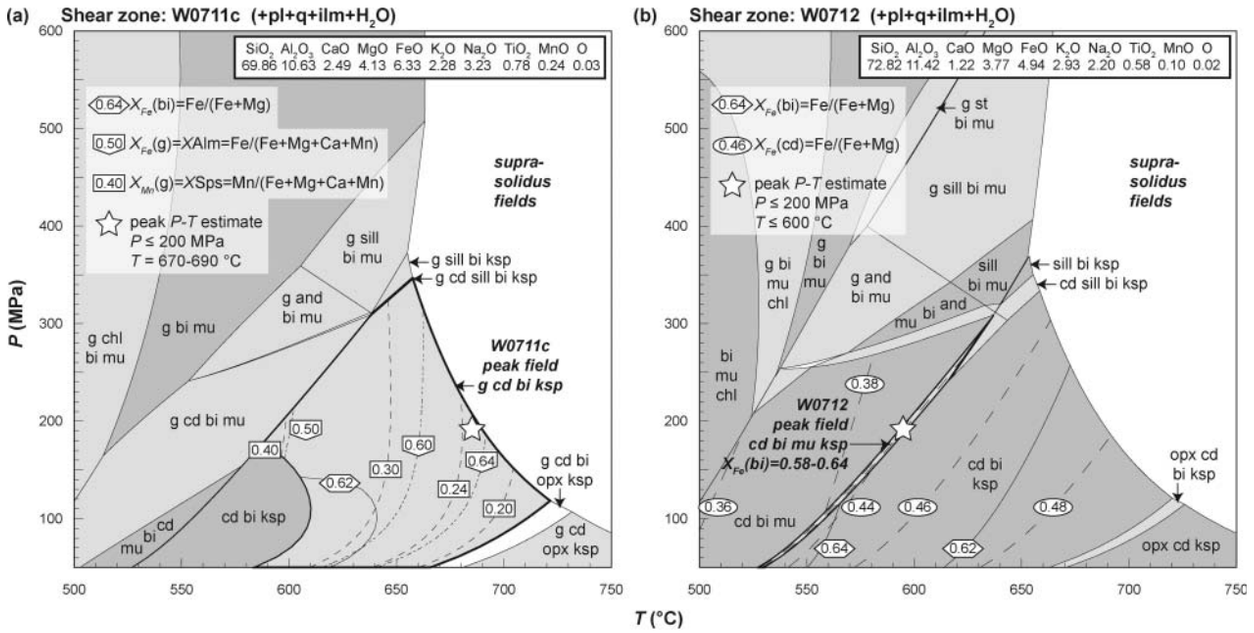

Figure 6 (a, b) *P–T* pseudosections calculated for the bulk compositions of two shear zone samples. The inferred peak assemblage fields are labelled and outlined in bold. Mineral compositional contours are shown in relevant fields. The star indicates the best peak *P–T* estimate.

The inferred peak assemblage for the second augen schist sample (W0712) from the Glen Mohr Shear Zone contains cordierite, biotite, muscovite, potassium feldspar, plagioclase, quartz and ilmenite. Inferred peak *P–T* conditions correspond to a narrow quinivariant field (Figure 6b). Calculated cordierite compositional isopleths (X_{Fe}(cd)) are largely *T*-sensitive with a positive gradient at higher-*T*. Calculated biotite compositional isopleths (X_{Fe}(bi)) are also *T*-sensitive in the narrow peak field. The intersection of X_{Fe}(bi) and X_{Fe}(cd) for the mineral compositions from this sample (Table 3) occurs around $P = 200$ MPa and indicates peak conditions of approximately $P \leq 200$ MPa and $T \leq 600$°C (Figure 6b).

AGE OF METAMORPHISM

Two thin-sections of hornfels (W0708 and W0709) and two thin-sections of augen schist sampled within the Glen Mohr Shear Zone (W0711c and W0712) contain common accessory monazite. Analysed monazite grains in all samples (<75 μm, commonly < 30 μm in the two hornfels samples) predominately occur in the matrix, commonly located at the contacts between grains of biotite, muscovite, feldspar and/or quartz. Rare grains are included within quartz, feldspar, mica, cordierite and apatite.

A frequency histogram (Figure 7a) shows the spread of individual monazite ages from each sample. No correlation between Th/U ratio, age and textural setting was observed. The population from the hornfels samples has a wide spread in ages, whereas the population from the Glen Mohr Shear Zone samples has one main peak near the Carboniferous/Permian boundary (Figure 7a). Thirty-nine analyses from samples W0708 and W0709 range between 390 ± 25 Ma and 193 ± 23 Ma (1σ error, Table S1) and yield a pooled tanh age of 314.6 ± 6.6 Ma (95% confidence). Seventy-two individual monazite ages from samples W0711c and W0712 range between 337 ± 17 Ma and 220 ± 14 Ma (Supplementary Paper). The pooled tanh age for the two shear zone samples is 291.5 ± 1.8 Ma (Figure 7b). We suggest the age of the two hornfels samples may be affected by the inclusion of marginally older detrital grains on the basis of the large spread in ages. If grains >340 Ma and >330 Ma are removed from age calculations on the basis that they may be detrital, the pooled age of the hornfels samples approaches *ca* 300 Ma (Table 4). The age of metamorphism in samples of hornfels is poorly constrained. The age of the two samples from the Glen Mohr Shear Zone likely represents a real metamorphic age on the basis of tight clustering of data and a lack of relationship between textural setting and age.

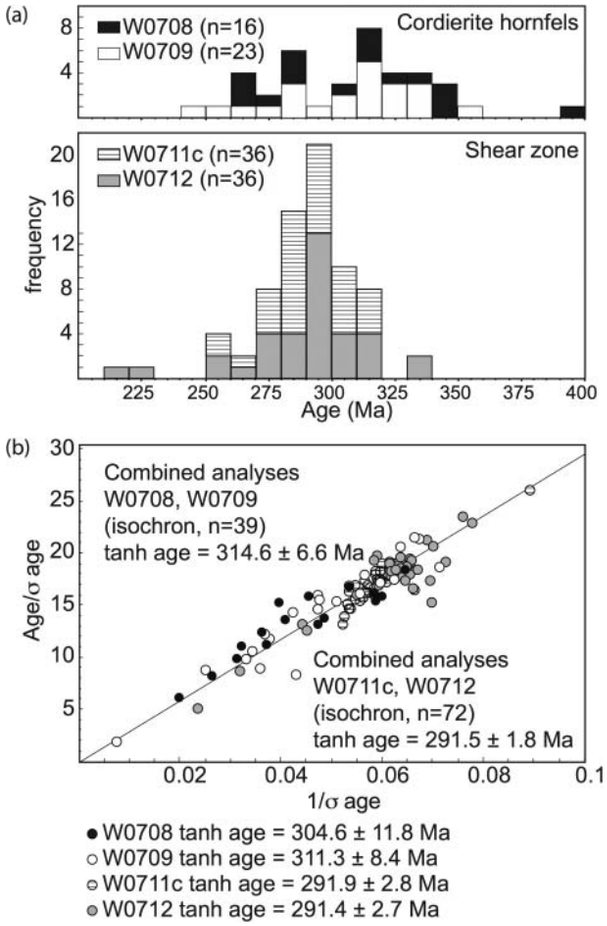

Figure 7 (a) Stacked frequency histograms of individual monazite ages for two samples of cordierite hornfels and two samples of in the shear zone. A broad spread in monazite ages in the cordierite hornfels samples possibly reflects a mix of detrital, diagenetic and metamorphic grains. A single age peak near the Carboniferous/Permian boundary for the shear zone samples likely reflects a metamorphic age. Bin size = 10 Ma. (b) The combined monazite ages from the hornfels samples define a poor isochron at 314.6 ± 6.6 Ma. The combined monazite ages from the shear zone samples define an excellent isochron at 291.5 ± 1.8 Ma.

DISCUSSION

P–T–t history of the Wongwibinda Metamorphic Complex

The MnNCKFMASHTO pseudosections and monazite dating presented for the Wongwibinda Metamorphic Complex improve our understanding of the *P–T–t* history of the cordierite-bearing rocks and refine the discontinuous pattern of metamorphic field gradient. Peak *T* in variably textured cordierite-bearing samples form a cluster (570–690°C), defining at least two high-*T* domains in a profile across the complex (A–A′, Figures 2, 8). The high-*T* domains are small (km-scale) and discontinuous (Figure 8), with locally very steep metamorphic field gradients (~100°C km^{-1}; Craven *et al.* 2012). The patchy development of high-*T* rocks in a largely biotite-grade complex exposes east–west metamorphic field gradients that are composite and variable, with at least two peaks or 'hot-spots' at the scale of the complex (Figure 8). We term this type of field gradient *discontinuous* to distinguish it from smooth *continuous* field gradients as would be expected for conductive mechanisms of heating the crust (Figure 8). Our new *P* estimates show a pattern of maximum *P* in the east of the Wongwibinda Metamorphic Complex and minimum *P* in the west. These data resolve tilting of the complex to at least 10° about a northerly axis, defining an oblique paleo-direction for

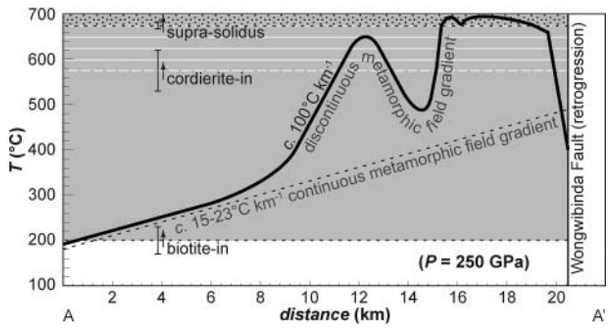

Figure 8 Temperature *vs* distance cartoon for section A–A' shown on Figure 2. The range of temperatures of biotite bearing, cordierite bearing and supra-solidus conditions (at 250 MPa) are determined from THERMOCALC (Figures 5, 6) for four different bulk rock compositions. The ~15–23°C km^{-1} metamorphic field gradient is determined from the difference in temperature between the biotite-in isograd (200°C) and the temperatures determined by Craven *et al.* (2012) for biotite grade rocks ~10 km east of the biotite-in isograd (350–430°C). The ~100°C km^{-1} metamorphic field gradients are from Craven *et al.* (2012).

the regional discontinuous metamorphic field gradient. Our new *P–T* estimates do not extend the maximum possible pressure of the peak metamorphism above 300–350 MPa, confirming that the regional metamorphic field gradient developed at less than ~12 km depth (Craven *et al.* 2012).

Two samples from within the Glen Mohr Shear Zone, collected within a few tens of metres from each other, record differences in *T* of ~70–90°C, but their age of metamorphism is indistinguishable using monazite dating. These results are consistent with rapid cooling or variable thermal structure in the shear zone. Given that the age of monazite in the shear zone (291.5 ± 1.8 Ma) overlaps the age of local Hillgrove Plutonic Suite granitoids (*ca* 292–290 Ma; Cawood *et al.* 2011; Craven *et al.* 2012), and parts of the suite are undeformed (Craven *et al.* 2012), the final deformation in these shear zones (D3 of Farrell 1992) and emplacement of granitoids are the final events during a short-lived metamorphic cycle. These data also demonstrate that the D3 shear zones were active during peak metamorphism. Extensive quartzite and quartz veins along the Glen Mohr Shear Zone indicate it was likely a channel for hot fluids. Previous dating of monazite in migmatite samples returned an age of 296.8 ± 1.5 Ma (Craven *et al.* 2012), and combined with a *ca* 300 Ma age of metamorphism in the hornfels samples of this study, these data suggest the whole metamorphic cycle lasted less than *ca* 10 m.y.

Heat advection by aqueous fluid

Aqueous fluids vastly influence the evolution of the crust; fluids are fundamental agents of chemical mass transfer and will promote metamorphic reactions, thus modifying crustal rheology. Yardley (2009) simplifies crustal aqueous fluids into three types: (i) those *buried* in sediments and sedimentary rocks with water held in pores or hydrous minerals; (ii) those *infiltrated* along crustal fractures that provide a pathway for penetration of meteoric or marine water; and (iii) *magmatic* aqueous fluids released upon crystallisation of silicate melts. Geophysical evidence using magnetotelluric and seismic velocity studies (e.g. Wannamaker *et al.* 2002; Bedrosian *et al.* 2004) points to the presence of deep crustal aqueous fluids in tectonically active areas. Surface fluids containing mantle isotopic signatures for the gas components show that fluids released at depth are able to rise through the crust (e.g. Clauser *et al.* 2002). Indeed, the observation of geological processes such as metasomatism has been interpreted as indicating significant ancient fluid flow through the crust (e.g. Oliver 1996; Cartwright 1997; Cui *et al.* 2001). However, the sustained fluid flux required for heat advection by aqueous fluid is problematic (Yardley 2009), especially when invoked as the only heat source.

Although some early researchers pondered a causal relationship between S-type magmatism and HTLP metamorphism in the Wongwibinda Metamorphic Complex based on their close spatial and temporal association (Binns 1966; Vernon 1982), Farrell (1992) challenged this view. He found that the aerial extent of the metamorphic field gradient in the Wongwibinda Metamorphic Complex is much larger than aureoles around other S-type plutons locally and elsewhere in the New England Orogen. Craven *et al.* (2012) showed that the plutonism is late in the metamorphic history of the Wongwibinda Metamorphic Complex, precluding magmatic advective heat transfer as the key local driver of HTLP metamorphism. These results focus attention on a cause of coeval S-type magmatism and HTLP metamorphism.

Our field observations note a spatial association of cordierite-bearing high-*T* rocks and quartzite units both within and outside D3 shear zones. Cordierite grainsize increases in meta-turbidites with proximity to quartzite units. The minor obliquity between layering in quartzite units and bedding in meta-turbidite units and the increased abundance and complexity of quartz veins in cordierite-bearing rocks are consistent with formation of the quartzite units by precipitation of quartz from aqueous fluids. These observations are consistent with the quartzite units in the Wongwibinda Metamorphic Complex as tracers of major fluid flux within D3 shear zones and nearby (above the termination of deeper faults?).

The biotite-in and cordierite-in isograds in meta-turbidites of the Wongwibinda Metamorphic Complex are calculated using THERMOCALC at 200 ± 30°C and 530–620°C respectively (Figures 2, 5, 6). The solidus is calculated at 675–680°C (Figures 5, 6). The higher-T biotite-grade rocks greater than 10 km to the east of the biotite-in isograd attained *T* = 350–430°C (Craven *et al.* 2012), suggesting a regional metamorphic field gradient of 15–23°C km^{-1} in the biotite-grade rocks (Figure 8). Conductive heating during lithospheric thinning plausibly resulted in the regional 'background' biotite-grade metamorphism. The add-on effect of channelled hot fluid flux is inferred to have very locally heated the rocks by approximately 150–250°C in km-scale zones to produce cordierite ± garnet-bearing rocks, these 'hot-spots' defining a discontinuous metamorphic field gradient (Figure 8).

Regional tectonic model

Extensive deposition and accretion of sedimentary rocks derived from the western Keepit-Connors arc formed the voluminous accretionary wedge of the Tablelands Complex, the protolith to metamorphic rocks of the Wongwibinda Metamorphic Complex (Cawood *et al.* 2011). At *ca* 305 Ma, arc magmatism in the southern New England Orogen stopped in the western Keepit-Connors arc and moved eastward. Based on a late Carboniferous to early Permian inception of extensive rift sedimentary basins (Bowen–Gunnedah–Sydney and Barnard) and eruption of juvenile basalts (Werrie, Cranky Corner) through thin crust (Craven 1987; Flood *et al.* 1988), previous research in the New England Orogen supports an extensional setting during the Carboniferous to early Permian (Jenkins *et al.* 2002; Glen 2005, 2013; Collins & Richards 2008; Kemp *et al.* 2009; Cawood *et al.* 2011). We infer that a rift tectonic setting developed a thermal perturbation that ultimately drove HTLP metamorphism in the upper crust above a zone of extensive metamorphism and partial melting, which produced coeval to late S-type granitoids of the Hillgrove Plutonic Suite. In this model, extension thins the lithosphere and draws hot asthenosphere nearer to the base of the thinning crust. Conduction and magmatic advective heat transfer are likely mechanisms near the base of an underplated crust. A key ingredient in our model is that the thin crust includes a thick pile of recently accreted sedimentary rocks (accretionary wedge of the Tablelands Complex; Cawood *et al.* 2011). Having not been an earlier metamorphic cycle, heating during extension of the deepest portions of this type of crust would expel volatiles as metamorphism progresses. Hydrous fluids focused into channels such as shear zones advect heat to shallow crustal levels. Eventually the deepest portions of the crust will reach solidus and begin to partially melt to produce S-type granites that likely move up the same channels used by the hydrous fluids. The system shuts down once the deepest portions of recently accreted sedimentary rocks are metamorphosed and partially melted to leave a dry refractory lower crust; i.e. once the deepest parts of the crust dry out, the tap of advection is turned off. Advection of hot aqueous fluid ($T < 650^{\circ}$C) during metamorphism, owing to fluid pressure or buoyancy forces followed by advection of S-type magma and release of hot aqueous fluid upon crystallisation at shallower levels, provide good and prolonged sources of hot aqueous fluid to flux the shallow crust, especially if focused into channels. The migration of these fluids is likely initially pervasive in the deepest crust becoming more channelled into structures such as shear zones and faults at shallower crustal levels. The advection of hot fluids and then S-type magmas along the same channels (shear zones and faults) develops a spatial and temporal relationship in the shallow crust that predicts HTLP metamorphism should be spatially associated with but shortly followed by S-type magmatism.

The association of HTLP metamorphism and S-type magmatism with extensional tectonics has been recognised repeatedly in the Tasmanides of eastern Australia (Collins & Richards 2008; Kemp *et al.* 2009) and similar local-scale examples elsewhere include the Trois Seigneurs Massif in the Pyrenees (Wickham 1987) and orogen-scale examples that include the Proterozoic (1.92–1.81 Ga) Trans-Hudson orogen of Canada (Ansdell *et al.* 1995; Hollings & Ansdell 2002) and the Damara orogen of Namibia (Gray *et al.* 2007). We propose that tectonic settings involving the extension and attenuation of accretionary orogens that have not experienced a previous metamorphic cycle are conducive to the development of HTLP metamorphic complexes in the shallow crust and production of S-type granite. In order to explain discontinuous metamorphic field gradients in HTLP metamorphic complexes, we propose a model involving regional conductive heating to biotite-grade coupled with heat advection by aqueous fluid to locally heat km-scale zones of the shallow crust to high-*T*. Other mechanisms of heating the shallow crust that have been previously proposed may still be valid for some regions, but others may need to be re-evaluated in the context of the model presented here.

CONCLUSION

Biotite-grade metamorphic rocks in the Wongwibinda Metamorphic Complex host zones of HTLP rock, spatially associated with quartz veins and quartzite units. These zones define a discontinuous metamorphic field gradient that is consistent with conductive mechanisms of heating the shallow crust to biotite-grade in combination with local advective heating by aqueous fluids to cordierite-grade. We propose that heat advection by aqueous fluid locally drove km-scale HTLP metamorphism. A high density of pure quartz and quartz-rich layers in quartzite units are interpreted as sites of high aqueous fluid flux. Other observations that support the quartzite units as the focus of the thermal perturbation resulting in local HTLP metamorphism include: (i) cordierite isograds are largely centred on quartzite outcrops; (ii) cordierite grainsize increases with proximity to quartzite units; (iii) there are local differences in strike between layering in quartzite and bedding in meta-turbidite; and (iv) quartz veins are more common, thicker and contain complex accessory mineralogy near quartzite units. Monazite geochronology indicates that metamorphism in the highest-grade rocks (296.8 $\pm$ 1.5 Ma; Craven *et al.* 2012) shortly predates deformation in shear zones (291.5 $\pm$ 1.8 Ma; this study) and the intrusion of the Abroi Granodiorite (290.5 $\pm$ 1.6 Ma; Craven *et al.* 2012). These relationships indicate that HTLP metamorphism in the Wongwibinda Metamorphic Complex developed during a short cycle (<*ca* 10 m.y.), consistent with the transient character of hydrothermal processes.

ACKNOWLEDGEMENTS

Macquarie University Research Development Grant funding to NRD provided financial support to conduct this research. We thank the local landowners for permission to visit and sample localities in the Wongwibinda Metamorphic Complex. I. Wainwright (University of New South Wales) performed XRF analyses. K. Goemann is thanked for help with the monazite geochronology at UTAS. Catherine Stuart and Kim Jessop provided the

photomicrographs for Figure 3 (e, f). A critical review by an anonymous reviewer was helpful. The analytical data were obtained using instrumentation funded by DEST Systemic Infrastructure Grants, ARC LIEF, NCRIS, industry partners and Macquarie University. This is contribution 887 from the Australian Research Council National Key Centre for the Geochemical Evolution and Metallogeny of Continents (http://www.gemoc.mq.edu.au).

REFERENCES

Ansdell K. M., Lucas S. B., Connors K. & Stern R. A. 1995. Kisseynew metasedimentary gneiss belt, Trans-Hudson orogen (Canada): back arc orogen and collisional inversion. *Geology* **23**, 1039–1043.

Bedrosian P. A., Unsworth M. J., Egbert G. D. & Thurber C. H. 2004. Geophysical images of the creeping segment of the San Andreas fault: implications for the role of crustal fluids in the earthquake process. *Tectonophysics* **385**, 137–158.

Berry R. F., Chmielowski R. M., Steele D. A. & Meffre S. 2007. Chemical U–Th–Pb monazite dating of the Cambrian Tyennan Orogeny, Tasmania. *Australian Journal of Earth Sciences* **54**, 757–771.

Binns R. A. 1966. Granitic intrusions and regional metamorphic rocks of Permian age from the Wongwibinda district, northeastern New South Wales. *Journal of the Proceedings, Royal Society of N.S.W.* **99**, 5–36.

Bodorkos S., Sandiford M., Oliver N. H. S. & Cawood A. 2002. High-*T*, low-*P* metamorphism in the Paleoproterozoic Halls Creek Orogen, northern Australia: the middle crustal response to a mantle-related transient thermal pulse. *Journal of Metamorphic Geology* **20**, 217–237.

Brady J. D. 1988. The role of volatiles in the thermal history of metamorphic terranes. *Journal of Petrology* **29**, 1187–1213.

Cartwright I. 1997. Permeability generation and resetting of tracers during metamorphic fluid flow: implications for advection-dispersion models. *Contributions to Mineralogy and Petrology* **129**, 198–208.

Cawood P. A., Leitch E. C., Merle R. E. & Nemchin A. A. 2011. Orogenesis without collision: Stabilizing the Terra Australis accretionary orogen, eastern Australia. *Geological Society of America Bulletin* **123**, 2240–2255.

Chamberlain C. P. & Rumble D. 1988. Thermal anomalies in a regional metamorphic terrane: An isotopic study of the role of fluids. *Journal of Petrology* **29**, 1215–1232.

Chamberlain C. P. & Rumble D. 1989. The influence of fluids on the history of a metamorphic terrane: New Hampshire, USA. *In*: Daly J. S., Cliff R. A. & Yardley B. W. D. eds. *Evolution of Metamorphic Belts*, pp. 203–213. Geological Society of London, Special Publication **43**.

Clauser C., Griesshaber E. & Neugebauer H. J. 2002. Decoupled thermal and mantle helium anomalies: Implications for the transport regime in continental rift zones. *Journal of Geophysical Research* **107 B11**, 2269.

Coggon R. & Holland T. J. B. 2002. Mixing properties of phengitic micas and revised garnet–phengite thermobarometers. *Journal of Metamorphic Geology* **20**, 683–696.

Collins W. J. & Richards S. W. 2008. Geodynamic significance of S-type granites in circum-Pacific orogens. *Geology* **36**, 559–562.

Collins W. J. & Vernon R. H. 1991. Orogeny associated with anticlockwise *P*–*T*–*t* paths: Evidence from low-*P*, high-*T* metamorphic terranes in the Arunta inlier, central Australia. *Geology* **19**, 835–838.

Craven S. J. 1987. REE and $^{87}Sr/^{86}Sr$ geochemistry of the Warrigundi Volcanic Centre, Werris Ck, NSW. M.Sc. thesis, Macquarie University, Sydney (unpubl.).

Craven S. J., Daczko N. R. & Halpin J. A. 2012. Thermal gradient and timing of high-*T*–low-*P* metamorphism in the Wongwibinda Metamorphic Complex, southern New England Orogen, Australia. *Journal of Metamorphic Geology* **30**, 3–20.

Cui X., Nabelek P. I. & Liu M. 2001. Heat and fluid flow in contact metamorphic aureoles with layered and transient permeability, with application to the Notch Peak aureole, Utah. *Journal of Geophysical Research* **106 B4**, 6477–6491.

Daczko N. R., Milan L. A. & Halpin J. A. 2009. Metastable persistence of pelitic metamorphic assemblages at the root of a Cretaceous magmatic arc—Fiordland, New Zealand. *Journal of Metamorphic Geology* **27**, 233–247.

Danis C. R., Daczko N. R., Lackie M. A. & Craven S. J. 2010. Retrograde metamorphism of the Wongwibinda Complex, New England Fold Belt and the implications of 2.5D subsurface geophysical structure for the metamorphic history. *Australian Journal of Earth Sciences* **57**, 357–375.

Diener J. F. A. & Powell R. 2010. Influence of ferric iron on the stability of mineral assemblages. *Journal of Metamorphic Geology* **28**, 599–613.

De Yoreo J. J., Lux D. R. & Guidotti C. V. 1989. The role of crustal anatexis and magma migration in the thermal evolution of regions of thickened continental crust. *In:* Daly J. S., Cliff R. A. & Yardley B. W. D. eds. *Evolution of Metamorphic Belts*, pp. 187–202. Geological Society of London, Special Publication **43**.

De Yoreo J. J., Lux D. R. & Guidotti C. V. 1991. Thermal modeling in low-pressure/high-temperature metamorphic belts. *Tectonophysics* **188**, 209–238.

Farrell T. R. 1992. Deformation, metamorphism and migmatite genesis in the Wongwibinda Metamorphic Complex. PhD thesis, University of Newcastle, Newcastle (unpubl.).

Flood R. H., Craven S. J., Elmes D. C., Preston R. J. & Shaw S. E. 1988. The Warrigundi Igneous Complex: volcanic centres for the Werri Basalt, NSW. *In*: Kleeman J. D. ed. *New England Orogen: Tectonics and Metallogenesis*, pp. 166–171. University of New England, Armidale.

Glen R. A. 2005. The Tasmanides of eastern Australia. *In*: Vaughan A. P. M., Leat P. T. & Pankhurst R. J. eds. *Terrane Processes at the Margins of Gondwana*, pp. 23–99. Geological Society of London, Special Publication **246**.

Glen R. A. 2013. Refining accretionary orogen models for the Tasmanides of eastern Australia. *Australian Journal of Earth Sciences* **60**, 315–370.

Gray D. R., Foster D. A., Maas R., Spaggiari C. V., Gregory R. T., Goscombe B. & Hoffmann K. H. 2007. Continental growth and recycling by accretion of deformed turbidite fans and remnant ocean basins: Examples from Neoproterozoic and Phanerozoic orogens. *In*: Hatcher R. D., Carlson M. P., McBride J. H. & Martinez Catalan J. R. eds. *4-D Framework of Continental Crust*, pp. 63–92. Geological Society of America, Memoir **200**.

Halpin J. A., Crawford A. J., Direen N .G., Coffin M. F., Forbes C. J. & Borissova I. 2008. Naturaliste Plateau, offshore western Australia: A submarine window into Gondwana assembly and breakup. *Geology* **36**, 807–810.

Hand M., Mawby J., Kinny P. & Foden J. 1999. U–Pb ages from the Harts Range, central Australia: evidence for early Ordovician extension and constraints on Carboniferous metamorphism. *Journal of the Geological Society London* **156**, 715–730.

Hoisch. T. D. 1987. Heat transport by fluids during Late Cretaceous regional metamorphism in the Big Maria Mountains, southeastern California. *Geological Society of America Bulletin* **98**, 549–553.

Hoisch. T. D. 1991. The thermal effects of pervasive and channelised fluid flow in the deep crust. *Journal of Geology* **99**, 69–80.

Holland T. J. B. & Powell R. 1998. An internally consistent thermodynamic dataset for phases of petrological interest. *Journal of Metamorphic Geology* **16**, 309–343.

Holland T. J. B. & Powell R. 2003. Activity–composition relations for phases in petrological calculations: an asymmetric multicomponent formulation. *Contributions to Mineralogy and Petrology* **145**, 492–501.

Holland T. J. B. & Powell R. 2011. An improved and extended internally consistent thermodynamic dataset for phases of petrological interest, involving a new question of state for solids. *Journal of Metamorphic Geology* **29**, 333–383.

Holland T. J. B., Baker J. & Powell R. 1998. Mixing properties and activity–composition relationships of chlorites in the system MgO–Al_2O_3–SiO_2–H_2O. *European Journal of Mineralogy* **10**, 395–406.

Hollings P. & Ansdell K. 2002. Paleoproterozoic arc magmatism imposed on an older backarc basin: implications for the tectonic evolution of the Trans-Hudson orogen, Canada. *Geological Society of America Bulletin* **114**, 153–168.

Jenkins R. B., Landenberger B. & Collins W. J. 2002. Late Palaeozoic retreating and advancing subduction boundary in the New England Fold Belt. *Australian Journal of Earth Sciences* **49**, 476–489.

Kelsey D. E., Powell R., Wilson C. J. L. & Steele D. A. 2003. (Th + U)–Pb monazite ages from Al–Mg-rich metapelites, Rauer Group, east Antarctica. *Contributions to Mineralogy and Petrology* **146**, 326–340.

Kemp A. I. S., Hawkesworth C. J., Collins W. J., Gray C. M., Blevin P. L. & Eimf 2009. Isotopic evidence for rapid continental growth in an extensional accretionary orogen: The Tasmanides, eastern Australia. *Earth and Planetary Science Letters* **284**, 455–466.

Korsch R. J. 1978. Stratigraphic and igneous units in the Rockvale–Coffs Harbour region, New South Wales. *Journal and Proceedings, Royal Society of New South Wales* **111**, 13–17.

Korsch R. J. 1981. Structural geology of the Rockvale Block, northern New South Wales. *Journal of the Geological Society of Australia* **28**, 51–70.

Landenberger B., Farrell T. R., Offler R., Collins W. J. & Whitford D. J. 1995. Tectonic implications of Rb–Sr biotite ages for the Hillgrove Plutonic Suite, New England Fold Belt, N.S.W. Australia. *Precambrian Research* **71**, 251–263.

Langone A., Godard G., Prosser G., Caggianelli A., Rottura A. & Tiepolo M. 2010. *P–T–t* path of the Hercynian low-pressure rocks from the Mandatoriccio complex (Sila Massif, Calabria, Italy): new insights for crustal evolution. *Journal of Metamorphic Geology* **28**, 137–162.

Leitch E. C. 1978. Structural succession in a Late Palaeozoic slate belt and its tectonic significance. *Tectonophysics* **47**, 311–323.

Leitch E. C., Neilson M. J. & Hobson E. 1971. Dorrigo–Coffs Harbour 1:250 000 Geological Sheet SH/56-10 & part SH/56-11, 1st edition, Geological Survey of New South Wales, Sydney.

Lux D. R., De Yoreo J. J., Guidotti C. V. & Decker E. R. 1986. Role of plutonism in low-pressure metamorphic belt formation. *Nature* **323**, 794–797.

McKenzie D. & Priestley K. 2008. The influence of lithospheric thickness variation on continental evolution. *Lithos* **102**, 1–11.

Mahar E. M., Baker J. M., Powell R., Holland T. J. B. & Howell N. 1997. The effect of Mn on mineral stability in metapelites. *Journal of Metamorphic Geology* **15**, 223–238.

Mikhail E. M. 1976. *Observations and least squares*. Dun-Donelly, New York, 479 pp.

Oliver N. H. S. 1996. Review and classification of structural controls on fluid flow during regional metamorphism. *Journal of Metamorphic Geology* **14**, 477–492.

Powell R. & Holland T. J. B. 1988. An internally consistent dataset with uncertainties and correlations: 3. Applications to geobarometry, worked examples and a computer program. *Journal of Metamorphic Geology* **6**, 173–204.

Powell R., Hergt J. & Woodhead J. 2002. Improving isochron calculations with robust statistics and the bootstrap. *Chemical Geology* **185**, 191–204.

Rosenbaum G., Li P. & Rubatto D. 2012. The contorted New England Orogen (eastern Australia): new evidence from U -Pb geochronology of early Permian granitoids. *Tectonics* **31**, TC1006, doi: 10.1029/2011TC002960.

Rubatto D., Williams I. S. & Buick I. S. 2001. Zircon and monazite response to prograde metamorphism in the Reynolds Range, central Australia. *Contributions to Mineralogy and Petrology* **140**, 458–468.

Runnegar B. N. 1970. The Permian faunas of northern New South Wales and the connection between the Sydney and Bowen basins. *Journal of the Geological Society of Australia* **16**, 697–710.

Sandiford M. & Powell R. 1986. Deep crustal metamorphism during continental extension: modern and ancient examples. *Earth and Planetary Science Letters* **79**, 151–158.

Sandiford M., Hand M. & McLaren S. 1998. High geothermal gradient metamorphism during thermal subsidence. *Earth and Planetary Science Letters* **163**, 149–165.

Sandiford M., Martin N., Shaohua Z. & Fraser G. 1991. Mechanical consequences of granite emplacement during high-*T*, low-*P* metamorphism and the origin of anticlockwise *P–T* paths. *Earth and Planetary Science Letters* **107**, 164–172.

Sisson V. B. & Hollister L. S. 1988. Low-pressure facies series metamorphism in an accretionary sedimentary prism, southern Alaska. *Geology* **16**, 358–361.

Sisson V. B., Hollister L. S. & Onstott T. C. 1989. Petrologic and age constraints on the origin of a low-pressure/high-temperature metamorphic complex, southern Alaska. *Journal of Geophysical Research* **94**, 4392–4410.

Stephenson N. C. N. & Hensel H. D. 1979. Intergrown calcic and Fe–Mg amphiboles from the Wongwibinda Metamorphic Complex, N.S.W., Australia. *Canadian Mineralogist* **17**, 11–23.

Stephenson N. C. N. & Hensel H. D. 1982. Amphibolite related rocks from the Wongwibinda Metamorphic Complex, northern N.S.W., Australia. *Lithos* **15**, 59–75.

Stuart C. 2012. Aqueous fluid advection: a plausible mechanism for heating the shallow crustto form HTLP metamorphic belts. BSc (Hons) thesis, Macquarie University, Sydney (unpubl.).

Thompson A. B. & England P. C. 1984. Pressure–temperature–time paths of regional metamorphism II. Their inference and interpretation using mineral assemblages in metamorphic rocks. *Journal of Petrology* **25**, 929–955.

Vernon R. H. 1982. Isobaric cooling of two regional metamorphic complexes related to igneous intrusions in southern Australia. *Geology* **10**, 76–81.

Vernon R. H. & Clarke G. L. 2008. *Principles of Metamorphic Petrology*. Cambridge University Press, New York, USA, pp. 7.

Wannamaker P. E., Jiracek G. R., Stodt J. A., Caldwell T. G., Gonzales V. M., McKnight J. D. & Porter A. D. 2002. Fluid generation and pathways beneath an active compressional orogen, the New Zealand Southern Alps, inferred from magnetotelluric data. *Journal of Geophysical Research* **107**, article number 2117.

White A. J. R. & Chappell B. W. 1988. Some supracrustal (S-type) granites of the Lachlan Fold Belt. *Transactions of the Royal Society of Edinburgh*: Earth Sciences **79**, 169–181.

White R. W., Powell R. & Clarke G. L. 2002. The interpretation of reaction textures in Fe-rich metapelitic granulites of the Musgrave Block, central Australia: constraints from mineral equilibria calculations in the system K_2O–FeO–MgO–Al_2O_3–SiO_2–H_2O–TiO_2–Fe_2O_3. *Journal of Metamorphic Geology* **20**, 41–55.

White R. W., Pomroy N. E. & Powell R. 2005. An *in-situ* metatexite–diatexite transition in upper amphibolite facies rocks from Broken Hill, Australia. *Journal of Metamorphic Geology* **23**, 579–602.

White R. W., Powell R. & Holland T. J. B. 2007. Progress relating to calculation of partial melting equilibria for metapelites. *Journal of Metamorphic Geology* **25**, 511–527.

Wickham S. M. 1987. Segregation and emplacement of granitic magmas. *Journal of the Geological Society, London* **144**, 281–297.

Wickham S. M. & Oxburgh E. R. 1985. Continental rifts as a setting for regional metamorphism. *Nature* **318**, 330–333.

Yardley B. W. D. 2009. The role of water in the evolution of the continental crust. *Journal of the Geological Society, London* **166**, 585–600.

Received 13 February 2013; accepted 9 June 2013

SUPPLEMENTARY PAPER

Table 1 U–Th–Pb chemical data for all monazite analyses.

Chapter 3

Retrograde metamorphism of the Wongwibinda Complex, New England Fold Belt and the implications of 2.5D subsurface geophysical structure for the metamorphic history

C. R. DANIS, N. R. DACZKO, M. A. LACKIE AND S. J. CRAVEN

GEMOC ARC National Key Centre, Department of Earth and Planetary Sciences, Macquarie University, NSW 2109, Australia

Australian Journal of Earth Sciences (2010) **57**, (357–375)

Retrograde metamorphism of the Wongwibinda Complex, New England Fold Belt and the implications of 2.5D subsurface geophysical structure for the metamorphic history

C. R. DANIS*, N. R. DACZKO, M. A. LACKIE AND S. J. CRAVEN

GEMOC ARC National Key Centre, Department of Earth and Planetary Sciences, Macquarie University, NSW 2109, Australia.

Garnet-bearing schists and migmatites sampled from the high-*T*, low-*P* Wongwibinda Complex in the New England Fold Belt, northern New South Wales, contain S_1 and S_2 assemblages that are inferred to have formed within error of each other at $T = 700$ and 650°C, respectively, and $P = 400$ and 380 MPa, respectively. Garnet grains commonly display a zoning profile that includes a flat unzoned interior with narrow (< 350 μm) rims of variable composition. We interpret the unzoned cores as resulting from elemental homogenisation at peak D_1 metamorphic conditions and the narrow rims (with increased Mn) as resorbed grain edges that formed during retrograde conditions (D_2 and thereafter). The retrograde overprint is nearly pervasive across the complex and is most notable nearer to shear zones and intrusive rocks that cut S_1, including the Hillgrove Plutonic Suite. A gravity traverse across the complex determined the Wongwibinda Fault is best modelled with a dip of 65° towards the west but did not identify any substantial concealed mafic plutons, suggesting that the heat source for the shallow crustal thermal perturbation is not imaged beneath the complex today.

KEY WORDS: garnet–cordierite, gravity surveys, regional aureoles, retrograde metamorphism, Wongwibinda Complex.

INTRODUCTION

High-*T* (> 650°C) metamorphism at shallow crustal levels ($P < 500$ MPa) requires significantly perturbed geothermal gradients. These conditions are generally restricted to narrow thermal aureoles adjacent to shallowly emplaced mafic and felsic plutons, with the exception of metamorphic belts surrounding regional aureole granites (White *et al.* 1974). In these metamorphic belts, high-*T* metamorphism extends to greater than 10 km from felsic plutons, for example granite in the Cooma Complex, southern New South Wales (Joplin 1942, 1943; White *et al.* 1974; Flood & Vernon 1978; Richards & Collins 2002). Examples of other regional aureole granites include the Proterozoic Mt Stafford region, Arunta inlier in central Australia (Vernon *et al.* 1990; Collins *et al.* 1991; Collins & Williams 1995; Greenfield *et al.* 1998; White *et al.* 2002), the Forrest Creek granites at Walwa in Victoria (White *et al.* 1974), and the Tia and Wongwibinda Complexes in the New England Fold Belt, northern New South Wales (Binns 1966; Gunthorpe 1970; Korsch 1981; Stephenson & Hensel 1979, 1982; Vernon 1982; Farrell 1988, 1992; Dirks *et al.* 1992, 1993).

Regional aureoles are localised around plutons, and the high-*T* thermal perturbation is commonly attributed to the intrusion of magma (Vallance 1969; White *et al.* 1974; Fagan 1979; Stuwe *et al.* 1993; Johnson 1999; Richards & Collins 2002). The common association between mafic igneous rocks and granitoids (Blundy & Sparks 1992; Barbarin 2005) led Annen & Sparks (2002) and Annen *et al.* (2006, 2008) to suggest that mafic magmas play a fundamental role in granitoid production. The magma bodies believed to be responsible for high-*T* metamorphism in regional aureoles either once lay above the currently exposed level (Collins 1998) or may remain concealed (Vernon 1982; Johnson 1999). Alternate models for the development of regional aureoles include: (i) diapirism (Flood & Vernon 1978), where a rising granite diapir drags high-*T* rocks up from below; and (ii) advective heating beneath a batholith by multiple sheeting (Richards & Collins 2002) or by the passage of magma through a localised transfer zone (De Yoreo *et al.* 1991). Therefore, the driving mechanism for the perturbation of the geothermal gradient and development of a regional aureole remains controversial.

This study involved the examination of the low-*P*, high-*T* regional aureole of the Wongwibinda Complex, New England Fold Belt, northern New South Wales (Figure 1). The region contains rare exposures of deep

*Corresponding author: cdanis@science.mq.edu.au

ISSN 0812-0099 print/ISSN 1440-0952 online © 2010 Geological Society of Australia
DOI: 10.1080/08120091003678361

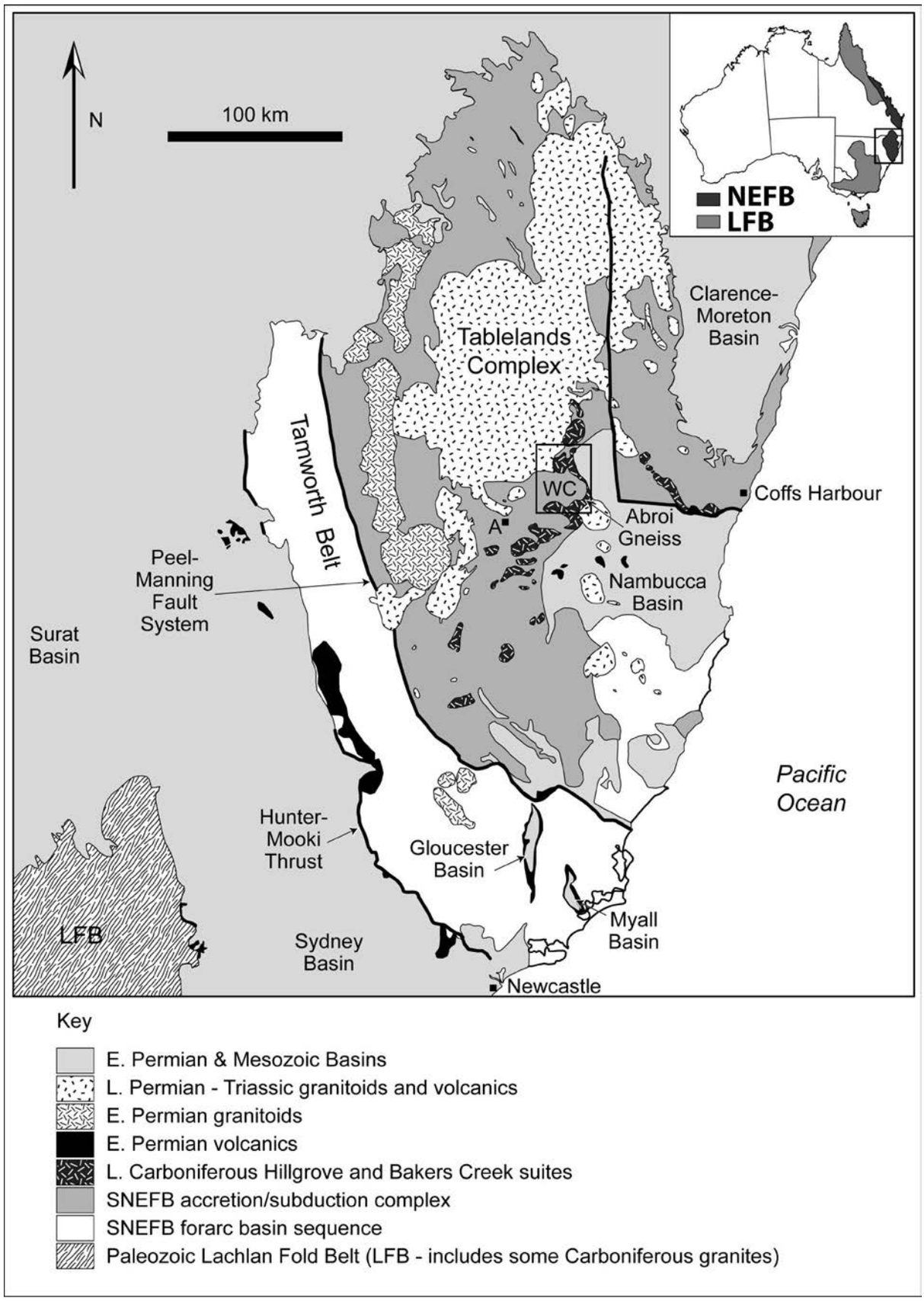

Figure 1 Regional geology of the Southern New England Fold Belt (modified from Jenkins *et al.* 2002). NEFB, New England Fold Belt; WC, Wongwibinda Complex.

(>10 km) New England Fold Belt crust that includes amphibolite-facies pelitic to psammopelitic schists, migmatites, amphibolite and deformed S-type granitoids (Binns 1966; Farrell 1988, 1992; Landenberger *et al.* 1995). The regional aureole extends up to 20 km west from the inferred heat source, a deformed granodiorite pluton called the Abroi Gneiss that is part of the Hillgrove Plutonic Suite (Figures 1, 2; Appendix 1). In this contribution, we present new petrologic, mineral chemistry and thermobarometric data to document the metamorphic evolution in the Wongwibinda Complex, focusing on the retrograde history. In addition, we construct a 2.5D subsurface east–west cross-section through the centre of the Wongwibinda Complex based on the interpretation of a new gravity survey. We explore the possible role magmatism may have played in producing the high-*T* low-*P* regional aureole using the new gravity data. The survey was carried out in order to investigate the subsurface geology and to: (i) explore for concealed plutons that may have been the heat source for the thermal perturbation; and (ii) explore the subsurface orientation of the Wongwibinda Fault, which defines the eastern boundary of the complex.

REGIONAL GEOLOGY

The Wongwibinda Complex (Figure 2) is a low-*P*–high-*T* regional metamorphic aureole that comprises metasediments that vary in metamorphic grade from very low-grade metamorphosed sedimentary rocks (Girrakool beds), through greenschist facies to upper amphibolite facies rocks (Rampsbeck Schists, Zone of Migmatites) (Binns 1966; Farrell 1988, 1992). Rocks of the highest metamorphic grade occur in the eastern part of the Complex, adjacent to the plutonic rocks of the Late Carboniferous Hillgrove Plutonic Suite (which includes deformed granitoids such as the Abroi Gneiss). The north–south- to north-northwest-trending Wongwibinda Fault juxtaposes the Abroi Gneiss and Wongwibinda Complex against the low-grade Dyamberin beds (Figure 2).

The Tablelands Complex, in which the Wongwibinda Complex lies, largely consists of Devonian and Carboniferous deep-marine sedimentary rocks (Jenkins *et al.* 2002). The Girrakool beds (Korsch 1978) form part of a subduction–accretion complex that occurred east of a volcanic front during the Carboniferous (Jenkins *et al.* 2002).

During eastward migration of the convergent boundary (Jenkins *et al.* 2002), the volcanic front shifted east of the Wongwibinda Complex, a rift basin began forming, and the S-type granitoids of the ~300 Ma Hillgrove Plutonic Suite (Kent 1994), including the Abroi Gneiss, and coeval gabbro/diorite bodies of the Bakers Creek Suite (Jenkins *et al.* 2002) were emplaced. The geochemistry of the Bakers Creek Suite reflects an intra-oceanic backarc signature which progressively develops (290–280 Ma) into a MORB signature to reflect the extension period which lasted through to the Early Permian (~290–275 Ma) (Jenkins *et al.* 2002). MORB-like basalts normally are associated with high degrees of lithospheric extension. However, a lack of Early Permian rift-related sedimentary rocks in the Wongwibinda Complex suggests a limited rift basin formed in this area, a feature typical in the cold lithosphere of old forearc regions (Buck *et al.* 1988).

Four deformation events are recognised in the Wongwibinda Complex (Korsch 1981; Farrell 1988). Two amphibolite-facies deformation events (D_1 and D_2) are coeval with the intrusion of the Hillgrove Plutonic Suite and resulted in the formation of the Rampsbeck Schists and Zone of Migmatites. D_1 is generally an intense deformation, with amphibolite-facies metamorphism and migmatisation of rocks east of the Glen Bluff 'Fault' (Figure 2). It is best preserved in low-D_2 strain zones in the western part of the Wongwibinda Complex, particularly in the low-grade Girrakool beds. S_1 is defined by biotite, muscovite and thin leucosomes in the highest-grade rocks with or without garnet, cordierite, sillimanite and potassium feldspar (Binns 1966; Farrell 1988). S_1 warps around cordierite porphyroblasts (2–10 mm), which Farrell (1988, 1992) concluded formed in a pre-D_1/S_1 thermal event.

D_2 involves east–west shortening, continued migmatisation under amphibolite-facies conditions with similar metamorphic mineral assemblages to those developed during D_1 and the intrusion of the Hillgrove Plutonic Suite granites. The intensity of D_2 increases eastward in the Wongwibinda Complex toward the Wongwibinda Fault. S_2 is defined by widely spaced (0.1–1 m) leucosomes separating small domains of partially to wholly transposed S_1 and may be defined by a weak penetrative biotite schistosity (Farrell 1988). A weak gneissic S_2 fabric cuts the Abroi Gneiss that was interpreted by Farrell (1988) to have been intruded post D_1.

During the Hunter–Bowen Orogeny (270–250 Ma) uplift of the Wongwibinda Complex, by reverse movement on the steeply dipping ductile Wongwibinda Fault took place. Evidence in support of this uplift is shown by the relationships of Au and Sb mineralisation in the Hillgrove area, ~20 km south of Rockvale. This area displays ductile structures overprinted by an array of brittle structures interpreted by Ashley & Craw (2004) to be related to orogenic uplift and consequent exhumation during the development of a hydrothermal system.

D_3 in the Wongwibinda Complex evolved from amphibolite to greenschist-facies conditions and resulted in the formation of a number of ductile, west-over-east reverse-shear zones (Wongwibinda, Glen Mohr and Glen Bluff Shear Zones) which deform the Abroi Gneiss and adjacent Rampsbeck Schists (Farrell 1992; Landenberger *et al.* 1995) in the east of the complex. S_3 is defined by micas, chlorite, deformed quartz aggregates, potassium feldspar and flattened xenoliths of Abroi Gneiss (Farrell 1988). The Wongwibinda Complex cooled during D_3 and into D_4, based on the Rb–Sr biotite ages in the Hillgrove Plutonic Suite. Subsequently the Wongwibinda Shear Zone evolved into a progressively more brittle fault zone (Landenberger *et al.* 1995). D_4 produced kink folds and minor brittle faulting, marking the end of ductile shearing (Farrell 1988, 1992).

The re-establishment of a steeper subduction system in the Late Permian–Early Triassic (250–230 Ma) reactivated arc magmatism with intrusion of later parts of the

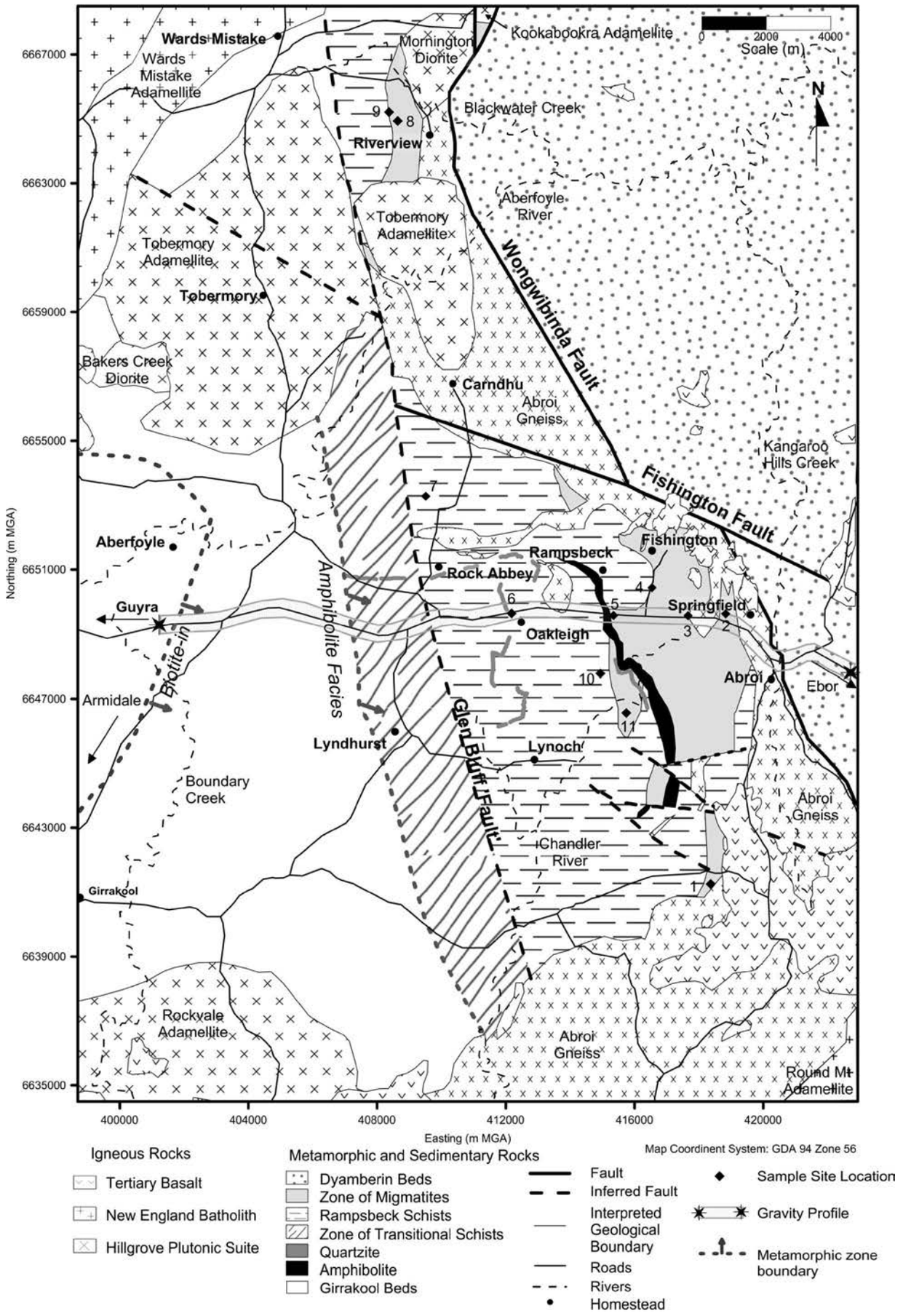

New England Batholith (Jenkins *et al.* 2002). Landenberger *et al.* (1995) implied that major uplift (up to 12 km) of deeper level rocks occurred between 266 and 256 Ma (constrained by Rb–Sr ages of the Hillgrove Plutonic Suite granitoids), accommodated by the Wongwibinda and Chandler Fault systems (Ashley & Craw 2004). If this uplift occurred within a period of ~10 Ma, then Ashley & Craw (2004) suggested uplift rates must have been locally rapid.

METHODS

Mineral chemistry and thermobarometry

The mineral major-element oxides SiO_2, TiO_2, Al_2O_3, Cr_2O_3, FeO, MnO, MgO, CaO, Na_2O and K_2O were determined by electron microprobe at the Geochemical Analysis Unit housed in the Australian Research Council National Key Centre for Geochemical Evolution and Metallogeny of Continents based in the Department of Earth and Planetary Sciences, Macquarie University, Sydney (Table 1). Average P–T calculations were determined using the major-element chemistry. The average P–T method involves the determination of the activities of mineral end members as described by Holland & Powell (2003) and uses the computer software THERMOCALC (v.3.25: Powell & Holland 1988, 1998; data file created November 2003). All mineral end-member activities were calculated using the computer program AX (Holland 2006) and the defaults suggested in Powell and Holland (1988).

The general formula for garnet is $Alm_aSps_bPrp_c Grs_d$ where $Alm = X_{Alm} = 100\ Fe/(Fe + Mg + Ca + Mn)$, $Sps = X_{Sps} = 100\ Mn/(Fe + Mg + Ca + Mn)$, $Prp = X_{Prp} = 100\ Mg/(Fe + Mg + Ca + Mn)$, $Grs = X_{Grs} = 100\ Ca/(Fe + Mg + Ca + Mn)$, and a, b, c and d are the end-member percentages.

Density measurements

Gravity modelling yields non-unique models. Therefore, to reduce the number of potential models matching the data, it is essential to assess the range of densities of major lithologies. A total of 67 (25 mm diameter × 22 mm) cores were drilled from field samples collected from the six main geological units along the gravity profile for density measurement. Samples were weighed both dry and wet using an AG204 Delta Range Mettler Toledo Scale and density was calculated using the formula:

$$D = [(A\partial_L)/(A - B)] + C$$

where D = density (g/cm^3), A = dry weight (g), B = wet weight (g), ∂_L = liquid density and $C = 0.0012$ (air buoyancy constant). Table 2 provides a summary of the measured density results for the six main geological units.

Gravity profile

In order to produce an accurate 2.5D gravity model of the Wongwibinda Complex subsurface, a high-resolution east–west gravity traverse with 152 readings through the centre of the Wongwibinda Complex was completed (Figure 2). The profile is approximately perpendicular to the regional north–south strike of the geology. All readings were taken along a ~20 km length of the Ebor–Guyra Road using a Scintrex CG-3 automated gravity meter that has a measurement range of over 7000 mgal without resetting and a reading resolution of 0.005 mgal. The elevation and horizontal position of the measurement points were determined using an Ashtech RTK DGPS. Gravity measurements were made at a spacing of 100 m or 200 m depending on access. The gravity readings were reduced to Bouguer anomaly, for drift, free air and Bouguer corrections using the standard reduction techniques described by Reynolds (2003). A terrain correction was not applied as the area is of low relief and latitude correction was also not applied as the profile was oriented east–west. All corrections were reduced to the GDA 94 Zone 56. The gravity base station was located on the western side of the Ebor–Gurya Road at the intersection with Rockvale Road (403217.42E, 6649402.48N), with a relative gravity of 0.00 mgal. Modelling of the gravity data was performed with the interactive potential-field modelling package Model Vision Pro (v7.10) supplied by Pitney Bowes Business Insite® (formerly Encom Technology®).

OBSERVATIONS AND RESULTS

Petrography

Binns (1966) and Farrell (1988, 1992) provided detailed petrographic descriptions of the region, and the descriptions given here are complementary. Though garnet is rare in the Wongwibinda Complex, this study focused on garnet-bearing samples from the Rampsbeck Schists and Zone of Migmatites, as these are most useful for determination of P–T conditions. A wide area of the Wongwibinda Complex was examined from near Riverview in the north to a few kilometres south of Lynoch and from Boundary Creek to just east of the Wongwibinda Fault (Figure 2). The key petrological features of these two units are described below, building on the detailed research of Binns (1966) and Farrell (1992).

Rampsbeck Schists

The Rampsbeck Schists are commonly biotite schists that very rarely contain garnet. Low-strain areas

Figure 2 Geology of the Wongwibinda Complex showing gravity profile location and sample sites (modified from Binns 1966 and Farrell 1988, 1992). Biotite-in and amphibolite-facies metamorphic boundaries after Leitch (1978). 1, 0501c; 2, MU61737; 3, MU61739, MU61744; 4, MU61746; 5, 61749; 6, MU61751; 7, MU61756; 8, MU61761; 9, MU61762, MU61763; 10, MU61775; 11, MU61777. See Appendix 1 for location coordinates.

Table 1 Representative mineral chemistry of metamorphic assemblages.

	0501c						MU61737					MU61744					
	grt core	grt rim	plag	bt	ms	crd	grt core	grt rim	plag	kfs	bt	grt core	grt rim	plag	kfs	bt	ms
SiO_2	36.92	37.07	62.72	35.04	48.75	48.49	36.63	36.60	61.51	63.81	35.81	37.27	37.49	61.92	64.39	35.43	45.34
TiO_2	0.02	0.00	0.02	3.52	0.11	0.00	0.00	0.00	0.02	0.00	2.33	0.00	0.05	0.02	0.00	3.25	0.00
Al_2O_3	20.34	20.47	23.40	18.07	35.11	31.33	20.99	21.01	24.11	18.44	18.09	20.51	20.71	23.22	18.09	18.64	34.49
Cr_2O_3	0.03	0.05	0.00	0.04	0.01	0.00	0.00	0.00	0.01	0.01	0.05	0.02	0.03	0.00	0.00	0.05	0.01
FeO	28.92	28.65	0.20	20.17	0.78	9.33	28.51	27.65	0.13	0.23	20.48	27.73	29.48	0.04	0.16	18.73	1.41
MnO	11.01	11.43	0.06	0.18	0.02	1.14	12.11	13.21	0.04	0.01	0.29	11.88	9.96	0.00	0.00	0.26	0.00
MgO	2.03	1.92	0.00	8.53	0.56	7.08	1.64	1.40	0.00	0.01	8.80	2.69	2.74	0.00	0.00	10.04	0.98
CaO	0.91	0.90	5.32	0.01	0.00	0.01	1.16	1.13	5.69	0.00	0.05	0.93	0.77	5.24	0.01	0.02	0.01
Na_2O	0.02	0.01	7.71	0.13	0.52	0.20	0.00	0.01	8.06	1.15	0.06	0.02	0.01	7.94	1.45	0.10	0.32
K_2O	0.00	0.00	0.23	9.13	6.26	0.00	0.00	0.02	0.17	14.78	9.54	0.00	0.01	0.20	14.35	9.52	7.78
Total	100.20	100.51	99.66	94.83	92.13	97.57	101.06	101.04	99.73	98.44	95.50	101.04	101.24	98.57	98.45	96.05	90.34
Oxygen	12	12	8	22	22	18	12	12	8	8	22	12	12	8	8	22	22
Si	3.01	3.01	2.78	5.39	6.47	5.08	2.97	2.97	2.74	2.99	5.48	3.00	3.00	2.78	3.00	5.35	6.25
Ti	0.00	0.00	0.00	0.41	0.01	0.00	0.00	0.00	0.00	0.00	0.27	0.00	0.00	0.00	0.00	0.37	0.00
Al	1.95	1.96	1.22	3.28	5.49	3.87	2.00	2.01	1.26	1.02	3.26	1.95	1.96	1.23	0.99	3.32	5.61
Cr	0.00	0.00	0.00	0.00	0.00	0.00	0.00	0.00	0.00	0.00	0.01	0.00	0.00	0.00	0.00	0.01	0.00
Fe	1.97	1.94	0.01	2.59	0.09	0.82	1.93	1.87	0.00	0.01	2.62	1.87	1.98	0.00	0.00	2.36	0.16
Mn	0.76	0.79	0.00	0.02	0.00	0.10	0.83	0.91	0.00	0.00	0.04	0.81	0.68	0.00	0.01	0.03	0.00
Mg	0.25	0.23	0.00	1.95	0.11	1.10	0.20	0.17	0.00	0.00	2.01	0.32	0.33	0.00	0.00	2.26	0.20
Ca	0.08	0.08	0.25	0.00	0.00	0.00	0.10	0.10	0.27	0.00	0.01	0.08	0.07	0.25	0.00	0.00	0.00
Na	0.00	0.00	0.66	0.04	0.13	0.04	0.00	0.00	0.69	0.10	0.02	0.00	0.00	0.69	0.00	0.03	0.09
K	0	0	0.013	1.792	1.06	0.00	0.00	0.00	0.01	0.882	1.86	0.00	0.00	0.01	0.13	1.83	1.37
Total	8.02	8.01	4.94	15.48	13.37	11.01	8.03	8.03	4.98	5.00	15.56	8.03	8.01	4.96	0.85	15.55	13.67
X_{Fe}	–	–	–	0.57	–	0.43	–	–	–	–	0.57	–	–	–	–	0.51	–
X_{An}	–	–	0.28	–	–	–	–	–	0.28	–	–	–	–	0.27	–	–	–
X_{Alm}	0.64	0.64	–	–	–	–	0.63	0.61	–	–	–	0.61	0.65	–	–	–	–
X_{Prp}	0.08	0.08	–	–	–	–	0.06	0.06	–	–	–	0.10	0.11	–	–	–	–
X_{Grs}	0.03	0.03	–	–	–	–	0.03	0.03	–	–	–	0.03	0.02	–	–	–	–
X_{Sps}	0.25	0.26	–	–	–	–	0.27	0.30	–	–	–	0.26	0.22	–	–	–	–

(*continued*)

Table 1 (*Continued*).

	MU61746						MU61749					MU61751			
	grt core	grt rim	plag	kfs	bt	ms	grt core	grt rim	plag	kfs	bt	grt	plag	bt	ms
SiO_2	36.77	36.54	62.37	64.58	34.47	46.60	37.15	37.31	62.73	64.36	35.59	36.76	61.55	35.93	47.56
TiO_2	0.01	0.00	0.00	0.00	0.70	0.08	0.02	0.00	0.00	0.02	2.35	0.01	0.00	3.34	1.28
Al_2O_3	20.97	20.93	23.63	18.40	18.70	33.19	21.13	21.12	23.47	18.33	19.38	20.49	24.34	16.91	31.62
Cr_2O_3	0.02	0.00	0.00	0.01	0.00	0.01	0.05	0.04	0.00	0.00	0.00	0.02	0.02	0.00	0.06
FeO	32.22	27.71	0.09	0.02	24.11	3.16	33.62	33.22	0.06	0.01	21.05	24.05	0.05	20.77	2.29
MnO	7.97	13.07	0.02	0.01	0.43	0.09	5.63	6.55	0.00	0.01	0.12	15.60	0.02	0.45	0.04
MgO	1.54	0.91	0.00	0.00	6.22	1.05	2.76	2.39	0.00	0.00	8.67	1.19	0.00	8.40	1.52
CaO	1.35	1.08	4.92	0.00	0.09	0.03	0.77	0.86	4.72	0.00	0.02	2.19	6.03	0.11	0.04
Na_2O	0.01	0.03	8.95	0.91	0.15	0.26	0.00	0.02	8.74	0.11	0.08	0.03	8.34	0.17	0.13
K_2O	0.00	0.00	0.23	15.35	9.37	10.46	0.00	0.00	0.26	16.68	9.48	0.00	0.16	9.25	9.46
Total	100.87	100.28	100.20	99.28	94.24	94.93	101.13	101.52	99.98	99.51	96.74	100.34	100.50	95.33	93.99
Oxygen	12	12	8	8	22	22	12	12	8	8	22	12	8	22	22
Si	2.98	2.99	2.76	3.00	5.45	6.28	2.98	2.99	2.78	2.99	5.37	3.00	2.72	5.52	6.40
Ti	0.00	0.00	0.00	0.00	0.08	0.01	0.00	0.00	0.00	0.00	0.27	0.00	0.00	0.39	0.13
Al	2.00	2.02	1.23	1.01	3.49	5.27	2.00	1.99	1.22	1.01	3.45	1.97	1.27	3.06	5.02
Cr	0.00	0.00	0.00	0.00	0.00	0.00	0.00	0.00	0.00	0.00	0.00	0.00	0.00	0.00	0.01
Fe	2.18	1.89	0.00	0.00	3.19	0.36	2.26	2.22	0.00	0.00	2.66	1.64	0.00	2.67	0.26
Mn	0.55	0.90	0.00	0.00	0.06	0.01	0.38	0.44	0.00	0.00	0.02	1.08	0.00	0.06	0.00
Mg	0.19	0.11	0.00	0.00	1.47	0.21	0.33	0.28	0.00	0.00	1.95	0.14	0.00	1.92	0.31
Ca	0.12	0.09	0.23	0.00	0.01	0.00	0.07	0.07	0.22	0.00	0.00	0.19	0.29	0.02	0.01
Na	0.00	0.01	0.77	0.08	0.05	0.07	0.00	0.00	0.75	0.01	0.02	0.00	0.72	0.05	0.03
K	0.00	0.00	0.01	0.91	1.89	1.80	0.00	0.00	0.01	0.99	1.83	0.00	0.01	1.81	1.62
Total	8.02	8.01	5.01	5.00	15.69	14.01	8.02	8.02	4.99	5.00	15.56	8.02	5.00	15.50	13.79
X_{Fe}	–	–	–	–	0.68	–	–	–	–	–	0.58	–	–	0.58	–
X_{An}	–	–	0.23	–	–	–	–	–	0.23	–	–	–	0.29	–	–
X_{Alm}	0.72	0.63	–	–	–	–	0.74	0.73	–	–	–	0.54	–	–	–
X_{Prp}	0.06	0.04	–	–	–	–	0.11	0.09	–	–	–	0.05	–	–	–
X_{Grs}	0.04	0.03	–	–	–	–	0.02	0.02	–	–	–	0.06	–	–	–
X_{Sps}	0.18	0.30	–	–	–	–	0.13	0.15	–	–	–	0.35	–	–	–

(*continued*)

Table 1 (*Continued*).

	MU61761						MU61762					MU61777						
	grt core	grt rim	plag	kfs	bt	ms	grt core	grt rim	plag	bt	ms	grt core[a]	grt rim[a]	grt core[b]	grt rim[b]	plag	kfs	bt
SiO_2	36.48	36.36	64.43	64.33	34.89	47.01	36.74	36.08	62.29	35.21	45.59	37.27	37.141	37.10	37.38	62.05	64.75	36.03
TiO_2	0.01	0.04	0.00	0.01	1.27	0.02	0.00	0.03	0.00	2.22	0.28	0.00	0.0062	0.02	0.01	0.00	0.00	1.62
Al_2O_3	20.41	20.19	21.88	18.02	17.55	33.64	20.99	20.73	23.81	18.44	34.78	21.14	20.893	20.93	21.34	24.17	18.48	18.48
Cr_2O_3	0.00	0.00	0.01	0.01	0.02	0.00	0.02	0.04	0.00	0.03	0.04	0.01	0.0121	0.00	0.01	0.00	0.01	0.02
FeO	34.77	31.52	0.13	0.31	27.18	2.75	32.87	29.32	0.03	21.51	1.61	26.95	25.115	32.98	32.40	0.08	0.04	21.86
MnO	5.63	10.45	0.02	0.06	0.55	0.02	7.78	12.49	0.00	0.43	0.02	13.70	15.306	4.27	6.69	0.04	0.00	0.49
MgO	1.46	0.62	0.00	0.01	4.66	0.68	1.96	1.21	0.00	8.58	0.65	1.56	1.2101	3.94	2.89	0.00	0.00	8.63
CaO	1.10	1.03	3.56	0.00	0.07	0.00	0.85	0.89	5.23	0.03	0.01	1.15	1.6836	1.02	0.98	5.58	0.00	0.04
Na_2O	0.07	0.01	9.51	0.23	0.05	0.36	0.01	0.01	8.20	0.10	0.28	0.02	0.0056	0.02	0.00	8.64	0.83	0.10
K_2O	0.01	0.00	0.21	16.31	8.42	11.04	0.01	0.03	0.24	9.43	10.85	0.01	0.0142	0.00	0.0227	0.21	15.67	9.71
Total	99.95	100.24	99.75	99.289	94.66	95.54	101.24	100.81	99.81	95.97	94.12	101.81	101.39	100.28	101.71	100.78	99.776	96.99
Oxygen	12	12	8	8	22	22	12	12	8	22	22	12	12	12	12	8	8	22
Si	2.99	2.99	2.85	3.00	5.55	6.30	2.97	2.95	2.76	5.39	6.17	2.99	2.9944	2.98	2.98	2.74	2.99	5.46
Ti	0.00	0.00	0.00	0.00	0.15	0.00	0.00	0.00	0.00	0.26	0.03	0.00	0.0004	0.00	0.00	0.00	0.00	0.18
Al	1.97	1.96	1.14	0.99	3.29	5.31	2.00	2.00	1.24	3.33	5.54	2.00	1.9858	1.98	2.00	1.26	1.01	3.30
Cr	0.00	0.00	0.00	0.00	0.00	0.00	0.00	0.00	0.00	0.00	0.00	0.00	0.0008	0.00	0.00	0.00	0.00	0.00
Fe	2.38	2.17	0.00	0.01	3.61	0.31	2.22	2.00	0.00	2.75	0.18	1.81	1.6934	2.22	2.16	0.00	0.00	2.77
Mn	0.39	0.73	0.00	0.00	0.07	0.00	0.53	0.86	0.00	0.06	0.00	0.93	1.0453	0.29	0.45	0.00	0.00	0.06
Mg	0.18	0.08	0.00	0.00	1.10	0.14	0.24	0.15	0.00	1.96	0.13	0.19	0.1454	0.47	0.34	0.00	0.00	1.95
Ca	0.10	0.09	0.17	0.00	0.01	0.00	0.07	0.08	0.25	0.00	0.00	0.10	0.1454	0.09	0.08	0.26	0.00	0.01
Na	0.01	0.00	0.82	0.02	0.02	0.09	0.00	0.00	0.71	0.03	0.07	0.00	0.0009	0.00	0.00	0.74	0.07	0.03
K	0.00	0.00	0.01	0.9703	1.71	1.89	0.00	0.00	0.01	1.84	1.87	0.0013	0.0015	0.00	0.0023	0.01	0.9244	1.88
Total	8.03	8.02	4.99	5.00	15.52	14.04	8.03	8.05	4.98	15.62	14.00	8.01	8.0131	8.03	8.0216	5.01	5.00	15.65
X_{Fe}	–	–	–	–	0.77	–	–	–	–	0.58	–	–	–	–	–	–	–	0.59
X_{An}	–	–	0.17	–	–	–	–	–	0.26	–	–	–	–	–	–	0.26	–	–
X_{Alm}	0.78	0.71	–	–	–	–	0.72	0.65	–	–	–	0.60	0.56	0.72	0.71	–	–	–
X_{Prp}	0.06	0.02	–	–	–	–	0.08	0.05	–	–	–	0.06	0.05	0.15	0.11	–	–	–
X_{Grs}	0.03	0.03	–	–	–	–	0.02	0.03	–	–	–	0.03	0.05	0.03	0.03	–	–	–
X_{Sps}	0.13	0.24	–	–	–	–	0.17	0.28	–	–	–	0.31	0.35	0.09	0.15	–	–	–

bt, biotite; crd, cordierite; grt, garnet; kfs, potassium feldspar; ms, muscovite; plag, plagioclase feldspar.
[a]spessartine-rich.
[b]pyrope-rich.

Table 2 Summary of density data for lithology samples.

Samples	Density (g/cm^3)			
	Range	Mean	SD	*n*
Girrakool beds	2.618–2.713	2.675	0.025	7
Dyamberin beds	2.659–2.747	2.700	0.034	6
Amphibolite	3.116–3.157	3.133	0.011	6
Rampsbeck Schists	2.659–2.747	2.707	0.026	16
Rare garnet–biotite schists	2.660–2.709	2.694	0.016	8
Zone of Migmatites	2.604–2.759	2.730	0.035	9
Abroi Gneiss	2.567–2.709	2.673	0.027	23
Sheared Abroi Gneiss	2.647–2.665	2.657	0.007	6

contain unusual muscovite–cordierite–potassium-feldspar hornfels as indicated by random fine-grained mica in spotted rocks. Microscopically, they (Figure 3a, b) are commonly fine- (<0.01–0.3 mm) to coarse-grained (0.06–0.5 mm), pelitic to psammitic schists, comprising biotite, plagioclase, potassium feldspar, quartz and minor muscovite with accessory apatite, sericite, titanite, zircon and opaque minerals of hematite and goethite. Goethite is presumed to result from the weathering of either magnetite or pyrite. The opaque minerals occur in layers and may represent relic bedding; aligned biotite defines S_1 (Figure 3a). Though cordierite was not observed in this study, Farrell (1992) reported pre-kinematic cordierite and potassium-feldspar porphyroblasts enveloped by weakly developed S_1. Quartz is dynamically recrystallised and exhibits subgrains and undulose extinction. Small anhedral plagioclase porphyroblasts (0.3–0.6 mm) may be partly pseudomorphed by white mica and potassium feldspar is commonly partially replaced by myrmekite growths adjacent to plagioclase. Microcline twinning is rare in potassium feldspar. Muscovite is commonly the same grainsize as the biotite. It may be aligned with S_1 or S_2. Rare leucosome and quartz veins cut the S_1 fabric. These are variably boudinaged and folded. Myrmekite textures and microcline twining are observed in some potassium feldspars occurring in leucosomes.

Rare garnet-bearing biotite schists (MU 61751, 61756 and 61763) are texturally and mineralogically similar to the biotite schists. The garnet is pink spessartine-rich almandine (Table 3) and varies in diameter from 0.05 to 0.8 mm. It varies from small inclusion-poor porphyroblasts to slightly larger poikiloblasts. S_1 envelops asymmetric porphyroblasts of garnet at Site 9 (Figure 2). Garnet may be completely pseudomorphed by biotite with lesser muscovite and rarely chlorite near shear zones and younger plutons (Figure 3c). In lower-grade schists, rare garnet is small (<0.1 mm) partially pseudomorphed by muscovite, indicating the early growth of garnet. Where S_1 has been transposed parallel to S_2, both fabrics envelop the partially pseudomorphed garnet.

Zone of Migmatites

The migmatites of the Wongwibinda Complex are located adjacent to the Wongwibinda Fault in an elongate mass from near Riverview to south of Springfield (Figure 2). Migmatites are generally melanosome rich with folded leucosomes (Figure 3d). Vein structure and thick pegmatite dykes cut S_1 and are folded by F_2 (Figure 3d). The migmatites comprise quartz (~20–50%), biotite (10–40%), plagioclase (20–35%), microcline (<10%) and garnet (<10%) with accessory muscovite, chlorite, zircon, opaque minerals, apatite and white mica. In folded and foliated granitic veins, axial-planar biotite and minor muscovite define the S_2 foliation. The pegmatite dykes are composed of plagioclase, potassium feldspar and quartz with accessory biotite and sericite.

Pink almandine garnet porphyroblasts (0.05–0.5 mm) occur in both melanosome and leucosome (Figure 3e). Garnet poikiloblasts commonly contain random inclusions of biotite and quartz. Garnet rarely forms very large (3–7 mm) red-purple irregular porphyroblasts (MU61777) surrounded by smaller grains of garnet. The smaller garnet grains are only located directly adjacent to the larger porphyroblasts in S_2 strain shadows.

Plagioclase porphyroblasts (0.2–0.4 mm) are partially sericitised, particularly when enveloped by S_2. They rarely contain inclusions of garnet and may be zoned. Partial replacement of potassium-feldspar poikiloblasts by myrmekite is uncommon in the leucosomes. Recrystallised quartz and plagioclase-bearing leucosomes show quartz exhibiting subgrain development and undulose extinction.

Migmatites in the northern part of the Wongwibinda Complex adjacent to the Tobermory Adamellite and Mornington Diorite (Figure 2) contain a greater abundance of muscovite both parallel to S_2 and as randomly oriented grains. Chlorite also occurs, pseudomorphing biotite, and garnet is partially to completely pseudomorphed by biotite and to a lesser extent by muscovite and chlorite.

Xenoliths of migmatite in the Abroi Gneiss

Migmatite xenoliths are found in the Abroi Gneiss near Springfield (Figure 3f). These migmatites are similar in appearance to outcrops in the Zone of Migmatites. However, only one foliation is observed in each xenolith consistent with entrainment of the xenolith prior to D_2. Therefore, the gneissosity within the Abroi Gneiss is likely to be S_2. Pink almandine garnet porphyroblasts (0.06–0.4 mm) are common throughout the melanosomes and leucosomes. Garnet within the melanosome is finer grained (0.05–0.1 mm) and contains fewer inclusions (Figure 3g) compared with the leucosome-hosted garnet. Some fibrolitic sillimanite along the plagioclase and garnet grain boundaries is pseudomorphed by muscovite. Cordierite porphyroblasts are commonly pseudomorphed by muscovite and pinnite (Figure 3h).

MINERAL CHEMISTRY

In this section we outline the major-element mineral chemistry of minerals in key assemblages for 11 samples to explore the variation in composition between samples and to give context to the P–T calculations. Samples selected for analysis exhibited the least degree of alteration and weathering based on petrological analysis. We also avoided the analysis of garnet in contact

with biotite, where possible, to reduce zoning caused by late Fe–Mg exchange during cooling. The mineral chemistry is presented in Table 1.

Plagioclase is slightly variable in composition within a rock sample and shows limited zoning within grains. Most samples of both the Rampsbeck Schists and Zone of

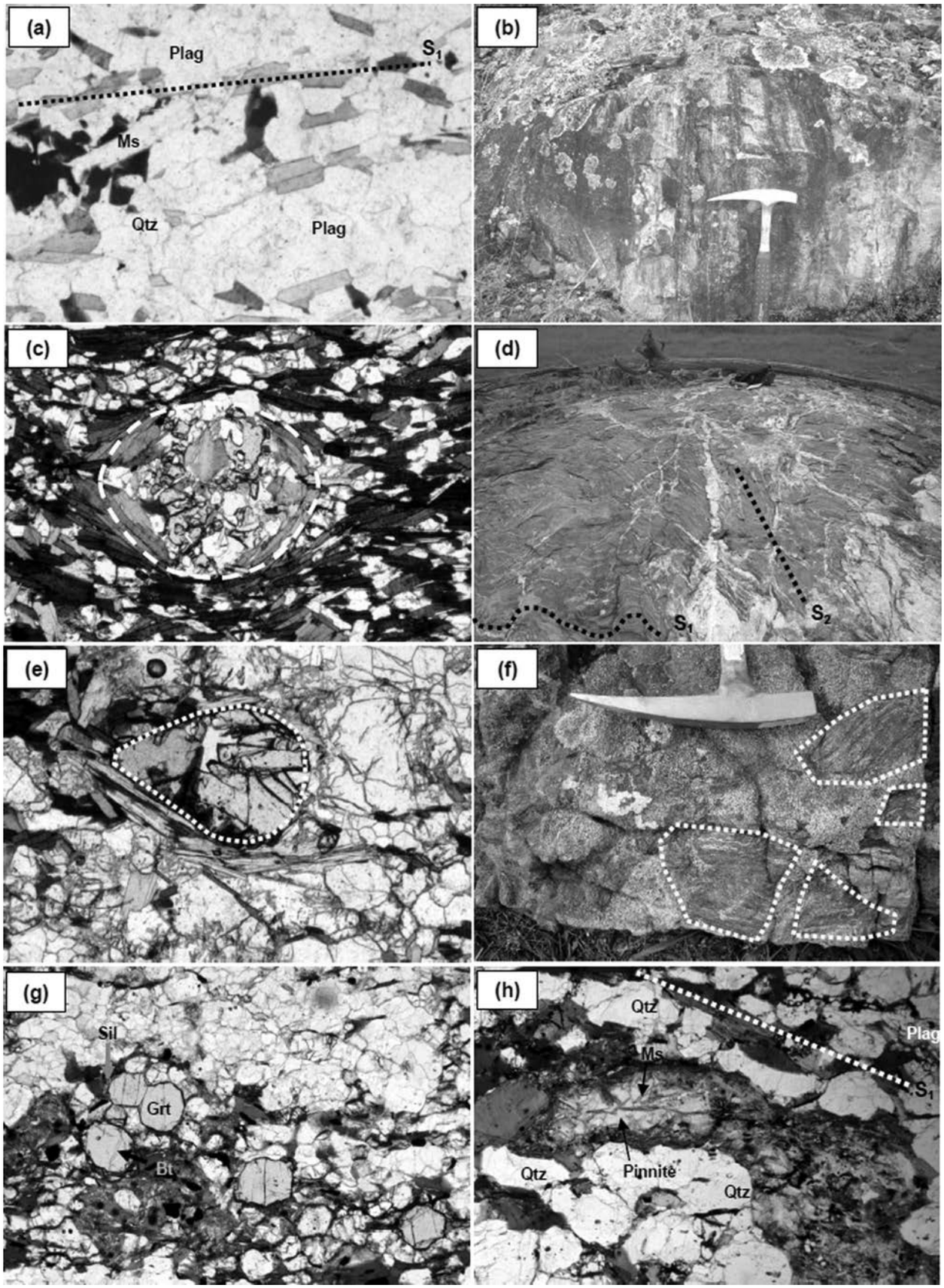

Migmatites (except MU61761) have XAn [=100 Ca/(Ca + Na + K)] between 22 and 27, and rarely as low as 20 or as high as 33. MU61761 is exceptional in that some grains have XAn = 12–18 and others with XAn < 3. Potassium feldspar is more common in the Zone of Migmatites and is limited in composition in all rocks to XOr [=100 K/(Ca + Na + K)] > 90, except for MU61761 that has XOr as low as 83. No perthitic feldspar was observed.

All biotite grains within a sample generally contain > 8–9 K_2O (wt% oxide) except for samples MU61744 and MU61761, in which biotites are altered, as indicated by very low K_2O contents (< 5 wt% oxide). XFe [=100 Fe/(Fe + Mg)] ranges between 49 and 63 for both the Rampsbeck Schists and Zone of Migmatites. Three samples (MU61746, 61761 and 61762) show anomalously high vales of XFe (up to 79) and MU61744 shows anomalously low values of XFe (down to 39). The Ti content of biotite in the samples ranges from 0.02 to 0.42 cations of Ti per formula unit (based on 22 oxygen). Chlorite in the Zone of Migmatites (MU61744, 61761 and 61777) has XFe = 58–61.

Garnet (Table 3) is commonly spessartine-rich almandine. The most common garnet zoning profile (Figure 4) contains a flat (i.e. unzoned) interior with a narrow (< 350 μm) rim of variable composition. All samples, except MU61744, show lower almandine and higher spessartine at the grain rim compared with the core (Figure 4). The XFe *vs* spessartine content (Figure 5) shows limited chemical variation for 0501c, MU61744 and MU61751 and a positive correlation for all other samples.

CALCULATED AVERAGE P–T

In this section we estimate the conditions of metamorphism during D_1 and D_2. All samples used here contain garnet, biotite, plagioclase, potassium feldspar and quartz. In addition, S_1 assemblages contain cordierite and S_2 assemblages contain muscovite (Table 4). The mineral chemistry in these assemblages are used to calculate average P–T using the methods of Powell & Holland (1988, 1998). The mineral end-members paragonite and celadonite were excluded in the analysis when a result failed statistical tests with Thermacalc. The results of our analyses suggest that the S_1 assemblage equilibrated at peak conditions of $P = 400$ MPa and $T = 700$°C and the S_2 assemblage equilibrated at $P = 380$ MPa and $T = 650$°C (Table 4), but both are within error of each other. The smallest two sigma errors on these results are ± 50 MPa and ± 22°C (Table 4). These results indicate that both S_1 and S_2 evolved under amphibolite-facies conditions.

DENSITY MEASUREMENT

The density of lithologies in the Wongwibinda Complex, excluding the amphibolite, ranges from 2.567 to 2.759 g/cm^3 (Table 2) and includes weathered samples where fresh rock was unavailable. Density values ranging below 2.650 g/cm^3 for the Zone of Migmatites and Abroi Gneiss represent samples from weathered rock. In general, the density ranges for each lithology in Table 2 of the Wongwibinda Complex are limited, and most overlap, with the exception of the amphibolite. However, when the field distribution of each lithology is considered, differences are observed in the average density. The average density of the Rampsbeck Schists (2.707 g/cm^3) is higher than the rare garnet-bearing Rampsbeck Schists (2.694 g/cm^3) but lower than the average density for the Zone of Migmatites (2.730 g/cm^3). Similarly the average density for sheared Abroi Gneiss (2.657 g/cm^3) is lower than the average for the Abroi Gneiss (2.673 g/cm^3) and Dyamberin beds (2.700 g/cm^3).

From the average density of each lithology in Table 2, the average bulk country-rock density of 2.700 g/cm^3 is calculated.

2.5D GRAVITY MODELLING

The aims of the gravity modelling are to constrain the orientation of the Wongwibinda Fault and search for any potential buried mafic pluton that may have been the heat source for the thermal perturbation. The location of the profile is shown in Figure 2, and the modelled profile in Figure 6.

The model was constructed using an assembly of polygonal bodies (Abroi Gneiss, blind plutons, Rampsbeck Schists and Zone of Migmatites) and rectangular prisms (Girrakool and Dyamberin beds), forming a 2.5D model, for which the north–south extent of the bodies could be constrained perpendicular to the profile. The geological units of the Wongwibinda Complex were generally modelled individually, with the exception of the Zone of Transitional Schists and Rampsbeck Schists which were modelled as a package. The model background density is set at 2.700 g/cm^3 after the bulk country-rock average calculated from measured hand

Figure 3 (a) Photomicrograph of coarse-grained biotite–muscovite schist. S_1 shown by dashed line. Field of view is 1.75 mm; PPL. MU61775, Rampsbeck Schist. (b) Rampsbeck Schist outcrop along Ebor–Guyra Road (56H 416770E, 6649520N). Hammer head is 175 mm. (c) Photomicrograph showing garnet rim (dashed line) pseudomorphed by biotite and chlorite. Garnet core contains inclusions of quartz, plagioclase and biotite. Field of view is 1.75 mm; PPL. MU61762, Rampsbeck Schist. (d) Melanosome-rich migmatite northeast of Lynoch with large folded leucosomes and pegmatite veins. Field of view ~4 m across. MU61777, Zone of Migmatites. (e) Photomicrograph of garnet porphyroblast (dashed line) in leucosome. Field of view is 1.75 mm; PPL. MU61746; Zone of Migmatites. (f) Abroi Granodiorite containing xenoliths of melanosome-rich migmatite (dashed lines) from contact with the Zone of Migmatites near Springfield, MU61739. Hammer head is 175 mm. (g) Photomicrograph of xenolith shown in Figure 3f showing sillimanite (fibrolite) and garnet with minor inclusions of quartz and biotite. Field of view is 3.5 mm; PPL. MU61744, Zone of Migmatites. (h) Photomicrograph showing cordierite pseudomorphed by pinnite and muscovite. Field of view is 3.5 mm; PPL. MU61744, Zone of Migmatites.

Table 3 Summary of garnet composition.

Sample no.	Core	Rim
MU61737	$Alm_{59–62}$ $Sps_{27–32}$ $Prp_{5–6}$ Grs_{3}	$Alm_{61–67}$ $Sps_{21–28}$ $Prp_{6–8}$ Grs_{3}
MU61744	$Alm_{60–61}$ $Sps_{23–26}$ $Prp_{10–12}$ Grs_{2}	$Alm_{61–64}$ $Sps_{22–25}$ $Prp_{9–12}$ Grs_{2}
MU61746	$Alm_{69–73}$ $Sps_{15–21}$ $Prp_{5–7}$ $Grs_{3–4}$	$Alm_{60–69}$ $Sps_{22–30}$ $Prp_{3–5}$ $Grs_{3–7}$
MU61749	Alm_{746} $Sps_{11–12}$ $Prp_{0–11}$ Grs_{2}	$Alm_{73–75}$ $Sps_{12–14}$ $Prp_{9–10}$ Grs_{2}
MU61751	$Alm_{54–55}$ $Sps_{33–34}$ Prp_{4} Grs_{6}	$Alm_{53–54}$ Sps_{35} $Prp_{4–5}$ Grs_{6}
MU61761	$Alm_{64–78}$ $Sps_{12–30}$ $Prp_{2–5}$ $Grs_{2–3}$	$Alm_{63–79}$ $Sps_{14–31}$ $Prp_{2–4}$ $Grs_{2–3}$
MU61762	$Alm_{68–73}$ $Sps_{15–22}$ $Prp_{6–8}$ $Grs_{2–3}$	$Alm_{63–65}$ $Sps_{26–28}$ $Prp_{4–5}$ Grs_{2}
MU61777	Alm_{72} Sps_{9} $Prp_{15–16}$ Grs_{3}	$Alm_{63–73}$ $Sps_{9–22}$ $Prp_{8–14}$ $Grs_{2–4}$
MU61777	Alm_{59} Sps_{30} Prp_{6} Grs_{3}	Alm_{53} Sps_{36} Prp_{4} Grs_{5}

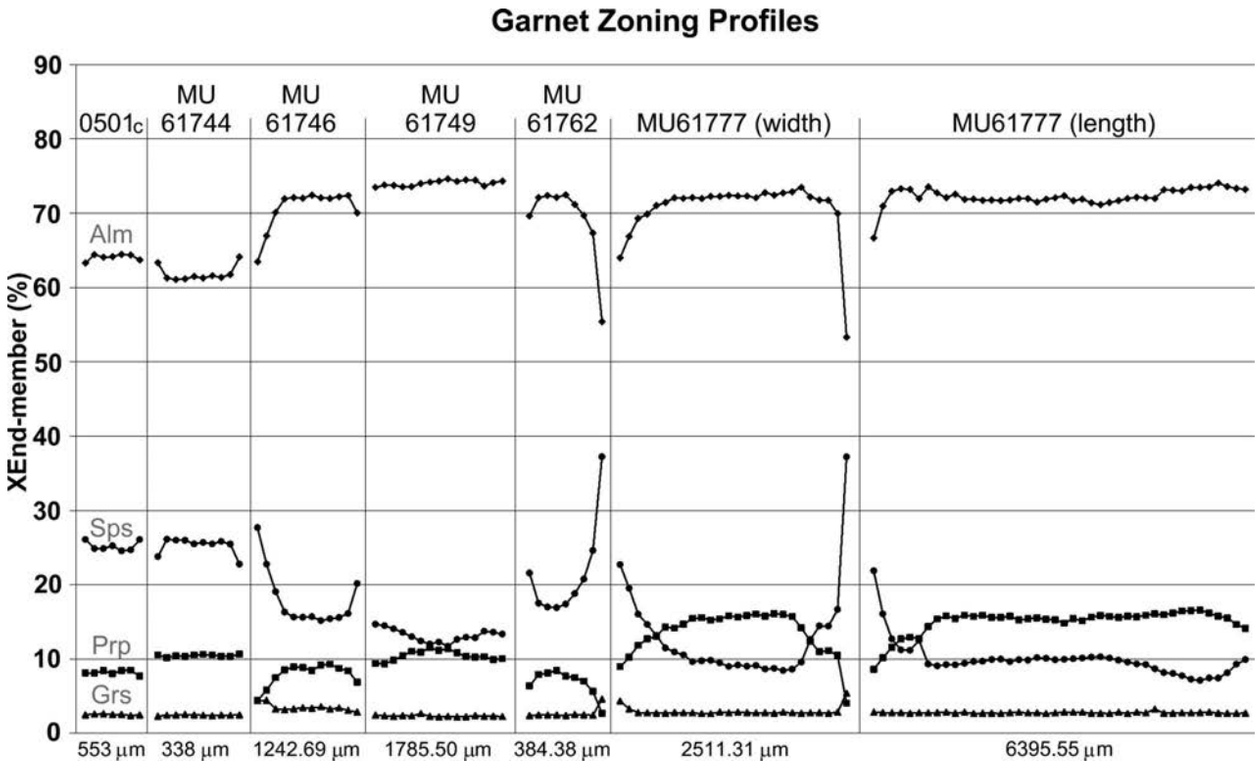

Figure 4 Garnet zoning profiles of end-member composition.

samples. Densities of the modelled lithologies, with the exception of blind plutons, were kept within the ranges measured in this study (Table 2). Where possible the densities from fresh rock samples are used but the weathered rock samples represent the lowest considered density. The density of the felsic blind pluton is based on the nearby Bundarra Suite granite 2.60–2.68 g/cm^3 (Guo *et al.* 2007) and the density of the mafic blind pluton is based on the composition of the nearby Bakers Creek Suite gabbro and Mornington Diorite (2.8–3.0 g/cm^3: Reynolds 2003).

The model profile was derived using the geometry from published geological maps with field validation, structural measurements (this study) and published structural data (Binns 1966; Stephenson & Hensel 1979; Korsch 1981). Given the limited density contrast within the Rampsbeck Schists, the Glen Bluff 'Fault' could not be modelled. Initial modelling (not shown) determined that a geological model derived from surface geological data was applicable at depths of 2 km, 5 km and 10 km with minor adjustments to density, within the calculated range of Table 2, required for some units. In this study, the profile was modelled to a depth of 2 km.

The Wongwibinda Fault was modelled using shallow to vertical easterly and westerly dips, and the response was analysed both visually and using the residual method outlined by Cooley & Naft (1990) to determine the best dip orientation. The orientation of the Wongwibinda Fault, at the intersection with the model profile, is best modelled at 65°W.

Between the Girrakool beds and Rampsbeck Schists, a boundary is identified petrographically between lithologies displaying amphibolite-facies metamorphism and those that display low-grade metamorphism. Modelling the orientation of the amphibolite-facies boundary, in the same fashion as the Wongwibinda Fault, could not determine a single preferred orientation for the boundary. Changes in the orientation of the

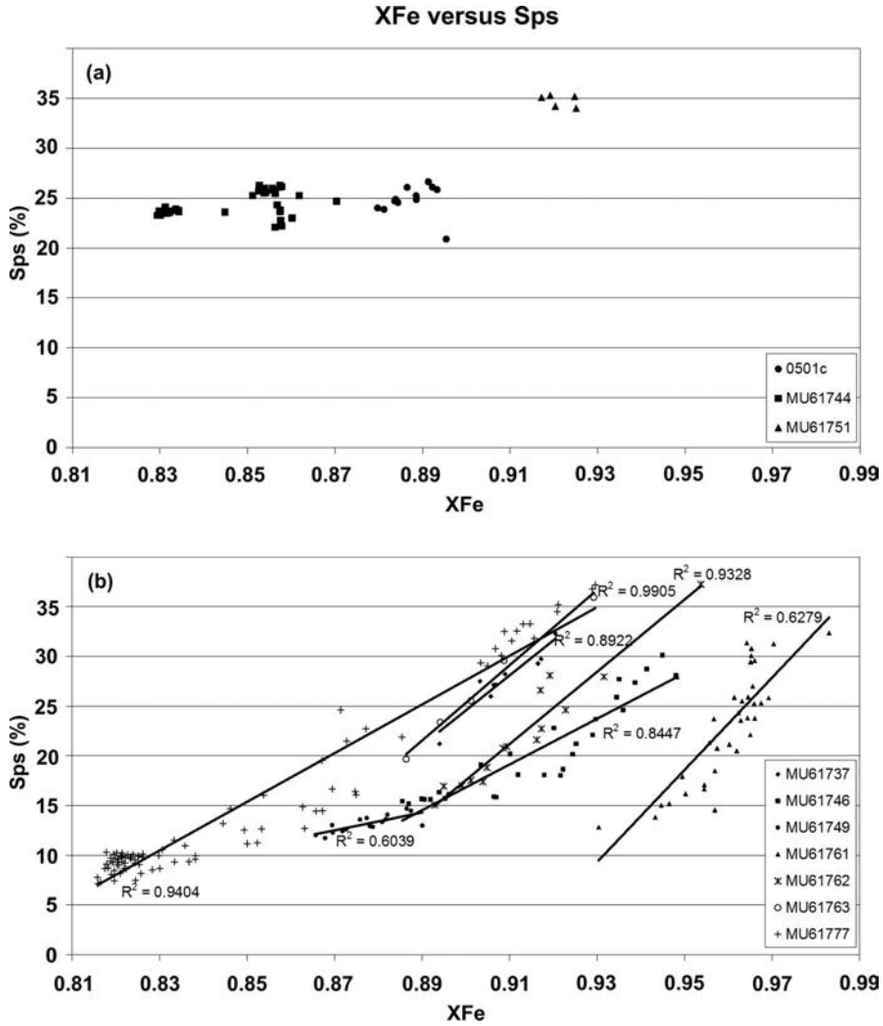

Figure 5 XFe *vs* spessartine for (a) garnet with limited zoning and (b) garnet with extensive zoning.

Table 4 Results of thermobarometric analysis of peak metamorphic mineral assemblages in samples with limited retrogression.

	Average *P–T*	Average *P* (MPa)	Average *T* (°C)	Assemblage	Number of reactions	Correlation coefficient	SD (Fit)
0501c	687 ± 50°C 390 ± 120 MPa	400 ± 54	695 ± 22	grt-bt-crd-plag-kfs-qtz	7	0.937	0.93
MU61744	710 ± 67°C 400 ± 280 MPa	400 ± 370	706 ± 76	grt-bt-plag-kfs-qtz [crd]	4	0.099	0.85
MU61749	768 ± 115°C 480 ± 370 MPa	460 ± 454	764 ± 106	grt-bt-plag-kfs-qtz	3	−0.133	1.20
MU61751	663 ± 46°C 480 ± 160 MPa	420 ± 120	647 ± 36	grt-bt-plag-kfs-qtz	5	0.782	0.91

bt, biotite; crd, cordierite; grt, garnet; kfs, potassium feldspar; ms, muscovite; plag, plagioclase feldspar; qtz, quartz.
[crd], mineral interpreted to be part of the assemblage but has been replaced.

amphibolite-facies boundary were also insufficient in modelling the gravity high at 5 km along the profile without the inclusion of a small blind pluton. The density contrast either side of the amphibolite-facies boundary is too low to determine its orientation, so it was modelled vertically in accordance with the interpretation of heating from a vertical magma transfer zone.

The introduction of two small buried plutons, one mafic and one felsic, was necessary to model the abrupt increase in gravity at 5 km along the profile. The alternative, sedimentary rocks (the transitional schists of Binns 1966) between a fault at the boundary between the Girrakool beds and Rampsbeck Schists and the Glen Bluff 'Fault,' modelled at a higher density could produce the required modelled response without buried plutons but is considered unrealistic, as petrological evidence suggests the sedimentary rocks of the transitional schists should be less dense than the Rampsbeck Schists given their mineral composition.

During initial modelling a large buried pluton was constructed to link the surface western outlier of Abroi

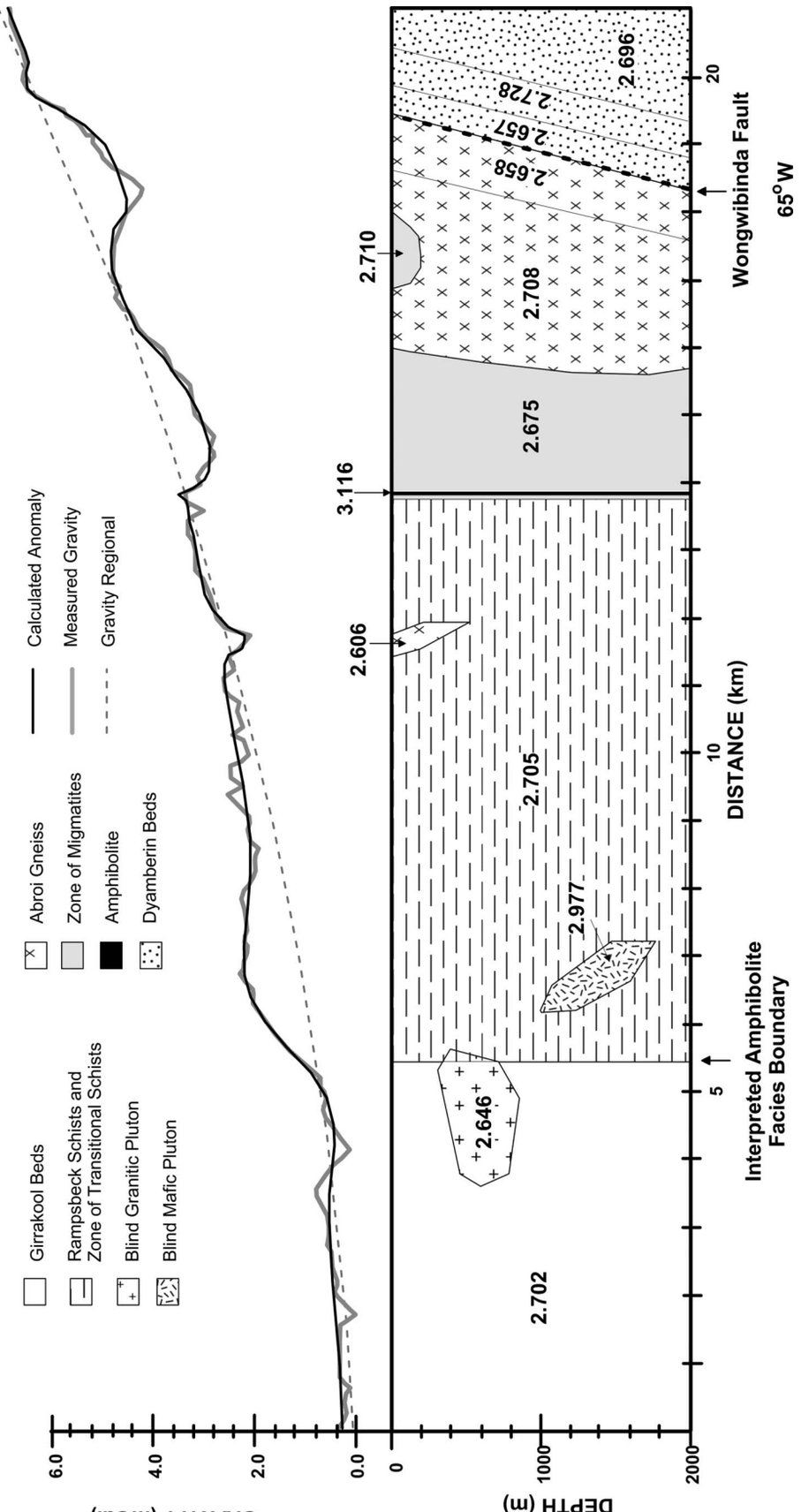

Figure 6 Preferred 2.5D subsurface model of the gravity transect. Density in g/cm^3; dashed grey line is the gravity regional removed from the data and the solid black line is the calculated anomaly response to the measured gravity (solid grey line).

Gneiss to the main body near the Wongwibinda Fault, to assess the possibility of the Abroi Gneiss representing a large buried heat source. The ensuing model required density values outside the measured range for most lithologies and resulted in a poor fit of the observed data and therefore was not explored further.

DISCUSSION

P–T and mineral chemistry

The new garnet mineral chemistry, *P–T* calculations and the geophysical subsurface model allow a re-evaluation of the presently understood metamorphic history of the Wongwibinda Complex.

Garnet is a key metamorphic indicator mineral for the Wongwibinda Complex and developed pre- to syn-D_1 on the basis of the S_1 fabric enveloping the garnet. Muscovite has variably been included in (Vernon 1982; Farrell 1992; Landenberger *et al.* 1995) and excluded from (Binns 1966; Stephenson & Hensel 1979) the peak high-grade regional metamorphic assemblage. In this study, muscovite commonly defines the S_2 foliation in the higher-grade rocks, muscovite porphyroblasts overgrow the main fabric in garnet–biotite schists, sillimanite is pseudomorphed by muscovite in the migmatite xenolith (MU61739 to 61744) and cordierite is replaced by muscovite. These relationships indicate that muscovite is unlikely to have been a part of the S_1 assemblage in the higher-grade rocks and formed throughout later events. This does not preclude the possibility of S_1 muscovite in lower-grade rocks.

We define the peak metamorphic mineral assemblage (D_1) as comprising garnet, biotite, plagioclase, potassium feldspar, quartz and cordierite. In the lower-grade Rampsbeck Schists muscovite may be included as part of the peak mineral assemblage due to a slightly lower temperature of formation. Muscovite replacing cordierite porphyroblasts in lower-grade samples appears later than D_2 and probably represents greenschist retrograde conditions during D_3–D_4.

Petrographic observations, *P–T* determinations and mineral chemistry reveal a distinctive pattern in mineral composition which provides new evidence for D_2 retrograde conditions though *P–T* determinations suggest only slightly lower temperatures. For example, biotite provides some information of metamorphic grade, with metamorphic biotite typically Fe-rich with XFe >50. MU61746, 61761 and 61762 have the highest concentrations of XFe suggesting either lower-grade metamorphic conditions, Fe–Mg exchange with other phases or alteration from the intrusion of late-stage plutons. Low values of wt% K_2O may be indicative of partial chloritisation due to low-grade alteration.

Garnet generally contains 60–70% almandine 10–36% spessartine, 8–15% pyrope and <5% grossular. Garnet growth phase equilibria and mass balance require the Mn content decreases with growth thus producing a bell-shaped growth zoning profile of decreasing Mn from core to rim (Spear 1993). However, when garnet is partially resorbed, i.e. during retrograde metamorphism, Ca and Mn are enriched in the rim due to limited lattice diffusion and effective intergranular element migration of Fe and Mg (Hwang *et al.* 2003).

In this study, zoning profiles and rim–core analysis of garnet in six samples from the Zone of Migmatites and three from the Rampsbeck Schists are not typical of normal garnet growth zoning. Mn concentrations are greater in the rim compared with the core for all samples, with the exception of MU61744. The most common zoning profile observed is a flat unzoned interior with narrow ($<350\ \mu$m) rims of variable composition (Figure 4). We propose that the unzoned cores represent elemental homogenisation at peak D_1 metamorphic conditions and the narrow rims (with increased Mn) represent resorbed grain edges during retrograde conditions (D_2). Textural evidence that supports resorption includes corroded garnet in MU61777. The retrograde resorbed grain edges may reflect post-peak cooling under amphibolite-facies conditions.

MU61744, from a migmatite xenolith in the Abroi Gneiss, shows a garnet zoning profile of slightly decreased Mn and increased Fe in the rim with a relatively uniform core (Figure 4). This suggests that neither diffusion during cooling or retrograde resorbing affected the garnet. The rim composition most likely reflects changes in the bulk composition of the xenolith following entrainment by the Abroi Gneiss during D_2.

MU61737, 61746, 61749, 61761, 61751, 61762, 61763 and 61777 demonstrate the effects of retrograde metamorphism with increases in Mn from core to rim. XFe *vs* Mn (Figure 5) evaluates the degree of retrograde resorbing of garnet grain edges. As XFe increases Mn also increases, consistent with diffusion during cooling from a metamorphic event (Spear 1993). Samples less affected by retrograde resorbing (0501c, MU61744, 61749 and 61751) plot as clusters of data (Figure 5a) and those more strongly affected by retrograde resorbing (MU61761, 61762 and 61763) form a positive correlation (Figure 5b). In highly resorbed samples (MU61746) metamorphic biotite is Fe-rich (XFe 65–74) suggesting Fe lost from the garnet diffused into the biotite.

The spatial distribution of samples affected by retrograde resorbing highlights that the degree of resorbing is related to D_2 strain and the proximity to shear zones or post-tectonic granites (i.e. the Abroi Gneiss, which intruded during D_2). MU 61737 and 61761 are the closest to the Wongwibinda Shear Zone and show highly resorbed garnet, while MU61751 is furthest away from the Wongwibinda Shear Zone and contains less resorbed grains.

The evidence for a D_2 retrograde event as suggested by the compositional zoning in the garnet is further supported by the average P–T calculations. For this analysis garnet cores of samples least affected by retrogression were used for D_1 and garnet rims of samples affected by retrogression were used for D_2. Average *P–T* analysis of the S_1 and S_2 assemblages indicated that both D_1 and D_2 occurred under amphibolite facies conditions. With respect to average-*P* there was no evidence for a pressure gradient across the Wongwibinda Complex as all calculated pressures are within error. For average-*T* the lowest temperature calculated for a D_1 sample (Table 4) is only 40°C higher than the highest temperature calculated for a D_2 sample (Table 5). This suggests

Table 5 Results of thermobarometric analysis of retrograde metamorphic mineral assemblages in samples with zoned garnet.

	Average *P–T*	Average *P* (MPa)	Average *T* (°C)	Assemblage	Number of reactions	Correlation coefficient	SD (Fit)
MU61737	660 ± 154°C 400 ± 420 MPa	380 ± 452	653 ± 144	grt-bt-plag-kfs-qtz	3	−0.168	1.94
MU61746	651 ± 52°C 420 ± 210 MPa	360 ± 136	637 ± 38	grt-bt-plag-kfs-qtz	6	0.789	1.31
MU61762	706 ± 89°C 410 ± 250 MPa	380 ± 198	697 ± 72	grt-bt-ms-plag-qtz	6	0.696	1.34
MU61763	673 ± 70°C 380 ± 270 MPa	380 ± 192	677 ± 48	grt-bt-ms-plag-kfs-qtz	7	0.828	1.38
MU61777	624 ± 126°C 500 ± 350 MPa	510 ± 310	615 ± 112	grt-bt-plag-kfs-qtz	3	−0.175	1.68

bt, biotite; crd, cordierite; grt, garnet; kfs, potassium feldspar; ms, muscovite; plag, plagioclase feldspar; qtz, quartz.

that the onset of retrograde conditions during D_2 was the result of isobaric cooling (as previously proposed by Vernon 1982) between D_1 and D_2. These results are within the range of those calculated by Farrell (1992), whose data also showed no regional pressure variations. The D_2 event was then followed by a second period of retrograde conditions during D_3–D_4 under greenschist-facies conditions. Greenschist retrograde conditions are unlikely to have altered the garnet mineral chemistry except in samples close to the intrusion of Upper Permian to Triassic granites (i.e. Tobermory and Kookabookra Adamellites). Garnet in these locations is almost completely replaced by biotite. The spatial association between these textures and the Tobermory and Kookabookra Adamellites suggests these textures related to contact metamorphism.

Subsurface structure

For the model we assumed that the Wongwibinda Complex surface geology projected down to the subsurface geology (i.e. with no hidden plutons) and using the calculated densities, determined that depths of 2–5 km could be effectively modelled. A depth of 2 km was most sensitive to the slight density variations observed between lithologies and best represents the limit of the gravity data. When the geological boundaries were transferred to the measured gravity data they were generally representative of the distinctive gravity responses. Oscillations in the measured Bouguer gravity anomaly most likely relate to subtle changes in the geology i.e. compositional changes in the Rampsbeck Schists between psammitic and pelitic layers, and an inherent noise level within the data. In the model, the small Abroi Gneiss and the Amphibolite could represent features of the inherent noise level of the data. The Abroi Gneiss outcrops along the profile and thus has been modelled as a small weathered pluton. The Amphibolite appears not to outcrop at the surface but according to published geology maps crosses the profile at this location and is therefore modelled as a thin sheet.

The Wongwibinda Fault, the eastern boundary of the complex, is considered structurally responsible for uplift of the Wongwibinda Complex and has been reactivated several times (Binns 1966; Landenberger *et al.* 1995). The present-day orientation of the fault is best modelled with a 65°W dip which agrees with the structural work of Binns (1966) who measured a steep angle (75°W and 80°W) south of the Wongwibinda homestead and a gradual shallowing northward to 35°W in the Kookabookra Adamellite. An attempt was made to model the other structural feature of the Wongwibinda Complex, the Glen Bluff 'Fault,' but a preferred orientation could not be obtained due to a lack of density contrast within the Rampsbeck Schists. This fault lacks geological and geophysical evidence for inclusion in the model and may not be present in the central part of the Wongwibinda Complex. On the geological map (Figure 2) the boundary between the Girrakool beds and Rampsbeck Schists coincides with an area of transitional schists, where Leitch (1978) determined a boundary between amphibolite-facies metamorphism and lower-grade rocks. In our model the preferred orientation of this boundary was modelled as being vertical in accordance with our interpretation of heating from a vertical magma transfer zone as part of the metamorphic history of the complex.

The gravity anomaly at 4–8 km along the profile occurs in the area of the zone of transitional schists around the amphibolite facies boundary and could not be explained by modelling the surface geology. This was because the density contrasts between the lithologies were insufficient in producing a matched response to the data from modelling boundary orientation. When the geological history is considered, backarc sedimentary basin formation with early extensional magmatism can produce both mafic and felsic intrusive rocks (Foden *et al.* 2007). The introduction of two small buried plutons, one mafic and one felsic, produced the necessary response of the observed gravity anomaly. The exact size, orientation and density of these small hidden plutons cannot be tightly constrained, but they are unlikely to be the heat source for the Wongwibinda Complex given their small size.

During initial modelling, attempts were made to create a subsurface link between all outcrops of Abroi Gneiss to produce a large pluton, as well as modelling of a large buried pluton at depths >2 km. Both scenarios required density values outside the range measured for most lithologies and produced a poor visual fit of the observed data. The sensitivity of the model is also limited and responses from deep sources cannot be modelled. If a large intrusion were to shallowly (>10 km) underlie the Wongwibinda Complex it would

produce a local gravity anomaly centred on the highest-grade rocks, although no major gravity anomaly exists. The geophysical data are not consistent with an underlying magmatic heat source.

Implications of subsurface structure and retrograde metamorphism on metamorphic history

Metamorphism of the Wongwibinda Complex began under amphibolite-facies conditions during D_1, D_2 and was followed by greenschist-facies conditions (D_3, D_4). The systematic drop in metamorphic grade observed from east to west has given rise to several models to explain the origins of the heat source. As the regional aureole of the Wongwibinda Complex is localised around the Abroi Gneiss, Vernon (1982) proposed that a large buried heat source was responsible for the regional aureole. Geophysical evidence shows no major gravity anomaly within the Wongwibinda Complex and subsurface modelling is not consistent with a shallowly underlying magmatic heat source. Therefore, the heat source for the Wongwibinda Complex may have been removed by faulting during subsequent tectonics (e.g. Hunter–Bowen Orogeny) or it may have been largely eroded.

One possible mechanism to achieve the high-*T* thermal perturbation of the Wongwibinda Complex involves intrusion of the Hillgrove Plutonic Suite through a root feeder zone centred about the Abroi Gneiss. A wide metamorphic aureole will develop in this scenario (Richards & Collins 2002).

Annen *et al.* (2008) argued that mafic magmas in deep hot zones play a fundamental role in silicic melt generation for crustal melting and that this crustal melt accumulates in shallow reservoirs (~3–10 km depth). If not erupted, such shallow reservoirs consolidate to form granite plutons, with mafic igneous rocks being a minor component (Annen *et al.* 2006). Barton & Hanson (1989) demonstrated that multiple granite intrusions can elevate regional geothermal gradients. The amalgamation of many small intrusions, commonly of magmas with very similar bulk chemical composition but subtle textural differences (John & Blundy 1993) or radiometric ages (Coleman *et al.* 2004) may also form granite plutonic rocks. In the Wongwibinda Complex, Binns (1966) and Farrell (1992) noted that the field relationships, outcrop pattern and petrological evidence of the Abroi Gneiss, Rockvale Adamellite and Tobermory Adamellite, plutons of the Hillgrove Plutonic Suite, suggest these plutons are part of a composite pluton.

Barton *et al.* (1991) have shown that migmatites form centrally to a subhorizontal, flat-bottomed, tabular-shaped pluton with a root or feeder zone around which a wide metamorphic aureole has developed. A similar model has been proposed for the Cooma Complex by Richards & Collins (2002), whereby the overlying pluton is the Murrumbidgee Batholith, which has since been eroded, exposing a wide aureole and central migmatite zone and the Cooma Granodiorite. Advective heat associated with magma transfer could, according to Richards & Collins (2002) enhance the development of an extensive low-*P*–high-*T* metamorphic terrane beneath a granitic batholith, particularly if the intrusion mechanism is multiple sheeting, which required leucosome migration through the migmatite zone. Sustained advective heat flow may also be provided via the passage of magma through a localised transfer zone (De Yoreo *et al.* 1991). In the Wongwibinda Complex migmatites formed west of the Abroi Gneiss, which may be a root feeder zone for the Hillgrove Plutonic Suite in this type of scenario. Therefore, sustained magma transfer through this zone could have the potential to produce the regional aureole observed. With this model, the orientation of the amphibolite–facies boundary would therefore be closely linked to the orientation of the magma transfer zone. Simple thermal modelling (from standard formulas in Turcotte & Schubert 2002) of a conduit of granodiorite magma, at the Wongwibinda Fault, at ~850°C (assuming continuous heat from magma replenishment), to replicate observed thermal conditions would take ~3–5 Ma to heat sample MU61751 (8 km away) to ~600°C and 1 Ma or less to heat sample MU61744 (2 km away) to ~700°C.

The uplift of the Wongwibinda Complex along the Wongwibinda Fault and subsequent erosion has exposed the regional thermal aureole underneath the Hillgrove Plutonic Suite, centred on the Abroi Gneiss—the inferred feeder zone. If the intrusion of the Hillgrove Plutonic Suite took place in several pulses over 10 Ma, then advective heat has the potential to heat the Wongwibinda Complex and sustain amphibolite-facies conditions while under low pressure. The retrograde metamorphism of the Wongwibinda Complex documented here for the first time between the D_1 and D_2 events is most probably a result of cooling of the feeder zone.

ACKNOWLEDGEMENTS

Macquarie University funding to NRD (MURDG) provided financial support to conduct this research. This work began with the honours project of CRD. CRD thanks Norman Pearson for his assistance with the geochemical analyses and Craig O'Neill for help with the thermal modelling. Critical reviews by Dick Flood and Robin Offler improved an earlier version of this manuscript. The analytical data were obtained using instrumentation funded by ARC LIEF and DEST, Systemic Infrastructure Grants, industry partners and Macquarie University. This is contribution 629 from the Australian Research Council National Key Centre for Geochemical Evolution and Metallogeny of Continents (URL: <http://www.gemoc.mq.edu.au>).

REFERENCES

Annen C., Blundy J. D. & Sparks R. S. J. 2006. The genesis of calcalkaline intermediate and silicic magmas in deep crustal hot zones. *Journal of Petrology* **47**, 505–539.

Annen C., Blundy J. D. & Sparks R. S. J. 2008. The source of granitic melt in Deep Hot Zones. *Transactions of the Royal Society of Edinburgh: Earth Sciences* **97**, 297–309.

Annen C. & Sparks R. S. J. 2002. Effects of repetitive emplacement of basaltic intrusions on thermal evolution and melt generation in the crust. *Earth and Planetary Science Letters* **203**, 937–955.

Ashley P. M. & Craw D. 2004. Structural controls on hydrothermal alteration and gold–antimony mineralisation in the Hillgrove area, NSW, Australia. *Mineralium Deposita* **39**, 223–239.

Barbarin B. 2005. Mafic magmatic enclaves and mafic rocks associated with some granitoids of the central Sierra Nevada batholith, California: nature, origin and relations with the hosts. *Lithos* **80**, 155–177.

Barton M. D. & Hanson R. B. 1989. Magmatism and the development of low-pressure metamorphic belts: implications from the western United States and thermal modelling. *Geological Society of America Bulletin* **101**, 1051–1065.

Barton M. D., Staude J. M., Snow E. A. & Johnson D. A. 1991. Aureole systematics. *In*: Kerrick M. D. ed. *Contact metamorphism*, pp. 723–847. Reviews in Mineralogy **26**.

Binns R. A. 1966. Granitic intrusions and regional metamorphic rocks of Permian ages from the Wongwibinda District, north-eastern New South Wales. *Journal and Proceedings of the Royal Society of New South Wales* **99**, 5–36.

Blundy J. D. & Sparks R. S. J. 1992. Petrogenesis of mafic inclusion in granitoids of the Adamello massif, Italy. *Journal of Petrology* **33**, 1039–1104.

Buck W. R., Martinez F., Steckler M. S. & Cochran J. R. 1988. Thermal consequences of lithospheric extension: pure and simple. *Tectonics* **7**, 213–234.

Coleman D. S., Gray W. & Glazner A. F. 2004. Rethinking the emplacement and evolution of zoned plutons: geochronologic evidence for incremental assembly of the Tuolumne Intrusive Suite, California. *Geology* **32**, 433–436.

Collins W. J. 1998. Evaluation of petrogenetic models for Lachlan Fold Belt granitoids: implications for crustal architecture and tectonic models. *Australian Journal of Earth Sciences* **45**, 483–500.

Collins W. J., Vernon R. H. & Clarke G. L. 1991. Discrete Proterozoic structural terranes associated with low-*P*, high-*T* metamorphism, Anmatjira Range, Arunta Inlier, central Australia: tectonic implications. *Journal of Structural Geology* **13**, 1157–1171.

Collins W. J. & Williams I. S. 1995. SHRIMP ion probe dating of short-lived Proterozoic tectonic cycles in the northern Arunta Inlier, central Australia. *Precambrian Research* **71**, 91–105.

Cooley R. L. & Naft R. L. 1990. *Regression modelling of groundwater flow*. US Geological Survey Techniques of Water-Resources Investigations, Book 3, Chapter B4.

De Yoreo J. J., Lux D. R. & Guidotti C. V. 1991. Thermal modelling in low-pressure/high-temperature metamorphic belts. *Tectonophysics* **188**, 209–238.

Dirks P. H. G. M., Hand M., Collins W. J. & Offler R. 1992. Structural–metamorphic evolution of the Tia Complex, New England fold belt: thermal overprint of an accretion–subduction complex in a compressional back-arc setting. *Journal of Structural Geology* **14**, 669–688.

Dirks P. H. G. M., Hand M., Offler R. & Collins W. J. 1993. Timing of emplacement and deformation of the Tia Granodiorite, southern New England Fold Belt, NSW: implications for the metamorphic history. *Australian Journal of Earth Sciences* **40**, 103–108.

Fagan R. K. 1979. Deformation, metamorphism and anatexis in an Early Palaeozoic flysch sequence in northeastern Victoria. PhD thesis, University of New England, Armidale (unpubl.).

Farrell T. R. 1988. Structural geology and tectonic development of the Wongwibinda Metamorphic Complex. *In*: Kleeman J. D. ed. *New England Orogen: tectonics and metallogenesis*, pp. 117–124. University of New England, Armidale.

Farrell T. R. 1992. Deformation, metamorphism and migmatite genesis in the Wongwibinda Metamorphic Complex. PhD thesis, University of Newcastle, Newcastle (unpubl.).

Flood R. H. & Vernon R. H. 1978. The Cooma Granodiorite, Australia: an example of in situ crustal anatexis? *Geology* **6**, 81–84.

Foden J., Hand M., Lawley C. & Burdett M. 2007. Granite formation in extensional accretionary orogens: the generation of maximum I-S type granite geochemical distinction. *Geological Society of Australia Abstracts* **86**, 28–31.

Greenfield J. E., Clarke G. L. & White R. W. 1998. A sequence of partial melting reactions at Mt Stafford, central Australia. *Journal of Metamorphic Geology* **16**, 363–378.

Gunthorpe R. J. 1970. Plutonic and metamorphic rocks of the Walcha–Nowendoc–Yarrowitch district. PhD thesis, University of Newcastle, Newcastle (unpubl.).

Guo B., Lackie M. A. & Flood R. H. 2007. Upper crustal structure of the Tamworth Belt, New South Wales: constraints from new gravity data. *Australian Journal of Earth Sciences* **54**, 1073–1087.

Holland T. J. B. 2006. Computer Program AX. Online <http://www.esc.cam.ac.uk/research/research-groups/holland>

Holland T. J. B. & Powell R. 2003. Activity–composition relations for phases in petrological calculations: an asymmetric multicomponent formulation. *Contributions to Mineralogy and Petrology* **145**, 492–501.

Hwang S. L., Shen P., Yui T. F. & Chu H. T. 2003. On the mechanism of resorption zoning in metamorphic garnet. *Journal of Metamorphic Geology* **21**, 761–769.

Jenkins R. B., Landenberger B. & Collins W. J. 2002. Late Palaeozoic retreating and advancing subduction boundary in the New England Fold Belt, New South Wales. *Australian Journal of Earth Sciences* **49**, 467–489.

John B. E. & Blundy J. D. 1993. Emplacement-related deformation of granitoid magmas, Southern Adamello Massif, Italy. *Geological Society of America Bulletin* **105**, 1517–1541.

Johnson S. E. 1999. Deformation and possible origins of the Cooma Complex, southeastern Lachlan Fold Belt, New South Wales. *Australian Journal of Earth Sciences* **46**, 429–442.

Joplin G. A. 1942. Petrological studies in the Ordovician of New South Wales. I. The Cooma Complex. *Proceedings of the Linnean Society of New South Wales* **67**, 156–196.

Joplin G. A. 1943. Petrological studies of the Ordovician of New South Wales. II. The northern extension of the Cooma Complex. *Proceedings of the Linnean Society of New South Wales* **68**, 159–183.

Kent A. J. R. 1994. Geochronology and geochemistry of Palaeozoic intrusive rocks in the Rockvale region, Southern New England Orogen, New South Wales. *Australian Journal of Earth Sciences* **41**, 365–379.

Korsch R. J. 1978. Stratigraphic and igneous units in the Rockvale–Coffs Harbour region, northern New South Wales. *Journal and Proceedings of the Royal Society of New South Wales* **111**, 13–17.

Korsch R. J. 1981. Structural geology of the Rockvale Block, northern New South Wales. *Journal of the Geological Society of Australia* **28**, 51–70.

Landenberger B., Farrell T. R., Offler R., Collins W. J. & Whitford D. J. 1995. Tectonic implications of Rb–Sr biotite ages for the Hillgrove Plutonic Suite, New England Fold Belt, NSW, Australia. *Precambrian Research* **71**, 251–263.

Leitch E. C. 1978. Structural succession in a Late Palaeozoic slate belt and its tectonic significance. *Tectonophysics* **47**, 311–323.

Powell R. & Holland T. J. B. 1988. An internally consistent dataset with uncertainties and correlations: 3. Applications to geobarometry, worked examples and a computer program. *Journal of Metamorphic Geology* **6**, 173–204.

Powell R. & Holland T. J. B. 1998. An internally consistent thermodynamic data set for phases of petrological interest. *Journal of Metamorphic Geology* **16**, 309–343.

Reynolds J. M. 2003. *An introduction to applied and environmental geophysics*. John Wiley and Sons, London.

Richards S. W. & Collins W. J. 2002. The Cooma Metamorphic Complex, a low-*P*, high-*T* (LPHT) regional aureole beneath the Murrumbidgee Batholith. *Journal of Metamorphic Geology* **20**, 119–134.

Spear F. S. 1993. *Metamorphic phase equilibria and pressure–temperature–time paths*. Mineralogical Society of America Monograph.

Stephenson N. C. N. & Hensel H. D. 1979. Intergrown calcic and Fe–Mg amphiboles from the Wongwibinda Metamorphic Complex, NSW, Australia. *Canadian Mineralogist* **17**, 11–23.

Stephenson N. C. N. & Hensel H. D. 1982. Amphibolites and related rocks from the Wongwibinda metamorphic complex, northern N.S.W., Australia. *Lithos* **15**, 59–75.

Stuwe K., Sandiford M. & Powell R. 1993. Episodic metamorphism and deformation in low-pressure, high-temperature terranes. *Geology* **21**, 829–832.

Turcotte D. L. & Schubert G. 2002. *Geodynamics*. Cambridge University Press, Cambridge.

WHITE A. R. J., CHAPPELL B. W. & CLEARY J. R. 1974. Geologic setting and emplacement of some Australian Palaeozoic batholiths and implications for intrusive mechanisms. *Pacific Geology* **8**, 159–171.

WHITE R. W., POWELL R. & CLARKE G. L. 2002. Prograde metamorphic assemblage evolution during partial melting of metasedimenary rocks at low pressures: migmatites from Mt Stafford, Central Australia. *Journal of Petrology* **44**, 1937–1960.

VALLANCE T. G. 1969. Southern and central highlands fold belt: plutonic and metamorphic rocks. *Journal of the Geological Society of Australia* **16**, 180–200.

VERNON R. H. 1982. Isobaric cooling of two regional metamorphic complexes related to igneous intrusions in southeastern Australian. *Geology* **10**, 76–81.

VERNON R. H., CLARKE G. L. & COLLINS W. J. 1990. Local mid-crustal granulite facies metamorphism and melting: an example in the Mount Stafford area, central Australia. *In*: Ashworth J. R. & Brown M. eds. *High-temperature metamorphism and crustal anatexis*, pp. 272–319. Unwin Hyman, London.

Received 3 June 2009; accepted 3 February 2010

APPENDIX 1: LOCALITY COORDINATES

Site no.	Macquarie University (MU) sample no.	Easting	Northing
1	0501c	418368	6641251
2	MU61737	418838	6649735
3	MU61739, MU61744	417707	6649625
4	MU61746	416560	6650483
5	MU61749	415284	6649556
6	MU61751	412210	6649674
7	MU61756	409511	6653324
8	MU61761	408580	6665070
9	MU61762, MU61763	408406	6665238
10	MU61775	414937	6647838
11	MU61777	415763	6646629

Location coordinates are Geodetic Datum Australia 94 Zone 56. All rock samples and slides are held at Macquarie University.

Part 2. Zircon U-Pb-Hf characteristics of the rocks

Chapter 4

Using detrital zircon geochemistry to characterise the protolith to the Wongwibinda Metamorphic Complex, southern New England Orogen, Australia

S. J. Craven and N. R. Daczko

GEMOC ARC National Key Centre, Department of Earth and Planetary Sciences, Macquarie University, NSW 2109, Australia

Using detrital zircon geochemistry to characterise the protolith to the Wongwibinda Metamorphic Complex, southern New England Orogen, Australia.

Abstract

The Wongwibinda Metamorphic Complex (WMC) of the southern New England Orogen exhibits small exposures of high-T–low-P metamorphic rocks that formed in an extensional accretionary orogen. A steep metamorphic field gradient provides the opportunity to compare virtually unmetamorphosed sedimentary rocks to high-grade metamorphic rocks (migmatite). The comparison of trace element and U-Pb-Hf-isotope composition of detrital zircon in rocks of variable metamorphic grade facilitated a better understanding of the processes that modify zircon during metamorphism and the identification of the protolith to the metamorphic rocks. The inferred protolith (Girrakool Beds) is dominantly well-bedded semi-pelitic to silicic mudstone with rare volcaniclastic sandstone interbeds. A comparison of the trace element and U-Pb-Hf-isotope composition of detrital zircon across the metamorphic sequence demonstrates that the Girrakool Beds are the protolith to all the metamorphic rocks within the Wongwibinda Metamorphic Complex. U-Pb geochronology of zircon grains separated from rocks and collected as alluvial grains in modern stream sediment identifies a maximum deposition age of c. 309 Ma. The majority of detrital zircon is c. 320–350 Ma with a peak at c. 330 Ma, and there are very few Proterozoic and Archean grains. The new zircon U-Pb geochronology supports petrographic evidence of a volcanic arc provenance for the Girrakool Beds. The trace element composition and

age of detrital zircon points to the Keepit arc, a volcanic arc along the western margin of the Tamworth Belt, as the likely provenance. The Hf isotope data for c. 320–350 Ma detrital grains become less radiogenic over the 30 million year record, representing a short-term isotopic reversal of the pattern of becoming more radiogenic, common to extensional accretionary orogens.

Morphologically modified zircon was identified in two metamorphic rock samples; the crystal faces on these grains are embayed and narrow overgrowths or delicate decorations adorn the surface. The internal structure may be ghosted and the Th trace element content increases along with discordance. Discordance of the Pb^{207}-U^{235} and Pb^{206}-U^{238} ages, related to high-grade metamorphism, demonstrates that caution is required when conducting protolith studies on high-grade metamorphic rocks. Zircon CL and BSE images should be scrutinized for structural evidence of alteration and where possible physical variations probed for chemical variations. The detrital zircon contained within the Girrakool Beds and metamorphic equivalents mirror the Carboniferous evolution of the Keepit arc. Volcanic activity in the Keepit arc is inferred to decrease rapidly at c. 320 Ma based on a major change in the detrital zircon age distribution at this time. This decrease is inferred to coincide with the onset of trench retreat, slab roll back and the eastward migration of the magmatic arc that led to the Late Carboniferous to Early Permian period of extension, S-type granite production, HTLP metamorphism and development of rift basins such as the Sydney-Gunnedah-Bowen system.

INTRODUCTION

Mineralogical and textural changes that occur during metamorphism make it difficult to identify the protolith of metamorphic rocks, especially at higher-grades (Gower, 2007). Knowledge of the provenance and nature of a protolith can lead to a better understanding of the tectonic setting and geological history of the region. Clues to the nature of a protolith are found in the metamorphic mineral assemblage, whole rock geochemistry and preservation of original textures. In addition, the persistence of the accessory mineral zircon during metamorphism commonly preserves a wealth of information about the protolith and its source (e.g. Belousova, et al., 2002). Detrital zircon studies of sedimentary, metasedimentary rocks and modern stream sediments are now routine in protolith and provenance studies (Vermeesch, 2004; Belousova et al., 2009; Belousova et al., 2010; Thomas, 2011). The TerraneChron® method, involving sampling of alluvial zircons, is an efficient way to directly link zircon populations in modern-day alluvial sediments to their currently exposed potential sources at local to regional scales (Belousova, et al., 2006a, 2010; Griffin, et al., 2007), and is particularly useful in areas of limited rock exposure.

The Wongwibinda Metamorphic Complex (WMC) is a high-T–low-P (HTLP) metamorphic terrane located within the Central Tablelands Complex of the southern New England Orogen, NE NSW, Australia (Fig. 1). It affords a rare exposure of medium- to high-grade metamorphic rocks in the New England Orogen. The Girrakool Beds are the major unit in, and most likely protolith to, the WMC. The Girrakool Beds are a thick turbidite sequence originally named the Lyndhurst Beds by Binns (1966) and subsequently

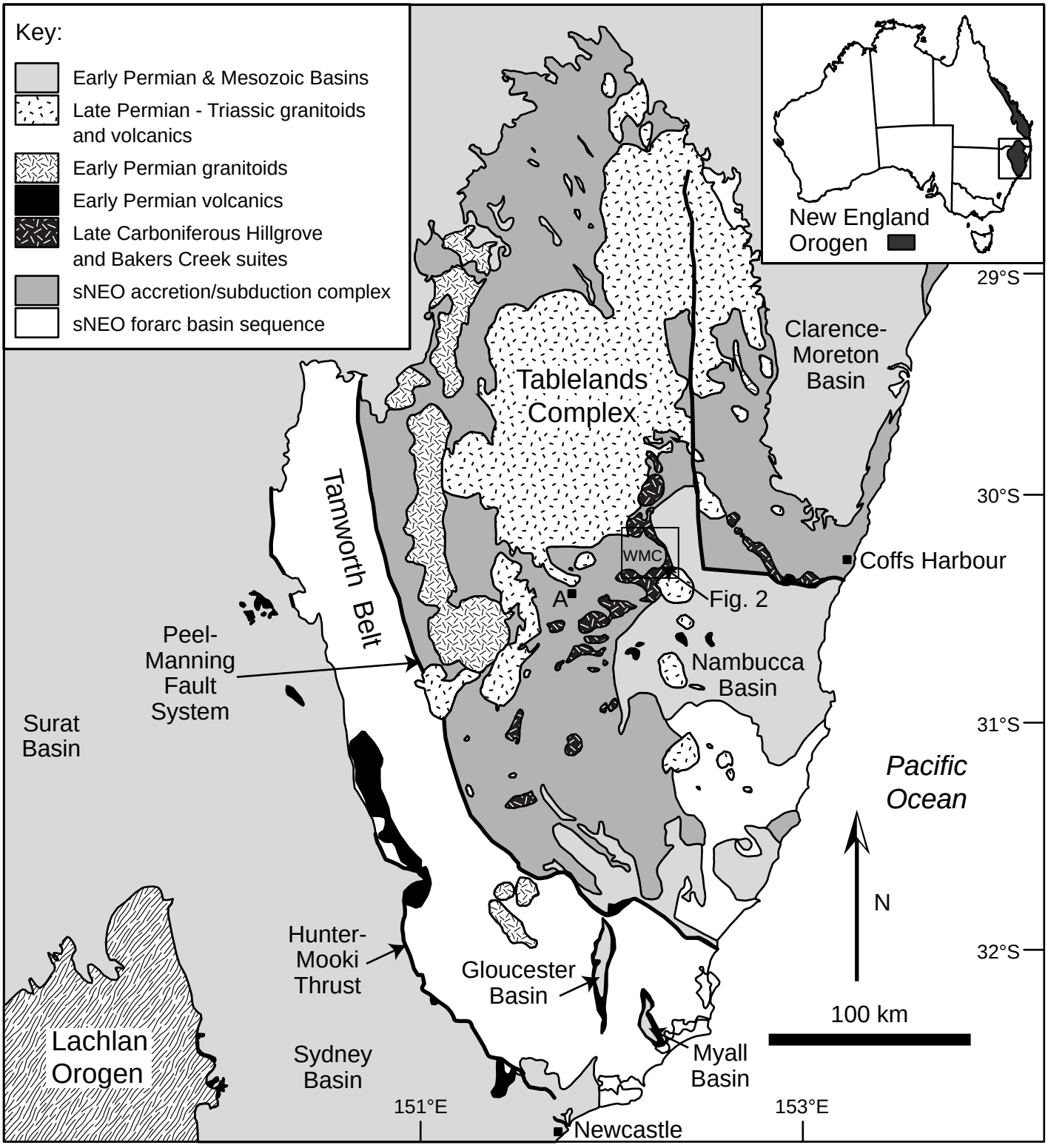

Figure 1: Regional geology of the southern New England Orogen (sNEO; modified from Jenkins et al., 2002). WMC, Wongwibinda Metamorphic Complex; A, Armidale.

named the Girrakool Beds by Korsch, (1978). Binns (1966) divided the WMC into four “Formations”, the Girrakool Beds, the Transitional Schists, the Rampsbeck Schists and the Zone of Migmatites. The term “Formation” is not strictly correct usage, but has been perpetuated by a number of other authors (Henson, 2000; Danis et al., 2010; Teague, 2010). Farrell (1992) more correctly describes them as lithotypes while Chapter 1 found evidence of one protolith (Girrakool Beds) showing a gradational increase in metamorphic grade from west to east.

Geochronological studies of the WMC are few (e.g. Binns, 1966; Landenberger et al., 1995; Chapters 1 and 2) and this study is the first to examine detrital zircon. A Permian biostratigraphic marker, the lamellibranch Myonia, identified in the Girrakool Beds (Runnegar, 1970; Binns, 1966) overlaps crystallisation ages for local members of the Hillgrove Plutonic Suite (c. 296-288 Ma; Cawood et al., 2011; Rosenbaum et al., 2012; Chapter 1). Metamorphic monazite ages in WMC migmatite samples return c. 297 Ma (Chapter 1) and amphibolite facies shear zones return c. 292 Ma (Chapter 2), suggesting a short-lived metamorphic history, closely following deposition of the protolith. Exhumation along the Wongwibinda Fault (eastern boundary of WMC) and rapid cooling of the WMC was dated by biotite Rb–Sr at 266–258 Ma (Landenberger et al., 1995). Late Permian to Early Triassic I-type plutonic rocks and Tertiary basalt postdate metamorphism in the WMC.

This study combines field relationships and petrography with U/Pb ages and Hf isotopic and trace element composition of detrital zircon from variably metamorphosed Girrakool Beds. It examines zircon separated from rocks and modern stream sediments. The aims are (1) identify the

provenance of the Girrakool Beds, (2) determine the depositional age(s) of the sedimentary protoliths of the WMC, (3) place these rocks into the broader context of the central Tablelands Complex, and (4) explain the tectonic context for the metamorphic geology of the WMC.

REGIONAL GEOLOGY

The Tasmanide orogenic system in eastern Australia (Glen, 2005, 2013) comprises three eastward younging turbidite–granite orogens: Delamerian (dominantly Neoproterozoic to Cambrian; western), Lachlan (dominantly Late Cambrian to Carboniferous; medial) and New England (dominantly Late Devonian to Triassic; eastern). Magmatic arc derived volcanogenic detritus, volcanism on the Whitsunday Islands and 155-100 Ma granites in mainland Queensland (Allen et al., 1997; Tulloch et al., 2010; Glen, 2013) comprise the final history of the Tasmanide orogenic system preserved in eastern Australia. Suites of S-type granite comprise up to half the plutonic rocks of the orogens (White and Chappell, 1988) and are commonly associated with HTLP metamorphic complexes. The New England Orogen manifests ~135 million years of west-dipping subduction between 365 Ma and 230 Ma (Glen, 2013). It is widely interpreted as an ancient, deformed fore-arc basin/accretionary wedge pair, the Tamworth Belt and Tablelands Complex, respectively (Scheibner, 1973; Leitch, 1975; Roberts and Engel, 1987; Fig. 1). The WMC (Fig. 2; >400 km^2) is located within the central Tablelands Complex and although the depositional age is not well constrained, it is broadly agreed that the sediment provenance is dominated

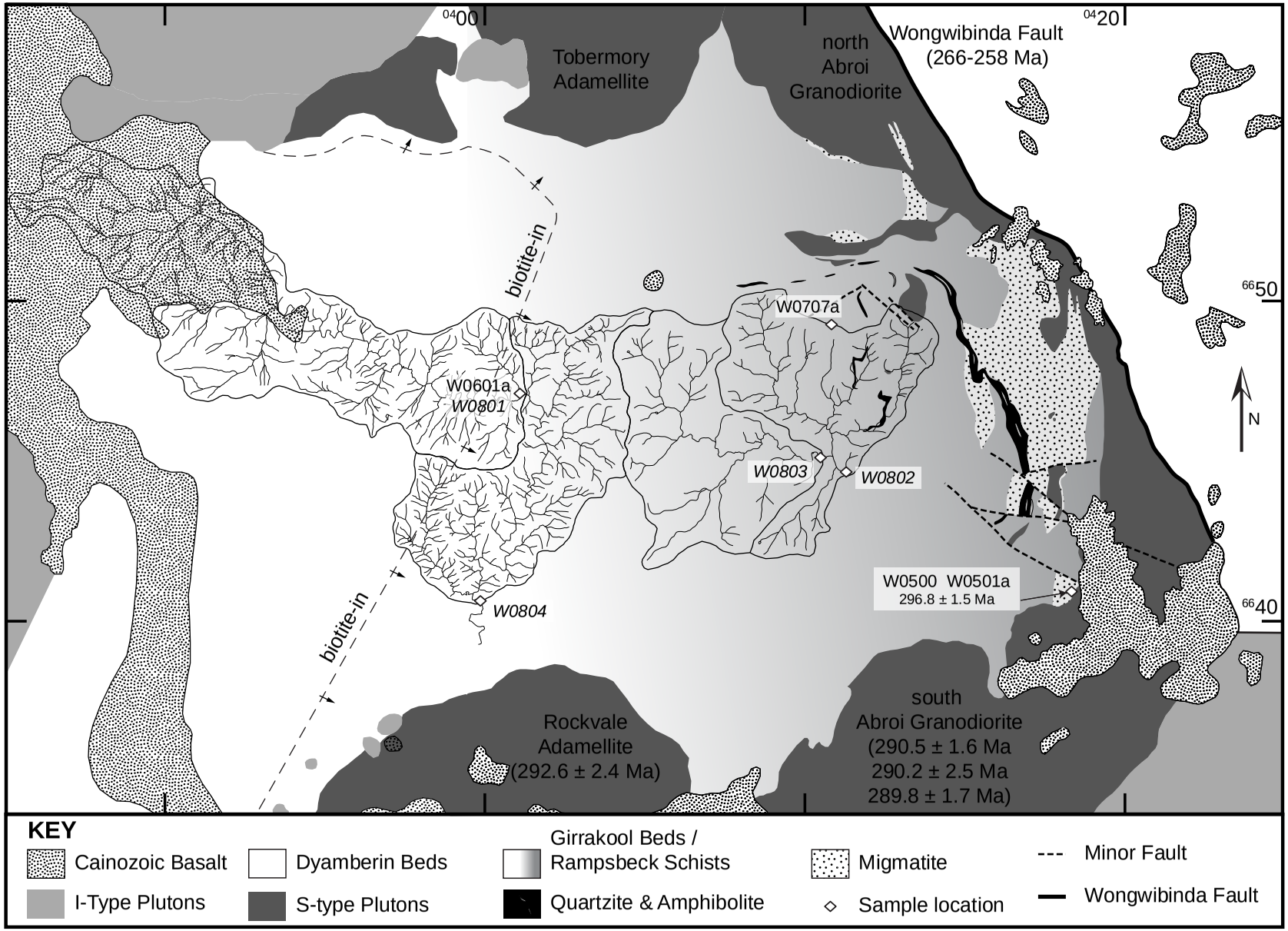

Figure 2: Geology of the Wongwibinda Metamorphic Complex, indicating locations discussed in the text (modified from Leitch 1978; Farrell 1992) and Dorrigo 1:100 000 Sheet (Leitch et al. 1971). Darker shading in the Girrakool Beds/ Rampsbeck Schists represents increasing metamorphic grade. Age of Rockvale Adamellite and Abroi Granodiorite from Cawood et al. (2011). Age of Abroi Granodiorite and metamorphic age for migmatite unit from Craven et al. (2012). Age of faulting and uplift along the Wongwibinda Fault from Landenberger et al. (1996).

by arc volcanism that ceased by 308-305 Ma (Roberts et al., 2004; Claoue-Long and Korsch, 2003, Cawood et al., 2011; Glen, 2013).

The Girrakool Beds, and inferred metamorphosed versions thereof, dominate the WMC (Fig. 2; Korsch, 1978, 1981; Jenkins et al. 2002). These rocks are a monotonous sequence of medium to fine grained turbidites with minor chert lenses and rare basalt and calcareous nodules. The sedimentary rocks comprise beds down to less than a centimetre thick and dip steeply (60° – 70°; Fig. 3a), making representative sampling difficult, as the composition varies between beds. Plutonic rocks of the S-type Hillgrove Plutonic Suite (296-288 Ma, Cawood et al., 2011; Rosenbaum et al., 2012; Chapter 1) intrude the Girrakool Beds; three plutons forming the southern, eastern and northern boundaries of the WMC (Fig. 2).

Binns (1966) determined petrographically, using lithic grains, that the provenance of the Girrakool Beds was a felsic volcanic terrane that also contained some intermediate volcanic material. Similarly, Korsch (1978) identified the provenance for Girrakool Beds to be a volcanic source on the basis of lithic grains and bipyramidal quartz. Korsch (1984), applying sandstone petrography and the “detrital framework modes” provenance fields of Dickenson and Suczek (1979), found that sandstones from the New England Orogen are mainly quartz-poor, lithic to feldspathic types derived from a volcanic arc terrane. A variation in detritus, from the Lower Devonian to Permian in the Tamworth Belt, records a change in the nature of volcanism in the magmatic arc; the detritus becomes relatively more felsic upwards from andesitic to dacitic and rhyolitic (Korsch, 1984; Cawood, 1991).

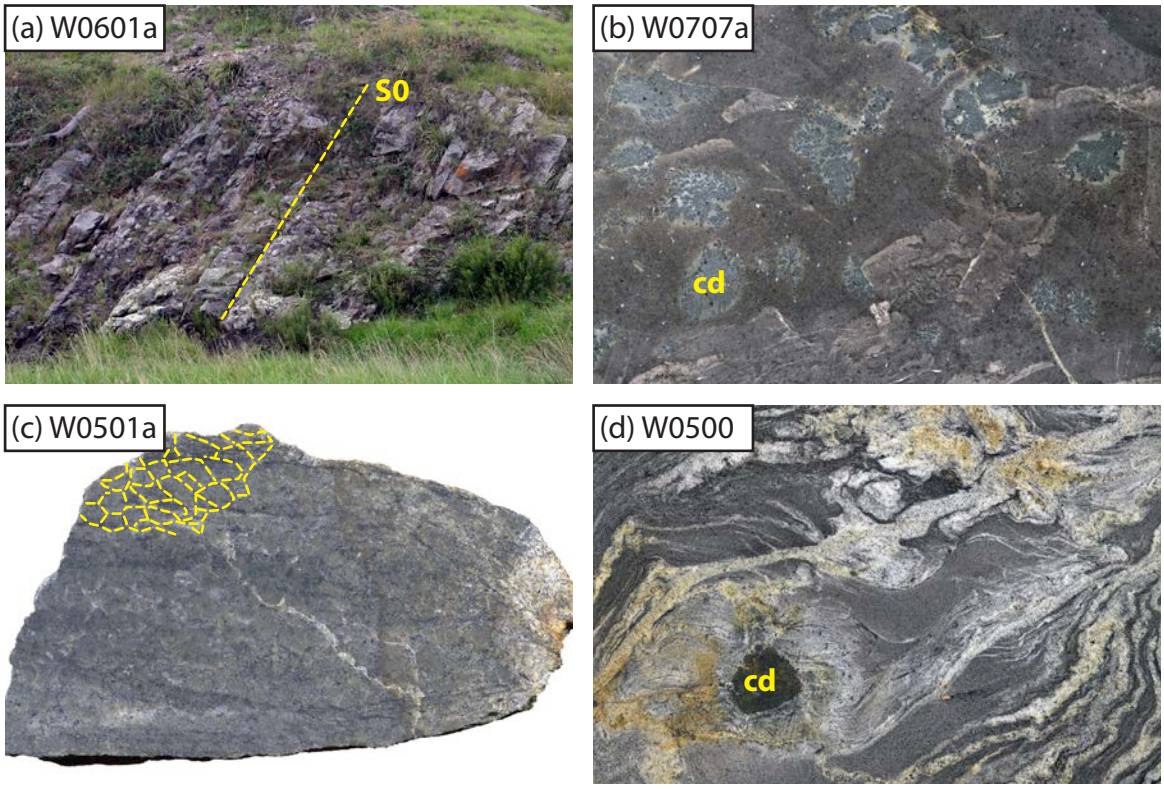

Figure 3: (a) Site of sample W0601a; low-grade metapsammite interbedded with metapelite. Steeply dipping (~60° NE) bedding (S0) marked by dashed line. (b–d) Cut and polished slabs. (b) Cordierite hornfels sample W0707a with large cordierite poikiloblasts (blue-grey). (c) Migmatite sample W0501a with pervasive fine network of leucosome (trace by dashed lines in top left). (d) Migmatite sample W0500 with leucosome veins and large cordierite (dark) surrounded by leucosome. Field of view for (a) is c. 4m across and for (b–d) is 14cm.

METHODS

Sampling: Two field-sampling methods were employed in this study.

Conventional rock sampling

Rock samples representative of the sedimentary and metasedimentary rocks exposed in the WMC were collected for this study. No attempt was made to tie the samples to any petrological subdivisions, for example the Rampsbeck Schists (Binns, 1966; Chapter 1), but rather to explore the variation across the complex from low-grade (west) to high-grade (east) (Chapter 1). Samples were selected on the basis of petrography, and bulk rock and mineral chemistry as being typical of the WMC. Homogeneous samples were sought from the Girrakool Beds, that were relatively free of quartz veining and other heterogeneities so that the whole rock and zircon composition would, as near as possible, reflect the protolith. Samples were also collected from the high-grade, amphibolite facies, migmatite zone. Four rock samples (Fig. 2) were selected for petrography and zircon analysis: (i) two amphibolite facies metasedimentary migmatites (W0500, W0501a), (ii) a metapelitic cordierite hornfels (W0707a), and (iii) a biotite-grade metapsammite (W0601a).

Polished thin sections were prepared for each rock specimen and a sub-sample was taken for zircon extraction. Geotrack International (Melbourne) prepared the zircon concentrates using standard magnetic and heavy liquid separation techniques.

Stream sediment sampling for alluvial zircons

A TerraneChron® survey was employed to collect alluvial zircon. It involves collecting alluvial zircon from stream sediments; it has the advantage

of easily sampling zircon eroded from the protolith and its metamorphic equivalents, over an extended area. This facilitated the collection of a zircon concentrate more representative of the targeted rocks compared to a random rock sample collected from the same area. All sample sites were designed to avoid drainage from the surrounding S-type granites. It was not possible to avoid younger Permian I-Type intrusions and Tertiary basalt. A watershed runs east-west across the complex (Fig. 2), concordant with the metamorphic gradient, which further facilitates the collection of samples along the metamorphic gradient. W0801 was selected to represent the least metamorphosed sedimentary rocks of the Girrakool Beds, W0804 the upper greenschist facies, biotite zone rocks, W0803 the transition from greenschist to amphibolite facies and W0802 the amphibolite facies migmatite zone.

The drainage basin map (Fig. 2) was digitized from the 1:25,000 topographic map using Adobe Illustrator. Boundaries were traced along the ridges between drainage basins. Sample locations were chosen at the point where the main stream exits the drainage basin.

Alluvial zircon was sampled from gravel lags within the streams. Approximately 20kg of gravel was wet screened at 4 mm and then 2 mm. The <2 mm sand was panned, using a Russian Lotok, to concentrate the heavy minerals in the field. Zircon was separated in the laboratory using heavy liquid separation (sodium polytungstate solution, density approximately 3 g/cm^3), followed by magnetic separation using a Frantz Magnetic Barrier Laboratory Separator.

Background and Instrumental Analysis

The zircon grains from both rock and alluvial samples were hand picked onto double-sided adhesive on a stainless steel stub and set in epoxy resin. The epoxy mounts were then lapped and polished to expose the centres of the grains for in situ zircon analysis.

Mineral equilibrium modelling of the WMC (Chapter 1) indicates a peak metamorphic temperature of 350 – 450 °C in the lowest grade rocks, those below the cordierite isograd and ~660 °C in the highest grade rocks and a maximum pressure of 3.5 kbar. The conditions of metamorphism are summarised to give context to the following review of mineral blocking temperatures relevant to this chapter.

It has previously been determined that the blocking temperature, the temperature where there is no longer any significant diffusion of the daughter isotopes, for radiogenic lead in the U-Th-Pb isotopic system, is greater than 900°C (Lee et al., 1997; Cherniak and Watson, 2001). This is far in excess of the 660°C determined for the WMC. Therefore, the U/Pb age of all zircons in the metamorphic rocks should remain unaffected by the amphibolite facies metamorphism. This argument also applies to tetravalent Th and U whose diffusion rates are slower by about four orders of magnitude (Lee et al., 1997) with blocking temperatures around 1100°C, similar for other incompatible, high field strength elements (HFSE), Ti (Cherniak and Watson, 2007), Hf (Cherniak et al., 1997a), and rare earth elements (REE) (Cherniak et al., 1997b). These findings support the application of trace element and U-Pb-Hf-isotope composition studies of detrital zircon grains that are inferred to be relicts from the protolith of the WMC.

Electron Microprobe Analysis

The mounted grains were imaged on a CAMECA SX 100 electron microprobe (EMP) in BSE-CL mode, located within the Geochemical Analysis Unit (GAU), GEMOC, Department of Earth and Planetary Sciences, Macquarie University, Sydney. The imaging operating parameters were 15kV accelerating voltage and 20nA beam current. External shape and internal structures such as zoning were captured for each grain.

Selected major elements, SiO_2 and ZrO_2 and trace elements HfO_2 and Y_2O_3 were spot analysed using the CAMECA SX100 EMP with operating parameters 15kV accelerating voltage and 20nA beam current. Hafnium oxide EMP data was later used as an internal standard for the zircon trace element analysis.

Laser Ablation Microprobe Inductively Coupled Plasma Mass Spectrometry (LAM-ICP-MS) for Zircon U/Pb and Trace Element Analysis

Zircon U/Pb isotopic composition and trace element chemistry were determined, concurrently, by LAM-ICPMS. Contamination from environmental lead was avoided by washing the sample in dilute HNO_3. The excitation source was a New Wave UP 213 nm Nd: YAG Laser with mass spectrometric analysis by an AGILENT 7500 series ICPMS at GAU, Macquarie University, Sydney. Zircon BSE/CL images were employed when selecting, where possible, suitable sites for analysis, although in many cases crystal size, shape and condition dictated the analysis site. Many crystals were less than 50μm across, and the laser beam diameter was set to either 30μm or 40μm

for U/Pb analysis. U/Pb analysis followed by Hf isotope analysis, beam diameter 40μm, resulted in the total destruction of many grains.

Six isotopes were measured for U-Pb dating, ^{206}Pb, ^{207}Pb, ^{208}Pb, ^{235}U, ^{238}U, ^{232}Th and trace element analysis examined Y, Nb, Ce, Sm, Eu, Yb, Hf, Ta, Th, and U (Norman et al., 1996, 1998; Jackson et al., 2004). Analyses were run in sets of ten bracketed by external standards GJ for U/Pb isotopes and NIST612 for trace elements, and pre-referenced by reference zircon standards Mud Tank and 91500.

Data reduction was performed using GLITTER (GEMOC Laser ICPMS Total Trace Element Reduction) v4.4.1 software (van Achterbergh et al., 2001). Corrections for common lead were made using the ComPbCorr, a common lead correction Microsoft Excel spreadsheet devised by Anderson (2002).

Laser Ablation Microprobe-Multi Collector-Inductively Coupled Plasma Mass Spectrometry (LAM-MC-ICPMS) for Zircon Hafnium Isotopic Analysis

Hafnium isotopic analysis was carried out separately using a New Wave/ Merchantech UP 213 nm laser ablation microprobe attached to a Nu Plasma 34 multi-collector ICPMS at GAU, Macquarie University, Sydney. Microsoft Excel and Isoplot 3.75 (Ludwig, 2012) were used to plot and display the U/Pb results.

RESULTS

Field relationships and Petrography

Sample W0601a is a weakly metamorphosed sublitharenite (Folk, 1980) from an outcrop composed of a steeply dipping, weakly foliated sequence of metamorphosed feldspathic and lithic sandstones interbedded with mudstones (Fig. 3a). The sample is immature, moderately sorted and fine-grained (Fig. 4a). It consists of variably metamorphosed very angular, microcrystalline lithic grains (150µm-200µm), plagioclase, potassium feldspar, quartz, and minor calcite and opaque minerals (10µm-100µm) in a very fine-grained matrix that includes feldspars, biotite, muscovite, chlorite, zircon and ilmenite (Fig. 4a; Danis et al., 2010).

Sample W0707a is a muscovite-biotite-K-feldspar-quartz-cordierite hornfels, a metapelite lacking any foliation (Fig. 3b) from the cordierite zone toward the middle of the metamorphic field gradient. Large (500µm – 1000µm) poikiloblastic cordierite and K-feldspar grains (Fig. 3b) have inclusions of matted, fine-grained, muscovite and quartz, biotite exhibiting many pleochroic haloes, and smaller (c. 100µm) muscovite poikiloblasts, with quartz inclusions (Fig. 4b). The fine-grained (< 100µm) matrix is dominantly quartz and biotite with accessory ilmenite and zircon (Fig. 4b).

Sample W0501a is an illmenite-feldspar-tourmaline-muscovite-cordierite-biotite-quartz migmatite (Fig. 3c). Quartz is the predominant mineral with some grains exhibiting undulose extinction and others polygonal with 120° triple junctions (Fig. 4c). Poikiloblastic cordierite is easy to detect due to strong yellow pleochroism and incipient alteration around the edges of some grains. Polygonisation results in a granoblastic texture. Biotite is randomly

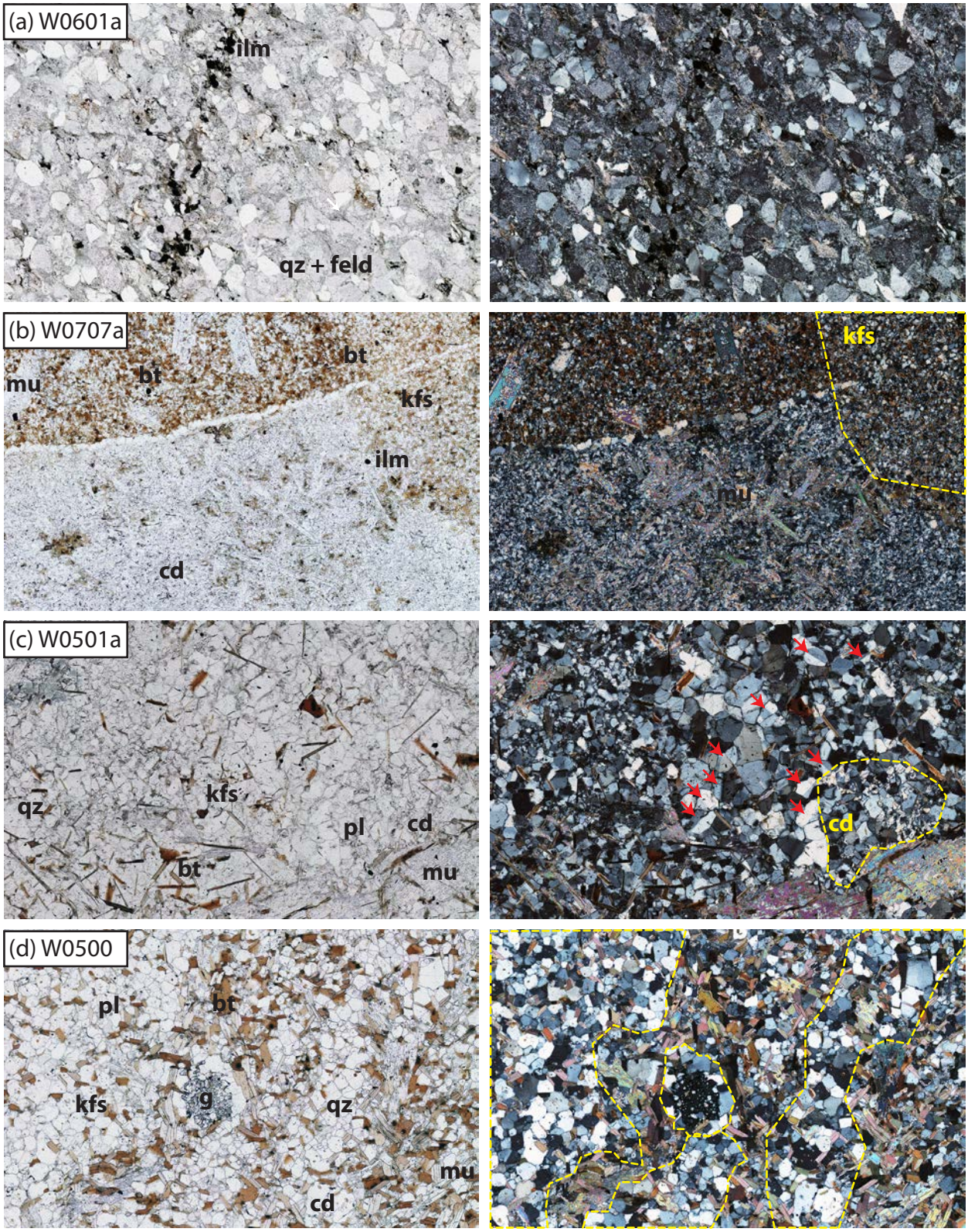

Figure 4: Stitched image photomicrographs (plane-polarised light on left, crossed-polarised light on right). Field of view is 5 mm across. (a) Sample W0601 showing relict detrital quartz and feldspar. (b) Sample W0707a showing large cordierite and K-feldspar poikiloblasts and smaller muscovite poikiloblasts. (c) Sample W0501a showing small cordierite poikiloblast and leucosome rich in simply twinned feldspar (red arrows). (d) Sample W0500 showing small garnet poikiloblast surrounded by leucosome and leucosome veins (outlined by dashed lines).

oriented (Fig. 4c) and displays prolific pleochroic haloes in grains cut parallel to the cleavage; rare zircon grains were observed in the centre of some haloes. Accessory ilmenite and tourmaline, along with rare plagioclase and K-feldspar grains are sparsely distributed throughout the thin-section. Decussate muscovite poikiloblasts (Fig. 4c) exhibit various degrees of replacement by cordierite or biotite; suggesting it is a relict mineral in the assemblage (Chapter 1).

Sample W0500 is a garnet-cordierite biotite-K-feldspar-quartz migmatite with ptygmatic folds of leucosome veins and schlieren structures (Fig. 3d). The melanosomes contain plagioclase, K-feldspar, garnet, muscovite, cordierite, quartz and biotite, with accessory zircon and tourmaline. The melanosomes display a granoblastic texture with poorly aligned biotite, rare muscovite and recrystallised quartz (Fig. 4d). Garnet grains surrounded by a quartz-rich leucosome (Fig. 4d) are inferred to be peritectic. Cordierite is poikiloblastic or skeletal, interstitial to polygonal quartz and K-feldspar grains. It may be unaltered, partially altered or completely altered and pseudomorphed by an aggregate of fine-grained minerals including muscovite and clays. The leucosomes contain muscovite, biotite, K-feldspar, cordierite and quartz. Polygonisation results in a granoblastic texture. Biotite is peppered with pleochroic haloes. A radiating mat of acicular crystals appears along the grain boundaries of some polygonal quartz grains; these may be fibrolitic sillimanite or a retrograde pseudomorph of it. The quartz ranges from c. 100–300µm in the leucosome and c. 50–150µm in the melanosome.

Modern stream sediment samples (W0801–W0804). The panned heavy mineral concentrates all appeared similar in composition being dominated by zircon and apatite, except for W0803 which was observed to additionally contain almandine (red) garnet, consistent with this drainage basin containing the highest grade rocks sampled by this method.

Results of Zircon Analysis

Zircon Crystal Morphology and Internal Structure

Zircon grains separated from the rocks of the WMC display a range of morphological variations and grain boundary modifications. The BSE-CL images reveal the two-dimensional shape of grains and provide some indication of the internal zoning, but are not as good a CL images for examining the internal zoning.

Zircon morphology and crystal structure can manifest a complex history of crystallization (magmatism), metamorphism, metasomatism and physical abrasion due to transport and deposition. The morphology of the BSE-CL images were considered in the light of a number of schemes using zircon morphology and structure (Pupin, 1980; Vavra, 1993; Sturm, 1999; and Corfu et al., 2003) to provide petrogenetic information applicable to the provenance study.

Zircon is tetragonal and generally crystallises as euhedral, doubly terminated, equant to columnar prismatic grains with a length to breadth ratio that ranges between 1 and 5, the number commonly believed to reflect crystallization velocity (Corfu et al., 2003). Elongated grains are inferred to

result from faster cooling, as in volcanic rocks; shorter stubby crystals the result of slow cooling, as in the case of plutonic rocks.

Magmatic zircon grains may display oscillatory zoning, sometimes truncated by newer zoning or resorbed surfaces, or at inherited core boundaries (Corfu et al., 2003). Zoning reflects minor compositional variations. Brighter zones in BSE/CL images reflect enrichment in U, Th and REE. Variations may result from, changes in temperature, pauses in crystallization, degassing, fractionation, or the mixing of two magmas of differing temperature and/or composition (Corfu et al., 2003; Hoskin and Schaltegger, 2003; Belousova et al., 2006a).

Zircon grains may show well developed crystal faces or have been modified by subsequent magmatic, metamorphic, metasomatic or depositional processes.

The Girrakool Beds are represented by sample W0601a (Fig. 3a) from the least metamorphosed rocks of the WMC. Zircon grains are commonly euhedral and exhibit well-defined crystal faces and sharp, pristine, terminations (Fig. 5 a-d). They range from equant to columnar and exhibit oscillatory zoning (Fig. 5 b,c) that is rarely discontinuous. Some grains contain homogeneous cores (Fig. 5 a,d).

The cordierite hornfels (W0707a; Fig. 3b) contains equant to columnar, sub-rounded zircon grains displaying embayments and delicate decorations (Fig. 5 e-h). Rare euhedral grains are similar to those in W0601a. Oscillatory zoning is weak and patchy in the decorated grains, and well preserved in the rare euhedral grains.

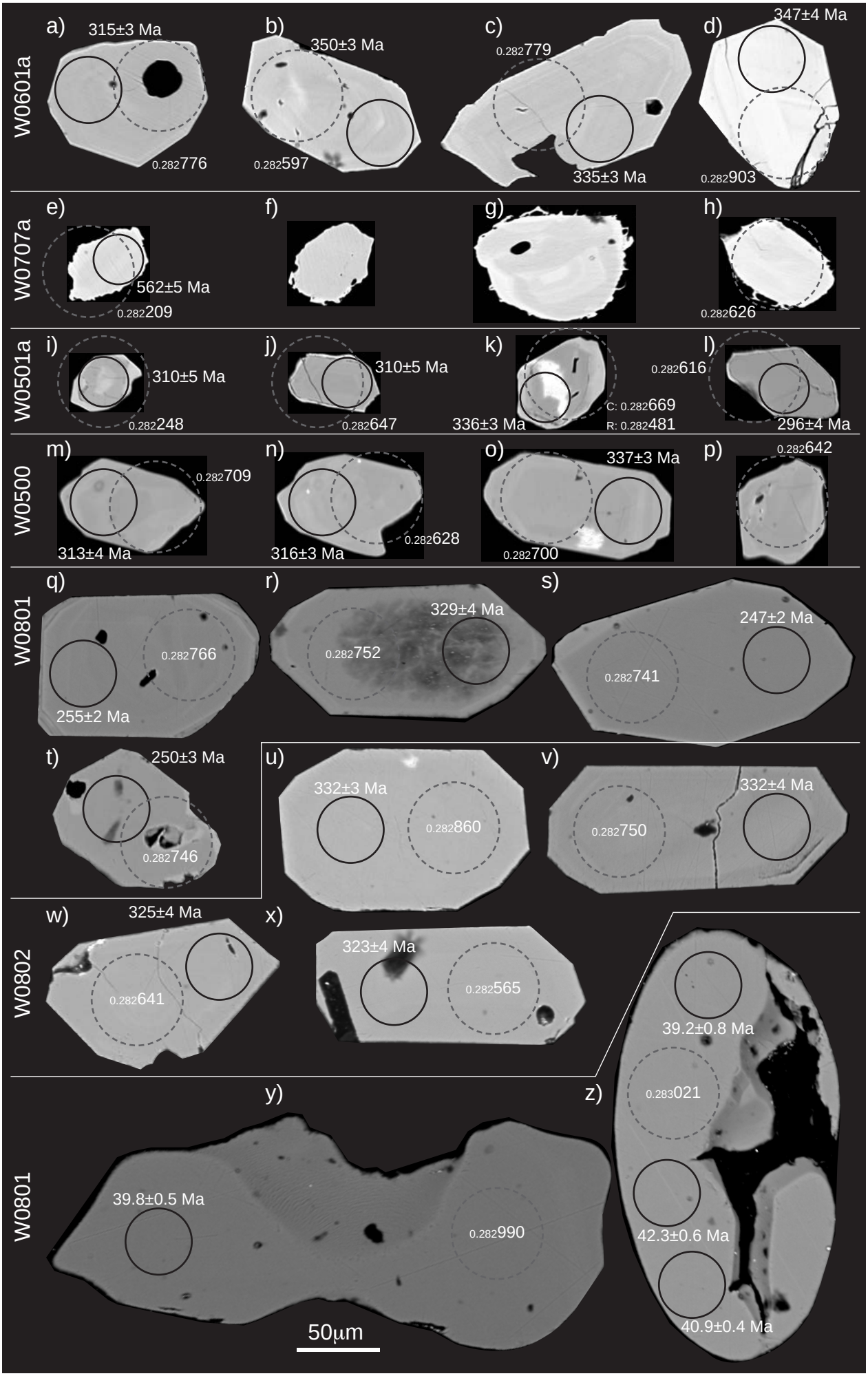

Figure 5: BSE/Cathodoluminescence images of representative zircon grains. Images g-x are also representative of W0803 and W0804.

Two samples were taken from the migmatite zone in close proximity. Both W0501a (Fig. 3c) and W0500 (Fig. 3d) represent the highest metamorphic grade for the WMC. Both samples contain zircon grains that exhibit curved edges and rounded corners, with featureless, homogeneous cores. Most grains in W0501a display a brighter BSE response rim (Fig. 5 i-l), whereas these are lacking in W0500 (Fig. 5 m-p).

Zircon grains from the stream sediment survey were placed in one of two groups according to morphology: (1) grains preserving crystal faces (Fig. 5 q-x), and (2) rounded grains (Fig. 5 y,z). The first group contains small (50–200µm long), euhedral to subhedral zircon grains with well-preserved terminations. They range from equant to columnar and commonly exhibit oscillatory zoning.

The Group 2 grains are large (260–400µm long), well rounded, elongate, “jelly bean” shaped zircon grains and occur mainly in W0801. They are very pale to colourless with homogenous internal structure. Biotite inclusions were noted in some grains.

Zircon Geochronology

Common lead corrected LAM-ICPMS data was refined into two groups, ≤30% and ≤10% discordance for rock samples (Fig.6) and alluvial samples (Fig.7). Data combined for the four rocks (n=90, ≤30% discordance) is dominated by a peak at c. 333 Ma with a very minor contribution of older grains (n=10, ≤30% discordance; Fig. 6). The youngest (c. 290 – 310 Ma) zircon grains are all from migmatite sample W0501a and were eliminated when determining a minimum deposition age, having >10% discordance.

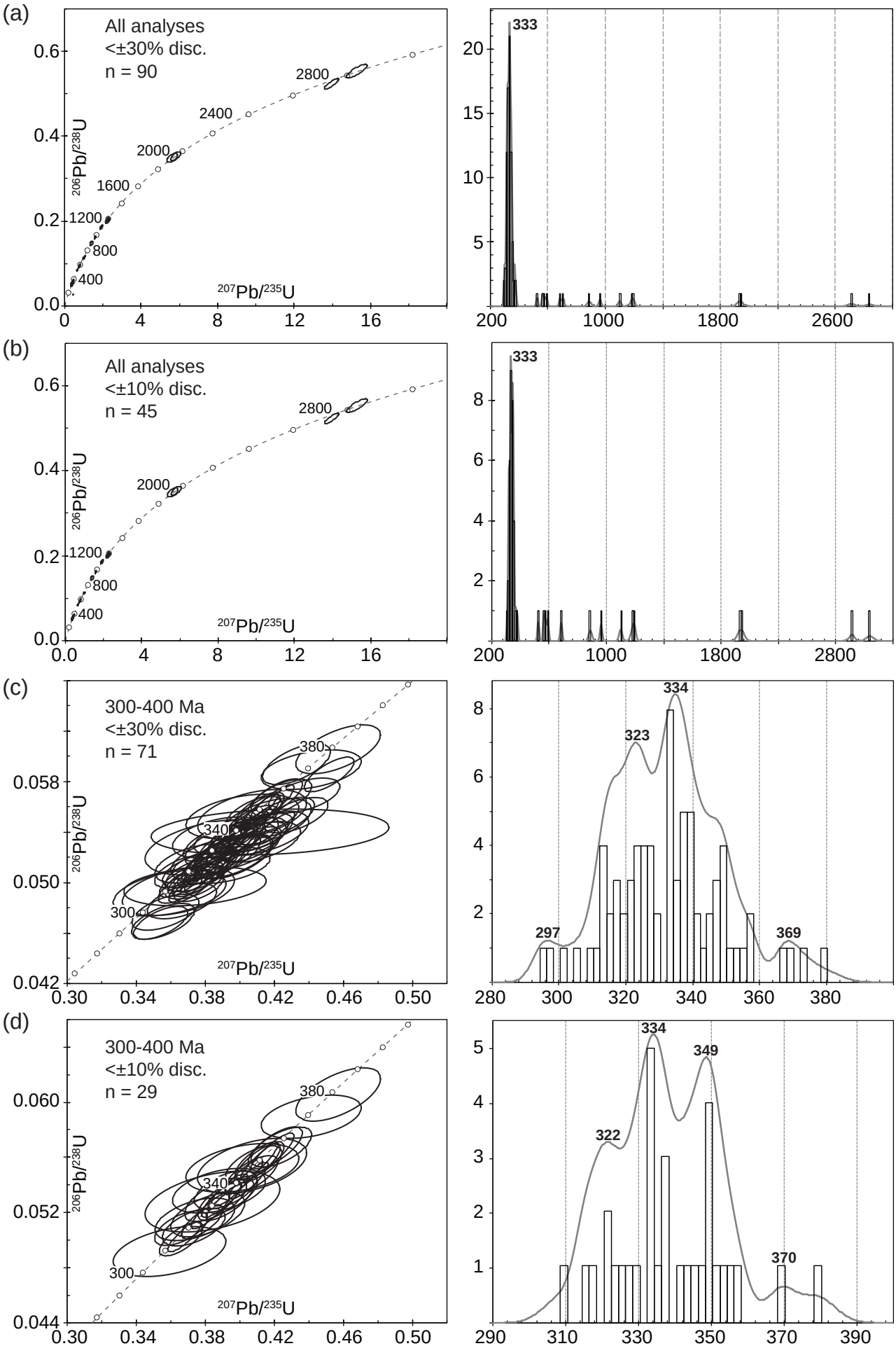

Figure 6: Concordia diagrams and Gaussian-summation probability density distribution and stacked column frequency histograms for detrital zircon in rock samples.

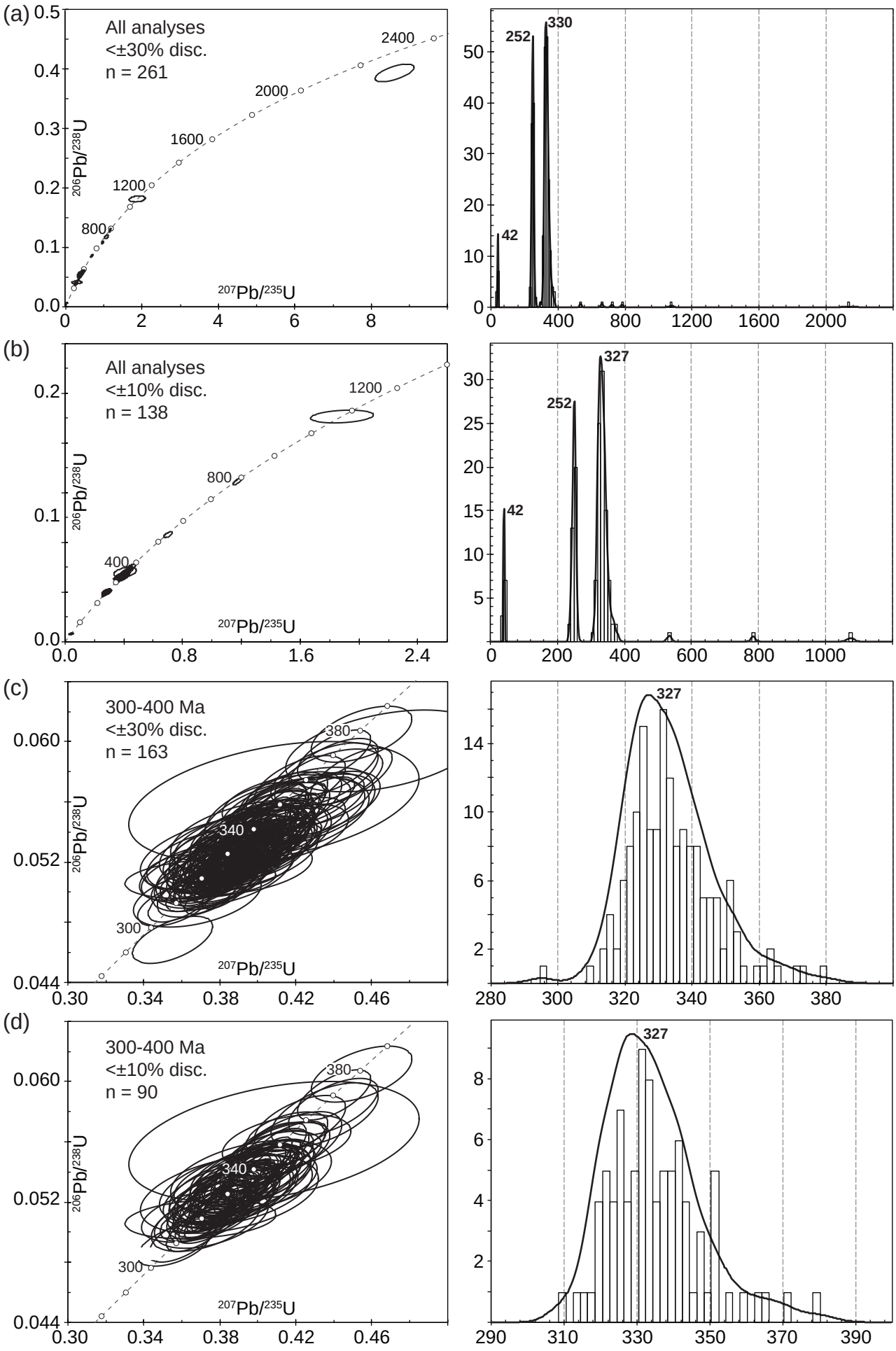

Figure 7: Concordia diagrams and Gaussian-summation probability density distribution and stacked column frequency histograms for alluvial zircon in modern sediment.

Seven grains, 309–320 Ma (≤10% discordance) from three of the rock samples (W0500, W0501a and W0601a), are the best estimate of the maximum deposition age for the protolith to the metamorphic rocks. The youngest grain is 309 ± 5 Ma.

Grains from the TerraneChron® alluvial survey (n=261, ≤30% discordance) identified well-defined populations at c. 42 Ma, c. 252 Ma, and a broad population at c. 327 Ma (Fig. 7a,b), with rare grains (n=6, ≤30% discordance) yielding Proterozoic ages (Fig. 7a,b). The youngest two populations are likely derived from the Tertiary basalts and the Late Permian to Triassic I-type granitoids and volcanics in the area (Fig. 1,2). These younger zircon grains are not considered further. Similar to the rock samples, a small population (n=11, ≤10% discordance) of grains 309-320 Ma is the best estimate of the minimum deposition age for the Girrakool Beds. The youngest grain is 309 ± 4 Ma.

Zircon Trace elements

Th/U values are commonly <1 (Fig. 8). Rare grains (n=10) contain Th/U >1.5 and include discordant grains from migmatite sample W0501a. Low Th/U values (<0.25) are very rare in the dataset. The discriminant framework proposed by Grimes et al. (2007) compares U/Yb and Y; the high U/Yb and low Y in all grains in this study is consistent with a continental (arc magma) rather than oceanic MORB origin. The discriminant framework proposed by Shnukov et al. (1997) shows the majority of data plotting in field II: ultrabasic, basic and intermediate rocks (Fig. 9a). The remaining discriminant frameworks on Figure 9 are from Belousova et al. (2002). Although the data

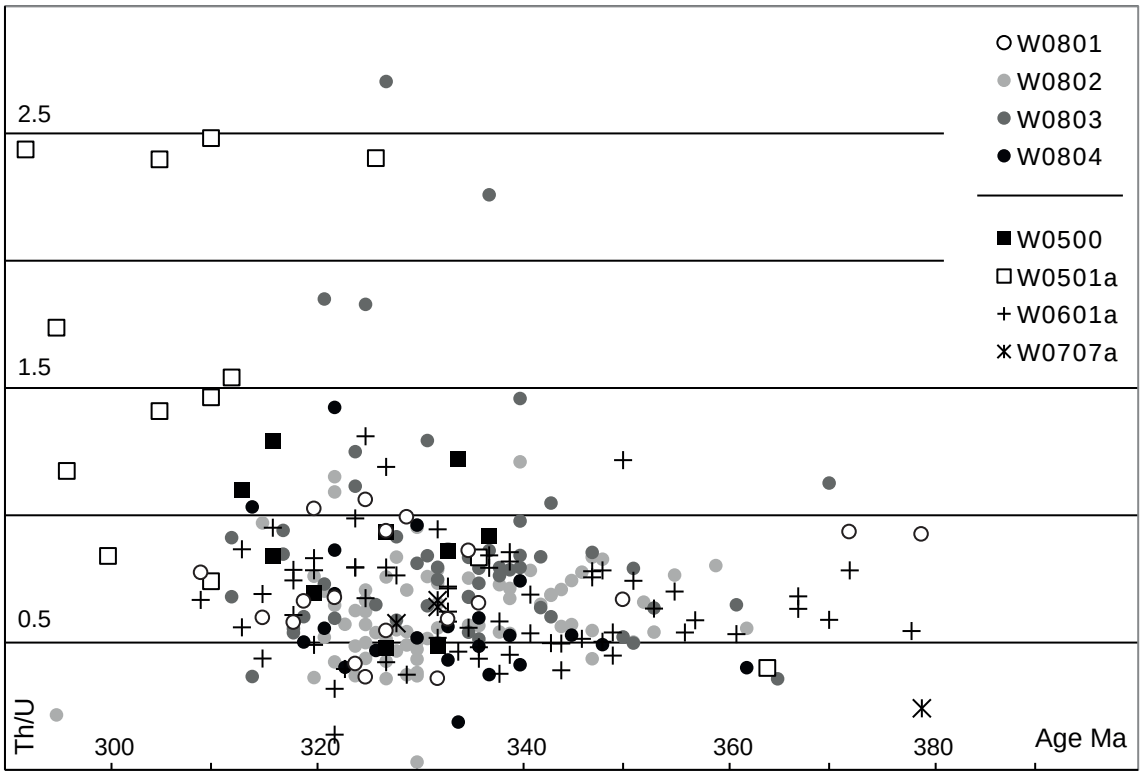

Figure 8: Th/U versus apparent age (≤30% discordance). Note: much of the data younger than c. 310 Ma is >10% discordant. The high Th/U analyses are inferred to be from modified zircon grains.

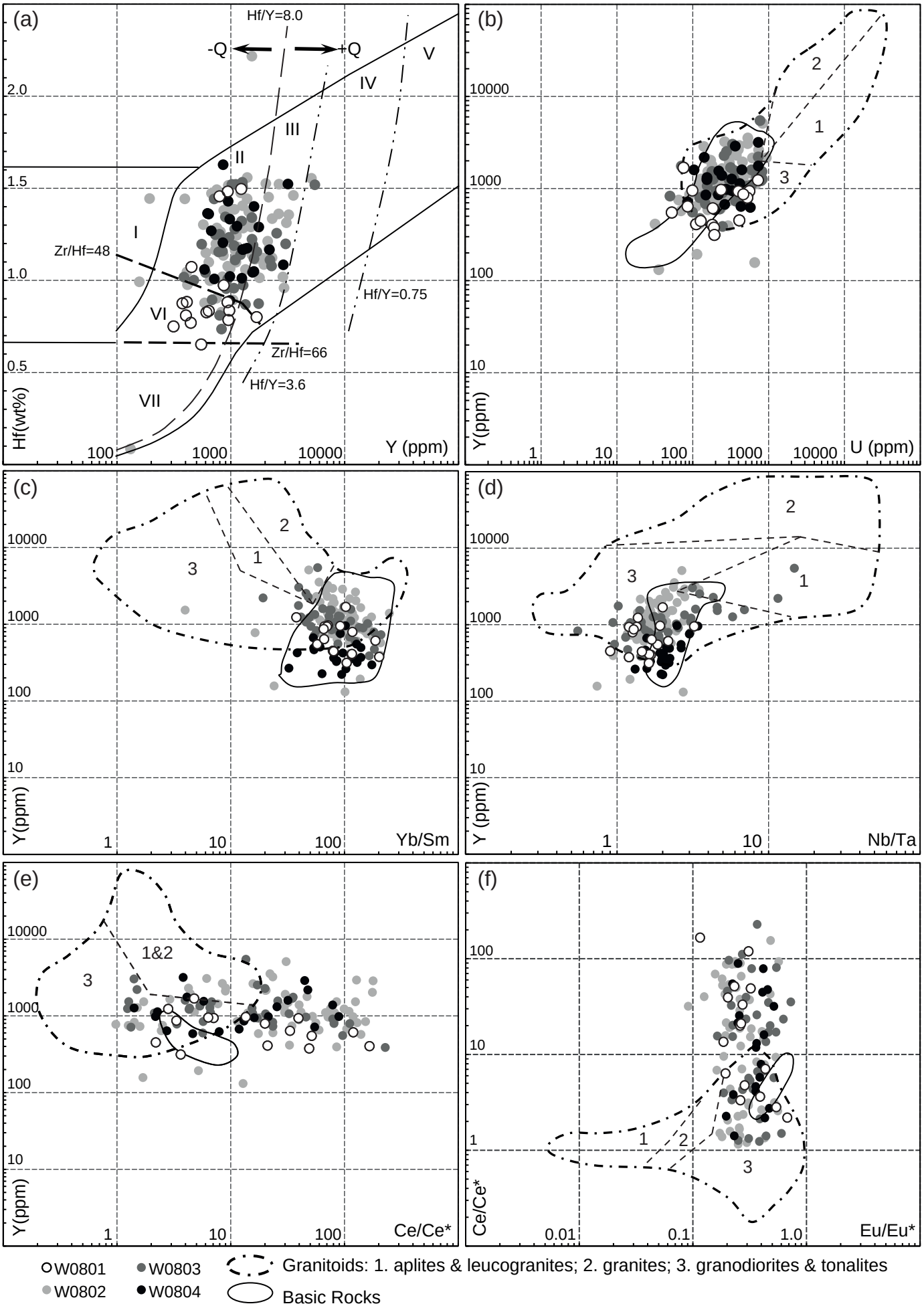

Figure 9: Zircon trace element discrimination diagrams after (a) Shnukov (1997) and (b–f) Belousova et al. (2002).

lie largely within the basic rocks field on Y versus U (Fig. 9b), Y versus Yb/Sm (Fig. 9c) and Y versus Nb/Ta (Fig. 9d), this is not true for the Y versus Ce/Ce* (Fig. 9e) and Ce/Ce* versus Eu/Eu* diagrams. The data overlap field 3: granodiorites and tonalities on all the Belousova et al. (2002) discrimination diagrams. The high Ce/Ce* data (Fig. 9e,f) can be explained if the zircons crystallise from a magma with a higher oxidation state suggestive of a higher crustal component. Ce^{3+} when oxidized to Ce^{4+} can proxy for Zr or Hf and is more compatible with the zircon lattice (Trail et al., 2012). Y^{3+} is unaffected by oxidation. The effect of oxidation of Eu^{2+} to Eu^{3+} is less pronounced compared to Ce (Fig. 9f). Nb content in zircon correlates positively with Ta (Fig. 10a). The data show no trends when grouped by age (Fig. 10b).

Zircon Hf Isotopes

162 analyses of Hf isotopes in zircon, for grains with ages between c. 370 and 290 Ma, range from strongly positive $\varepsilon Hf = 15$ ($^{176}Hf/^{177}Hf$ initial, $Hf_i > 0.28285$) to strongly negative $\varepsilon Hf = -15$ ($Hf_i < 0.28260$; Fig. 11). The most radiogenic grains are older than c. 330 Ma, while the least radiogenic grains are younger than c. 330 Ma. Time resolved signals were uniform for all samples except for one of the migmatite samples (W0501a). The last time segments of the signals in this sample (as the laser drilled through the rim on the underside of the grains) returned the least radiogenic signatures. The vertical arrows on Figure 11 run from core to rim, showing overgrowths on zircon in this migmatite sample are the least radiogenic.

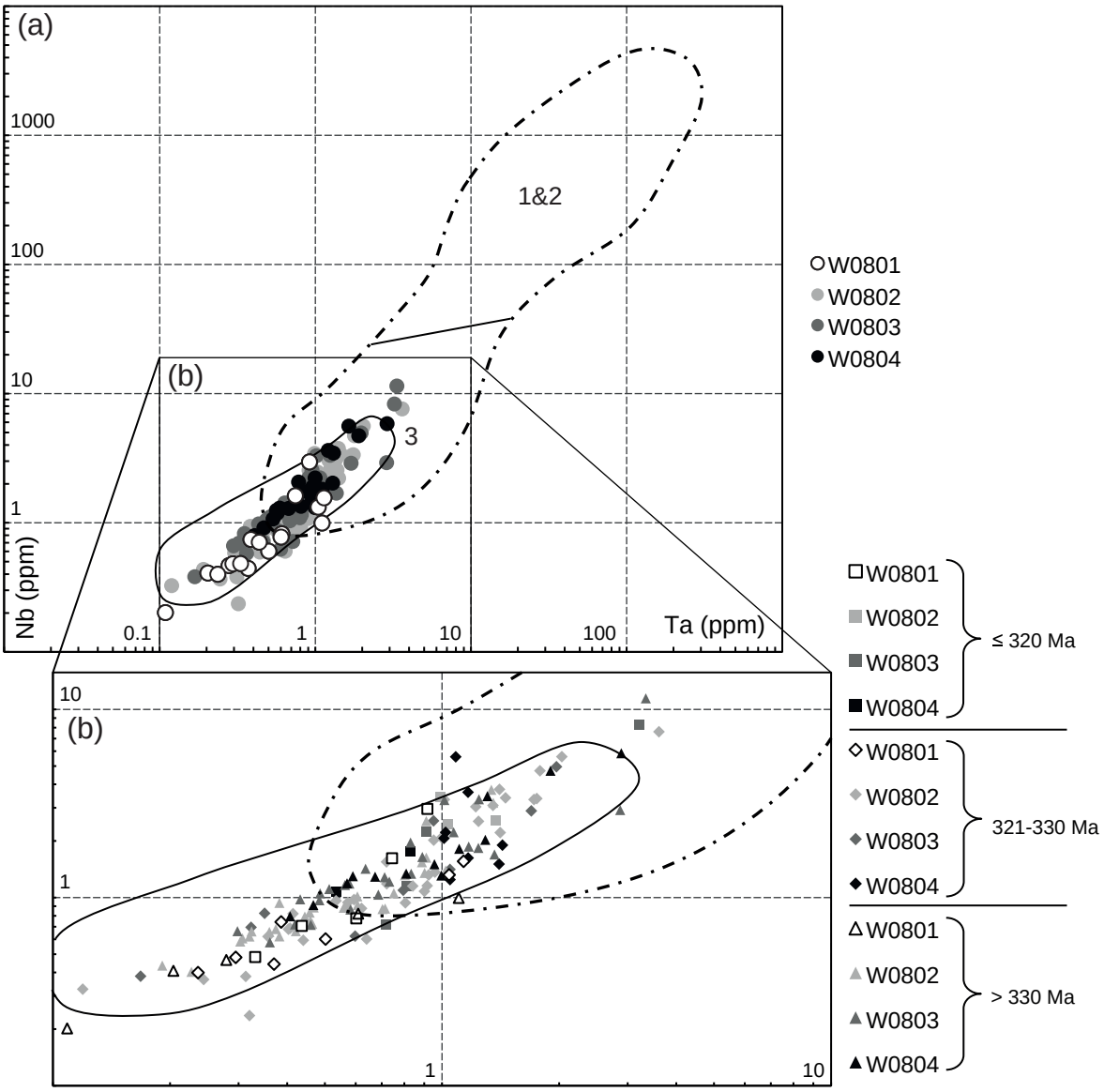

Figure 10: Zircon trace element discrimination diagram using Nb versus Ta from Belousova et al. (2002). Circled fields are the same as for figure 9. (a) data grouped by sample. (b) data grouped by sample and age showing there is no correlation of Nb versus Ta with age.

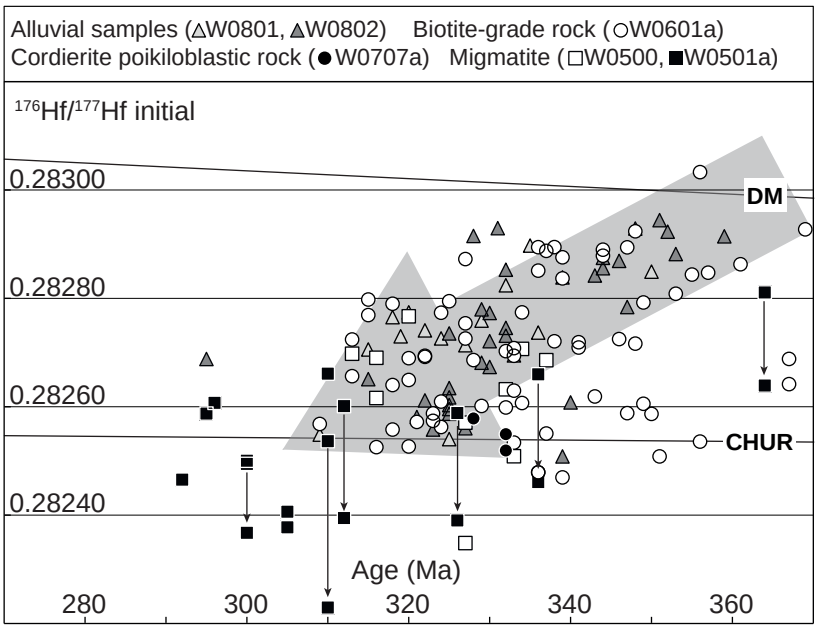

Figure 11: $^{176}Hf/^{177}Hf$ initial versus age. Grey arrow depicts overall trend to less radiogenic detrital zircon with younger age. Black arrows tie core and rim data split from single time resolved analyses for sample W0501a. The first part of the signal was more radiogenic than the last part of the signal which is inferred to have drilled through the rim.

DISCUSSION

Zircon is a uniquely important mineral in geological sciences because, due to it's chemical and physical robustness, it persisting over billions of years. Fortuitously, it also possesses an atomic structure that allows the incorporation of uranium and the exclusion of lead, allowing accurate dating of the time of crystallization utilising the U-Pb decay series. Also, trace elements in zircon can be used to identify the broad composition of its parent magma (Belousova, 2002).

Comparison of zircon separated from rocks and modern stream sediments

The modern stream sediments in small catchments that drain the WMC contain zircon grains sourced from Tertiary basalt (c. 42 Ma, Eocene-aged grains) and Late Permian to Early Triassic I-Type plutons (c. 252 Ma), both exposed in the northwestern parts of the drainage basins. The Eocene zircon grains are inferred to be resorbed xenocrysts in the host Tertiary basalt on the basis of the basalt likely being Zr-undersaturated and their large, very rounded shape (Fig 5. w and x). Therefore, these grains provide a maximum eruption age for the local basalt. The Late Permian to Early Triassic zircon grains overlap in age with numerous dated I-type plutons of the Clarence River, Moonbi and Uralla suites (Shaw and Flood, 1981). These components of the zircon grains sampled in modern stream sediments postdate the Girrakool Beds and metamorphism in the Wongwibinda Metamorphic Complex. Therefore, they are not discussed further.

Carboniferous zircon grains dominate (76%) the four rock samples of the Girrakool Beds and metamorphic equivalents studied here (Fig. 7). There is a very minor contribution of older zircon (Fig. 7). Though better resolved in the modern stream sediment samples, the age pattern is the same as in the rock samples (compare Figures 6 and 7). An advantage of the Terranechron® sampling method is that it tends to result in the recovery of larger zircon grains better suited to laser ablation analysis methods. For example, typical grains separated from the metapelitic rocks in the Wongwibinda Metamorphic Complex are commonly < 80µm long (Fig. 5e-p) and those from the metapsammitic rock are typically < 150µm long. In comparison, the similarly aged Carboniferous grains collected from the modern stream sediments are c. 200-250µm long (Fig. 5t-v). Laser ablation spot size is usually set at 40µm for optimum analysis but can be operated at 30µm with reduced precision. Ideally, the zircon grain has to be big enough to support two analyses, one for U/Pb and another for Hf isotopes. The large number of grains available in the stream sediment facilitated the collection of a large data set to examine the rate of zircon production related to volcanism during the Carboniferous (Fig. 6d).

Comparison of the Girrakool Beds and metamorphic equivalents

The new data presented here provide evidence that the Girrakool Beds are the protolith to metamorphic rocks in the Wongwibinda Metamorphic Complex. A combination of regional geology, sedimentary geology, mineralogy, fossils or lack thereof and zircon chemistry is needed establish the Girrikool beds as the protolith for the WMC.

The Girrakool Beds are a small part of the Tablelands Complex accretionary prism; they are variously described as quartz bearing greywackes, silty greywackes and slaty argillaceous rocks/mudstones (Binns, 1966; Farrell, 1992). Korsch (1978) described the Girrakool Beds as indurated mudstone, siltstone and lithic to feldspathic greywacke and from this inferred a volcanic source. The detritus in the accretionary prism is andesitic in the Devonian and becomes dacitic and rhyolitic in the Carboniferous to Permian (Korsch, 1978). The metamorphic sequence in the WMC (Binns, 1966; Farrell, 1992; Chapter 1) increases in metamorphic grade from diagenesis through anchizonal (Farrell, 1992) into greenschist and then into amphibolite facies metamorphism. The argument for the Girrakool Beds being the protolith to the higher-grade rocks becomes less convincing with increasing grade, due to the destruction of sedimentary structures by recrystallisation and, to a lesser extent, deformation. The ubiquity and chemical and physical durability of detrital zircons, combined with high precision U/Pb geochronology, Hf isotope and trace element determinations, and the ability to analyse large zircon populations from rock and alluvial samples has made detrital zircon analyses vital in provenance studies (Belousova et al., 2006b, Hoskin and Schaltegger, 2003; Thomas, 2011).

The stream sediment catchments were chosen to sample across the metamorphic gradient from unmetamorphosed areas to the most strongly metamorphosed areas of the WMC (Fig 2). Site W0801 predominantly samples the least metamorphosed area to the west; site W0804 samples the biotite grade area, while W0803 and W0802 sample the most strongly metamorphosed cordierite and migmatite zones respectively.

Carboniferous zircons separated from these samples fall within the same U/Pb age, trace element and Hf isotope compositional ranges (Fig, 5-10) as the data from zircon separated from rocks.

The U/Pb age of zircon grains with <30% discordance dominantly ranges between 309±5 and 378±4 for sample W0601a and all other rock and alluvial samples fall within this range. Craven (2010) demonstrated that the combined alluvial samples, aged between 350 and 280 Ma plot in a wide almost Gaussian distribution ranging from about 350 to 310 Ma with a median of 329 Ma. The individual rock samples share a very similar age distribution: sample W0601a has a peak at 326 Ma, sample W0707a at 331 Ma, W0500 at 326 Ma, and W0501a at 335 Ma. Craven's (2010) results were determined using unfiltered data but a comparison with data presented here shows very little difference.

Hf_i for W0601a ranges from 0.282483 to 0.283044 and with the exception of some modified grains from the most highly metamorphosed migmatite (W0501a) all zircon grains analysed fall within this range. The trend to less radiogenic zircon with decreasing age is generally supported by all of the detrital grains.

A variety of zircon trace element plots follow a similar pattern. The data patterns in Figure 9 all exhibit fairly tight groupings. Although only the alluvial samples were analysed for trace elements, when all data was plotted together all points plotted randomly. This suggests that there is little difference in zircon trace element data between samples from the least metamorphosed and the most highly metamorphosed rocks in the WMC.

These zircon data confirm, along with contiguous regional geology, similar, metamorphically barren, mineralogy and comparable bulk rock chemistry (Farrell, 1992; Hensen, 2000), that the Girrakool Beds are the protolith for all the metamorphic rocks of the WMC.

On a regional basis, a traverse across the province from weakly metamorphosed Girrikool Beds, where the sedimentary character is obvious, into the more strongly metamorphosed amphibolite facies rocks, where the original sedimentary textures have been obliterated, demonstrates a gradual increase in metamorphic grade. This gradual transition leads to the inference that similar sedimentary rocks form the protolith to the higher-grade rocks. The zircon data are used to support this inference.

Differentiating units adjacent to the Girrikool Beds

Li and Rosenbaum (2014) have reviewed the differences between the Sandon Beds, to the west, and the Girrikool Beds. The distinction between these two units was made based on a lithological difference manifest as a decrease in the abundance of chert layers in the Girrakool Beds (Korsch, 1978).

Poor exposure (Appendix 1) obscures the boundary between these two units, making it difficult to recognise in the field. Li and Rosenbaum (2014) noted that Leitch et al. (1971) and Gilligan et al. (1992) inferred that the boundary between the two units is a NE–SW fault, while Cuddy (1978) inferred a stratigraphic contact, with the Girrakool beds overlying the Sandon Beds. Li and Rosenbaum also noted Brown (2003) showed that this

boundary shows a contrast in radiometric intensity. However, the exact nature of the contact remains unclear.

To the east, the WMC is truncated by the Wongwibinda Fault (WF); across the WF lies the Dyamberin Beds of the Coffs Harbour Block. Binns (1966) compared the petrology of the Girrikool and Dyamberin Beds finding that the provenance of both formations was a very similar acid volcanic terrain containing intermediate volcanic material, but that the petrological and sedimentary features of the Dyamberin beds suggested that they were deposited closer to source, likely in shallower water.

The lithological differences between the Sandon Beds and the Girrikool Beds, and petrological differences of the Dyamberin Beds, and that this unit is across a major fault, make the both these units less likely protoliths than the Girrakool Beds for the high-grade metamorphic rocks of the WMC.

U/Pb geochronology carried out by Korsch et al., (2009) from samples taken from the accretionary wedge-trench-fill sediments from both the north and south NEO, demonstrated that the volcanic arc-derived sedimentary rocks of the accretionary complex have very similar detrital age spectra. Therefore, geochronology alone will not provide conclusive evidence of any particular formation being the protolith to high-grade metamorphic rocks.

Provenance

Geochronological data from both the rock and stream sediment samples contain abundant Carboniferous zircon with a peak at c. 330 Ma on the Gaussian-summation probability density distribution and stacked column frequency histogram (Fig. 6d, 7d). The distribution is weakly skewed to older

ages that taper to c. 380 Ma. There is an abrupt drop in the number of zircon grains younger than c. 320 Ma (Fig. 6d), where there are 5 grains in the rocks and 11 grains in the modern stream sediment samples ≤ 320 Ma (Fig. 6d, 7d). Though there are very few grains > c. 400 Ma in any sample, more of these were analysed in the rock samples (22% of ≤10% discordant grains separated from the rocks versus 4% in the modern stream sediment samples). Regardless, there is very little input into the sediment from Precambrian parts of the eastern Gondwana margin. Instead, the detritus is almost solely sourced from the Carboniferous components of the Keepit arc, which lies to the west of and is contiguous with the Tamworth Belt, largely covered by the Sydney and Gunnedah basins (Fig. 1). The zircon trace element data (Fig. 9,10) support a provenance dominated by granodiorite and tonalite or their volcanic equivalents. The number of zircon grains in each two million year bracket of the stacked column frequency histogram is > 4 between 318 and 344 Ma (Fig. 6d). The abrupt drop in the number of grains younger than c. 320 Ma likely reflects the onset of an inferred period of trench roll back and migration of the arc into the subduction complex (Collins, 2002a,b; Jenkins et al., 2002; Cawood et al., 2011; Glen 2013). The few zircon grains ≤320 Ma probably record the final stages of volcanism in the Keepit arc as it shut down. Deeper parts of the subduction wedge have been inferred as the source for xenocrysts (down to c. 305 Ma; Cawood et al., 2011) in S-type granites sourced from partial melting of the wedge (Flood and Shaw, 1977). These xenocrysts record the final activity in the Keepit arc (Cawood et al., 2011).

An investigation by Korsch et al. (2009) in the northern NEO accretionary complex, recognised two main zircon populations interpreted as

reflecting two provenances. One population has a continental margin volcanic arc origin and the other is a combination of volcanic arc and quartz-rich detritus, mostly derived from the continental cratonic interior.

All but two of their volcanic arc-derived samples have detrital zircon peaks that fall within an age range of 355 to 315 Ma, indicating that the accretionary wedge in the New England Orogen is dominated by Carboniferous zircon over a period of ~40 m.y., with the principal source being the contemporaneously active continental margin magmatic arc (Korsch, 2009).

These detrital zircon spectra from across the central Tablelands Compelx are remarkably consistent with data presented here. Detrital zircon data from the Girrikool Beds, with few exceptions, fall within the range 360 to 310 Ma (<±10% discordance). Combined rock samples from the Girrikool Beds define a broad population at ~333 Ma while the combined alluvial samples gave a broad population at ~327 Ma. Two of the Korsch et al, (2009) samples from the southern NEO Coff's Harbour Association, considered by Korsch (1977, 1990) to be associated with the central Tablelands Complex and the Girrikool Beds, give very similar weighted mean average ages (323±3 Ma and 320±2 Ma). In Figure 6d, the Gaussian-summation probability density distribution stacked column frequency histogram for all rock samples exhibits a composite distribution of a number of peaks with the youngest at 322 Ma, comparable to the Korsch et al. (2009) Coff's Harbour Block samples.

Volcanic arc-derived sandstone samples from the northern NEO compare even more favourably with the Girrikool Beds with 10 average ages ranging from 351 Ma to 330 Ma and indicating that the sediments composing

the accretionary prism in the northern NEO contain slightly older detrital zircon compared to those from the south.

A dearth of older detrital zircon grains (>360 Ma) characterises both the Girrikool Beds, (alluvial=3 of n=138 <±10% and rock=11 in n=45 <±10%) and samples presented by Korsch et al. (2009). They found that from all volcanic–derived sandstones, their data (n=471) contained only 26 individual grain ages that were older than 370 Ma with no grains >2000 Ma. In the Girrikool Beds, only 2 grains from the rocks and 1 grain from the alluvium were found >2000 Ma. There is only one noted difference between the Girrikool Beds and the samples analysed by Korsch et al. (2009) and that is the Girrikool Beds do not contain detrital hornblende, which may indicate that the provenance may be less juvenile than the other parts of the NEO. Zircon Hf and trace element characteristics may help in clarifying this situation.

This study of sedimentary rocks and metamorphic equivalents from the WMC should be a useful additional contribution to the study of Korsch et al. (2009), adding data from the volcanic arc-derived sediments of the southern NEO.

It may then be broadly interpreted, from regional geological relationships and sedimentology backed up by zircon U/Pb geochronology, that the bulk of the material in the NEO accretionary prism has the same, volcanic arc-derived, distributive provenance. The exception is the cratonic component only recognised, so far, in the northern NEO.

The variations in the trace element content of zircon grains are due to processes within the arc (e.g. magmatic fractionation), but the difference between zircon grains is due to changes in the source rock composition. The

variations are not temporal, as the full range is observed in all age groups (Fig. 10), suggesting that the arc did not significantly change over time, but rather had a range of processes (e.g. fractionation, assimilation, etc.) active throughout its history. However, the Hf isotope data do show a strong temporal pattern becoming less radiogenic with time (Fig. 11). This is a pattern observed with maturation of many continental volcanic arcs (Collins et al., 2011).

It is inferred that the longer an arc is in one location, the arc lower crust will become hotter and the arc will become thicker. Therefore, partial melting of older crust in the deep arc and interaction with a thickened arc will increase the proportion of less radiogenic magma in the system over time, thus explaining the pattern observed in the Hf isotope data. Alternatively, advance of the slab toward the continent over the 30 m.y. record will progressively increase the proportion of ancient crust involved in the arc system, similarly explaining the Hf isotope data pattern.

Modification of zircon during metamorphism

A comparison of the low- and high-grade rock samples, along with the stream sediment samples demonstrates the remarkable stability of detrital zircon during metamorphism. Only two of the rock samples show modification of the zircon. The cordierite hornfels sample (W0707a) shows textural modification of zircon grains with the delicate decorations observed on very curved grain edges (Fig. 5e-h) and internal structures (e.g. oscillatory zoning) fade as the degree of external modification increases. Not all grains exhibit this textural modification inferring that they were armored in more resistant

minerals. These grains generally exhibit sharp uncorroded faces and fine oscillatory zoning. The trace element and U-Pb-Hf-isotope composition of grains within the hornfels sample are not distinguishable from lower grade samples.

Zircon grains separated from each of the two migmatite samples are different. Although both are amphibolite grade (<3.3 kbar and 660°C; Chapter 1), sample W0500 contains zircon grains with relatively unmodified shapes, whereas W0501a contains more grains with curved edges and rounded terminations. In addition, zircon grains from W0501a show narrow overgrowths with brighter BSE/CL response (Fig. 5i-l). A high proportion of U-Pb analyses are discordant (-22% to -65%) from sample W0501a, whereas the data from W0500 are concordant and overlap those from lower grade samples. The metamorphic rims of zircon grains in W0501a are likely to be c. 300 Ma on the basis of EMP U/Pb chemical dating of monazite in migmatite samples (Chapter 1). The closeness in age between the rims (c. 300 Ma) and the cores (c. 330 Ma) is too short a time period to cause a discordance due to mixing of these domains during analysis; a mix of these two domains would give a concordant age somewhere between c. 300 Ma and c. 330 Ma. The modification of the zircon must also have involved the addition of U or loss of Pb to create the discordant data. Lead loss occurs when the zircon lattice is disturbed by metamictization (Mezger and Krogstad, 1997) or crystal plastic deformation (Timms et al., 2006) yet neither of these processes is considered applicable to sample W0501a zircons. These discordant zircon grains from sample W0501a are among those with the highest Th/U (Fig. 8), further suggesting the mobility of trace elements during amphibolite grade

metamorphism. The open system injection of melt or in situ partial melting involving the breakdown of monazite could provide a possible source for the observed increase in Th content of the modified zircon grains in sample W0501a.

Rubatto et al. (2001) found that zircon does not appear to react to metamorphism below c. 700°C in the HTLP metasedimentary rocks at Mt Stafford, Central Australia. These authors noted an increased thickness of zircon overgrowths with increased partial melting at temperatures greater than 700°C. A possible explanation for the difference between the migmatite samples from the WMC is that W0501a interacted with a higher proportion of partial melt (locally derived or injected), thus facilitating the growth of new zircon. The time resolved Hf isotope data shows the rims to be less radiogenic than the cores (Fig.11), consistent with the growth of a metamorphic rim.

The results from W0501a need to be considered carefully in the context of understanding the protolith; modified grains are indicators of the metamorphic processes involved in the formation of these rocks and likely misleading when examining the protolith. Further study of these grains might involve ion probe analysis of the overgrowths and Energy BackScatter Detector (EBSD) analysis to eliminate the possibility of grain scale deformation.

The modern alluvial sample W0802 was sourced from the highest-grade rocks and modification of the zircon might be expected. This sample contains the majority of outlier data on the trace element discrimination diagrams (Fig. 9), suggesting that a small subset of the grains may be chemically modified. However, the sub-sample (W0803) has four grains with

high Th/U (Fig. 8) suggesting that some rocks in this part of the complex might be higher grade than previously mapped (Binns, 1966, Farrell, 1992). This is consistent with the discovery of garnet in the heavy mineral fraction of the alluvial sample W0803.

CONCLUSION

Numerous treatises on the southern New England Orogen and the central Tablelands Complex place the Girrakool Beds in an accretionary wedge (Binns, 1966; Korsch, 1984; Farrell, 1992; Chapter 1). The unit comprises marine turbidites composed of fine-grained psammites and pelites. The zircon U/Pb geochronology is generally unaffected by the amphibolite grade metamorphism, but it has been demonstrated that care must still be exercised when examining zircon images and U/Pb data from the highest-grade rocks. Uniform zircon trace element and U-Pb-Hf data indicate that the Girrakool Beds are the likely protolith to all the rocks of the WMC.

Detrital zircon grains in the Girrakool Beds are dominated by a c. 320-350 Ma age population. There are very few older grains. These data point to the Keepit arc as the most likely provenance. Zircon trace element data are also consistent with an arc provenance with most grains sharing chemical signatures with zircon analysed from granodiorites and tonalities (Belousova et al., 2002). Initial Hf data exhibits a trend from more radiogenic at c. 350 Ma to less radiogenic at c. 320 Ma. This trend defines the evolution of the Keepit arc.

References

Allen, C. M., Wooden, J. L. and Chappell, B. W., 1997. Late Paleozoic crustal history of central coastal Queensland interpreted from geochemistry of Mesozoic plutons: the effects of continental rifting. Lithos, **42**, 67–88.

Andersen, T., 2002. Correction of common lead in U–Pb analyses that do not report 204 Pb. Chemical Geology, **192**, 59–79.

Belousova, E. A., Griffin, W .L., O'Reilly, S. Y. and Fisher, N. I., 2002. Igneous zircon: trace element composition as an indicator of source rock type. Contributions to Mineralogy and Petrology, **143**, 216–622.

Belousova, E. A., Griffin, W. L. and O'Reilly, S. Y., 2006a. Zircon crystal morphology, trace element signatures and Hf isotope composition as a tool for petrogenetic modelling: examples from Eastern Australian granitoids. Journal of Petrology, **47**, 329–353.

Belousova, E. A., Reid, A. J., Schwartz, M. P., Griffin, W. L. and Fairclough, M. C., 2006b. "Crustal evolution of the Gawler Craton, South Australia: application of the TerraneChron technique to detrital zircon from modern stream sediments. South Australia. Department of Primary Industries and Resources. Report Book 4: **192**.

Belousova, E. A., Reid, A. J., Griffin, W. L. and O'Reilly, S. Y., 2009. Rejuvenation vs. recycling of Archean crust in the Gawler Craton, South Australia: evidence from U–Pb and Hf isotopes in detrital zircon. Lithos, **113**, 570–582.

Belousova, E. A., Kostitsyn, Y. A., Griffin, W. L., Begg, G. C., O'Reilly, S. Y. and Pearson, N. J., 2010. The growth of the continental crust: constraints from zircon Hf-isotope data. Lithos, **119**, 457–466.

Belousova, E. A., Griffin, W. L., Begg, G. and O'Reilly, S. Y., 2010. The Terranchron® approach to crustal evolution studies and implications for continental growth. 5th International Archean Symposium. Abstracts, 44–46.

Binns, R. A., 1966. Granitic intrusions and regional metamorphic rocks of Permian age from the Wongwibinda district, northeastern New South Wales. Journal of the Proceedings of the Royal Society of N.S.W., **99**, 5–36.

Cawood, P. A. (1991). Characterisation of intra-oceanic magmatic arc source terranes by provenance studies of derived sediments. *New Zealand Journal of Geology and Geophysics*, *34*(3), 347-358.

Cawood, P. A., Leitch, E. C., Merle, R. E. and Nemchin, A. A., 2011. Orogenesis without collision: Stabilizing the Terra Australis accretionary orogen, eastern Australia. Geological Society of America Bulletin, **123**, 2240–2255.

Cherniak, D. J., Hanchar, J. M. and Watson, E. B., 1997a. Diffusion of tetravalent cations in zircon. Contributions to Mineralogy and Petrology, **127**, 383–390.

Cherniak, D. J., Hanchar, J. M. and Watson, E. B., 1997b. Rare-earth diffusion in zircon. Chemical Geology, 134, 289–301.

Cherniak, D. J. and Watson, E. B., 2001. Pb diffusion in zircon. Chemical Geology, **172**, 5–24.

Cherniak, D. J. and Watson, E. B., 2007. Ti diffusion in zircon. Chemical Geology, **242**, 470–483.

Claoué-Long, J. C. and Korsch, R. J., 2003. Numerical time measurement in the DM Tangorin DDH1 drillcore. Geology of the Cranky Corner Basin, Coal and Petroleum Bulletin, **4**, 179–206.

Collins, W. J., 2002a. Hot orogens, tectonic switching, and creation of continental crust. Geology, **30**, 535–538.

Collins, W. J., 2002b. Nature of extensional accretionary orogens. Tectonics, **21**, 6–1.

Collins, W. J. and Richards, S. W., 2008. Geodynamic significance of S-type granites in circum-Pacific orogens. Geology, **36**, 559–562.

Collins, W. J., Belousova, E. A., Kemp, A. I. and Murphy, J. B., 2011. Two contrasting Phanerozoic orogenic systems revealed by hafnium isotope data. Nature Geoscience, **4**, 333-337.

Corfu, F., Hanchar, J. M., Hoskin, P. W. and Kinny, P., 2003. Atlas of zircon textures. Reviews in Mineralogy and Geochemistry, **53**, 469–500.

Danis, C, R., Daczko, N. R., Lackie, M. A. and Craven, S. J., 2010. Retrograde metamorphism of the Wongwibinda Complex, New England Fold Belt and the implications of 2.5D subsurface geophysical structure for the metamorphic history. Australian Journal of Earth Sciences, **57**, 357–375.

Dickinson, W. R. and Suczek, C. A., 1979. Plate tectonics and sandstone compositions. AAPG Bulletin, 63, 2164–2182.

Farrell, T. R., 1992. Deformation, Metamorphism and Migmatite Genesis in the Wongwibinda Metamorphic Complex. Unpublished PhD thesis, University of Newcastle, Australia.

Flood, R. H. and Shaw, S. E., 1977. Two “S-type” granite suites with low initial 87Sr/86Sr ratios from the New England Batholith, Australia. Contributions to Mineralogy and Petrology, **61**, 163–173.

Folk, R. L., 1980. Petrology of sedimentary rocks. Hemphill Publishing Company.

Glen, R. A., 2005. The Tasmanides of eastern Australia. In: Terrane Processes at the margins of Gondwana (eds Vaughan, A. P. M., Leat, P. T. and Pankhurst, R. J.), **246**, pp. 23–99. Special Publication. Geological Society, London.

Glen, R. A., 2013. Refining accretionary orogen models for the Tasmanides of eastern Australia. Australian Journal of Earth Sciences, **60**, 315–370.

Gower, C.F., 2007. Protolith recognition of metamorphosed felsic volcanic/volcanoclastic rocks, with special reference to the Grenville province in southeast Labrador. Current Research (2007) Newfoundland and Labrador Department of Natural Resources Geological Survey. Report 07-1. Pp. 11–23.

Griffin, W. L., Belousova, E. A. and O’Reilly, S. Y., 2007. Crustal history and metallogenic fertility: Terrane-scale assessment with detrital zircons. In Proceedings of Exploration, **7**, 1–5.

Grimes, C. B., John, B. E., Kelemen, P. B., Mazdab, F. K., Wooden, J. L., Cheadle, M. J., Hanghoj, K. and Schwartz, J. J., 2007. Trace element chemistry of zircons from oceanic crust: a method for distinguishing detrital zircon provenance. Geology, **35**, 643–646.

Henson, A., 2000. EMP and LA-ICP-MS raster analysis: A new method for analyzing fine-grained metasediments and a geochemical study of the

Wongwibinda Metamorphic Complex, southern NEFB, Australia. Hons Thesis. Macquarie University, Australia (Unpubl.).

Hoskin, P. W. and Schaltegger, U., 2003. The composition of zircon and igneous and metamorphic petrogenesis. Reviews in mineralogy and geochemistry, **53**, 27–62.

Jackson, S. E., Pearson, N. J., Griffin, W. L. and Belousova, E. A., 2004. The application of laser ablation-inductively coupled plasma-mass spectrometry to in situ U-Pb zircon geochronology. Chemical Geology, **211**, 47–69.

Jenkins, R. B., Landenberger, B. and Collins, W. J., 2002. Late Palaeozoic retreating and advancing subduction boundary in the New England Fold Belt. Australian Journal of Earth Sciences, **49**, 476–489.

Kemp, A. I. S., Hawkesworth, C. J., Collins, W. J., Gray, C. M., Blevin, P. L. and EIMF, 2009. Isotopic evidence for rapid continental growth in an extensional accretionary orogen: The Tasmanides, eastern Australia. Earth and Planetary Science Letters, **284**, 455–466.

Kent, A. J. R., 1994. Geochronology and geochemistry of Palaeozoic intrusive rocks in the Rockvale region, Southern New England Orogen, New South Wales. Australian Journal of Earth Sciences, **41**, 365–379.

Korsch, R. J., 1978. Stratigraphic and igneous units in the Rockvale-Coffs Harbour region, New South Wales. Journal and Proceedings, Royal Society of New South Wales, **111**, 13–17.

Korsch, R. J., 1981. Structural geology of the Rockvale Block, northern New South Wales. Journal of the Geological Society of Australia, **28**, 51–70.

Korsch, R. J., 1984. Sandstone compositions from the New England Orogen, eastern Australia: implications for tectonic setting. Journal of Sedimentary Research, **54**, 192-–211.

Korsch, R. J., Harrington, H. J., Murray, C. G., Fergusson, C. L., & Flood, P. G. (1990). Tectonics of the New England Orogen. *The Eromanga–Brisbane Geoscience Transect: a guide to basin development across Phanerozoic Australia in southern Queensland*, 35-52.

Landenberger, B., Farrell, T. R., Offler, R., Collins, W. J. and Whitford, D. J., 1995. Tectonic implications of Rb-Sr biotite ages for the Hillgrove Plutonic Suite, New England Fold Belt, N.S.W. Australia. Precambrian Research, **71**, 251–263.

Lee, J. K., Williams, I. S. and Ellis, D. J., 1997. Pb, U and Th diffusion in natural zircon. Nature, **390**, 159–162.

Leitch, E. C., Neilson, M. J. and Hobson, E., 1971. Dorrigo Coffs Harbour 1:250000 Geological Sheet SH/56-10 and Part SH/56 11, 1st edn. Geological Survey of New South Wales, Sydney.

Leitch, E. C. (1975). Plate tectonic interpretation of the Paleozoic history of the New England Fold Belt. Geological Society of America Bulletin, **86**(1), 141-144.

Leitch, E. C., 1978. Structural succession in a Late Palaeozoic slate belt and its tectonic significance. Tectonophysics, **47**, 311-323.

Ludwig, K. R. (2012). Isoplot/Ex, v. 3.75. Berkeley Geochronology Center Special Publication, (5).

Mezger, K. and Krogstad, E. J., 1997. Interpretation of discordant U Pb zircon ages: an evaluation. Journal of metamorphic Geology, **15**, 127–140.

Norman, M., Griffin, W., Pearson, N., Garcia, M. and O'reilly, S., 1998. Quantitative analysis of trace element abundances in glasses and minerals: a comparison of laser ablation inductively coupled plasma mass spectrometry, solution inductively coupled plasma mass spectrometry, proton microprobe and electron microprobe data. Journal of Analytical Atomic Spectrometry, **13**, 477-482.

Pupin, J. P., 1980. Zircon and granite petrology. Contributions to Mineralogy and Petrology, **73**, 207–220.

Roberts, J., & Engel, B. A. (1987). Depositional and tectonic history of the southern New England Orogen. Australian Journal of Earth Sciences, **34(1),** 1-20.

Roberts, J., Offler, R. and Fanning, M., 2004. Upper Carboniferous to Lower Permian volcanic successions of the Carroll–Nandewar region, northern Tamworth Belt, southern New England Orogen, Australia. Boundary sequences of the Werri and Rouchel blocks. Australian Journal of Earth Sciences, **51**, 205–232.

Rosenbaum, G., 2012. Oroclines of the southern New England Orogen, eastern Australia. Episodes-Newsmagazine of the International Union of Geological Sciences, **35**, 187.

Runnegar, B. N., 1970. The Permian faunas of northern New South Wales and the connection between the Sydney and Bowen Basins. Journal of the Geological Society of Australia, **16**, 697–710.

Rubatto, D., Williams, I. S. and Buick, I. S., 2001. Zircon and monazite response to prograde metamorphism in the Reynolds Range, central Australia. Contributions to Mineralogy and Petrology, **140**, 458–468.

Sandiford, M., & Hand, M. (1998). Australian Proterozoic high-temperature, low-pressure metamorphism in the conductive limit. Geological Society, London, Special Publications, **138**(1), 109-120.

Scheibner, E. (1973). A plate tectonic model of the Palaeozoic tectonic history of New South Wales. Journal of the Geological Society of Australia, **20**(4), 405-426.

Shaw, S. E. and Flood, R. H., 1981. The New England Batholith, eastern Australia: geochemical variations in time and space. Journal of Geophysical Research: Solid Earth (1978–2012), **86**, 10530–10544.

Shnukov, S. E., Andreev, A. V. and Savenok, S. P., 1997. Admixture elements in zircons and apatites: a tool for provenance studies of terrigenous sedimentary rocks. European Union of Geosciences (EUG 9), 23–24 March 1997, Strasbourg, Abstract 65/ 4P16:597.

Sturm, R., 1999. Longitudinal and cross section of zircon: a new method for the investigation of morphological evolutional trends. Schweizerische Mineralogische und Petrographische Mitteilungen, **79**, 309–316.

Teague, E., 2010. A geochronological assessment into the evolution of the Wongwibinda Complex, Southern New England Fold Belt. Hons., Thesis. Macquarie University, Australia (Unpubl.).

Thomas, W. A., 2011. Detrital-zircon geochronology and sedimentary provenance. Lithosphere, **3**, 304–308.

Timms, N. E., Kinny, P. D. and Reddy, S. M., 2006. Enhanced diffusion of Uranium and Thorium linked to crystal plasticity in zircon. Geochemical transactions, **7**, 10.

Trail, D., Watson, E. B. and Tailby, N. D., 2012. Ce and Eu anomalies in zircon as proxies for the oxidation state of magmas. Geochimica et Cosmochimica Acta, **97**, 70–87.

Tulloch, A., Ramezani, J., Faure, K. and Allibone, A., 2010. Early Cretaceous magmatism in New Zealand and Queensland: intra-plate or intra-arc origin? In: Buckman S. & Blevin P. L. eds. New England Orogen 2010 Conference Proceedings, pp. 332–335. University of New England, Armidale.

Van Achterbergh, E., Ryan, C. G., Jackson, S. E., & Griffin, W. L. (2001). Data reduction software for LA-ICP-MS. Laser-Ablation-ICPMS in the earth sciences—principles and applications. Miner Assoc Can (short course series), **29**, 239-243.

Vavra, G., 1993. A guide to quantitative morphology of accessory zircon. Chemical Geology, **110**, 15–28.

Vermeesch, P., 2004. How many grains are needed for a provenance study? Earth and Planetary Science Letters, **224**, 441–451.

White, A. J. R. and Chappell, B. W., 1988. Some supracrustal (S-type) granites of the Lachlan Fold Belt. Transactions of the Royal Society of Edinburgh: Earth Sciences, **79**, 169-181.

Chapter 5

High-temperature–low-pressure metamorphism and the production of S-type granite

S. J. Craven and N. R. Daczko

GEMOC ARC National Key Centre, Department of Earth and Planetary Sciences, Macquarie University, NSW 2109, Australia

High-temperature–low-pressure metamorphism and the production of S-type granite.

Abstract

The Wongwibinda Metamorphic Complex (WMC) of the southern New England Orogen is bound by S-type granite plutons of the Hillgrove Supersuite to the north, east and south. New U-Pb geochronology of five samples of the Hillgrove Supersuite demonstrates that plutonism in the complex involved two pulses: c. 300 Ma and c. 292 Ma. This indicates that plutonism partially overlaps the age of high-T–low-P metamorphism (296.8±1.5 Ma), but also postdates it. Zircon grains identified as xenocrysts on the basis of age (≥310 Ma) have U-Pb-Hf isotopic character that largely overlaps detrital grains in the Girrakool Beds, indicating that crust similar to the country rocks is the likely source of these xenocrysts. The $^{176}Hf/^{177}Hf$ initial character for zircon for the c. 300 Ma plutons (three samples) is less radiogenic than those in the c. 292 Ma plutons (two samples). The progression in $^{176}Hf/^{177}Hf$ initial character for zircon infers an increasing mantle component in the Hillgrove Supersuite with time. These data are evidence of a rift tectonic setting, where mantle-derived magmas are predicted to increasingly migrate to shallower crustal levels over time as the crust thins and becomes hotter (metamorphism), and early partial melting of the metasedimentary crust depletes the source rocks, reducing the S-type component in subsequent anatexis. The evolution of the Hillgrove Supersuite coincides with a period of Early Permian slab roll back and extension that led

to S-type granite production, high-T–low-P metamorphism and development of rift basins such as the Sydney-Gunnedah-Bowen system.

INTRODUCTION

S-type granites, derived from the partial melting of metasedimentary crust, are found in close association with high-temperature low-pressure (HTLP) metamorphic complexes throughout the extensional accretionary orogenesis of the Tasmanides, Eastern Australia (Collins, 2002b; Glen, 2005, 2013; Kemp et al., 2009). The accreted material involves voluminous deep marine turbidites, which are variably metamorphosed and intruded by both S- and I-type granite plutons as the Eastern Australia magmatic arcs migrated eastward (Collins, 2002a,b; Glen, 2005, 2013; Kemp et al., 2009).

This study considers the relationship between HTLP metamorphism of metaturbidite rocks and the production of S-type granite by examining rocks from the Wongwibinda Metamorphic Complex (WMC), central Tablelands Complex, southern New England Orogen (NEO; Fig. 1). The WMC contains three S-type granite plutons of the Hillgrove Supersuite: the Tobermory and Rockvale monzogranites and the Abroi Granodiorite. These three plutons are peraluminous (Flood and Shaw, 1977), share similar mineralogy including biotite, K-feldspar, plagioclase and quartz, and intrude both the fine to medium grained turbidites of the Girrakool Beds and associated HTLP metamorphosed rocks of the WMC (Chapter 4).

The concept of S- and I-type granites originates from studies of granites in the Tasmanides, Eastern Australia (Chappell and White, 1974), where these are widespread. Chemical, mineralogical and field associations

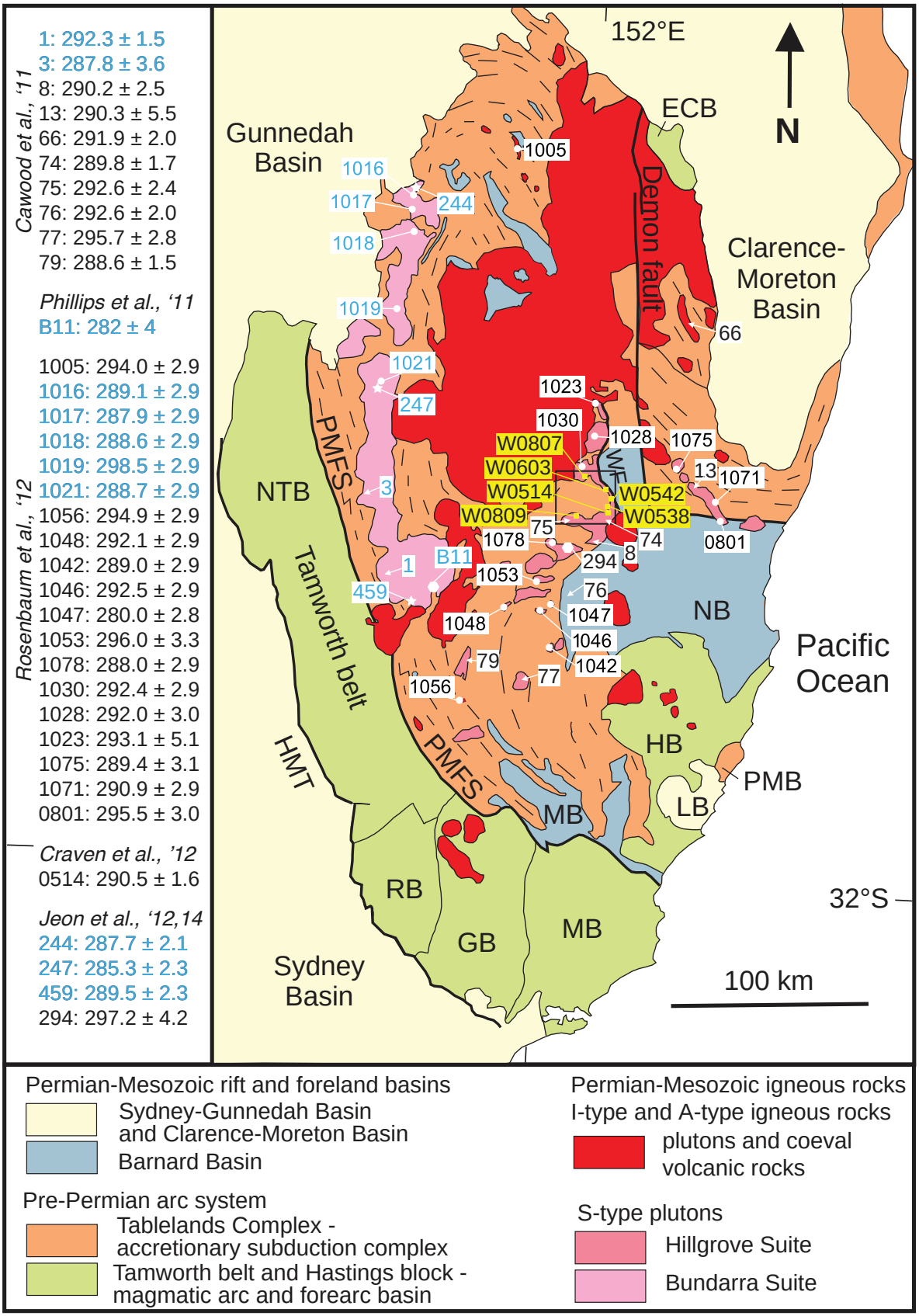

Figure 1: Regional geology of the southern New England Orogen (modified from Cawood et al., 2011) showing the location of dated rock samples (ages on left; blue = Bundarra Suite; Black = Hillgrove Suite). ECB—Emu Creek block; GB—Gresford block; HB—Hastings block; HMT—Hunter Mooki thrust; LB—Lorne Basin; MB—Myall block; NB—Nambucca block; NTB—Northern Tamworth block; PMB—Port Macquarie block; PMFS—Peel- Manning fault system; RB—Rouchel block; WF—Wongwibinda fault. Black box around Wongwibinda Metamorphic Complex.

may distinguish the two types of granite, inferred to be sourced from the partial melting of metamorphosed sedimentary (S) and igneous (I) crust. Chappell and White (1974) used geochemical parameters. For example, S-type granites have an aluminium saturation index (ASI) >1.1 which results also in >1% CIPW (named after the petrologists Cross, Iddings, Pirsson and the geochemist Washington) normative corundum. Normative calculations are used to produce an idealised mineralogy of a crystallized anhydrous melt from bulk rock chemistry. The validity of the method holds as true for metamorphosed igneous rocks as any igneous rock.

Various models for magma genesis imply that the composition of a granite pluton reflects the composition of its source rocks (Chappell and White, 1974; Clemens, 2003). Partial melting, fractionation, magma mingling, wall rock contamination, changes in temperature and pressure and influx of water and other volatiles, complicate direct geochemical and petrological comparisons between source and granite. Upon establishing the S-type character of a particular granite pluton, the question of specific source materials remains open. The study of the restitic, xenocrystic or inherited zircon in the granite may inform on this problem. Sedimentary source rocks commonly contain abundant detrital zircon, which, due to its chemical and physical robustness may persist during anatexis, particularly if the melt temperatures are relatively low (Belousova, 2002; Corfu et al., 2003). Therefore, it may be possible to compare the isotopic composition of xenocrystic zircon in S-type granite with detrital zircon datasets of potential source rocks.

This study uses zircon U-Pb ages and Hf isotope data from five samples of the Hillgrove Supersuite. We distinguish secondary xenocrysts from inferred primary magmatic grains to resolve: (i) the age range of Hillgrove Supersuite plutonism, (ii) the U-Pb-Hf character of xenocrysts, and (iii) how the character of the xenocrysts varies from pluton to pluton. The xenocrysts are compared to detrital grains in the Girrakool Beds to assess whether they are the likely source rocks.

REGIONAL GEOLOGY

The New England Orogen (NEO) is the youngest of the Tasmanides. The southern NEO is divided into two subduction-related regions (Voisey, 1959) separated by the Peel-Manning Fault System, the major structural feature of the region (Fig. 1). To the west of the Peel Fault lies the Tamworth Belt (Korsch, 1977), an Early Devonian to Late Carboniferous/Early Permian arc-forearc sequence, and to the east lies the central Tablelands Complex (cTC; Korsch, 1977), an accretionary fore arc basin, trench fill and wedge complex (Fig.1).

The WMC is located near the centre of the cTC. The protolith to the metamorphic rocks includes deep marine turbidites of the Girrakool Beds (Fig.1; Chapter 4). Farrell (1992) considered the Girrakool Beds to be a package of terrigenous, trench-fill, turbidites. He based this on the presence of layers and lenses of (i) calc-silicate intercalated with the sedimentary rocks (Binns, 1966), (ii) quartzite similar to that found in other parts of the cTC, where they are thought to be recrystallised radiolarian cherts (Aitchison, et al., 1988), and (iii) Mn-rich minerals

(rhodonite and spessartine) including Fe-Mn oxides found in the quartzite and thought to be of hydrothermal origin (Farrell, 1992) and (iv) amphibolites with chemical affinities to ocean floor tholeiites (Stephenson and Hensel, 1982). All these characteristics support a marine depositional environment. Korsch (1977) correlates the Girrakool Beds with the rest of the Coffs Harbour association, which is part of the late Devonian to late Carboniferous accretionary wedge in the southern NEO. If this interpretation is correct, the clastic sediment component of the Girrakool Beds would most likely have been deposited in the trench (Korsch et al., 1990), scraped off, accreted to the upper plate and incorporated into the accretionary wedge. Detrital zircons suggest a maximum deposition age of 309 Ma, i.e. latest Carboniferous (Chapter 4).

The WMC includes the following bounding structures and plutons: (i) Abroi Granodiorite/Gneiss adjacent to the NW-trending, Wongwibinda Fault, the major structural feature to the east, (ii), Tobermory Monzogranite and Abroi Granodiorite in the north; (iii) Rockvale Monzogranite and Abroi Granodiorite in the south (Fig.1; Chapter 1). The Girrakool Beds, protolith to the WMC, extend ~25-30 km to the west where any boundary, possibly with the Sandon Beds (Korsch, 1978) is concealed by overburden including Tertiary Basalts (Fig.1). Regional tilting (~10°), associated with Permian movement on the Wongwibinda Fault (266–258 Ma; Farrell, 1992; Landenberger et al., 1995), has revealed a metamorphic field gradient that increases gradually from west to east, from indurated sedimentary rocks to greenschist facies biotite-grade metamorphism and, as the Wongwibinda

Fault is approached, the metamorphic field gradient steepens to amphibolite grade, marked by the occurrence of cordierite and almandine garnet, with migmatites reflecting the maximum grade. These zones define a discontinuous metamorphic field gradient throughout the complex (Chapter 2) that is consistent with conductive mechanisms of heating the shallow crust to biotite-grade in combination with local advective heating by aqueous fluids to cordierite-grade, that is, heat advection by aqueous fluid locally drove km-scale HTLP metamorphism (Chapter 2). Shear zones are common in the higher-grade metamorphic rocks and affect both metasedimentary and plutonic rocks. These have been considered conduits (Chapter 2) for the hot aqueous fluids thought to have been responsible for heat advection driving high-grade metamorphism.

Two Lower Permian granitoid suites are members of the New England Batholith and significant to this study: (i) Bundarra Supersuite (Flood, 1971, Flood and Shaw, 1975), a group of cordierite-bearing monzogranites (previously adamellites); (ii) Hillgrove Supersuite (Binns, 1967), redefined by Flood and Shaw (1977) as biotite-bearing granodiorite and monzogranite (previously adamellite) plutons (Fig.1). All three WMC granitoids examined here belong to the S-type Hillgrove Supersuite (previously Hillgrove Plutonic Suite). Though overlapping in age (Fig. 1), the Bundarra Supersuite is not represented at Wongwibinda. All three Wongwibinda granitoids contain distinctive red-brown biotite, K-feldspar, minor plagioclase and quartz.

The Abroi Granodiorite is elongate along, and lies west of, the Wongwibinda Fault, extending over approximately 25 km. It is an elongate and irregular shaped intrusion with lobes in the north and south intruding west

away from the fault (Fig. 1). The northern lobe lies adjacent to the Tobermory Monzogranite and the southern lobe adjacent to the Rockvale Granodiorite thinning to a few kilometers across at Wongwibinda (Fig.1). Farrell (1992) found in contravention to Binns (1966) that the Tobermory Monzogranite and the Abroi Granodiorite are contiguous. A similar situation may also exist between the Abroi Granodiorite and the Rockvale Monzogranite (Hensel, 1982; Farrell, 1992). Along the Wongwibinda Fault is a diffuse zone of variably sheared Abroi Granodiorite, referred to here as the Abroi Gneiss. Shearing diminishes away from the fault into less-foliated granite.

The Tobermory Monzogranite is a sub-circular pluton located in the north of the WMC. It appears contiguous with the Abroi Granodiorite but Binns (1966) inferred an intrusive relationship on the basis of a sharp change in outcrop pattern. Xenoliths are common and large flakes of biotite define a weak foliation associated with the Glen Bluff Fault (Binns and Richards, 1965; Binns, 1966; Kleeman, 1975). Binns (1966) also noted that the margin of the pluton is coarser-grained and more granodioritic than at the centre of the intrusion.

The Rockvale Monzogranite (Landenberger et al., 2010) lies directly south of the WMC (Fig. 1). It is similar, in petrology, to the Tobermory Monzogranite; these units weather to typical granite tors, whereas the Abroi Granodiorite outcrops as flat lying whalebacks.

The geographical proximity between migmatite rocks (highest grade metamorphosed Girrakool Beds) and some Hillgrove plutons has previously raised questions about the relationship between these units. Investigation of the contact around the Abroi Granodiorite (Farrell, 1992; Chapter 1)

demonstrated that the contact aureole is narrow (tens of metres), indicating that the exposed granites are an unlikely source of heat for the HTLP metamorphism.

METHODS

Samples were collected and field observations made for the Tobermory (W0807) and Rockvale (W0809) monzogranites, and the Abroi Granodiorite (W0514, W0603) / Gneiss (W0542). Polished thin sections were prepared for microscopic examination and Electron MicroProbe (EMP) analysis. Thin section photomicrographs were taken on a Nikon 50iPOL petrographic microscope with Nikon DS-Fi1 digital camera and Nikon NIS Elements-D software for multiple photograph stitching. Representative rock samples were selected for whole rock analysis and the preparation of zircon concentrates by Geotrack International (Melbourne). Zircon mounts were prepared for EMP imaging, U-Pb geochronology and Hf isotope analysis.

All zircon grains were imaged by EMP Back Scattered Electron (BSE) and/or SEM Cathode Luminescence (CL) imaging. Elemental concentrations of silicon, zirconium, yttrium and hafnium were determined by EMP to confirm zircon prior to U-Pb and Hf analysis. Only grains with greater than 95 weight percent total oxides were considered.

U-Pb analysis was carried out by Laser Ablation Inductively Coupled Plasma Mass Spectrometry (LA-ICPMS) and Hf isotopes using Laser Ablation Multi-Collector Inductively Coupled Plasma Mass Spectrometry (LA-MC-ICPMS) as described in Chapter 4. Pb corrected data with discordance >5%, using the $^{206}Pb/^{238}U$ and $^{207}Pb/^{235}U$ ages, was rejected.

The LA-ICPMS age data were considered using two approaches: (i) grains with ages >300 Ma were considered inherited and those with ages <280 Ma were considered to have experienced Pb-loss using the parameters of Cawood et al. (2011); grains inferred to be primary magmatic are 280-300 Ma. Alternatively, (ii) grains with ages >309 Ma, the maximum deposition age determined, statistically, in Chapter 4, were considered inherited; grains inferred to be primary magmatic are 280-309 Ma. The results from this investigation were then compared with data from the country rocks (Chapter 4).

RESULTS

Petrography

The Abroi Granodiorite (W0514; Fig. 2a) is a K-feldspar-quartz-plagioclase-biotite-opaque±garnet-muscovite granodiorite with accessory zircon, monazite and apatite. This sample, collected some 5 km west of the Wongwibinda Fault, is the least deformed sample of Abroi Granodiorite examined, but still exhibits evidence of minor deformation (Fig. 3a). A foliation is lacking, as biotite grains are randomly oriented; some grains exhibit undulose extinction and warping of the basal cleavage. Biotite grains are subhedral, but have ragged grain boundaries. The biotite grains also have pleochroic haloes within the grain that evidence the presence of radioactive inclusions. Quartz exhibits undulose extinction, recrystallisation, sutured, and incipient sutured grain boundaries, at various stages of development. K-feldspar grains are weakly porphyritic. Euhedral to subhedral microcline is

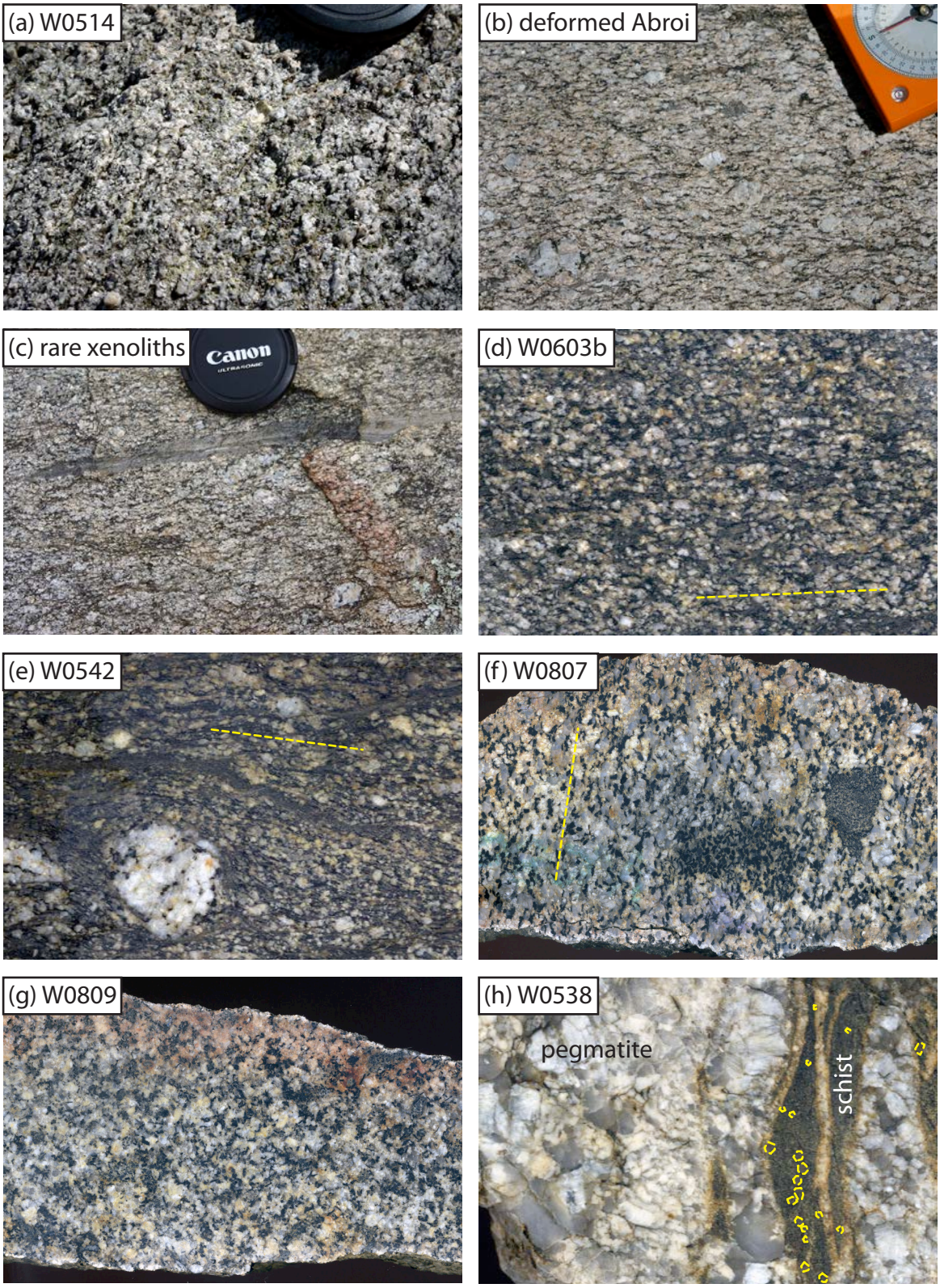

Figure 2: (a) Site of sample W0514, low-strain Abroi Granodiorite; (b) higher-strain Abroi Granodiorite near site W0514; (c) rare xenoliths in Abroi Granodiorite; (d–h) Cut and polished slabs. (d) Moderately strained Abroi Gneiss, sample W0603b; (e) Highly strained Abroi Gneiss, sample W0542; (f) Tobermory Adamellite, sample W0807; (g) Rockvale Granodiorite, sample W0809; (h) Pegmatite, sample W0538. Field of view for (a,b) is c. 12 cm across, (c) c. 20 cm across and for (d–h) is 14cm across. Dashed line denotes foliation in deformed samples (d,e,f) and highlights garnet grains in country rock schist within the pegmatite sample (h).

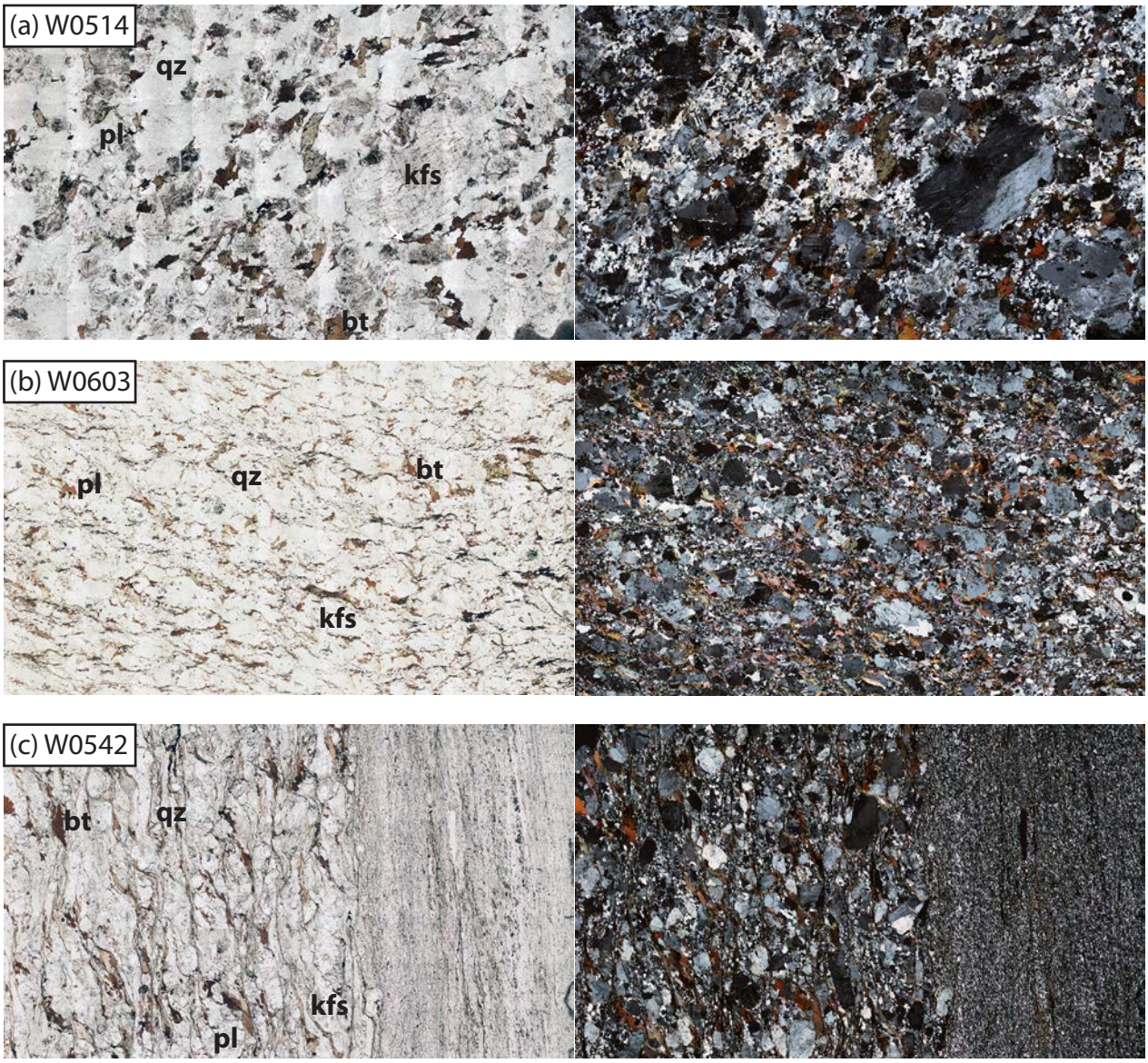

Figure 3: Stitched image photomicrographs (plane-polarised light on left, crossed-polarised light on right). Field of view is 20 mm across. (a) Sample W0514 showing relict igneous feldspar and recrystallised quartz; (b) Sample W0603 showing a moderately developed foliation defined by biotite and rare relict feldspar grains (partially recrystallised); (c) Sample W0542 showing the contact with a xenolith (right third of image), a well developed foliation defined by biotite, and rare relict feldspar grains (partially recrystallised).

finer grained and exhibits well-developed tartan twinning. Myrmekite (quartz and sodic plagioclase) partially replaces some K-feldspar grains. Oscillatory concentric zoning is observed in some plagioclase feldspar grains. Plagioclase exhibits bent twin boundaries.

The foliation becomes better developed (W0603, Fig. 2b) as the Wongwibinda Fault is approached. Near the fault zone itself, the foliation becomes strongly gneissic (W0542, Fig. 2e). Rare xenoliths of country rock occur in the Abroi unit, elongate with the foliation in some cases (Fig. 2c). Opaque phases include pyrite plus another opaque with bright grey reflectance in plane polarized reflected light. Recrystallisation of quartz is more advanced and the biotite foliation is more strongly defined but many of the biotite grains are randomly oriented with straight crystal faces (Fig. 3b). Primary quartz grains are still evident, but these display a core and mantle structure with recrystallised mantles. Interstitial quartz is almost entirely recrystallised and myrmekite intergrowth colonies are more common. Porphyritic K-feldspar becomes porphyroclastic. Garnet and cordierite are accessory phases, while the mode of opaque minerals decreases with increasing strain.

The Abroi Gneiss (W0542) presents a typical gneissic texture. Coarse biotite defines a well-developed foliation that wraps around K-feldspar porphyroclasts (Fig. 2e). Biotite is shredded in the high strain areas. Quartz is almost entirely recrystallised and the K-feldspar grains tend toward augen texture with quartz and biotite in the strain shadows. Myrmekite is less

common compared with W0603 and W0514. The thin section (Fig. 3c) shows the contact between the gneiss and a quartz-rich psammitic xenolith.

Similar to the Abroi Granodiorite, the Tobermory Monzogranite (W0807) (Fig. 2f) and the Rockvale Monzogranite (W0809; Fig. 2g), are K-feldspar-quartz-plagioclase-biotite-opaque±garnet-muscovite monzogranites (Fig. 2f and 2g respectively), with accessory zircon, monazite and apatite.

The Rockvale Monzogranite (W0809; Fig. 2g) is the least deformed of the three plutons. Incipient strain is evident by undulose extinction in quartz grains. Potassium feldspar exhibits rare zoning, incipient tartan twinning and varying degrees of sericitic alteration particularly in the cores of some grains. Perthite is common and myrmekite was not observed in this section (Fig. 4b). Biotite exhibits very minor warping and some corrosion of the grain boundaries is common. The opaque phase is commonly pyrite.

The Tobermory Monzogranite (W0807) exhibits some evidence of strain, similar to the Abroi Granodiorite sample W0514. Quartz exhibits undulose extinction, sutured, and incipient sutured grain boundaries and recrystallisation at various stages of development. Although strain is evident, the foliation is poorly developed, as biotite grains remain randomly oriented. Some biotite grains exhibit undulose extinction and warping of the basal cleavage. Biotite grains are subhedral, but have straight grain boundaries with embayments. Pyrite is a common accessory phase. Pleochroic haloes within biotite grains evidence the presence of radioactive inclusions. K-feldspar grains are subhedral with rare incipient perthite, and myrmekite was not observed. Rarely, K-feldspar has tartan twinning and concentric zonation in

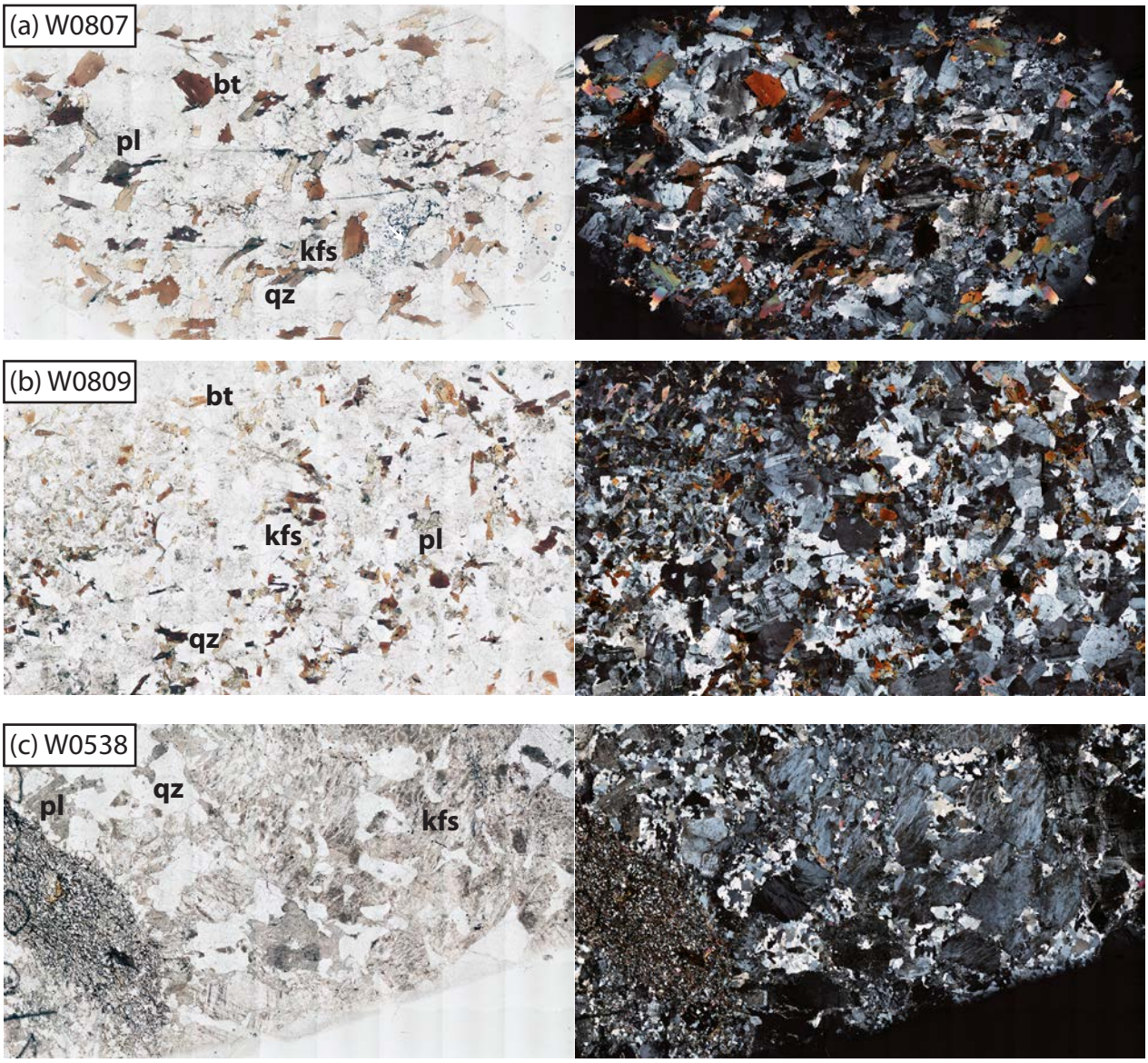

Figure 4: Stitched image photomicrographs (plane-polarised light on left, crossed-polarised light on right). Field of view is 20 mm across. (a) Sample W0807 showing weakly modified igneous microstructure; (b) Sample W0809 showing igneous microstructure including a microgranitoid enclave (top left corner); (c) Sample W0538 showing very large K-feldspar grains with recrystallised quartz domains and minor plagioclase feldspar. Note xenolith of schist on left.

some grains. Two enclaves with smaller grain size than the host, but similar mineralogy are also observed (Fig. 2f).

In addition to the three granitoid plutons, numerous pegmatite dykes intrude the Girrakool Beds and are not observed to cut the granites; one of these pegmatites was investigated. The pegmatite (W0538; Fig. 2h) contains K-feldspar-quartz-plagioclase-opaque-muscovite and is composed of very large, perthitic, potassium feldspar grains with interstitial quartz, plagioclase, muscovite and an opaque mineral (Fig. 4c). The opaque mineral is composed of radiating pale grey acicular crystals in plane polarised reflected light. The thin section exhibits a contact with a xenolith of psammopelitic country rock. The xenolith contains coarse garnet in the more pelitic layers (Fig. 2h).

The three granite plutons are mineralogically very similar, differing only in the proportions of major rock forming minerals of which they are composed.

Uranium-Lead Geochronology

Electron MicroProbe (EMP) / Scanning Electron Microscopy (SEM) - Zircon imaging

Figure 5 displays the results of EMP Back-Scattered Electron (BSE) (samples W0542, W0603, W0807 and W0809), the only method available for imaging at the time and SEM cathodoluminescence (CL) (samples W0514, W0538) imaging of zircon separated from the granite and pegmatite samples. BSE/CL images of grains from the lowest strain rocks (Abroi Granodiorite [W0514], Tobermory and Rockvale monzogranites [W0807 and W0809]) display euhedral crystals with sharp terminations and crystal faces. The

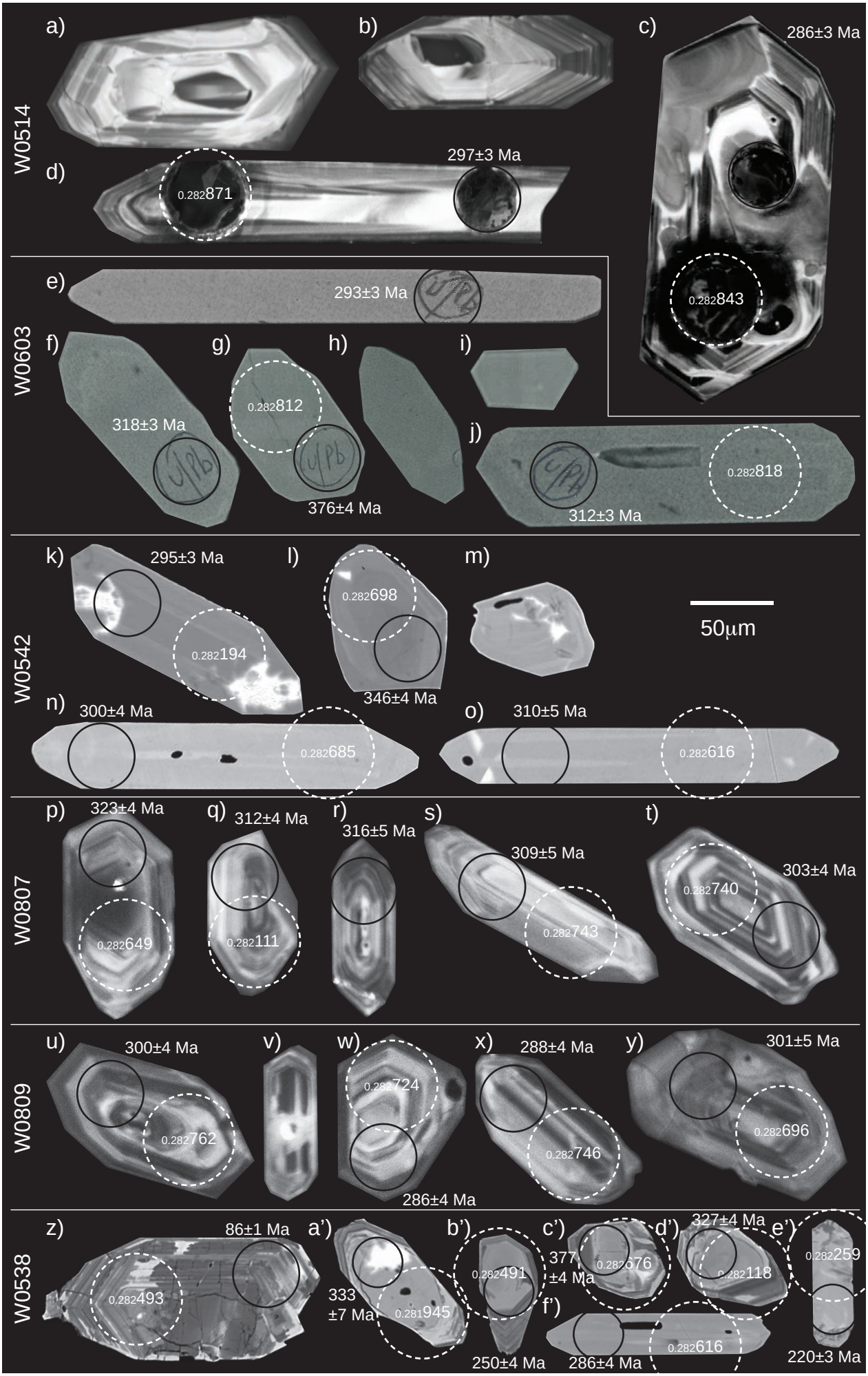

Figure 5: BSE/Cathodoluminescence images of representative zircon grains.

crystal shape varies from elongate-prismatic to equant. Most grains display oscillatory zoning (Fig. 5 a-d,p-y) with rare sector zoning (Fig. 5b). Some grains contain cores that are texturally different to the rims (e.g. Fig. 5 a,u). The BSE images of zircon from the higher strain samples (W0603 and W0542) do not show as much internal structure as well as in the other samples, but crystal size and shape appear very similar to the less metamorphosed granites, differing only by the fact that they are slightly rounded, with grains from W0542 more rounded than W0603. CL images of zircon separated from the pegmatite (W0538) show anhedral – subhedral, rounded shapes with homogeneous cores (Fig. 5a'- d'). Rare euhedral prismatic grains were also observed (Fig. 5e',f'). Grain sizes range from 70 to 330 μm (long axis) and have an elongation ratio varying from equant grains to elongate prismatic grains (1:11). Equant grains are more common.

LA-ICPMS – U-Pb Isotope Analysis

Geochronological results are presented on concordia diagrams (Fig. 6) and Gaussian-summation probability density distribution and stacked column frequency histograms (Fig. 7). A summary of the weighted average ages is presented in Table 1. All common lead (non-radiogenic) corrected data with common Pb > 2% and discordance > 5% were rejected. Grains with ages >360 Ma are very rare with one grain dated in the Tobermory Monzogranite and seven grains dated in the pegmatite (W0538). On the basis of previous work (Cawood et al., 2011), the remaining data was divided either side of 300 Ma, as this was the cutoff identified between primary magmatic grains and

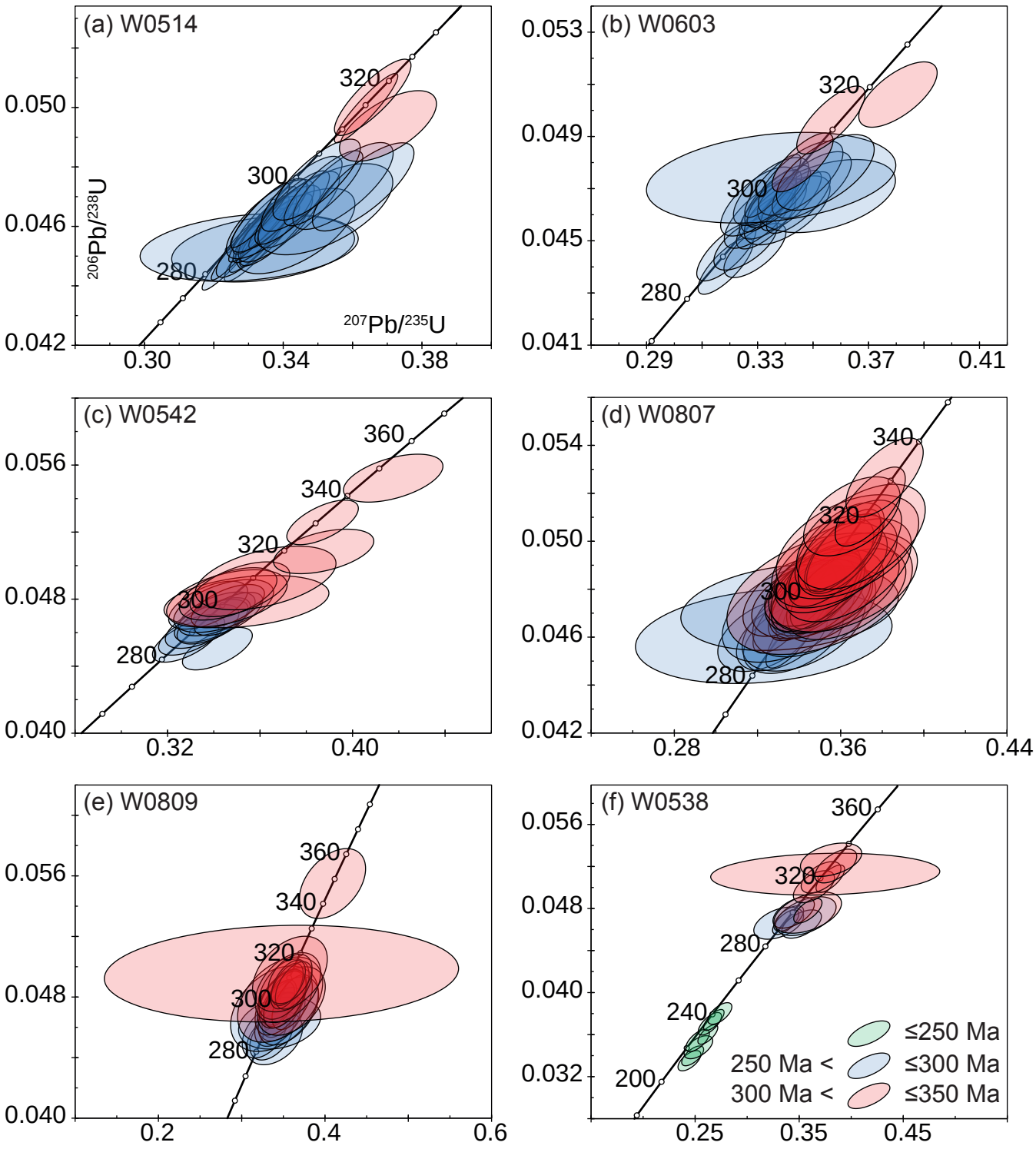

Figure 6: Concordia diagrams for the granite and pegmatite samples.

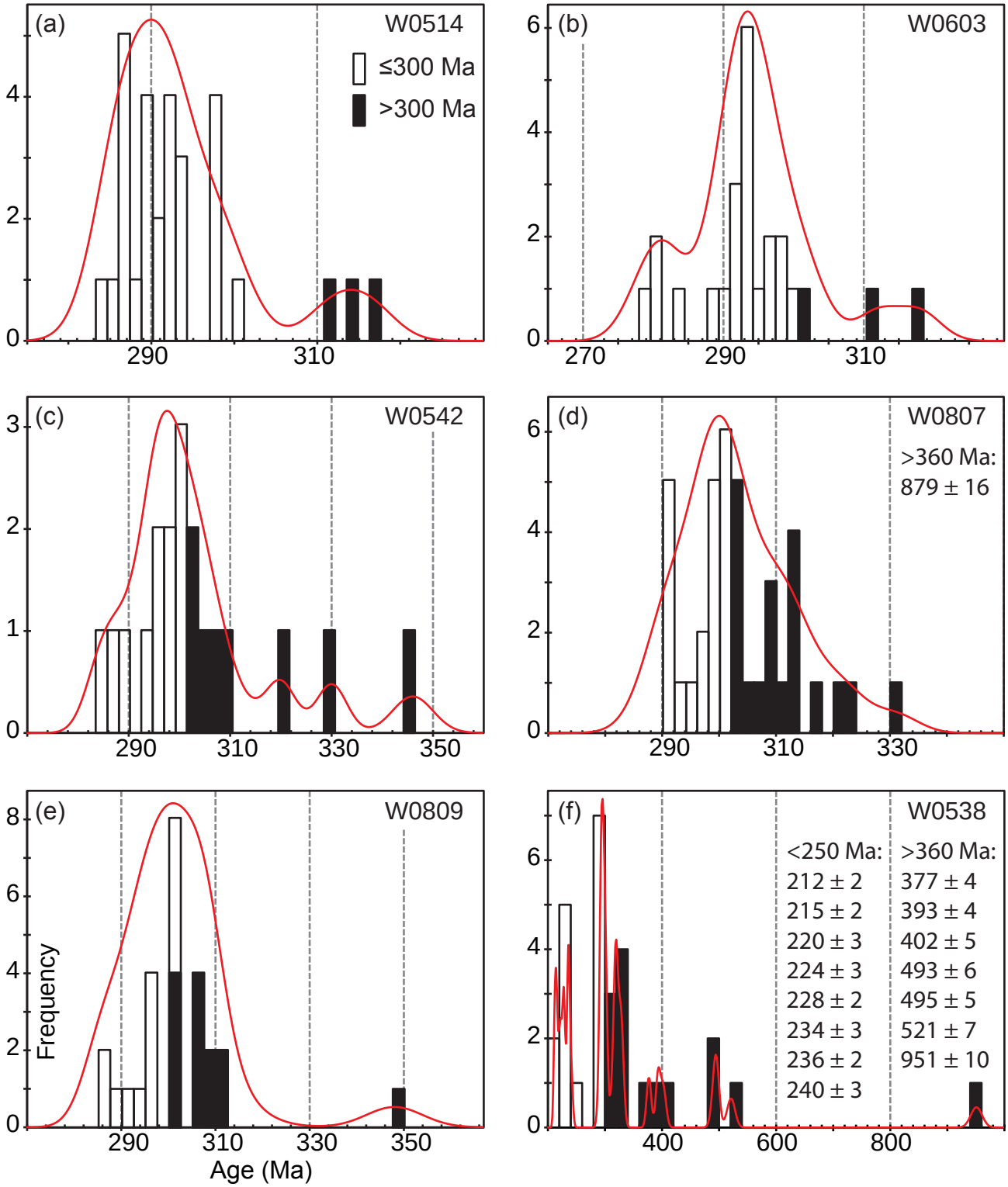

Figure 7: Gaussian-summation probability density distribution and stacked column frequency histograms for granite and pegmatite samples.

xenocrysts in the Bundarra and Hillgrove supersuites. Therefore, the data presented in Figures 6 and 7 are divided either side of 300 Ma: blue (≤300 Ma) versus red (>300Ma) error ellipses on the concordia diagrams and white (≤300 Ma) versus black (>300Ma) filled bars on the stacked column frequency histograms.

Abroi Granodiorite (W0514): The data from this sample have previously been published (Chapter 1) and are reiterated here for completeness. One grain of the 31 analysed was rejected with high discordance (>5%). Three grains are interpreted as inherited in the remaining 30 grains. Their ages are 311 Ma, 314 Ma and 317 Ma (Fig. 7a). Their age overlaps detrital zircons from the country rock (variably metamorphosed Girrakool Beds; Chapter 4). 27 remaining analyses of 27 grains (Fig. 6a) give a weighted average $^{206}Pb/^{238}U$ age of 291.0±1.7 Ma (MSWD = 2.1 and probability of fit = 0.001). Removing three grains from this population (284 Ma, 298 Ma and 300 Ma) with the largest weighted residuals gives an adjusted weighted average $^{206}Pb/^{238}U$ age of 290.5±1.6 Ma (MSWD = 1.5, probability of fit of 0.057), improving the statistics to better than 95% confidence. Considering the shape of the Gaussian-summation probability density distribution (Fig. 7a), **290.5±1.6 Ma** is interpreted as the best fit for the crystallization age for this part of the Abroi unit.

Weakly deformed Abroi Gneiss (W0603): Five grains of the 29 analysed were rejected with high discordance (>5%). Two grains are interpreted as inherited in the remaining 24 grains. These are 312 Ma and 318 Ma (Fig. 7b). Their age overlaps detrital zircons from the country rock

(variably metamorphosed Girrakool Beds; Chapter 4). One grain at 302 Ma was included in the primary population as it is within error of the 300 Ma cut off. Isoplot rejected one data point at 278 Ma from the 22 remaining analyses of 22 grains (Fig. 6b) to give a weighted average $^{206}Pb/^{238}U$ age of 291.7±2.5 Ma (MSWD = 1.6, probability of fit = 0.043). Two more, with the largest weighted residuals, were rejected to improve statistics. This gives an adjusted weighted average $^{206}Pb/^{238}U$ age of 292.6±2.5 Ma (MSWD = 1.3, probability of fit = 0.17). **292.6±2.5 Ma** is interpreted as the best fit crystallization age for this part of the Abroi unit.

Strongly deformed Abroi Gneiss (W0542): One grain of the 20 analysed was rejected with high discordance (>5%). Three grains are easily interpreted as inherited in the remaining 19 grains. Their ages are 320 Ma, 330 Ma and 346 Ma (Fig. 7c). Their age overlaps detrital zircons from the country rock (variably metamorphosed Girrakool Beds; Chapter 4). Unlike the first two samples of the Abroi unit, this sample does not have a data gap between c. 300 Ma and 310 Ma (Fig. 6c). In fact, half of the remaining grains are <300 Ma, the other half being 300–310 Ma. It is difficult to argue that the grains ≥300 Ma are all inherited given the continuous spread of data; two approaches were taken. Firstly, using the 11 grains ≤300 Ma, a weighted average $^{206}Pb/^{238}U$ age of 293.9±3.6 Ma (MSWD = 2.9, probability of fit of 0.001) was calculated. One data point from this population is removed on the basis of weighted residuals to give an adjusted weighted average $^{206}Pb/^{238}U$ age of 295.0±3.1 Ma (n=10, MSWD = 1.0, probability of fit = 0.047), at better than 95% confidence. Secondly, reconsidering the premise that all grains with

ages >300 Ma are inherited, the data within the Gaussian distribution were included in another age calculation. Employing data ≤310 Ma produced a weighted average $^{206}Pb/^{238}U$ age of 296.1±3.5 Ma (n = 16, MSWD = 3.9, probability of fit of 0). Adjusting this by rejecting a further three grains using the largest weighted residuals produced a weighted average $^{206}Pb/^{238}U$ age of 298.9±2.7 Ma (n=13, MSWD = 1.7, probability of fit = 0.06). Considering the shape of the Gaussian-summation probability density distribution (Fig. 7c), **298.9±2.7 Ma** is interpreted as the best fit crystallization age for this part of the Abroi unit.

Tobermory Monzogranite (W0807): Five grains of the 45 analysed were rejected with high discordance (>5%). Ten grains are interpreted as inherited in the remaining 40 grains. These are 311 Ma, 312 Ma, 313 Ma (x3), 316 Ma, 321 Ma, 323 Ma, 331 Ma and 879 Ma (Fig. 7d). Their age overlaps detrital zircons from the country rock (variably metamorphosed Girrakool Beds; Chapter 4). Similar to sample W0542, this sample has approximately half of the remaining grains being <300 Ma, the other half being 300–310 Ma (Fig. 6d). The same two approaches were used as for sample W0542. Firstly, using the 18 grains ≤300 Ma, a weighted average $^{206}Pb/^{238}U$ age of 295.9±1.9 Ma (n=18, MSWD = 0.9, probability of fit 0.57) is calculated. Employing data ≤310 Ma produced a weighted average $^{206}Pb/^{238}U$ age of 299.0±2.0 (n=30, MSWD = 1.5, probability of fit = 0.044). This was further adjusted to improve the statistics by removing two grains, both at 290 Ma, using the highest weighted residuals, resulting in a weighted average $^{206}Pb/^{238}U$ age of 299.6±1.9 Ma (n=28, MSWD = 1.2, probability of fit = 0.21). Considering the

shape of the Gaussian-summation probability density distribution (Fig. 7d), **299.6±1.9 Ma** is interpreted as the crystallization age of the Tobermory Monzogranite.

Rockvale Monzogranite (W0809): Ten grains of the 36 analysed were rejected with high discordance (>5%). Three grains are interpreted as inherited in the remaining 26 grains. These are 311 Ma, 312 Ma and 348 Ma (Fig. 7e). Their age overlaps detrital zircons from the country rock (variably metamorphosed Girrakool Beds; Chapter 4). Similar to samples W0542 and W0807, this sample has 9 of the remaining grains being <300 Ma, the other 14 being 300–310 Ma (Fig. 6e). The same two approaches were used as for samples W0542 and W0807. Firstly, using the 13 grains ≤300 Ma, a weighted average $^{206}Pb/^{238}U$ age of 294.8±3.3 Ma (n=13, MSWD =1.6, probability of fit = 0.076) was calculated. Employing data ≤310 Ma produced a weighted average $^{206}Pb/^{238}U$ age of 298.4±3.5 Ma (n=23, MSWD = 2.7, probability of fit = 0). Adjusting this result by rejecting three grains with the greatest weighted residuals (285 Ma, 286 Ma and 288 Ma), gave a weighted average $^{206}Pb/^{238}U$ age of 300.8±2.6 Ma (n=20, MSWD = 1.4, probability of fit = 0.096). Considering the shape of the Gaussian-summation probability density distribution (Fig. 7e), **300.8±2.6 Ma** was interpreted as the crystallization age for the Rockvale Monzogranite.

Pegmatite (W0538): Twenty-two grains of the 51 analysed were rejected with high discordance (>5%). The stacked column frequency histogram exhibits a number of age populations within the concordant grains: (i) a broad distribution from 212 Ma to 240 Ma, (ii) a peak at c. 295 Ma, (iii) an

age distribution from 315 Ma to 330 Ma, and (iv) a series of small peaks >360 Ma. The uranium concentration in the zircons from the youngest (212–240 Ma) group is one hundred times greater than uranium in the other grains, highlighting the likelihood of lead loss accompanying radioactive damage to the crystal lattice. Eight grains 291–302 Ma (Fig. 6f) gave a weighted average $^{206}Pb/^{238}U$ age of 296.2±2.4 Ma (n=8, MSWD = 0.82, probability of fit = 0.57). Thirteen grains are likely inherited. These are 315 Ma, 319 Ma, 320 Ma, 322 Ma, 327 Ma, 330 Ma, 377 Ma, 393 Ma, 402 Ma, 493 Ma, 495 Ma, 521 Ma and 951 Ma (Fig. 7f). **296.2±2.4 Ma** is interpreted as a good approximation of the crystallisation age of the pegmatite.

LA-MC-ICPMS – Hafnium Isotope Analysis

The Hf isotopic composition of 134 zircon grains is presented on Figure 8 from samples of the Hillgrove Supersuite (W0514, W0603, W0542, W0807 and W0809). In addition, 44 zircon grains from the pegmatite sample (W0538) were analysed. These new data are plotted (Fig. 8) along with the Hf isotope data from detrital zircon separated from the country rock (variably metamorphosed Girrakool Beds; Chapter 4). The Hillgrove Supersuite data includes 23 zircon xenocrysts that are ≥310 Ma (observed in all five samples). Fourteen of the 134 zircon grains analysed have an age between 301 and 309 Ma. These are from three samples (Abroi Granodiorite, W0542, Tobermory Monzogranite, W0807 and Rockvale Monzogranite, W0809) and are inferred to be primary magmatic grains on the basis of their age; they have been plotted on Figure 8 at the age of each pluton. The pegmatite data

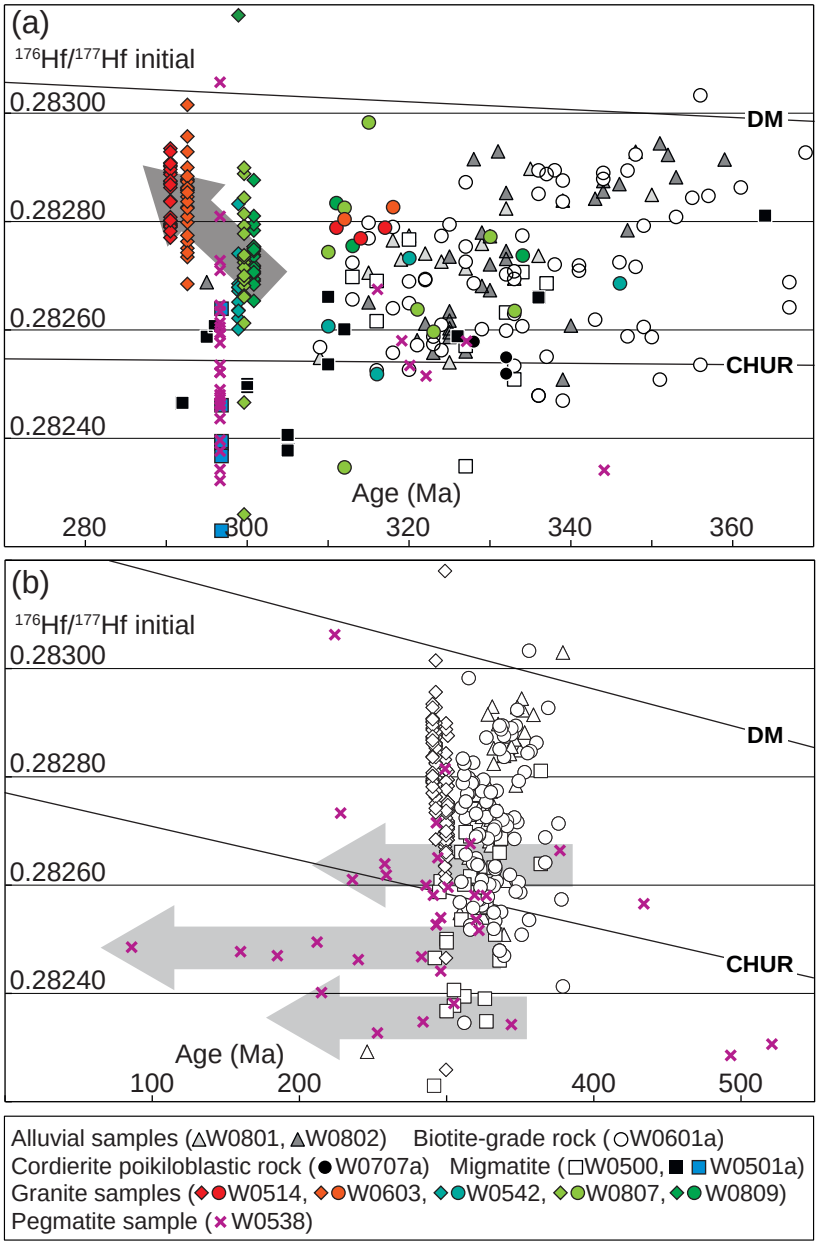

Figure 8: $^{176}Hf/^{177}Hf$ initial versus age. (a) Melt-crystallised zircon grains plotted at the weighted average age of each sample (diamonds), zircon xenocrysts (coloured circles), and pegmatite grains (coloured x) compared with data from the country rocks (greyscale symbols). Blue squares are plotted at the published metamorphic age: 296.8 ± 1.5 Ma (Craven et al., 2012); these are rim analyses of zircon from sample W0501a, inferred to have grown following partial melting. Dark grey arrow depicts trend to more radiogenic melt-crystallised zircon with younger age. (b) The same data as in (a) expanded to show the full range of pegmatite data, plotted at the apparent age of each grain. Horizontal grey arrows show the pattern for grains inferred to have lost Pb.

<310 Ma has been plotted at the approximate crystallization age (296.2±2.4 Ma), calculated using a small group of concordant grains. Whereas, pegmatite grains >310 Ma are plotted at their measured age.

Abroi Granodiorite (W0514) and weakly deformed Abroi Gneiss (W0603): These two samples contain primary magmatic zircon that is, on average, more radiogenic (higher $^{176}Hf/^{177}Hf$ initial) than the other three Hillgrove Supersuite samples (Fig. 8). Five xenocrysts have similar $^{176}Hf/^{177}Hf$ initial (0.282769–0.282826) at 311–318 Ma and one xenocryst plots just off the graph at 376 Ma and $^{176}Hf/^{177}Hf$ initial = 0.282714. The grains within the cluster of five xenocrysts are generally more radiogenic than similarly aged grains from the country rock (compare the red and orange coloured circles to the grey scale symbols in the age range 310–320 Ma on Figure 8).

Strongly deformed Abroi Gneiss (W0542), Tobermory Monzogranite (W0807) and Rockvale Monzogranite (W0809): These three samples contain primary magmatic zircon that is, on average, less radiogenic (lower $^{176}Hf/^{177}Hf$ initial) than the other two Hillgrove Supersuite samples (Fig. 8). Seventeen xenocrysts have variable $^{176}Hf/^{177}Hf$ initial over a broad range of ages. Five of these xenocrysts have similar $^{176}Hf/^{177}Hf$ initial (0.282743–0.282834) at 310–320 Ma and plot closely to the cluster of five xenocrysts in samples W0514 and W0603. Together these ten xenocrysts form a group of grains that are more radiogenic than similar aged grains from the country rock (Fig. 8). The remaining xenocrysts generally overlap grains from the country rock (Fig. 8).

Pegmatite (W0538): The large number of discordant grains and a correlation between high uranium content and the youngest grains strongly

suggest the age data for this sample are suspect, likely to have been affected by Pb-loss. However, the initial $^{176}Hf/^{177}Hf$ value of zircon is not modified during processes that lead to Pb-loss (Patchett, 1983; Kinny et al., 1991; Kinny and Maas, 2003; Lenting et al., 2010). The horizontal grey arrows on Figure 8b indicate that while the $^{176}Hf/^{177}Hf$ value is robust, the U–Pb age may have been modified (Bomparola et al., 2007; Whitehouse and Kemp, 2010; Halpin et al., 2012, 2013). Regardless of the problems in determining the true age of each grain, the data is dominated by low radiogenic zircon (lowest $^{176}Hf/^{177}Hf$ initial). The character of these grains overlaps the rims analysed in the migmatite sample W0501a (Chapter 4). Five xenocrysts generally overlap grains from the country rock (Fig. 8a), while the older grains (>360 Ma) also have low radiogenic character (Fig. 8b).

DISCUSSION

Age of Hillgrove Supersuite

Twenty-four U-Pb zircon ages have been published for the Hillgrove Supersuite since 2011 (Fig. 1; Cawood et al., 2011; Rosenbaum et al., 2012; Jeon et al., 2014; Chapter 1) with very few earlier data (e.g. Kent, 1994). The oldest plutons in the supersuite include the Hillgrove Monzogranite (c. 297 Ma; Jeon et al., 2014), Blue Knobby Monzogranite (c. 296 Ma; Rosenbaum et al., 2012) and Tia Granodiorite (c. 296 Ma; Cawood et al., 2011). The youngest plutons in the supersuite include the Cheyenne complex (c. 280 Ma; Rosenbaum et al., 2012), Hillgrove Monzogranite (c. 288 Ma; Rosenbaum et al., 2012) and Kilburnie Monzogranite (c. 289 Ma; Cawood et al., 2011). Note

the two different and separately dated samples of the Hillgrove Monzogranite are amongst the oldest and youngest parts of the supersuite, indicating that some plutons are likely composite. The ages of eighteen of the 24 dated samples cluster between c. 288 Ma and c. 294 Ma (Fig. 1), suggesting the main pulse of magmatism occurred at c. 291 Ma in the Hillgrove Supersuite. Two of the Abroi Granodiorite samples dated here (W0514 [290.5 ± 1.6 Ma] and W0603 [292.6 ± 2.5 Ma]) also overlap this main pulse. However, the Tobermory and Rockvale monzogranites and the Abroi Gneiss samples dated here return the oldest ages yet determined for the Hillgrove Supersuite (Table 1) when grains ≤310 Ma are considered primary magmatic zircon, on the basis of being part of a simple Gaussian distribution (e.g. Fig. 7e). This highlights the significance of grains dated between 300 Ma and 310 Ma, which Cawood et al. (2011) elected to exclude in their dating of the Rockvale Monzogranite; they excluded about a third of their data, inferring nine grains dated between 300-309 Ma are xenocrysts. Rosenbaum et al. (2012) had less trouble dating their sample of the Tobermory Monzogranite only excluding two grains dated between 300 Ma and 302 Ma of 17 dated in total. If data between 300 Ma and 310 Ma are excluded from our age calculations, these three samples are still amongst the oldest quarter of the dated samples of the Hillgrove Supersuite (Table 1).

Analysis of zircons for the pegmatite produced many enigmatically young ages. The young ages are inferred to be due to radiogenic lead loss and are explained as follows. Lead migration within crystalline zircon is extremely slow at the peak P-T conditions interpreted for the Wongwibinda

Metamorphic Complex. Lead loss may be associated with damage of the crystal lattice, most commonly due to metamictisation, the destruction of the crystal structure by intense radiation from decaying uranium. This allows lead initially bound by the lattice to diffuse out of the zircon grain. High uranium concentrations are necessary to cause metamictisation of zircon in short time spans. Uranium concentrations measured in the pegmatite sample (W0538) are very high, around one hundred times greater than those measured for the Hillgrove Supersuite samples. High uranium contents are expected in pegmatitic fluids, being late stage highly fractionated liquids. Therefore, the high number of discordant grains and young ages for some concordant grains in the pegmatite is expected.

Xenocrysts in the Hillgrove Supersuite

The youngest detrital grains dated in the country rock (variably metamorphosed Girrakool Beds) are c. 309 Ma; these are interpreted as originating from the Keepit Arc (Chapter 4). This value is used as the cut off to infer xenocrysts in the Hillgrove Supersuite in this study. Approximately two-thirds of xenocrysts (>309 Ma) cluster between 310 Ma and 320 Ma, suggesting the xenocrysts are sourced from young metasedimentary rocks that are no older than the Girrakool Beds. Though many of the xenocrysts have overlapping U-Pb-Hf isotopic character when compared to the Girrakool Beds (Fig. 8), the youngest xenocrysts are slightly more radiogenic. Together, the U-Pb and Hf isotope data indicate that crust very similar to the exposed Girrakool Beds is the likely source of the xenocrysts. This crust may have a

population of detrital zircon that is slightly more radiogenic than those in the Girrakool Beds at 310–320 Ma. Jeon et al. (2014) examined zircon separated from the Hillgrove Monzogranite and showed that the $\delta^{18}O_{zrn}$ of inherited grains is 4.9–7.9, whereas primary magmatic zircon grains have $\delta^{18}O_{zrn}$ of 8.7–11.4. The oldest primary magmatic zircon in the sample of Hillgrove Monzogranite examined by Jeon et al. (2014) is c. 308 Ma, whereas the youngest xenocryst is c. 310 Ma. These two grains are only distinguishable on the basis of $\delta^{18}O_{zrn}$, as their ages are within error of each other. This separation in $\delta^{18}O_{zrn}$ should resolve the issue of whether zircon grains dated between 300 Ma and 310 Ma are xenocrysts or not in future studies of the Hillgrove Supersuite, leading to a much better rationale for selecting which grains to include in weighted average age calculations.

Hafnium Isotopes in the Hillgrove Supersuite

The Hf isotope data presented here ($^{176}Hf/^{177}Hf$ initial typically 0.282600–0.283015) concurs, in part, with published data. For example, three samples of Hillgrove Supersuite examined by Kemp et al. (2009) have zircon with $^{176}Hf/^{177}Hf$ initial = 0.282651–0.282781 (Tia Granodiorite, Dundurabbin Granodiorite and Wollomombi Granodiorite), two samples of Hillgrove Supersuite examined by Shaw et al. (2011) have zircon with $^{176}Hf/^{177}Hf$ initial = 0.282621–0.282944 (Kilburnie Monzogranite and Abroi Granodiorite), and a sample of the Hillgrove Monzogranite contains zircon with $^{176}Hf/^{177}Hf$ initial = 0.282611–0.282786 (Jeon et al., 2014). The two younger (c. 292 Ma) plutons of Hillgrove Supersuite examined here (W0514 and W0603) have more

radiogenic (higher $^{176}Hf/^{177}Hf$ initial) zircon on average compared to the older (c. 300 Ma) plutons (dark grey arrow on Fig. 8a). The evolution with time to more radiogenic compositions is consistent with increasing mantle component in granite production. This is expected in a rift environment (Leitch, 1988; Jenkins et al., 2002; Glen, 2005, 2013; Collins and Richards 2008; Kemp et al. 2009; Cawood et al. 2011) as mantle-derived melts need only migrate through thinner continental crust, which is progressively getting hotter, such that mantle-derived melts are less likely to freeze at depth. In addition, early (c. 300 Ma) melting of metasedimentary crust will deplete the fertility of the deep crust during subsequent (c. 292 Ma) melting, thereby reducing the volume of S-type granite produced. At the same time, adiabatic decompression and partial melting of the mantle is likely to increase with time as the crust progressively thins, increasing the proportion of M-type (mantle-derived) melt produced. The early Permian inception of extensive rift sedimentary basins (Bowen–Gunnedah–Sydney and Barnard) and eruption of juvenile basalts (Werrie, Cranky Corner) through thin crust (Craven, 1987; Flood et al., 1988) indicates an extensional setting during the early Permian (Leitch, 1988; Jenkins et al., 2002; Glen, 2005, 2013; Collins and Richards 2008; Kemp et al. 2009; Cawood et al. 2011). The pattern of zircon having increasingly radiogenic Hf isotope character with time is consistent with the well-established rift tectonic setting.

The low $^{176}Hf/^{177}Hf$ initial character for zircon in the pegmatite sample (Fig. 8; W0538) is different to the Hillgrove Supersuite samples examined. It strongly suggests the pegmatite is unrelated to the examined plutons in the

area. Farrell (1992) identified two mica (i.e. inferred to have primary muscovite and biotite) granites within his mapping of the Abroi Granodiorite in the Wongwibinda Metamorphic Complex. A comparison of the $^{176}Hf/^{177}Hf$ initial character for zircon in two mica granite samples with the pegmatite data presented here may resolve this issue. The pegmatite data do overlap the $^{176}Hf/^{177}Hf$ initial character for zircon rims in the migmatite sample W0501a (Chapter 4), suggesting the pegmatite sample may be related to local partial melting. The broad spread in $^{176}Hf/^{177}Hf$ initial for the pegmatite sample implies incomplete mixing of multiple sources of Hf.

OVERVIEW AND CONCLUSIONS

Collins and Richards (2008) suggest that the association between some S-type granites, HTLP metamorphism and turbidite sequences, has a common tectonic setting, particularly in circum Pacific orogens. The spatial relationship between the S-type plutons (Abroi Granodiorite and Tobermory and Rockvale monzogranites) and HTLP metamorphism of the Girrakool Beds turbidite sequence is an example of this relationship. This study has shown that crust similar to the Girrakool Beds is the likely source of xenocrystic zircon in the Hillgrove Supersuite local to the Wongwibinda Metamorphic Complex. Plutonism in the Wongwibinda Metamorphic Complex involves two pulses: c. 300 Ma and c. 292 Ma. The $^{176}Hf/^{177}Hf$ initial character for zircon becomes more radiogenic with time, consistent with progression in a rift tectonic setting.

References

Aitchison, J.C., Blake, M.C., Flood, P.G. and Murchey, B., 1988. New and revised lithostratigraphic units and terranes from the southwestern New England Orogen. Geological Survey of NSW Quarterly Notes, **72**, 10–16.

Belousova, E. A., Griffin, W .L., O'Reilly, S. Y. and Fisher, N. I., 2002. Igneous zircon: trace element composition as an indicator of source rock type. Contributions to Mineralogy and Petrology, **143**, 216–622.

Binns, R.A. and Richards, J.R., 1965. Regional metamorphic rocks of Permian age from the New England district of New South Wales. Australian Journal of Science, **27**, 233.

Binns, R.A., 1966. Granitic intrusions and regional metamorphic rocks of Permian age from the Wongwibinda district, northeastern New South Wales. Journal of the Proceedings, Royal Society of N.S.W., **99**, 5–36.

Binns, R. A. and Department of Geology staff, 1967. Geological map of New England-New England Tableland-Southern part, with explanatory text, scale 1:250,000, Univ. of New England, Armidale, New South Wales, Australia.

Bomparola, R. M., Ghezzo, C., Belousova, E., Griffin, W. L. and O'Reilly, S. Y., 2007. Resetting of the U–Pb Zircon System in Cambro-Ordovician intrusives of the deep freeze range, Northern Victoria Land, Antarctica. Journal of Petrology, **48**, 327–364.

Cawood, P. A., Leitch, E. C., Merle, R. E. and Nemchin, A. A., 2011. Orogenesis without collision: Stabilizing the Terra Australis

accretionary orogen, eastern Australia. Geological Society of America Bulletin, **123**, 2240–2255.

Chappell, B. and White, A., 1974. Two contrasting granite types. Pacific Geology, **8**, 173–174.

Clemens, J. D., 2003. S-type granitic magmas—petrogenetic issues, models and evidence. Earth-Science Reviews, **61**, 1–18.

Collins, W. J., 2002a. Hot orogens, tectonic switching, and creation of continental crust. Geology, **30**, 535–538.

Collins, W. J., 2002b. Nature of extensional accretionary orogens. Tectonics, **21**, 6–1.

Collins, W. J. and Richards, S. W., 2008. Geodynamic significance of S-type granites in circum-Pacific orogens. Geology, **36**, 559–562.

Corfu, F., Hanchar, J. M., Hoskin, P. W. and Kinny, P., 2003. Atlas of zircon textures. Reviews in Mineralogy and Geochemistry, **53**, 469–500.

Craven S. J., 1987. REE and $^{87}Sr/^{86}Sr$ geochemistry of the Warrigundi Volcanic Centre, Werris Ck, NSW. M.Sc. thesis, Macquarie University, Sydney (unpubl.).

Farrell, T. R., 1992. Deformation, Metamorphism and Migmatite Genesis in the Wongwibinda Metamorphic Complex. Unpublished PhD thesis, University of Newcastle, New South Wales, Australia.

Flood, R. H., 1971. A study of part of the New England Batholith, New South Wales, Unpublished PhD thesis, Univ. of New England, Armidale, New South Wales, Australia.

Flood, R. H. and Shaw, S. E., 1975. A cordierite-bearing granite suite from the New England Batholith, NSW, Australia. Contributions to Mineralogy and Petrology, **52**, 157–164.

Flood, R. H. and Shaw, S. E., 1977. Two “S-type” granite suites with low initial 87Sr/86Sr ratios from the New England Batholith, Australia. Contributions to Mineralogy and Petrology, **61**, 163–173.

Flood R. H., Craven S. J., Elmes D. C., Preston R. J. and Shaw S. E., 1988. The Warrigundi Igneous Complex: volcanic centres for the Werri Basalt, NSW. In: Kleeman J. D. ed. New England Orogen: Tectonics and Metallogenesis, pp. 166–171. University of New England, Armidale.

Glen, R. A., 2005. The Tasmanides of eastern Australia. In: Terrane Processes at the margins of Gondwana (eds Vaughan, A. P. M., Leat, P. T. and Pankhurst, R. J.), **246**, pp. 23–99. Special Publication. Geological Society, London.

Glen, R. A., 2013. Refining accretionary orogen models for the Tasmanides of eastern Australia. Australian Journal of Earth Sciences, **60**, 315–370.

Halpin, J. A., Daczko, N. R., Milan, L. A. and Clarke, G. L., 2012. Decoding near-concordant U–Pb zircon ages spanning several hundred million years: recrystallisation, metamictisation or diffusion? Contributions to Mineralogy and Petrology, **163**, 67–85.

Halpin, J. A., Daczko, N. R., Clarke, G. L. and Murray, K. R., 2013. Basin analysis in polymetamorphic terranes: An example from east Antarctica. Precambrian Research, **231**, 78–97.

Hensel, H. D., 1982. The mineralogy, petrology and geochronology of granitoids and associated intrusives from the southern portion of the New England Batholith. Unpublished PhD thesis, University of New England, New South Wales, Australia.

Jenkins, R. B., Landenberger, B. and Collins, W. J., 2002. Late Palaeozoic retreating and advancing subduction boundary in the New England Fold Belt. Australian Journal of Earth Sciences, **49**, 476–489.

Jeon, H., Williams, I. S. and Bennett, V. C., 2014. Uncoupled O and Hf isotopic systems in zircon from the contrasting granite suites of the New England Orogen, eastern Australia: Implications for studies of Phanerozoic magma genesis. Geochimica et Cosmochimica Acta, **146**, 132–149.

Kemp, A. I. S., Hawkesworth, C. J., Collins, W. J., Gray, C. M., Blevin, P. L. and EIMF, 2009. Isotopic evidence for rapid continental growth in an extensional accretionary orogen: The Tasmanides, eastern Australia. Earth and Planetary Science Letters, **284**, 455–466.

Kent, A.J.R., 1994. Geochronology and geochemistry of Palaeozoic intrusive rocks in the Rockvale region, Southern New England Orogen, New South Wales. Australian Journal of Earth Sciences, **41**, 365–379.

Kinny, P. D., Compston, W. and Williams, I. S., 1991. A reconnaissance ion-probe study of hafnium isotopes in zircons. Geochimica et Cosmochimica Acta, **55**, 849–859.

Kinny, P. D. and Maas, R., 2003. Lu–Hf and Sm–Nd isotope systems in zircon. Reviews in Mineralogy and Geochemistry, **53**, 327–341.

Kleeman, J. D., 1975. Geological age measurements using fission tracks, A.A.E.C. Journal, Atomic Energy in Australia, **18**, 3–8.

Korsch, R. J., 1977. A framework for the Palaeozoic geology of the southern part of the New England Geosyncline. Journal of the Geological Society of Australia, **25**, 339–355.

Korsch, R. J., 1978. Stratigraphic and igneous units in the Rockvale–Coffs Harbour region, New South Wales. Journal and Proceedings, Royal Society of New South Wales, **111**, 13–17

Korsch, R. J., 1981. Some tectonic implications of sandstone petrofacies in the Coffs Harbour Association, New England Orogen, New South Wales. Journal of the Geological Society of Australia, **28**, 261–269.

Korsch, R. J., Harrington, H. J., Murray, C. G., Fergusson, C. L., & Flood, P. G. (1990). Tectonics of the New England Orogen. *The Eromanga–Brisbane Geoscience Transect: a guide to basin development across Phanerozoic Australia in southern Queensland*, 35-52.

Landenberger, B., Farrell, T. R., Offler, R., Collins, W. J. and Whitford, D. J., 1995. Tectonic implications of Rb-Sr biotite ages for the Hillgrove Plutonic Suite, New England Fold Belt, N.S.W. Australia. Precambrian Research, **71**, 251–263.

Landenberger, B., McKibbin, S. and Collins, B., 2010. Genesis and age of magmas of the Hillgrove Batholith, southern New England Orogen. New England Orogen 2010, 200–206.

Leitch, E.C., 1988. The Barnard Basin and the Early Permian development of the southern part of the New England fold belt, in Kleeman, J.D., ed., New England Orogen; Tectonics and Metallogenesis: Armidale,

Department of Geology and Geophysics, University of New England, p. 61–67.

Leitch, E., Cawood, P., Merle, R. and Nemchin, A., 2010. A chapter in the orogenic history of an accretionary orogen: the Early Permian transition in the southern New England Fold Belt. New England Orogen 2010, 207–212.

Lenting, C., Geisler, T., Gerdes, A., Kooijman, E., Scherer, E. E. and Zeh, A., 2010. The behavior of the Hf isotope system in radiation-damaged zircon during experimental hydrothermal alteration. American Mineralogist, **95**, 1343–1348.

O'Neil, J. R., Shaw, S.E. and Flood, R.H., 1977. Oxygen and hydrogen isotope compositions as indicators of granite genesis in the New England Batholith, Australia, Contributions to Mineralogy and Petrology, **62**, 313–328.

Patchett, P. J., 1983. Importance of the Lu-Hf isotopic system in studies of planetary chronology and chemical evolution. Geochimica et Cosmochimica Acta, **47**, 81–91.

Rosenbaum, G., Li, P. and Rubatto, D., 2012. The contorted New England Orogen (eastern Australia): New evidence from U-Pb geochronology of early Permian granitoids. Tectonics, **31**, 1–14.

Shaw, S. E., Flood, R. H. and Pearson, N. J., 2011. The New England batholith of eastern Australia: evidence of silicic magma mixing from zircon $^{176}Hf/^{177}Hf$ ratios. Lithos, **126**, 115–126.

Stephenson, N. C. N. and Hensel, H. D., 1982. Amphibolites and related rocks from the Wongwibinda metamorphic complex, northern NSW, Australia. Lithos, **15**, 59–75.

Voisey, A. H., 1959. Tectonic evolution of northeastern New South Wales, Australia. Journal of the Proceedings of the Royal Society of NSW, **92**, 191–203.

Whitehouse, M. J. and Kemp, A. I. S., 2010. On the difficulty of assigning crustal residence, magmatic protolith and metamorphic ages to Lewisian granulites: constraints from combined in situ U–Pb and Lu–Hf isotopes. Geological Society, London, Special Publications, **335**, 81–101.

Synthesis

The Evolution of the Wongwibinda High-T–Low-P Metamorphic Complex, New England Orogen, NSW, Australia

Synthesis

The Evolution of the Wongwibinda High-Temperature Low-Pressure Metamorphic Complex, New England Orogen, NSW, Australia.

There are two broad topics examined in this thesis:

1) Metamorphism - Geological evolution of the Wongwibinda Metamorphic Complex;
2) The Zircon U-Pb-Hf and trace element characteristics of the rocks.

The geological evolution of the complex begins with deposition of the Girrakool Beds, exposed and preserved unmetamorphosed west of the Wongwibinda Metamorphic Complex. This unit is a thick sequence of deep marine turbidites that were deposited as trench-fill (Korsch, 1977; 1990) and accreted to the Australian plate to become part of the accretionary wedge. The metasedimentary rocks of the WMC share similar U-Pb-Hf characteristics with the unmetamorphosed turbidites (Girrikool Beds) exposed to the west of the complex, which are thus interpreted to be their precursor. The detrital zircons are dominated by Early (79%) and Late (8%) Carboniferous grains. The two youngest grains (c. 309 Ma; Chapter 4) are used to infer a Late Carboniferous maximum deposition age, at least for this part of the sedimentary pile. Minor components include Late Devonian (5%), Cambrian (<1%), Proterozoic (6%) and Archean (<1%) detrital zircon grains.

Volcanic lithic grains and bipyramidal quartz identified in sandstone petrography of the Girrakool Beds suggest the mainly quartz-poor, lithic to

feldspathic sandstone rocks were derived from a volcanic arc terrane (Binns, 1966; Korsch, 1978, 1984). The dominance (92%) of Late Devonian to Carboniferous detrital zircon grains in the Girrakool Beds, and metamorphosed versions thereof, is consistent with the provenance of the Girrakool Beds mostly involving the western magmatic arc of the New England Orogen, called the Keepit Arc by Cawood et al. (2011). Older arc crust indicates an intra-oceanic island arc setting from the Silurian to Middle Devonian (Offler and Gamble, 2002). However, $^{176}Hf/^{177}Hf$ initial data for these detrital zircon grains exhibit a trend from more radiogenic Late Devonian grains to less radiogenic Late Carboniferous grains, suggesting that the western (Keepit) magmatic arc was largely stationary or slightly advancing relative to the Australian plate, and the arc increasingly reworked crust throughout its history. A relatively stationary arc is consistent with the mapped extent of Late Devonian to Late Carboniferous volcanic and plutonic rocks (e.g. Roberts et al., 2004).

Less than a quarter of the Carboniferous detrital zircon grains analysed from the Girrakool Beds are >340 Ma, approximately two-thirds are 320–340 Ma, and just over 10% are <320 Ma (Chapter 4). The limited number of detrital zircon grains <320 Ma are used to infer that volcanic activity in the Keepit Arc abated at c. 320 Ma, consistent with it eventually shutting off at c. 305 Ma (Cawood et al., 2011). The geodynamic setting changed during this time from a long-lived stationary magmatic arc (Late Devonian to Carboniferous Keepit Arc) to a retreating plate boundary, likely driven by slab rollback (e.g. Jenkins et al., 2002; Glen, 2005, 2013; Cawood et al., 2011).

This change in geodynamic setting is the key factor in forming the Wongwibinda high-T–low-P metamorphic rocks.

The Late Carboniferous to Early Permian slab rollback caused migration of the subduction trench eastward and with it the locus of slab flux melting in the mantle wedge. Two outcomes are inferred to accompany slab rollback: (i) new hot mantle asthenosphere moves into the mantle wedge, and (ii) the locus of slab flux melting migrates, in this case eastward to lie beneath the recently accreted sedimentary rocks of the accretionary complex. The interaction of hot asthenosphere with and the intrusion of slab flux melt into the base of the accretionary complex starts the first metamorphic cycle of the young sedimentary rocks. In chapter 2, it is inferred that these first cycle metamorphic fluids are channeled up structures such as the Wongwibinda and Glen Mohr shear zones to facilitate the rapid and local advection of heat to the shallow crust. This inference is based on (i) the spatially restricted nature of amphibolite facies rocks in the Wongwibinda Metamorphic Complex that have locally steep (>50°C km^{-1} and possibly as high as 155°C km^{-1}) metamorphic field gradients as determined by Thermocalc pseudosection modelling (Chapters 1 and 2), (ii) spatial association of shear zones and quartzite units and an increased abundance of quartz veins above the cordierite isograd (Chapter 2).

A 3 km long west-east traverse (Chapter 1) more closely constrains the metamorphic field gradient noted by earlier researchers (Binns, 1966; Farrell, 1992). The lowest grade greenschist facies, chlorite bearing zone, was calculated to form at P < 3 kbar and T = 350–430°C; two samples from the

central biotite zone formed at P < 3 kbar and T = 510–550°C and P < 3.5 kbar and T = 510–650°C, and two samples of the migmatite zone formed at P < 3.3 kbar and T = 630–660°C and P < 3.3 kbar and T = 615–660°C (Chapter 1). Cordierite-bearing rocks from elsewhere in the complex formed at P ≤ 2 kbar at T = 570–620°C, to ≤ 3.5 kbar at 600–690°C (Chapter 2). Monazite chemical dating indicates that metamorphism in the highest-grade rocks (296.8 ± 1.5 Ma, Chapter 1) shortly predates final recrystallisation in the Glen Mohr shear zone (291.5 ± 1.8 Ma, Chapter 2) and the intrusion of the youngest parts of the Abroi Granodiorite (290.5 ± 1.6 Ma, Chapter 1). The geochronology data indicate that high-T–low-P metamorphism in the Wongwibinda Metamorphic Complex began approximately 12 million years after deposition of the sedimentary rocks and is cut by post-tectonic granite 6-7 million years later, consistent with the transient nature of hydrothermal processes.

Chapter 1 demonstrated the highest-grade metamorphism (migmatisation at 296.8±1.5 Ma) shortly predated intrusion of part of the Abroi Granodiorite (290.5±1.6 Ma). However, subsequent U-Pb geochronology (Chapter 5) of four other samples of the Hillgrove Supersuite indicates that plutonism in the complex involved two pulses: c. 300 Ma and c. 292 Ma, showing that plutonism partially overlaps the age of high-T–low-P metamorphism (296.8±1.5 Ma). Therefore, it is likely that the mechanisms of heat transfer that drove the metamorphism of the complex were threefold: (i) *conductive heating* caused by shallowing of a thermal boundary layer such as the mantle during continental extension, (ii) *hydrothermal advection of heat* with hot water sourced from the first metamorphic cycle in the deeper parts of

the accretionary complex, and (iii) *advective transfer of heat by magma* as metamorphic conditions in the deep crust surpassed the solidus and partially melted the metasedimentary rocks to produce S-type granite magma. The spatial association of high-grade metamorphic rocks and the younger S-type plutons with the Wongwibinda and Glen Mohr shear zones suggests that the migration of hot metamorphic water in the structurally controlled conduits was followed by granite magma as metamorphism of the deep crust progressed. The crust beneath the Wongwibinda Metamorphic Complex is envisaged to share features with the Hidaka metamorphic belt in Japan, where granulite facies rocks formed due to enhanced heat flux attending subduction zone retreat and the addition of juvenile crust (e.g. Komatsu et al., 1989; Kemp et al., 2007).

The Hf isotopic analysis of plutonic zircon grains (Chapter 5) defines a trend toward more radiogenic values with younging of the Hillgrove Supersuite, consistent with an increasing mantle component contributing to granite production. Xenocrystic zircon grains share U-Pb-Hf isotopic characteristics with detrital grains analysed from the Girrakool Beds, indicating the xenocrysts are likely sourced from them.

Metamorphism results from conductive and advective heat transfer from the Earths interior (e.g. Sandiford and Hand, 1998; Sandiford et al., 1998). This thesis has shown that steep metamorphic field gradients are consistent with advection of heat. Advection of hot metamorphic water and granite magma is inferred to progressively heat the WMC to amphibolite facies conditions, just above the solidus. Well-studied examples of high-T–

low-P metamorphism in Australia include Mt Stafford in Central Australia, where the ancient tectonic setting is less well known (e.g. Warren, 1983; Stewart et al., 1984, Blake & Page, 1988; Clarke et al., 1990; Vernon et al., 1990; Compston, 1995; Greenfield et al., 1996; Vry et al., 1996; Rubatto et al., 2006; Wang et al., 2014) and the Cooma Complex and other examples in the Lachlan Fold Belt in New South Wales where the tectonic setting is similar to that of the Wongwibinda Metamorphic Complex (e.g. Joplin 1942; Vallance 1969; Morand 1990; Vernon & Johnson 2000; Vernon et al. 2001, 2003; Richards & Collins 2002). These regions share the following characteristics that here are outlined as the key ingredients in forming a Wongwibinda-like high-T–low-P metamorphic complex:

(1) A protolith of young sedimentary rocks that have not previously been metamorphosed;

(2) A spatial association among shear zones, S-type granite plutons and the highest-grade metasedimentary rocks;

(3) A short-lived metamorphic history; and

(4) An extensional geodynamic setting.

Two modern analogues involving recent arc settings that have had short-lived pulses of S-type magmatism are SW Japan and W-NW Sulawesi. Similar to the southern NEO, I and S-type plutons form linear belts. The S-type magma is considered to be formed during forearc thinning due to extension which in turn is the result of subduction rollback. HTLP metamorphism is observed in the Sulawesi metasedimentary rocks but is complicated as it overprints higher pressure metamorphism. In SW Japan the

	New England Orogen	SW Japan	W-NW Sulawesi
Age	**c. 297-288 (280) I-type c. >305 Ma S-type Permian**	**c. 17-12 Ma S-type c. 16-12 Ma I-type Neogene-Miocene**	**c.5-2.5 Ma (S-type) c. 8.5-4 Ma (I-type) Pliocene-Pleistocene**
Size	**c. 2000 km**	**c. 1000 km**	**c. 500km**
Forearc Magmatism			
S-type	**yes**	**yes**	**yes**
I-type	**yes**	**yes**	**yes**
other	**no**	**yes**	**yes**
Forearc volcanism			
S-type	**?**	**yes**	**?**
I-type	**?**	**yes**	**?**
other	**no**	**yes**	**?**
Forearc sedimentary rocks (protolith)	**Girrikool Beds**	**?**	**Tinombo & Latimojong Formations**
Turbidites - psammites	**yes**	**yes**	**yes**
Turbidites - pelites	**yes**	**yes**	**yes**
other	**no**	**yes**	**yes**
Slab Rollback	**Interp**	**Interp**	**Interp**
Forearc extension	**Interp.**	**yes**	**yes?**
Backarc	**no**	**yes**	**no?**
Distance from coast			
S-type	**?**	**20-50 km**	**?**
I-type	**?**	**80-100 km**	**?**
Separate belts	**yes**	**yes**	**yes**
HTLP Metamorphism	**yes (Buchan Style)**	**?**	**yes (Buchan Style)**
Formation	**Wongwabinda Metamorphic Complex**	**?**	**Palu Metamorphic Complex**
migmatite	**yes**	**yes**	**yes**
amphibolite facies	**yes**	**yes**	**yes**
granulite facies	**no**	**no**	**yes**

Table 1: Comparison of the Wongwibinda Metamorphic Complex with recent HTLP belts.

setting is similar to that inferred for the NEO, but is complicated by the subduction of a mid-ocean ridge spreading centre producing complex arc magmatism (Kimura, et al. 2005). W-NW Sulawesi (Hennig, 2015) is a very complex tectonic regime from a very active region. A comparison of the three regions is presented in Table 1.

This work has answered some questions raised by Farrell (1992) but, has in turn, raised even more. In particular the model presented in Chapter 2 of heat transfer by fluid advection needs to be more convincingly demonstrated by considering the fluid-rock interaction record of the migrating fluid. Future directions should include; (1) mass balance calculations, (2) fluid inclusion studies in metamorphic porphyroblasts including muscovite, K-feldspar, cordierite and garnet, (3) isotopic studies including Sr, Nd, Hf and O, and (4) detailed examination of veins, metasomatic rocks and the conduits.

References

Binns, R. A., 1966. Granitic intrusions and regional metamorphic rocks of Permian age from the Wongwibinda district, northeastern New South Wales. Journal of the Proceedings, Royal Society of N.S.W., **99**, 5–36.

Blake, D. H. and Page, R. W., 1988. The Proterozoic Davenport province, central Australia: regional geology and geochronology. Precambrian Research, **40/41**, 329–340.

Cawood, P. A., Leitch, E. C., Merle, R. E. and Nemchin, A. A., 2011. Orogenesis without collision: Stabilizing the Terra Australis accretionary orogen, eastern Australia. Geological Society of America Bulletin, **123**, 2240–2255.

Clarke, G. L., Collins, W. J. and Vernon, R. H., 1990. Successive overprinting granulite facies metamorphic events in the Anmatjira Range, central Australia. Journal of Metamorphic Geology, **8**, 65–88.

Compston, D. M., 1995. Time constraints on the evolution of the Tennant Creek Block, northern Australia. Precambrian Research, **71**, 107–129.

Farrell, T. R., 1992. Deformation, Metamorphism and Migmatite Genesis in the Wongwibinda Metamorphic Complex. Unpublished PhD thesis, University of Newcastle, Australia.

Glen, R. A., 2005. The Tasmanides of eastern Australia. In: *Terrane Processes at the margins of Gondwana* (eds Vaughan, A. P. M., Leat, P. T. & Pankhurst, R. J.), **246**, pp. 23–99. Special Publication. Geological Society, London.

Glen, R. A., 2013. Refining accretionary orogen models for the Tasmanides of eastern Australia. *Australian Journal of Earth Sciences*, **60**, 315–370.

Greenfield, J. E., Clarke, G. L., Bland, M. and Clark, D. C., 1996. In-situ migmatite and hybrid diatexite at Mt Stafford, central Australia. Journal of Metamorphic Geology, **14**, 413–426.

Jenkins, R. B., Landenberger, B. and Collins, W. J., 2002. Late Palaeozoic retreating and advancing subduction boundary in the New England Fold Belt. Australian Journal of Earth Sciences, **49**, 476–489.

Joplin G. A., 1942. Petrological studies in the Ordovician of New South Wales. I. The Cooma Complex. Proceedings of the Linnaean Society of New South Wales, 67, 156–196.

Kemp, A. I. S., Shimura, T. and Hawkesworth, C. J., 2007. Linking granulites, silicic magmatism, and crustal growth in arcs: Ion microprobe (zircon) U-Pb ages from the Hidaka metamorphic belt, Japan. Geology, **35**, 807–810.

Komatsu, M., Osanai, Y., Toyoshima, T. and Miyashita, S., 1989. Evolution of the Hidaka metamorphic belt, northern Japan. Geological Society, London, Special Publications, **43**, 487–493.

Korsch, R. J., 1977. A framework for the Palaeozoic geology of the southern part of the New England Geosyncline. Journal of the Geological Society of Australia, **25**, 339–355.

Korsch, R. J., 1978. Stratigraphic and igneous units in the Rockvale-Coffs Harbour region, New South Wales. Journal and Proceedings, Royal Society of New South Wales, **111**, 13–17.

Korsch, R. J., 1984. Sandstone compositions from the New England Orogen, eastern Australia: implications for tectonic setting. Journal of Sedimentary Research, **54**, 192–211.

Korsch, R. J., Harrington, H. J., Murray, C. G., Fergusson, C. L., & Flood, P. G. (1990). Tectonics of the New England Orogen. The Eromanga–Brisbane Geoscience Transect: a guide to basin development across Phanerozoic Australia in southern Queensland, 35-52

Morand V. J., 1990. Low-pressure regional metamorphism in the Omeo Metamorphic Complex, Victoria, Australia. Journal of Metamorphic Geology, **8**, 1–12.

Offler, R. and Gamble, J., 2002. Evolution of an intra-oceanic island arc during the Late Silurian to Late Devonian, New England Fold Belt*. Australian Journal of Earth Sciences, **49**, 349-366.

Richards S. W. and Collins W. J., 2002. The Cooma Metamorphic Complex, a low-P high-T (LPHT) regional aureole beneath the Murrumbidgee Batholith. Journal of Metamorphic Geology, **20**, 119–134.

Roberts, J., Offler, R. and Fanning, M., 2004. Upper Carboniferous to Lower Permian volcanic successions of the Carroll–Nandewar region, northern Tamworth Belt, southern New England Orogen, Australia. Boundary sequences of the Werri and Rouchel blocks. Australian Journal of Earth Sciences, **51**, 205-232.

Rubatto, D., Hermann, J. and Buick, I. S., 2006. Temperature and bulk composition control on the growth of monazite and zircon during low-pressure anatexis (Mount Stafford, central Australia). Journal of Petrology, **47**, 1973–1996.

Sandiford, M. and Hand, M., 1998. Australian Proterozoic high-temperature, low-pressure metamorphism in the conductive limit. *In:* Treloar, P. J. and O'Brian, P. J. (eds) What Drives Metamorphism and Metamorphic Reactions? Geological Society, London, Special Publications, **138**, 109–120.

Sandiford, M., Hand, M. and McLaren, S., 1998. High geothermal gradient metamorphism during thermal subsidence. Earth and Planetary Science Letters, **163**, 149–165.

Stewart, A. J., Shaw, R. D. and Black, L. P., 1984. The Arunta Inlier: a complex ensialic mobile belt in central Australia. Part 1: stratigraphy, correlations and origin. Australian Journal of Earth Sciences, **31**, 445–455.

Vallance T. G., 1969. Plutonic and metamorphic rocks. In: Packham G. H. ed. The geology of New South Wales. Journal of the Geological Society of Australia, **16**, 180–200.

Vernon R. H. and Johnson S. E., 2000. Transition from gneiss to migmatite and the relationship of leucosome to peraluminous granite in the Cooma Complex, SE Australia. In: Jessell M. W. & Urai J. L. eds. Stress, strain and structure. A volume in Honour of W. D. Means. Journal of the Virtual Explorer 2. www.virtualexplorer. com.au/VEjournal/Volume2

Vernon, R. H., Clarke, G. L. and Collins, W. J., 1990. Local, mid-crustal granulite facies metamorphism and melting: an example in the Mount Stafford area, central Australia. In: High Temperature Metamorphism and Crustal Anatexis (eds Ashworth, J.R. & Brown, M.), pp. 272–319. Unwin Hyman, London.

Vernon R. H., Richards S. W. and Collins W. J., 2001. Migmatite-granite relationships: origin of the Cooma Granodiorite magma, Lachlan Fold Belt, Australia. Physics and Chemistry of the Earth (A), **26**, 267–271.

Vernon R. H., Collins W. J. & Richards S. W. 2003. Contrasting magmas in metapelitic and metapsammitic migmatites in the Cooma Complex, Australia. Visual Geosciences, **8**, 45–54.

Vry, J., Compston, W. & Cartwright, I., 1996. SHRIMP II dating of zircons and monazites: reassessing the timing of high-grade metamorphism and fluid flow in the Reynolds Range, northern Arunta Block, Australia. Journal of Metamorphic Geology, **14**, 335–350.

Wang, W. E. I., Dunkley, E., Clarke, G. L., & Daczko, N. R., 2014. The evolution of zircon during low-P partial melting of metapelitic rocks: theoretical predictions and a case study from Mt Stafford, central Australia. Journal of Metamorphic Geology, **32**, 791–808.

Warren, R. G., 1983. Metamorphic and tectonic evolution of granulites, Arunta Block, central Australia. Nature, **305**, 300–303.

Appendices

Appendix 1

The Wongwibinda Complex: A HTLP metamorphic terrain

Stephen J. Craven

ARC Centre of Excellence for Core to Crust Fluid Systems (CCFS) and GEMOC, Macquarie University, Sydney, NSW 2109, Australia

THE WONGWIBINDA COMPLEX: A HTLP METAMORPHIC TERRAIN

S.J. Craven

Affiliation. GEMOC Key Centre, Dept. of Earth & Planetary Sciences, Macquarie University, Sydney, 2109, Australia.

Keywords: HTLP metamorphism, migmatite, metapsammite, metapelite, TerraneChron, U/Pb isotopes, Hf isotopes.

Introduction.

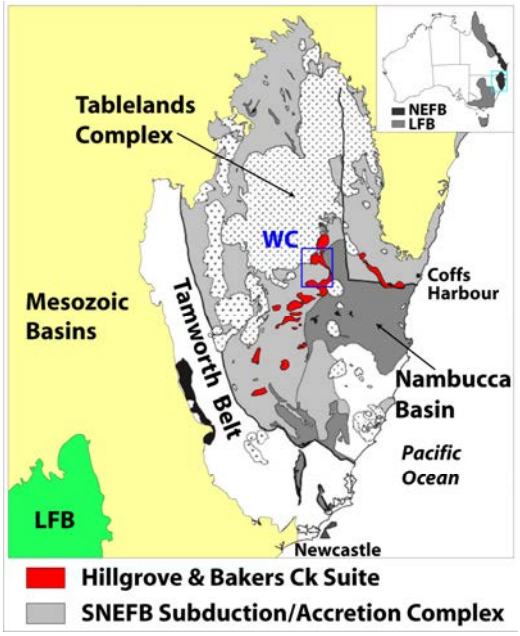

Fig 1. Location of the WC.

The Late Carboniferous Wongwibinda Complex (WC) is a region of high-temperature, low-pressure (HTLP) metamorphic rocks that occur in association with granites of the Hillgrove Plutonic Suite within the Tablelands Complex of the southern New England Fold Belt (Fig. 1; Binns, 1966; Vernon, 1982; Farrell, 1995). The WC exhibits a metamorphic progression from relatively unmetamorphosed sedimentary rocks to high-grade schists with migmatites abutting the Abroi Granodiorite/Gneiss. This project aims to understand the tectonic processes that generate HTLP terrains by studying the evolution of the WC. An interdisciplinary approach is being employed studying the interaction between deformation, metamorphism, partial melting and magmatism.

Methods.

The Wongwibinda Complex is composed mainly of the Girrikool Beds and their metamorphic equivalents, the Ramsbeck Schists and associated migmatites. The Girrikool Beds are a thick (15-20 km) turbidite sequence of interbedded, siliceous, intermediate- to fine-grained psammites and pelites (Fig. 2; Korsch, 1978).

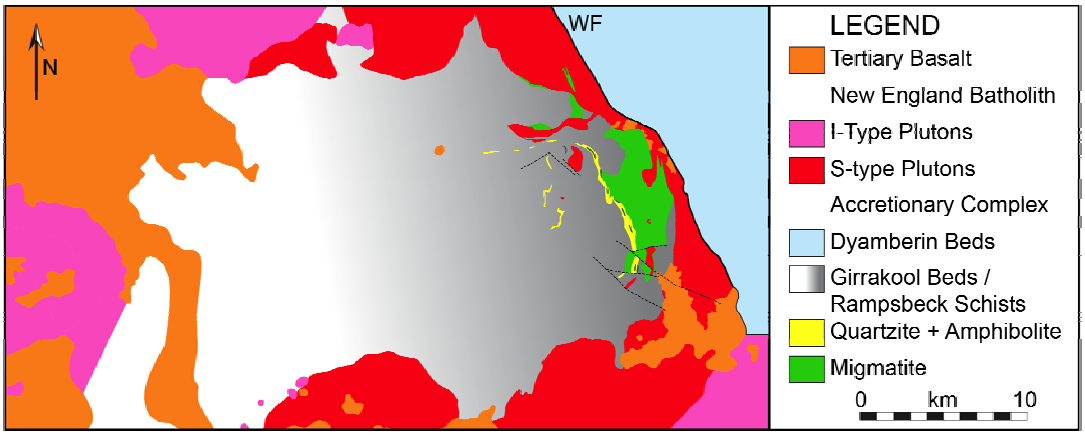

Fig 2. Geology of the WMC.

In order to better confine the age and character of this sequence, U-Pb and Hf-isotopes were measured from zircon separated from rock samples and a TerraneChron

drainage survey from the complex. EMP monazite chemical dating of some of the higher-grade metamorphic equivalents of the Girrikool Beds was also carried out. The monazite age of metamorphism of an unfoliated cordierite hornfels, a cordierite augen schist and a migmatite was determined. Zircon U/Pb ages were also determined for associated S-type granites, the Abroi, Rockvale and Tobermory plutons. Analyses were carried out employing a combination of EMP and LA-ICP-MS.

Results.

The TerraneChron survey identified well-defined populations at ~40 Ma, ~250 Ma, and ~290 Ma (Fig 3a) and a broad population at ~330 ± 20 Ma (Fig 3b). A small number of grains yielding Proterozoic and Archean ages (Fig 3a) are likely to have been inherited by the magmatic/volcanic rocks from which the Girrikool sediments were derived. Detrital zircon grains from a weakly metamorphosed metapsammite (333.7±3.6 Ma) (Fig 3c), an unfoliated metapelitic cordierite hornsfels (330.6±7.5 Ma) (Fig 3c) and a migmatite (325.9±6.4 Ma) (Fig 3e) adjacent to the Abroi (Figs 3g,h) exhibit U-Pb age distributions similar to the TerraneChron alluvial samples and suggest deposition of the sedimentary package by 320 Ma. A second migmatite sample yields a younger age distribution (306.9±8.6 Ma) (Fig 3f).

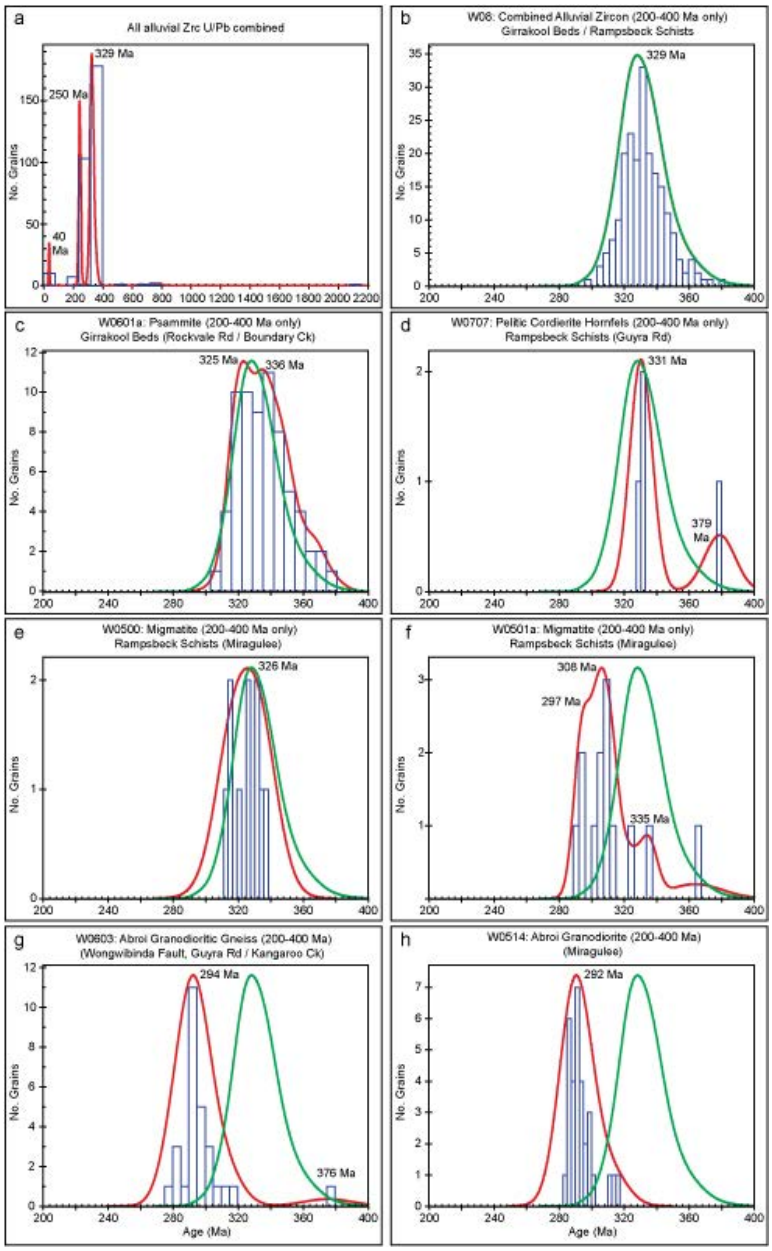

EMP monazite chemical dating was completed on unfoliated cordierite hornfels (311±8.4 Ma), cordierite augen schists (292±2.8 Ma) and migmatites (297±4.3 Ma). Two

zircon concentrates from strongly foliated/gneissic and relatively unfoliated samples of the Abroi Granodiorite/Gneiss returned U-Pb ages within error: 291.2 ± 2.3 Ma and 293.6 ± 3.5 Ma respectively. Each sample has few inherited grains. Zircon grains show no evidence of metamorphic effects such as overgrowths of new zircon or dissolution of igneous zircon. U-Pb zircon ages were also determined for the Rockvale (296.4 ± 3.2 Ma) and Tobermory (299.5 ± 2.7 Ma) adamellites.

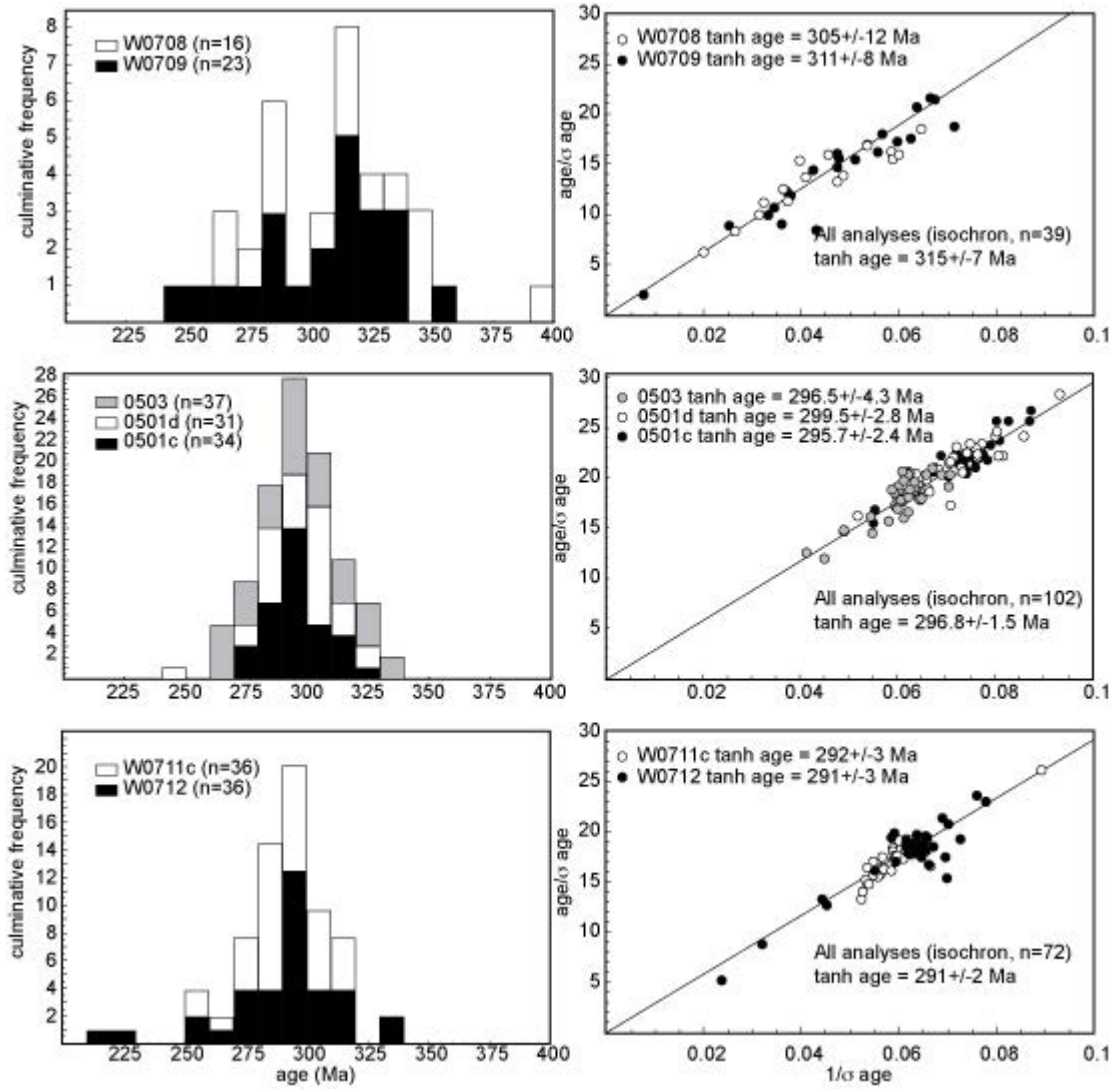

Field observations and mapping around three of the Hillgrove Suite plutons in the WC show that high-grade metamorphic rocks are limited to being located adjacent to the central portion of the Abroi Granodiorite/Gneiss and everywhere else, the contact aureoles are biotite grade at most (see also Leitch, 1978).

Discussion.

The TerraneChron survey identified well-defined populations at ~40 Ma, ~250 Ma, and ~290 Ma and a broad population at ~330 ± 20 Ma. Respectively, the first three populations reflect known ages of Tertiary Basalts, I-type plutons, and S-type plutons. The broad peak at ~310–350 Ma is interpreted as provenance for the sedimentary rocks being an Early to Late Carboniferous volcanic arc. The younger age population identified in one migmatite sample is interpreted as reflecting Pb disturbance of the detrital grains during metamorphism, on the basis of a spread of ages from ~360 Ma down to ~290 Ma and much of the data for that sample being > 10% discordant.

The metamorphic ages of the regional aureole range from ~320-290 Ma. The youngest metamorphic ages overlap the crystallisation age of the granites at 300-290 Ma. However, field relationships show that the highest-grade rocks are located next to the

youngest pluton (Abroi) and the older plutons (Rockvale and Tobermory) have very minor thermal perturbations adjacent to them. These data and observations suggest that granite magmatism was not the primary heat source for metamorphism.

The Hf data for the granite samples indicate a mix of juvenile and crustal components with the juvenile component increasing with time and an average Hf model age of 1.8 Ga. The Hf data from the alluvial detrital zircons also indicates a mix with the juvenile component decreasing with time (Fig 5).

The disparity in age data between emplacement of the Abroi at ~293 Ma and early metamorphism of the metasediments at ~311 Ma suggests that metamorphism largely pre-dates the emplacement of the Abroi Granodiorite/Gneiss by at least a few million years and possibly up to 15 million years.

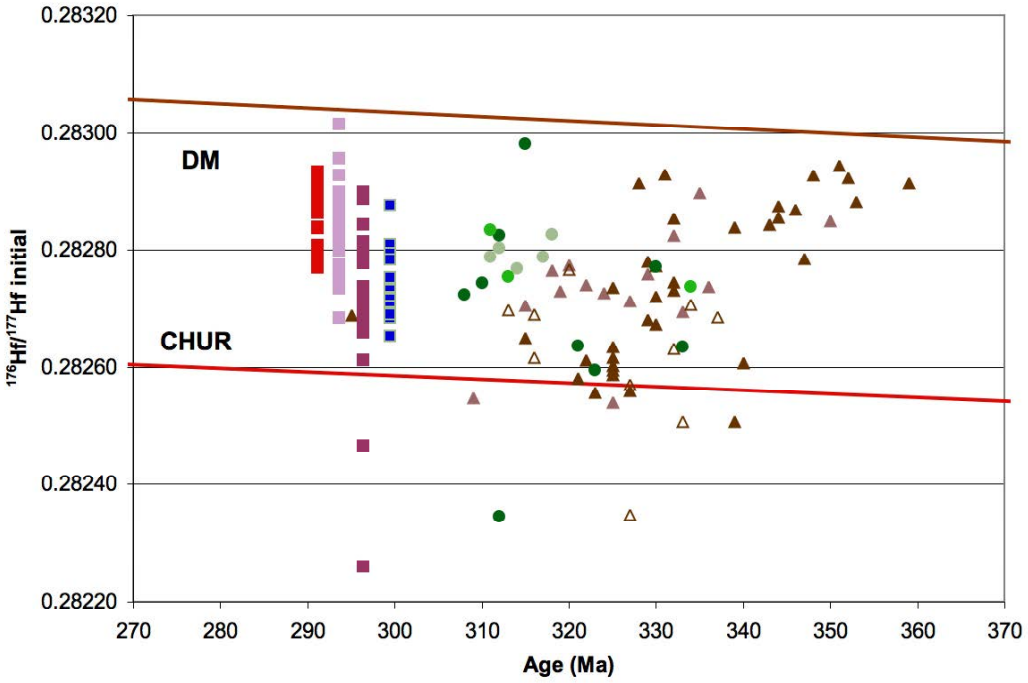

Fig 5. Initial hafnium.

Conclusions.

New detrital zircon data presented here has identified a broad 310-350 Ma age population in the Girrikool Beds, with very few older components. The geographical location of these rocks east of the Early to Late Carboniferous volcanic arc (western edge of the Tamworth Belt; Jenkins et al., 2002) and the age distribution of the detrital zircon are consistent with the sediment provenance being almost exclusively derived from the arc.

Field mapping shows there is no relationship between the location of the highest-grade metamorphic rocks and granite plutons, with the exception of part of the Abroi Granodiorite/Gneiss being in contact with migmatites. New monazite geochronology indicates that metamorphism in the highest-grade rocks likely shortly predates the intrusion of the adjacent Abroi Granodiorite/Gneiss. These relationships require a heat source other than advection of heat by the granites to produce the metamorphism and suggest that both the metamorphism and S-type granites are products of a thermal perturbation associated with a rift tectonic setting.

The distribution of Hf isotopes is supportive of a Late Palaeozoic advancing retreating subduction model for the New England Fold belt. The sediments of the Girrikool Beds reflect a weakly increasing crustal component in the Carboniferous volcanic arc with time, while the S-type granites of the Hillgrove Suite manifest a weakly increasing juvenile (mantle or young mafic underplate) component with time, reflecting respectively, an advancing, compressional environment and a retreating, crustal thinning, environment.

These data will be integrated with structural and metamorphic data to compile a complete temporal and spatial history of the Complex. The further research planned for the Wongwibinda Complex will provide important information about the New England Fold Belt,

the geological evolution of the Australian Plate and contribute to wider geodynamic interpretations.

References.

Binns, R.A., 1966. Granitic intrusions and regional metamorphic rocks of Permian age from the Wongwibinda district, northeastern New South Wales. *Journal of the Proceedings of the Royal Society of N.S.W* **99**: 5-36.

Farrell, T.R., 1992. Deformation, Metamorphism and Migmatite Genesis in the Wongwibinda Metamorphic Complex. Ph.D. Thesis, Department of Geology, University of Newcastle, Newcastle, N.S.W. (unpubl.).

Jenkins, R.B., Landenberger, B. and Collins, W.J., 2002. Late Palaeozoic retreating and advancing subduction boundary in the New England Fold Belt. *Australian Journal of Earth Sciences* **49**, 476 - 489.

Landenberger, B., Farrell, T.R., Offler, R., Collins, W.J. and Whitford, D.J., 1995. Tectonic implications of Rb-Sr biotite ages for the Hillgrove Plutonic Suite, New England Fold Belt, N.S.W.. Australia. *Precambrian Research* **71**, 251 – 263.

Vernon, R.H., 1982. Isobaric cooling of two regional metamorphic complexes relate to igneous complexes in southern Australia. *Geology* **10**, 76 – 81.

Appendix 2

The enigma of crustal zircons in upper-mantle rocks: Clues from the Tumut ophiolite, southeast Australia

Elena A. Belousova[1], José María González Jiménez[1,2], Ian Graham[3], William L. Griffin[1], Suzanne Y. O'Reilly[1], Norman Pearson[1], Laure Martin[4], Stephen Craven[1], and Cristina Talavera[5]

[1]ARC Centre of Excellence for Core to Crust Fluid Systems (CCFS) and GEMOC, Macquarie University, Sydney, NSW 2109, Australia [2]Department of Geology and Andean Geothermal Center of Excellence, Universidad de Chile, Plaza Ercilla # 803, 8370450
Santiago de Chile, Chile [3]School of Biological, Earth and Environmental Sciences, University of New South Wales, Sydney, NSW 2052, Australia [4]Centre for Microscopy Characterisation and Analysis, The University of Western Australia, Crawley, WA 6009, Australia [5]Department of Imaging and Applied Physics, Curtin University, Perth, WA 6102, Australia

Pages 211-214 of this thesis have been removed as they contain published material under copyright. Removed contents published as:

Elena A. Belousova, José María González Jiménez, Ian Graham, William L. Griffin, Suzanne Y. O'Reilly, Norman Pearson, Laure Martin, Stephen Craven, Cristina Talavera; The enigma of crustal zircons in upper-mantle rocks: Clues from the Tumut ophiolite, southeast Australia. Geology ; 43 (2): 119–122. doi: https://doi.org/10.1130/G36231.1

Appendix 3

The sherds of conquistadors: a petrological study of ceramics from Graciosa Bay and Pamua, Solomon Islands

SARAH J. KELLOWAY[1], MARTIN GIBBS[1], and STEPHEN CRAVEN[2]

[1]University of Sydney, and [2]Macquarie University

Pages 217-223 of this thesis have been removed as they contain published material under copyright. Removed contents published as:

Kelloway, S.J., Gibbs, M. and Craven, S. (2013), The sherds of conquistadors: a petrological study of ceramics from Graciosa Bay and Pamua, Solomon Islands. *Archaeology in Oceania*, 48: 53-59.
doi:10.1002/arco.5003

Appendix 4

Sourcing Olive Jars Using U-Pb Ages of Detrital Zircons: A Study of 16th Century Olive Jars Recovered from the Solomon Islands

Sarah J. Kelloway,[1,*] Stephen Craven,[2] Mark Pecha,[3] William R. Dickinson,[4] Martin Gibbs,[5] Timothy Ferguson,[6] and Michael D. Glascock[7]

[1]Department of Archaeology, University of Sydney, Sydney, Australia
[2]Department of Earth and Planetary Sciences, Macquarie University, Macquarie Park, Australia
[3]Department of Geosciences, University of Arizona, Tucson, Arizona
[4]Department of Geosciences, University of Arizona, Tucson, Arizona
[5]Department of Archaeology, University of Sydney, Sydney, Australia
[6]Department of Anthropology, University of Nevada, Las Vegas, Nevada
[7]Research Reactor Center, University of Missouri, Columbia, Missouri

Research Article

Sourcing Olive Jars Using U-Pb Ages of Detrital Zircons: A Study of 16th Century Olive Jars Recovered from the Solomon Islands

Sarah J. Kelloway,[1,*] Steven Craven,[2] Mark Pecha,[3] William R. Dickinson,[4] Martin Gibbs,[5] Timothy Ferguson,[6] and Michael D. Glascock[7]

[1]Department of Archaeology, University of Sydney, Sydney, Australia
[2]Department of Earth and Planetary Sciences, Macquarie University, Macquarie Park, Australia
[3]Department of Geosciences, University of Arizona, Tucson, Arizona
[4]Department of Geosciences, University of Arizona, Tucson, Arizona
[5]Department of Archaeology, University of Sydney, Sydney, Australia
[6]Department of Anthropology, University of Nevada, Las Vegas, Nevada
[7]Research Reactor Center, University of Missouri, Columbia, Missouri

Correspondence
*Corresponding author; E-mail: skel2534@uni.sydney.edu.au

Received
12 November 2012
Revised
8 January 2013
Accepted
8 June 2013

Scientific editing by Patrick Nunn

Published online in Wiley Online Library (wileyonlinelibrary.com).

doi 10.1002/gea.21462

We present U-Pb ages of zircons extracted from olive jars recovered from two sites associated with Alvaro de Mendaña y Neyra's colonising expedition to the Solomon Islands, *c.* 1595–1596 A.D. The olive jars were previously associated with Panamanian and Peruvian origins based on petrological and geochemical studies. To further define provenance, 143 zircons were extracted from five olive jar sherds, analyzed and dated. The resultant U-Pb ages range from the Archaean to the Cenozoic (2977.2 ± 29.0–3.2 ± 4.0 Ma), but the dominance of Cretaceous and Palaeogene ages (~ 90% of the total age population is between ~ 145 and 23 Ma) supports a Peruvian origin based on comparative geology, with the Coastal Batholith of Peru a prime candidate area of ceramic production. These results are significant for the characterization of 16th Century Peruvian-made pottery and our understanding of its production and trade.

INTRODUCTION

A wide range of techniques have been used to characterize Spanish colonial pottery from both Spain and the Americas, including thermoluminescence analysis, X-ray diffraction, petrology, scanning electron microscopy, laser ablation-inductively coupled-mass spectrometry, and instrumental neutron activation analysis (INAA). The resultant geochemical data in combination with archaeological and historical data typically allows provenance determination. Studies including chemical data resulting from INAA have proved particularly successful, and the technique has become popular for provenance studies, requiring little sample material for analysis and the results contributing to large comparative databases (Fournier & Blackman, 2008; Iñañez et al., 2008; Iñañez et al., 2010; Iñañez & Speakman, 2011; Jamieson & Hancock, 2004; Jamieson et al., 2012; Maggetti, Westley, & Olin, 1984; Olin & Blackman, 1989; Olin, Harbottle, & Sayre, 1978; Olin & Sayre, 1975; Padilla et al., 2005; Rovira et al., 2006; Vaz & Cruxent, 1975). In cases where provenance has not been determined or multiple regions of origin have been identified, other methods must be sought to define or further refine provenance, such as U-Pb dating of detrital zircons.

Zircon U-Pb dating has long been a successfully exploited tool in geochronological studies (Davis, Williams, & Krogh, 2003; Gehrels, 2011; Košler & Sylvester, 2003). The chemical and mechanical properties of zircons allow reliable age determinations using U/Pb isotope ratios (Davis, Williams, & Krogh, 2003; Elburg, 2011) and the age distributions can be used to trace the temper sources involved in pottery production, when used in conjunction with other chemical, petrographic, historical and archaeological data. This method of provenance determination is destructive but can provide significant insights into provenance, and relies on the comparison of age distributions of detrital zircons extracted from ceramics with age-distributions of detrital

Figure 1 Solomon Islands sites associated with Mendaña's second voyage, *c.* 1595–1596 A.D.: Pamua, Makira/San Cristobal and Graciosa Bay, Nendö/Santa Cruz.

zircons from identified source areas. Recently, U-Pb age determinations of zircons extracted from archaeological pottery were used to source ceramics from Roviana Lagoon, New Georgia Group, to Muyuw (Woodlark) Island in the Solomon Sea (Tochilin et al., 2012), and U-Pb dates of zircons from Mayan ceramics were also used to explore likely areas of provenance (Coffey et al., 2012).

In this study, we apply the methodology of U-Pb zircon dating to further determine the provenance of Red Earthenware olive jars (*botijas*) retrieved from two 16th Century colonial Spanish sites in the Solomon Islands (Allen, 1976; Allen & Green, 1972; Green, 1973). Previous research involving petrology and geochemistry (INAA) indicated possible Panamanian or Peruvian origins for these sherds (Bedford et al., 2009; Dickinson & Green, 1973; Kelloway, Gibbs, & Craven, 2013). This paper presents U-Pb ages of zircons extracted from five Red Earthenware sherds that indicate an Andean origin, and some implications for our understanding of production and distribution of 16th Century Peruvian-made pottery.

BACKGROUND

Archaeological research in the Solomon Islands over the last 40 years has yielded two large assemblages associated with Alvaro de Mendaña y Neyra's second expedition to the region, *c.* 1595–1596 A.D. (Allen, 1976; Allen & Green, 1972; Green, 1973). Mendaña's expedition left from Callao, Lima, and was an effort spearheaded from the Viceroyalty of Peru. The associated archaeological assemblages derive from Graciosa Bay (Nendö/Santa Cruz) and Pamua (Makira/San Cristobal) (Figure 1), both investigated archaeologically in the 1970s by Green, Allen, and Kaschko (Allen, 1976; Allen & Green, 1972; Gibbs, 2011; Green, 1973; Kaschko, 1979). Graciosa Bay was identified as the site of Mendaña's failed settlement, whereas Pamua, historically unknown, was proposed by Allen and Green (1972) as evidence of the lost *almiranta* of the fleet, *Santa Isabel*. The artefact assemblages are predominately ceramic and few other material types have been recovered, notably metal nails, a copper *aiglet* and skeletal material (Allen, 1976; Green, 1973).

Recently, archaeological research at Graciosa Bay and Pamua has been renewed, forming part of Gibbs' Australian Research Council funded "Beyond the New World" project (Gibbs, 2011). Investigations have focused on evaluating colonial Spanish-indigenous engagement, and indigenous trade and cultural practices at Pamua. Historical and archaeological research also aimed at placing the ceramic assemblages in their New World contexts, in part by studying the preparatory stages of Mendaña's voyage. This has included historical research on provisioning and geochemical analyses aimed at determining ceramic provenance, which afforded the opportunity to characterize ceramics made in 16th Century Peru and provide some insights into contemporary trade within the Viceroyalty of Peru.

Red Earthenware Olive Jars, and Previous Provenance Studies

Red Earthenware is of particular interest to provenance studies involving the ceramics from Graciosa Bay and Pamua as it constitutes the bulk of the ceramic assemblages.

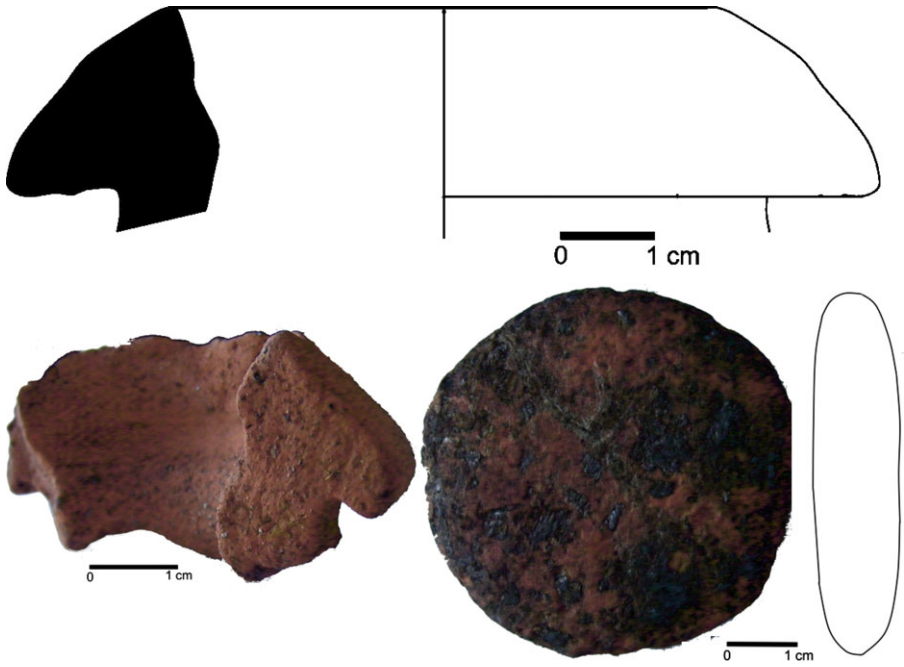

Figure 2 Drawing of Red Earthenware rim recovered from Pamua (ridge), A-3 (top), and rim sherd A007 (bottom left), and lid with profile, A015 (bottom right), recovered from Pamua (flats).

This ceramic type has a red-brick fabric and is associated with the olive jar/*botija* vessel form, specifically Goggin's Type B Middle Style Jar with semitriangular to triangular rim profiles (Figure 2) (Avery, 1997; Goggin, 1960; Marken, 1994). Lids have also been recovered (Figure 2). Olive jars were common storage and transport vessels in the Americas during the 16th Century, having been introduced from Spain, where they developed from Greek and Roman amphorae (Avery, 1997; Deagan, 1987; Lister & Lister, 1987; Marken, 1994; Peacock & Williams, 1986). Petrological analyses in the 1970s initially indicated either a South American or Spanish origin for the Solomon Islands jars (Dickinson & Green, 1973), later refined to a likely South American provenance (Bedford et al., 2009; Kelloway, Gibbs, & Craven, 2013).

Recent geochemical studies (INAA) have suggested either a Panamanian or Peruvian origin for some Red Earthenware sherds. A total of 133 sherds of various types from Graciosa Bay and Pamua were analyzed, including 49 Red Earthenware sherds. Statistical analyses of the chemical data showed that 41 of the 49 Red Earthenware sherds included in the study formed a distinct chemical group along with two other sherds, one of Green-glazed Ware and one Fine Tanware, whereas seven were identified as outliers and one sample clustered with Panamanian ceramics (SPA 002). This main Red Earthenware group was chemically distinct from olive jars made in Spain, but had a chemical signature similar to that of Redware/*contenedores de pasta roja (CPR)* published by Jamieson and Hancock (2004) and Rovira et al. (2006). Table I presents the means and standard deviations of chemical concentrations for various elements for the main Red Earthenware chemical group, as well as the means and standard deviations calculated using chemical data published by Jamieson and Hancock (2004) and Rovira et al. (2006). Comparing data from different laboratories over many years can be difficult, and some elements may not match well due to a variety of reasons including calibration differences, but interlaboratory comparisons are considered theoretically comparable within 20% relative (Jamieson & Hancock, 2004).

Jamieson et al. (2004, 2012) have suggested that Redware/*CPR* was Panamanian-made, having analyzed seven sherds as part of geochemical studies of colonial Ecuadorian ceramics. Rovira et al. (2006) also proposed that Redware/*CPR* sherds were potentially Panamanian but that possible Peruvian origins could not be excluded pending further research, based on a chemical study of Redware/*CPR* sherds (n = 23) and Panamanian ceramics and clay samples. The chemical similarity of Redware/*CPR* and the main Red Earthenware geochemical group thus suggested either a Panamanian or Peruvian source for the latter.

Table I Chemical composition comparisons of the main Red Earthenware geochemical group with Redware/*CPR* (ppm unless otherwise indicated).

	Jamieson and Hancock (2004) Redware		Rovira et al. (2006) *Contenedores de pasta roja*		Main Red Earthenware Geochemical Group**	
Element	Mean	Standard deviation	Mean	Standard deviation	Mean	Standard deviation
As	23.1	4.9	24.8	10.3	21.8	6.3
La	27.2	2.1	32.4	4.7	26.9	2.3
Lu			0.3	0.1	0.4	0
Nd			29.6	4.4	25.2	2.5
Sm	4.7	0.4	5.1	0.5	5.6	0.3
U			4.1	5.7	3.4	0.5
Yb			2.3	0.2	2.5	0.2
Ce	50.5	10.0	60.2	7.9	56.9	4.9
Co	17.6	2.8	22	4.9	20.8	2.2
Cr	32.0	4.3	31.5	7.2	27.1	2.8
Cs	19.3	7.3	18.6	9	12.6	1.8
Eu	0.6	0.1	1.1	0.1	1.2	0.1
Fe (%)	4.3	0.7	4.6	0.5	5.3	0.5
Hf	4.4	1.1	5.3	0.4	4.7	0.6
Rb	112.8	25.1	131.5	13.2	97.9	11.7
Sb			4.2	1.5	3.7	0.3
Sc	16.5	2.2	16.7	1.7	18.5	1.6
Sr			233.2*	219.4*	309.4	47.9
Ta	0.8	0.2	0.7	0.1	0.7	0
Tb			0.7	0.1	0.7	0.1
Th	11.4	2.2	14	2.6	13.7	1.4
Zn			141.4	19.4	142.9	18.9
Ba	512.5	81.8	666.3	98	554.6	75.7
Ca (%)	2.4	0.6	1*	1.4*	2.2	0.2
K (%)	2.5	0.2	2.1	0.3	2	0.3
Na (%)	1.8	0.2	1.7	0.4	1.8	0.1

*Large number of measurements below level of detection.
**Includes the two sherds of different ceramic types that are part of this chemical group described in the text.

U-Pb Ages of Detrital Zircons and Provenance

Having identified Panama and Peru as likely ceramic source regions for the main Red Earthenware chemical group, U-Pb dating of extracted zircons was undertaken to further refine provenance for these ceramics and by extension that of Redware/*CPR*. Differences in U-Pb age distributions would potentially indicate one region over the other, based on a best fit of U-Pb age distributions with respective geologic histories.

Panamanian rocks of interest here included: the Caribbean Large Igneous Provence (CLIP) formation consisting largely of submarine flood basalts (139–69 Ma); Soná-Azuero arc rocks (71–68 Ma); submarine mafic early arc rocks (66–42 Ma), and Miocene arc rocks (36–5 Ma) (Wegner et al., 2011; Wörner, Harmon, & Wegner, 2009). Few zircons would be expected from the older basement rocks as they are low in felsic igneous rocks, being submarine basalts and mafic, and they could not have produced the granitic sands identified in the olive jars under study. More specifically, colonial pottery production is historically and archaeologically known from Panama la Vieja, located in a region of eastern Panama defined as a major sedimentary basin of Tertiary and Quaternary (Eocene and younger) sedimentary rocks (Case, 1974; Goggin, 1968; Long, 1964; Rovira, 1997, 2001). If U-Pb age distributions did not compare well with Panamanian geology, a better geochronological match might be found in Peru. Detailed geologic histories of Panama and Peru have been summarized by Wegner et al. (2011), and Wörner, Harmon, and Wegner (2009), and Jailiard et al. (2000), respectively.

EXPERIMENTAL METHODOLOGY

Zircons were extracted from five Red Earthenware olive jars sherds from the Graciosa Bay (A13) and Pamua (A16, A21, 7001, 8002) archaeological assemblages; all belonging to the main Red Earthenware geochemical group discussed above. Zircon extraction is destructive and depending on the yield of zircons from each sherd— potentially quite variable—can require that large sherds and/or many sherds be selected for extraction. This is potentially restrictive in terms of sampling archaeological assemblages, and as such, only five sherds were selected for zircon extraction here.

Traditional methods were used to extract zircons: hand-crushing and pulverizing, followed by density separation through panning and heavy liquids, and separation of the heavy mineral fraction using a Frantz LB-1 magnetic barrier separator. For three of the samples (A16, 7001, and 8002), high-voltage electric pulse disintegration (SELFRAG) replaced the traditional methods of hand crushing and pulverizing. The entire zircon yield was incorporated into a 1″ epoxy mount along with multiple fragments of the primary Sri Lanka zircon standard (SL), which was sanded, polished, imaged and cleaned before analysis. More detailed descriptions are given elsewhere (Gehrels, Valencia, & Ruiz, 2008; Johnston et al., 2009).

Uranium-lead geochronology of zircons was conducted by laser ablation-multicollector-inductively coupled mass spectrometry (LA-MC-ICPMS) at the Arizona LaserChron Center (Gehrels, Valencia, & Pullen, 2006; Gehrels, Valencia, & Ruiz, 2008). The isotopic analyses involved ablation of zircon using a Photon Machines Analyte G2 excimer laser coupled to a Nu Instruments HR-MC-ICPMS. Analyses of A13 and A21 zircons were conducted with a 30 micron laser spot diameter. Faraday detectors measured ^{238}U, ^{232}Th, and $^{208–206}Pb$, while discrete dynode ion

counters measured ^{204}Pb and ^{202}Hg, all in static mode. Analyses of A16, 7001, and 8002 zircons were conducted with a 15 micron laser spot diameter. Faraday detectors measured ^{238}U and ^{232}Th, while discrete dynode ion counters measured $^{208-204}$Pb. The uncertainty resulting from calibration correction using a primary standard (SL) was between 0.8 – 1.4% (2σ) for both ^{206}Pb/^{238}U and ^{206}Pb/^{207}Pb. A discordance filter of 20% was applied but most of the grains were younger than 600 Ma, making the measure of discordance difficult, and as such discordance was not factored in for those zircons (Gehrels, 2011). More detailed descriptions of the Arizona LaserChron methodology are given elsewhere (Gehrels, Valencia, & Ruiz, 2008; Johnston et al., 2009).

Probability density function plots (Ludwig, 2008) were created by assuming normal distributions of age uncertainty at 1σ for each grain age, followed by the summing of all normal distributions into composites normalized to subtend equal areas under the curves (Figure 3). The Arizona Laserchron Center *Excel Age Pick, Normalized Probability Plot, K-S Test* and *Overlap* macros were used to determine age clusters and mean ages, graph age probability plots and perform overlap, similarity and Kolmogorov-Smirnov (K-S) tests (Gehrels, 2011; Guynn & Gehrels, 2010).

RESULTS

The extracted zircons ($n = 143$) produced a wide-ranging set of dates from the Archaean to the Quaternary (2977.2 ± 29.0–3.2 ± 4.0 Ma) (Table II). Sherds A13 and A21 produced the highest zircon yields and also the widest range of dates: 3.2 ± 4.0–2977.2 ± 29.0 Ma and 12.7 ± 1.4–1149.5 ± 52.5 Ma, respectively. The probability density plots for A13 showed a cluster ranging from 54–108 Ma with a mean age of 84.4 ± 0.9 Ma, and for A21 a cluster ranging from 57–102 Ma with a mean age of 83.0 ± 1.6 Ma (2σ) (Figure 3). None of the other sherds yielded large zircon numbers. Nine of the ten zircons extracted from the remaining three sherds yielded Cretaceous ages of 67–89 Ma, with one zircon giving an Oligocene age of 25 Ma. Together they yielded a cluster of 78–82 Ma with a mean age of 80.0 ± 1.4 Ma (2σ). Sherd A13 was the only sherd to provide sufficient numbers of zircons for a robust geological provenance study; however, the addition of ages from the remaining sherds shown in the combined plot did not significantly shift any of the prominent peaks found in A13. The zircon ages of all sherds combined produced peaks at 63–66 Ma, 81 Ma, and 92 Ma (Figure 3).

Overlap tests for A13 and A21 gave an age probability overlap of 0.6 and degree of similarity of 0.9. For 7001 compared with A13 and A21, the samples showed an overlap of 0.09 and 0.2, and a similarity of 0.6 and 0.5 respectively. The lower overlap values for 7001 are due largely to its smaller age set. These values increase slightly if 7001, A16, and 8002 ages are combined. A K-S test was performed on A13 and A21 dates only, as a minimum of 20 ages is required in a sample set for the test to be statistically meaningful (Guynn & Gehrels, 2010). K-S tests taking into account error in the Cumulative Distrbution Function (CDF), no error in the CDF and using the Monte-Carlo simulation resulted in P values of 0.87–1.0. This indicates that the age populations are statistically indistinguishable.

COMPARATIVE GEOLOGY

The most likely sources for the Red Earthenware olive jar sherds in this study were Panama and Peru, based on petrological, geochemical, historical, and archaeological data. A Spanish origin had been excluded as a result of geochemical studies and this is further supported here, as Spanish granites are Paleozoic with ages reported between 360–270 Ma, ages not observed in this study (Castro et al., 2002). With respect to Panama, although the younger rocks of Panama could yield granitic sands and abundant zircons, the majority of zircons in this study are pre-Eocene. Further, no sedimentary-metasedimentary lithics were identified in thin sections of the main INAA group sherds (Dickinson & Green, 1973; Kelloway, Gibbs, & Craven, 2013). Rather, the rock fragments in the olive jars under study are igneous suggesting derivation from a granitic source and the Panamanian granitic rocks are not as voluminous as Peruvian batholiths. Thus Panama is also an unlikely source for these ceramics.

Peru is a more likely source than Panama for the main geochemical Red Earthenware group based on U-Pb zircon ages. The Coastal Batholith of Peru potentially serves as a prime candidate, cropping out along the Western Cordillera and being formed of multiple plutons of appropriate granitic lithology and dates (Cobbing & Pitcher, 1972; Cobbing, Pitcher, & Taylor, 1977; Cobbing et al., 1981; Jailiard & Soler, 1996; McCourt, 1981; Mukasa, 1986; Pitcher, 1974). The Coastal Batholith was defined by the out-pouring of calc-alkaline plutons in the Andean arc area during the Late Albian and the age distributions in this study correspond well with geological events associated with the Coastal Batholith (Jailiard et al., 2000). In particular, volcanic activity is known in central-southern Peru from 101–94 Ma (Jailiard et al., 2000) and Soler (in Jailiard et al., 2000) proposed major plutonic pulses at 85–77 Ma and 74–69 Ma. Mukasa (1986) has suggested that emplacement was continuous rather than episodic

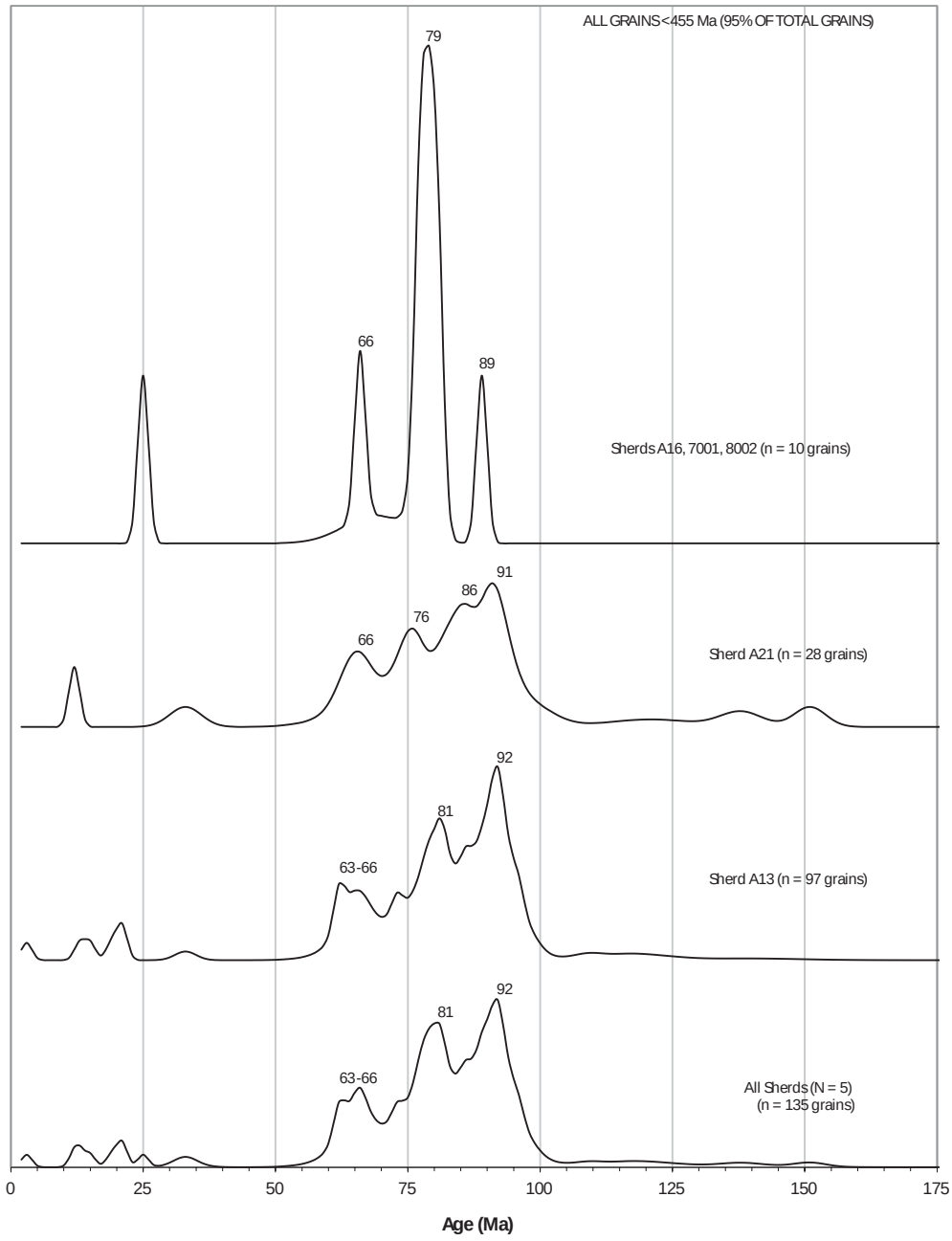

Figure 3 Age probability plots for sherds A16, 7001 and 8002 combined, A13, A21, and all sherds zircon age sets. Grains older than 455 Ma are excluded. *N* = number of sherds, *n* = number of zircons analyzed.

for the Lima and Arequipa segment with the most voluminous activity occurring at 86–70 Ma, based on a study of U-Pb dated zircons from the super-units of the Lima, Arequipa and Toquepala segments. Further, emplacement also occurred between 68–64 Ma, possibly accounting for the 63–66 Ma peak observed in Figure 3 (Jailiard et al., 2000).

Older zircon ages in this study (> 110 Ma) are likely inherited from pre-Albian/Early Cretaceous activity and the Proterozoic-Paleozoic Basement (>450 Ma) (Jailiard et al., 2000; Ramos, 2009) either as individual grains or from batholith wallrocks or roof pendants and stoped inclusions. Grains dated to the late Eocene and younger could have derived from local plutons or elsewhere,

Table II U-Pb geochronologic analyses of zircons extracted from five Red Earthenware olive jars.

						Isotope ratios					Apparent ages (Ma)								
Analysis (sherd-zircon#)	U (ppm)	$^{206}Pb/^{204}Pb$	U/Th	$^{206}Pb^*/^{207}Pb^*$	± (%)	$^{207}Pb^*/^{235}U^*$	± (%)	$^{206}Pb^*/^{238}U$	± (%)	error corr.	$^{206}Pb^*/^{238}U^*$	± (Ma)	$^{207}Pb^*/^{235}U$	± (Ma)	$^{206}Pb^*/^{207}Pb^*$	± (Ma)	Best age (Ma)	± (Ma)	Conc (%)
A13–6	159	218	1.2	0.8410	234.2	0.0811	266.0	0.0005	126.3	0.47	3.2	4.0	79.2	205.4	NA	NA	3.2	4.0	NA
A13–94	144	1504	1.3	3.6400	171.4	0.0820	173.2	0.0022	25.1	0.14	13.9	3.5	80.1	134.1	3333.2	823.4	13.9	3.5	NA
A13–33	475	1111	1.0	25.6223	33.4	0.0133	34.0	0.0025	6.2	0.18	15.9	1.0	13.4	4.5	−414.8	895.2	15.9	1.0	NA
A13–63	241	2033	1.6	19.7486	74.8	0.0214	77.9	0.0031	21.8	0.28	19.7	4.3	21.5	16.6	224.3	2049.1	19.7	4.3	NA
A13–60	595	401	0.7	17.3302	32.7	0.0265	33.5	0.0033	7.1	0.21	21.4	1.5	26.5	8.8	518.5	736.5	21.4	1.5	NA
A13–24	452	4705	0.8	21.6839	31.6	0.0215	32.0	0.0034	5.3	0.16	21.8	1.1	21.6	6.8	3.7	776.9	21.8	1.1	NA
A13–22	146	1032	1.0	13.7374	64.2	0.0516	64.7	0.0051	8.5	0.13	33.1	2.8	51.1	32.3	1008.2	1472.0	33.1	2.8	NA
A13–40	193	252	1.2	17.5431	41.6	0.0753	42.5	0.0096	8.6	0.20	61.4	5.3	73.7	30.2	491.6	956.2	61.4	5.3	NA
A13–64	490	19,000	1.5	19.9993	8.6	0.0666	8.9	0.0097	2.3	0.26	62.0	1.4	65.5	5.6	195.1	200.0	62.0	1.4	NA
A13–70	316	7343	1.0	23.9002	25.1	0.0564	25.3	0.0098	2.9	0.12	62.8	1.8	55.7	13.7	−236.1	641.8	62.8	1.8	NA
A13–13	327	7437	0.9	23.6431	9.0	0.0573	10.1	0.0098	4.6	0.45	63.0	2.9	56.6	5.5	−208.9	225.6	63.0	2.9	NA
A13–32	142	4675	1.4	22.7597	49.1	0.0600	49.6	0.0099	7.2	0.15	63.6	4.6	59.2	28.5	−114.2	1278.5	63.6	4.6	NA
A13–61	182	7462	1.2	22.2096	43.6	0.0624	43.9	0.0100	5.6	0.13	64.4	3.6	61.4	26.2	−54.3	1108.7	64.4	3.6	NA
A13–81	293	11,644	1.0	25.5290	21.5	0.0550	22.2	0.0102	5.4	0.24	65.4	3.5	54.4	11.8	−405.3	568.0	65.4	3.5	NA
A13–20	183	9205	1.6	28.2747	27.8	0.0500	28.4	0.0103	5.6	0.20	65.8	3.7	49.6	13.7	−679.7	780.7	65.8	3.7	NA
A13–30	179	9890	1.4	28.5769	38.5	0.0495	38.9	0.0103	4.9	0.13	65.8	3.2	49.1	18.6	−709.2	1105.9	65.8	3.2	NA
A13–75	139	4162	1.2	24.5275	59.4	0.0578	59.5	0.0103	4.4	0.07	66.0	2.9	57.1	33.0	−301.9	1653.9	66.0	2.9	NA
A13–109	187	4853	0.9	20.1530	25.9	0.0712	26.1	0.0104	3.5	0.13	66.8	2.3	69.9	17.6	177.2	612.8	66.8	2.3	NA
A13–104	249	6120	1.6	24.1514	16.8	0.0597	17.9	0.0105	6.0	0.34	67.1	4.0	58.9	10.2	−262.6	429.2	67.1	4.0	NA
A13–34	78	5413	1.1	25.7926	40.0	0.0562	44.0	0.0105	18.5	0.42	67.5	12.4	55.6	23.8	−432.2	1085.5	67.5	12.4	NA
A13–86	106	4196	1.4	33.8323	45.0	0.0430	45.2	0.0105	3.9	0.09	67.6	2.6	42.7	18.9	NA	NA	67.6	2.6	NA
A13–67	95	3053	1.7	20.9855	56.3	0.0713	57.6	0.0109	12.4	0.22	69.6	8.6	70.0	39.0	82.0	1446.0	69.6	8.6	NA
A13–79	114	2495	1.2	39.4174	53.6	0.0390	53.7	0.0111	4.4	0.08	71.5	3.1	38.8	20.5	NA	NA	71.5	3.1	NA
A13–77	398	5373	1.0	22.0268	11.1	0.0718	11.3	0.0115	2.4	0.21	73.6	1.7	70.4	7.7	−34.2	269.6	73.6	1.7	NA
A13–14	202	7324	1.2	22.5583	17.0	0.0704	17.4	0.0115	3.6	0.21	73.8	2.7	69.1	11.6	−92.3	420.3	73.8	2.7	NA
A13–37	85	2502	1.4	21.5416	44.7	0.0741	45.3	0.0116	7.4	0.16	74.2	5.5	72.6	31.7	19.6	1123.3	74.2	5.5	NA
A13–54	71	2622	1.5	4.0008	738.4	0.4002	738.4	0.0116	6.9	0.01	74.4	5.1	341.8	#NUM!	3184.4	589.0	74.4	5.1	NA
A13–59	192	246	1.1	14.8740	36.7	0.1098	37.0	0.0118	4.8	0.13	75.9	3.6	105.8	37.2	845.0	789.4	75.9	3.6	NA
A13–28	167	1718	0.7	8.9054	61.8	0.1852	62.4	0.0120	8.6	0.14	76.6	6.6	172.5	99.4	1836.8	1264.8	76.6	6.6	NA
A13–29	101	286	1.1	14.7619	37.7	0.1118	39.2	0.0120	10.8	0.28	76.7	8.3	107.6	40.0	860.6	809.6	76.7	8.3	NA
A13–36	352	8733	1.2	19.6477	8.0	0.0855	8.5	0.0122	2.8	0.33	78.0	2.2	83.3	6.8	236.1	184.5	78.0	2.2	NA
A13–102	92	2893	1.2	22.2347	42.9	0.0756	44.4	0.0122	11.6	0.26	78.1	9.0	74.0	31.7	−57.0	1089.6	78.1	9.0	NA
A13–50	256	13,539	1.2	22.9346	14.3	0.0736	14.5	0.0122	2.6	0.18	78.4	2.0	72.1	10.1	−133.1	355.0	78.4	2.0	NA
A13–12	70	3381	1.5	10.3039	80.4	0.1648	80.6	0.0123	6.0	0.07	78.9	4.7	154.9	116.3	1568.2	1931.5	78.9	4.7	NA
A13–55	693	55,456	1.2	21.0166	6.2	0.0813	6.3	0.0124	1.2	0.20	79.4	1.0	79.4	4.8	78.5	146.2	79.4	1.0	NA
A13–39	131	17,260	1.3	18.7524	20.9	0.0912	21.7	0.0124	6.1	0.28	79.4	4.8	88.6	18.4	342.7	476.7	79.4	4.8	NA
A13–105	118	4909	1.1	36.2261	58.7	0.0473	58.9	0.0124	4.6	0.08	79.7	3.7	46.9	27.0	NA	NA	79.7	3.7	NA
A13–21	92	247	1.1	20.0273	30.5	0.0857	33.4	0.0124	13.6	0.41	79.7	10.8	83.5	26.8	191.8	724.1	79.7	10.8	NA
A13–56	143	7472	0.9	19.8239	24.9	0.0866	25.2	0.0125	4.1	0.16	79.8	3.3	84.3	20.4	215.5	583.9	79.8	3.3	NA

Table II Continued

						Isotope ratios					Apparent ages (Ma)								
Analysis (sherd-zircon#)	U (ppm)	$^{206}Pb/^{204}Pb$	U/Th	$^{206}Pb^*/^{207}Pb^*$	± (%)	$^{207}Pb^*/^{235}U^*$	± (%)	$^{206}Pb^*/^{238}U$	± (%)	error corr.	$^{206}Pb^*/^{238}U^*$	± (Ma)	$^{207}Pb^*/^{235}U$	± (Ma)	$^{206}Pb^*/^{207}Pb^*$	± (Ma)	Best age (Ma)	± (Ma)	Conc (%)
A13–16	245	17,169	1.4	20.2005	12.1	0.0851	12.5	0.0125	3.0	0.24	79.9	2.4	82.9	10.0	171.7	284.4	79.9	2.4	NA
A13–90	168	4583	0.9	20.9883	15.2	0.0821	15.5	0.0125	3.1	0.20	80.1	2.5	80.1	12.0	81.7	362.7	80.1	2.5	NA
A13–51	74	3353	1.2	20.5586	59.4	0.0839	60.2	0.0125	9.9	0.16	80.1	7.9	81.8	47.3	130.6	1530.0	80.1	7.9	NA
A13–99	111	4901	1.2	18.7176	38.6	0.0929	39.1	0.0126	6.2	0.16	80.8	5.0	90.2	33.8	346.9	905.3	80.8	5.0	NA
A13–15	283	12,422	1.0	23.1574	9.6	0.0753	9.9	0.0127	2.2	0.22	81.1	1.8	73.8	7.0	−157.0	239.8	81.1	1.8	NA
A13–27	131	1277	1.9	-2.4928	1984.2	-0.7009	1984.2	0.0127	6.2	0.00	81.2	5.0	-1225.7	#NUM!	NA	NA	81.2	5.0	NA
A13–65	355	11,778	1.2	21.0381	10.9	0.0834	11.1	0.0127	1.8	0.17	81.5	1.5	81.4	8.6	76.1	259.8	81.5	1.5	NA
A13–25	156	11,093	1.2	20.5395	24.2	0.0862	24.5	0.0128	4.1	0.17	82.3	3.3	84.0	19.8	132.7	576.4	82.3	3.3	NA
A13–68	248	14,550	0.9	20.4762	14.3	0.0866	14.5	0.0129	2.2	0.15	82.4	1.8	84.3	11.7	140.0	338.0	82.4	1.8	NA
A13–18	334	24,747	0.8	24.3565	24.7	0.0737	24.8	0.0130	2.6	0.10	83.4	2.1	72.2	17.3	−284.0	637.3	83.4	2.1	NA
A13–69	137	5824	1.2	23.6231	32.9	0.0765	33.6	0.0131	6.7	0.20	84.0	5.6	74.9	24.3	−206.7	845.5	84.0	5.6	NA
A13–66	140	6804	1.1	21.8311	24.9	0.0837	25.5	0.0133	5.5	0.22	84.9	4.7	81.6	20.0	−12.6	608.5	84.9	4.7	NA
A13–38	718	15,679	1.0	21.4441	7.9	0.0852	8.8	0.0133	3.8	0.44	84.9	3.2	83.1	7.0	30.5	190.4	84.9	3.2	NA
A13–49	568	17,893	1.4	21.6184	8.3	0.0848	8.7	0.0133	2.7	0.31	85.1	2.3	82.6	6.9	11.0	200.0	85.1	2.3	NA
A13–82	244	3609	1.8	16.3962	8.8	0.1121	10.2	0.0133	5.2	0.51	85.4	4.4	107.9	10.5	638.9	190.4	85.4	4.4	NA
A13–46	138	4962	1.1	22.4387	25.4	0.0821	26.0	0.0134	5.5	0.21	85.5	4.7	80.1	20.0	−79.3	630.9	85.5	4.7	NA
A13–97	139	5099	1.7	22.2531	38.5	0.0833	39.3	0.0134	7.9	0.20	86.1	6.8	81.3	30.7	−59.0	970.5	86.1	6.8	NA
A13–85	339	17,825	1.4	23.0743	6.2	0.0804	7.7	0.0135	4.6	0.59	86.2	3.9	78.5	5.8	−148.1	154.2	86.2	3.9	NA
A13–10	498	4826	1.3	20.9017	7.5	0.0895	7.8	0.0136	2.1	0.27	86.9	1.8	87.1	6.5	91.5	177.3	86.9	1.8	NA
A13–71	109	6192	1.1	20.6497	38.1	0.0914	38.6	0.0137	6.3	0.16	87.6	5.5	88.8	32.8	120.2	928.1	87.6	5.5	NA
A13–101	263	7385	1.1	22.9156	11.3	0.0833	11.7	0.0138	3.2	0.27	88.6	2.8	81.2	9.2	−131.0	280.0	88.6	2.8	NA
A13–1	192	4966	1.2	24.0186	22.4	0.0804	22.8	0.0140	4.3	0.19	89.7	3.8	78.6	17.3	−248.6	573.3	89.7	3.8	NA
A13–52	162	5887	0.9	25.5853	18.9	0.0756	19.5	0.0140	4.9	0.25	89.9	4.4	74.0	13.9	−411.1	497.6	89.9	4.4	NA
A13–57	116	4285	2.2	16.4808	19.9	0.1178	20.9	0.0141	6.3	0.30	90.1	5.6	113.0	22.3	627.8	432.5	90.1	5.6	NA
A13–48	75	3297	1.6	25.5810	50.0	0.0759	52.3	0.0141	15.4	0.30	90.2	13.8	74.3	37.5	−410.6	1381.8	90.2	13.8	NA
A13–47	200	10,886	1.2	23.1803	22.4	0.0838	23.2	0.0141	5.9	0.25	90.2	5.2	81.7	18.2	−159.5	563.4	90.2	5.2	NA
A13–80	265	8628	1.1	21.1565	10.0	0.0924	10.5	0.0142	3.2	0.30	90.7	2.8	89.7	9.0	62.7	238.0	90.7	2.8	NA
A13–100	120	5437	1.8	26.1773	29.8	0.0747	30.1	0.0142	4.6	0.15	90.8	4.2	73.1	21.3	−471.2	802.6	90.8	4.2	NA
A13–78	294	12,812	1.9	23.2867	12.8	0.0842	13.0	0.0142	2.4	0.18	91.0	2.1	82.1	10.3	−170.9	319.6	91.0	2.1	NA
A13–73	238	13,548	2.2	22.1822	35.4	0.0887	35.6	0.0143	3.5	0.10	91.3	3.1	86.3	29.4	−51.2	885.8	91.3	3.1	NA
A13–41	196	6203	1.5	21.4487	15.2	0.0918	15.8	0.0143	4.3	0.27	91.4	3.9	89.1	13.5	30.0	365.5	91.4	3.9	NA
A13–26	173	13,615	1.7	20.6328	14.2	0.0955	14.6	0.0143	3.4	0.24	91.5	3.1	92.6	12.9	122.1	335.7	91.5	3.1	NA
A13–106	147	16,937	2.2	24.4073	14.5	0.0807	15.6	0.0143	5.8	0.37	91.5	5.3	78.8	11.8	−289.4	370.2	91.5	5.3	NA
A13–88	168	7367	1.1	22.1785	18.7	0.0889	19.5	0.0143	5.4	0.28	91.5	4.9	86.5	16.2	−50.8	459.1	91.5	4.9	NA
A13–95	124	6633	1.6	26.3917	36.3	0.0747	36.4	0.0143	2.6	0.07	91.5	2.4	73.2	25.7	−492.9	993.3	91.5	2.4	NA
A13–108	178	11,175	2.6	19.9782	14.7	0.0987	15.2	0.0143	3.7	0.25	91.6	3.4	95.6	13.8	197.5	343.0	91.6	3.4	NA
A13–98	650	29,545	1.6	20.6344	3.8	0.0958	4.5	0.0143	2.4	0.53	91.7	2.2	92.9	4.0	121.9	90.3	91.7	2.2	NA
A13–8	575	27,733	1.9	21.1384	6.0	0.0938	6.2	0.0144	1.7	0.28	92.0	1.6	91.0	5.4	64.8	142.6	92.0	1.6	NA
A13–110	247	9477	1.0	20.3055	10.7	0.0978	11.2	0.0144	3.3	0.30	92.2	3.0	94.7	10.1	159.7	251.0	92.2	3.0	NA
A13–4	267	30,549	1.5	21.6682	7.9	0.0916	8.7	0.0144	3.5	0.41	92.2	3.2	89.0	7.4	5.5	190.5	92.2	3.2	NA

Table II Continued

Analysis (sherd-zircon#)	U (ppm)	$^{206}Pb/^{204}Pb$	U/Th	$^{206}Pb^*/^{207}Pb^*$	± (%)	Isotope ratios $^{207}Pb^*/^{235}U^*$	± (%)	$^{206}Pb^*/^{238}U$	± (%)	error corr.	Apparent ages (Ma) $^{206}Pb^*/^{238}U^*$	± (Ma)	$^{207}Pb^*/^{235}U$	± (Ma)	$^{206}Pb^*/^{207}Pb^*$	± (Ma)	Best age (Ma)	± (Ma)	Conc (%)
A13–2	134	6536	1.2	30.0129	45.4	0.0662	45.5	0.0144	3.1	0.07	92.2	2.9	65.0	28.7	−847.6	1358.8	92.2	2.9	NA
A13–89	553	45,220	0.9	21.4730	5.4	0.0926	5.7	0.0144	1.7	0.30	92.3	1.5	89.9	4.9	27.3	130.2	92.3	1.5	NA
A13–5	289	6557	2.2	19.4051	14.1	0.1025	14.4	0.0144	3.1	0.21	92.3	2.8	99.1	13.6	264.7	325.2	92.3	2.8	NA
A13–7	203	8522	1.2	20.8767	16.6	0.0953	17.2	0.0144	4.3	0.25	92.4	4.0	92.4	15.2	94.3	396.3	92.4	4.0	NA
A13–74	535	19,639	1.1	21.9269	5.1	0.0911	6.0	0.0145	3.3	0.54	92.7	3.0	88.5	5.1	−23.1	123.1	92.7	3.0	NA
A13–84	357	19,748	0.9	22.4539	7.8	0.0898	8.1	0.0146	2.4	0.30	93.6	2.3	87.3	6.8	−81.0	190.3	93.6	2.3	NA
A13–87	144	7475	1.4	20.1889	25.9	0.1003	26.5	0.0147	5.3	0.20	94.0	5.0	97.1	24.5	173.1	614.2	94.0	5.0	NA
A13–9	337	24,059	1.0	18.8695	7.4	0.1075	7.9	0.0147	2.8	0.35	94.2	2.6	103.7	7.8	328.6	168.7	94.2	2.6	NA
A13–93	195	6201	1.1	22.7023	15.3	0.0897	16.0	0.0148	4.6	0.29	94.5	4.3	87.2	13.3	−108.0	378.4	94.5	4.3	NA
A13–53	283	12,348	1.4	20.9141	11.8	0.0975	12.0	0.0148	2.3	0.19	94.7	2.2	94.5	10.9	90.1	280.8	94.7	2.2	NA
A13–42	166	4609	1.9	18.6802	16.8	0.1093	18.0	0.0148	6.5	0.36	94.8	6.1	105.4	18.0	351.5	382.3	94.8	6.1	NA
A13–91	241	15,929	1.2	20.2133	13.0	0.1031	13.4	0.0151	3.5	0.26	96.7	3.3	99.7	12.7	170.3	304.2	96.7	3.3	NA
A13–83	153	5645	2.1	24.1929	25.2	0.0862	25.3	0.0151	1.9	0.08	96.8	1.8	84.0	20.4	−266.9	648.4	96.8	1.8	NA
A13–19	468	35,717	0.9	21.3950	8.2	0.0992	8.6	0.0154	2.4	0.28	98.5	2.3	96.0	7.8	35.9	197.2	98.5	2.3	NA
A13–96	381	29,751	1.5	20.7824	6.0	0.1140	6.6	0.0172	2.8	0.42	109.8	3.0	109.6	6.9	105.0	142.4	109.8	3.0	NA
A13–62	132	4792	1.5	23.2680	23.7	0.1078	24.0	0.0182	3.7	0.15	116.2	4.2	104.0	23.7	−168.9	598.1	116.2	4.2	NA
A13–76	154	6481	2.3	18.2174	27.6	0.1452	28.0	0.0192	4.7	0.17	122.5	5.7	137.7	36.1	407.8	629.1	122.5	5.7	NA
A13–23	141	5066	1.6	21.4054	16.8	0.1413	18.5	0.0219	7.8	0.42	139.9	10.7	134.2	23.3	34.8	404.6	139.9	10.7	NA
A13–45	117	39,567	0.7	17.4221	3.1	0.5793	3.6	0.0732	1.8	0.50	455.4	7.8	464.0	13.3	506.9	68.0	455.4	7.8	NA
A13–11	87	14,543	1.6	19.0245	9.3	0.5349	9.6	0.0738	2.3	0.24	459.0	10.0	435.0	33.8	310.0	211.8	459.0	10.0	NA
A13–43	93	1064	1.7	15.6375	13.2	0.7187	13.8	0.0815	4.1	0.30	505.2	19.9	549.9	58.7	739.9	280.2	505.2	19.9	NA
A13–92	97	19,005	1.0	17.2418	4.8	0.7016	5.1	0.0877	1.7	0.34	542.1	9.0	539.8	21.5	529.7	106.3	542.1	9.0	NA
A13–3	49	24,396	2.6	13.0959	3.8	1.8502	4.4	0.1757	2.2	0.50	1043.6	21.1	1063.5	29.0	1104.5	76.1	1104.5	76.1	94.5
A13–44	74	69,295	1.4	7.7773	1.0	6.3542	3.3	0.3584	3.2	0.95	1974.6	53.9	2026.0	29.2	2078.6	17.6	2078.6	17.6	95.0
A13–107	19	37,515	0.7	4.5553	1.8	14.9598	2.8	0.4942	2.1	0.76	2589.0	44.7	2812.7	26.3	2977.2	29.0	2977.2	29.0	87.0
A21–31	264	1324	1.0	7.1441	379.6	0.0382	379.8	0.0020	10.7	0.03	12.7	1.4	38.0	142.8	2226.9	622.2	12.7	1.4	NA
A21–27	93	1232	1.8	4.5564	263.5	0.1590	264.0	0.0053	15.4	0.06	33.8	5.2	149.8	385.1	2976.8	308.4	33.8	5.2	NA
A21–2	58	1787	1.8	9.8184	225.5	0.1386	225.9	0.0099	13.7	0.06	63.3	8.7	131.8	286.5	1658.1	515.6	63.3	8.7	NA
A21–1	229	23,883	1.1	20.5604	13.2	0.0683	14.3	0.0102	5.6	0.39	65.4	3.6	67.1	9.3	130.4	310.5	65.4	3.6	NA
A21–5	214	6739	1.4	23.8707	18.5	0.0589	19.3	0.0102	5.4	0.28	65.4	3.5	58.1	10.9	−233.0	470.6	65.4	3.5	NA
A21–14	129	4372	1.0	32.9112	38.5	0.0432	38.9	0.0103	5.6	0.14	66.2	3.7	43.0	16.4	−1119.9	1209.1	66.2	3.7	NA
A21–20	36	1399	2.2	15.3034	37.3	0.1023	45.7	0.0114	26.3	0.58	72.8	19.0	98.9	43.1	785.4	811.5	72.8	19.0	NA
A21–4	369	18,114	1.5	21.2442	6.0	0.0759	7.5	0.0117	4.6	0.61	75.0	3.4	74.3	5.4	52.8	142.4	75.0	3.4	NA
A21–28	272	11,934	0.8	21.2586	19.3	0.0766	19.7	0.0118	4.0	0.20	75.7	3.0	74.9	14.3	51.3	464.9	75.7	3.0	NA
A21–3	1217	42,389	18.4	21.5539	4.2	0.0765	5.1	0.0120	2.8	0.55	76.6	2.1	74.8	3.7	18.2	101.5	76.6	2.1	NA
A21–10	80	2561	0.9	12.7201	124.2	0.1337	124.4	0.0123	7.2	0.06	79.0	5.7	127.4	150.1	1162.5	352.0	79.0	5.7	NA
A21–16	65	2523	1.4	16.4633	65.0	0.1072	65.7	0.0128	9.5	0.14	82.0	7.7	103.4	64.6	630.1	1580.3	82.0	7.7	NA
A21–17	261	11,444	1.1	20.1952	15.1	0.0883	15.3	0.0129	2.7	0.17	82.8	2.2	85.9	12.6	172.4	353.2	82.8	2.2	NA
A21–29	175	5721	0.9	20.8872	12.6	0.0865	13.6	0.0131	5.2	0.38	83.9	4.3	84.2	11.0	93.1	300.4	83.9	4.3	NA
A21–8	1802	19,541	1.6	20.5615	2.5	0.0893	3.5	0.0133	2.5	0.70	85.3	2.1	86.9	2.9	130.3	59.2	85.3	2.1	NA

Table II Continued

Analysis (sherd-zircon#)	U (ppm)	$^{206}Pb/^{204}Pb$	U/Th	$^{206}Pb^*/^{207}Pb^*$	± (%)	Isotope ratios $^{207}Pb^*/^{235}U^*$	± (%)	$^{206}Pb^*/^{238}U$	± (%)	error corr.	Apparent ages (Ma) $^{206}Pb^*/^{238}U^*$	± (Ma)	$^{207}Pb^*/^{235}U$	± (Ma)	$^{206}Pb^*/^{207}Pb^*$	± (Ma)	Best age (Ma)	± (Ma)	Conc (%)
A21–21	171	5356	1.2	13.3877	39.4	0.1386	40.4	0.0135	9.0	0.22	86.2	7.7	131.8	50.0	1060.3	825.1	86.2	7.7	NA
A21–24	282	10,159	1.0	21.9928	8.9	0.0850	9.5	0.0136	3.4	0.36	86.8	2.9	82.8	7.6	− 30.4	215.7	86.8	2.9	NA
A21–13	79	3638	2.6	18.3977	21.9	0.1065	24.7	0.0142	11.4	0.46	91.0	10.3	102.8	24.1	385.8	497.7	91.0	10.3	NA
A21–11	236	5826	1.1	17.2429	25.7	0.1139	26.0	0.0142	4.2	0.16	91.1	3.8	109.5	27.0	529.6	571.3	91.1	3.8	NA
A21–12	119	3313	1.6	18.5713	19.4	0.1060	20.1	0.0143	5.4	0.27	91.4	4.9	102.3	19.6	364.6	440.2	91.4	4.9	NA
A21–18	427	26,901	2.5	21.1264	8.3	0.0935	8.6	0.0143	2.2	0.26	91.7	2.0	90.8	7.5	66.1	198.9	91.7	2.0	NA
A21–6	280	10,518	1.0	22.2792	13.1	0.0887	13.8	0.0143	4.3	0.31	91.8	4.0	86.3	11.4	− 61.9	321.5	91.8	4.0	NA
A21–15	177	5052	1.4	26.5443	26.9	0.0745	27.1	0.0143	3.4	0.13	91.8	3.1	73.0	19.1	− 508.2	727.5	91.8	3.1	NA
A21–32	211	10,870	1.4	23.7842	15.1	0.0844	15.5	0.0146	3.5	0.23	93.2	3.3	82.3	12.2	− 223.8	381.4	93.2	3.3	NA
A21–19	172	4235	1.7	20.2642	13.1	0.1058	14.0	0.0156	5.0	0.35	99.5	4.9	102.2	13.6	164.4	308.0	99.5	4.9	NA
A21–25	102	11,389	2.0	18.0807	25.1	0.1453	26.1	0.0191	7.4	0.28	121.7	9.0	137.8	33.7	424.7	566.9	121.7	9.0	NA
A21–30	136	14,414	1.6	20.0273	19.2	0.1497	19.4	0.0217	2.9	0.15	138.7	4.0	141.7	25.7	191.9	450.6	138.7	4.0	NA
A21–9	157	6810	1.0	21.5170	19.5	0.1522	19.7	0.0237	2.7	0.14	151.3	4.0	143.8	26.4	22.3	472.1	151.3	4.0	NA
A21–23	394	130,351	35.5	12.8035	2.6	1.9458	3.1	0.1807	1.7	0.54	1070.7	16.6	1097.0	21.0	1149.5	52.5	1149.5	52.5	93.1
A16–1B	275	4430	1.4	21.2040	1.0	0.0908	1.5	0.0140	1.1	0.73	89.4	0.9	88.3	1.2	57.4	23.6	89.4	0.9	NA
7001–1B	141	2960	1.0	20.4565	1.9	0.0825	2.2	0.0122	1.2	0.54	78.5	0.9	80.5	1.7	142.3	44.3	78.5	0.9	NA
7001–2A	297	6400	1.2	20.9384	1.2	0.0822	2.2	0.0125	1.8	0.82	80.0	1.4	80.2	1.7	87.4	28.9	80.0	1.4	NA
7001–3A	370	5574	0.9	20.7085	0.8	0.0820	3.7	0.0123	3.6	0.97	78.9	2.8	80.0	2.8	113.5	19.8	78.9	2.8	NA
7001–4B	330	5706	1.2	21.1045	1.9	0.0823	2.3	0.0126	1.3	0.57	80.7	1.1	80.3	1.8	68.6	45.8	80.7	1.1	NA
7001–5B	198	2678	1.3	20.7740	2.6	0.0693	2.9	0.0104	1.4	0.47	67.0	0.9	68.1	1.9	106.0	60.9	67.0	0.9	NA
7001–6A	257	2314	1.7	17.7134	26.1	0.0842	28.8	0.0108	12.0	0.42	69.4	8.3	82.1	22.7	470.3	587.4	69.4	8.3	NA
7001–7A	385	5267	0.8	20.1764	2.3	0.0273	2.4	0.0040	0.8	0.34	25.7	0.2	27.4	0.7	174.5	53.3	25.7	0.2	NA
7001–8B	145	4751	2.0	19.5894	1.5	0.0899	1.7	0.0128	0.7	0.42	81.8	0.6	87.4	1.4	243.0	35.5	81.8	0.6	NA
8002–1A	146	11,947	1.3	19.4421	3.0	0.0855	3.2	0.0121	1.1	0.34	77.2	0.8	83.3	2.6	260.4	69.1	77.2	0.8	NA

1. Analyses with >30% uncertainty (1-sigma) in $^{206}Pb/^{238}U$ age are not included, unless $^{206}Pb/^{238}U$ age is <10 Ma.
2. Analyses with >10% uncertainty (1-sigma) in $^{206}Pb/^{207}Pb$ age are not included, unless $^{206}Pb/^{238}U$ age is <500 Ma.
3. Best age is determined from $^{206}Pb/^{238}U$ age for analyses with $^{206}Pb/^{238}U$ age <900 Ma and from $^{206}Pb/^{207}Pb$ age for analyses with $^{206}Pb/^{238}U$age >900 Ma.
4. Concordance is based on $^{206}Pb/^{238}U$ age / $^{206}Pb/^{207}Pb$ age. Value is not reported for $^{206}Pb/^{238}U$ ages <600 Ma because of large uncertainty in $^{206}Pb/^{207}Pb$ age.
5. Analyses with $^{206}Pb/^{238}U$ age > 600 Ma and with >20% discordance (<80% concordance) are not included.
6. Analyses with $^{206}Pb/^{238}U$ age > 600 Ma and with >5% reverse discordance (<105% concordance) are not included.
7. All uncertainties are reported at the 1-sigma level, and include only measurement errors.
8. Systematic errors are as follows (at 2-sigma level): [samples A13 and A21: 0.9% ($^{206}Pb/^{238}U$) & 0.8% ($^{206}Pb/^{207}Pb$)]
9. Systematic errors are as follows (at 2-sigma level): [samples A16, 7001, and 8002: 1.4% ($^{206}Pb/^{238}U$) & 0.8% ($^{206}Pb/^{207}Pb$)]
10. Analyses conducted by LA-MC-ICPMS, as described by Gehrels, Valencia, & Ruiz (2008).
11. U concentration and U/Th are cal. relative to Sri Lanka zircon standard and are accurate to ~20%.
12. Common Pb correction is from measured ^{204}Pb with common Pb composition interpreted from Stacey and Kramers (1975).
13. Common Pb composition assigned uncertainties of 1.5 for $^{206}Pb/^{204}Pb$, 0.3 for $^{207}Pb/^{204}Pb$, and 2.0 for $^{208}Pb/^{204}Pb$.
14. U/Pb and $^{206}Pb/^{207}Pb$ fractionation is cal. relative to fragments of a large Sri Lanka zircon of 563.5 ± 3.2 Ma (2-sigma).
15. U decay constants and composition as follows: $^{238}U = 9.8485 \times 10–10$, $^{235}U = 1.55125 \times 10–10$, $^{238}U/^{235}U = 137.88$.
16. Weighted mean, probability density, and concordia plots determined with Isoplot (Ludwig, 2008).

having been taken up into streams draining from the Andes or as ash blown in from the Andes.

DISCUSSION

The results of U-Pb dating of zircons from the main geochemical group of Red Earthenware support the claim that these ceramics are a Peruvian product and by extension Redware/*CPR*. This enlarges both the chemical and petrological reference database for future comparative provenance research of Peruvian ceramics, in conjunction with other recent studies, including Chatfield's (2007, 2008, 2010) study of ceramics from Aqnapampa, VanValkenburgh's (2012, pers.comm.) characterization of ceramics from the Zaña and Chamán Valleys, and Rice's (2012a) chemical study of 120 ceramics from the Florida Museum of Natural History and the Moquegua Valley, the latter a major producer of wine and ceramics during the 16th and 17th Centuries (Rice, 1994, 1996; 1997a, 1997b, 2012b; Rice & Van Beck, 1993; Smith, 1991, 1997). These studies provide foundations on which to expand our understanding of 16th Century Peruvian ceramic production and trade.

Historically, the Peruvian colonial potting industry is known from the mid- to late 16th Century in various areas, though production details are scarce. Archaeologically, transitional-style ceramics and other possibly locally produced Spanish forms have also been recovered from 16th Century contexts (Acevedo, 2004; Astuhuamán Gonzáles, 2011; Mogrovejo Rosales, 1996; Rice, 1994, 1996, 1997a; Smith, 1991). In areas such as Ica and Moquegua, a ceramic industry grew to support the local wine industry, including containers such as olive jars. Presumably, this was the case in numerous areas that required the production of storage jars in support of local industries, both to store and transport goods (Rice, 2012b). The distribution of such jars was related to distribution of the primary commodities being shipped and stored, as well as other functions related to jar reuse. During the late 16th Century Arequipa and Moquegua products supplied southern Peru, whereas Nasca and Ica products supplied Lima and northern regions as far as Central America and New Spain, as well as Chile, indicating the potential distribution of jars produced within these areas (Rice, 2012b).

The distribution of Peruvian-made olive jars to areas such as Panama and Ecuador has also been suggested on the basis of historical research concerning trade, and the study of Red Earthenware presented here suggests evidence of wider trade of Peruvian-made olive jars than previously proven archaeologically. Based on the similarity of chemical fingerprints of olive jars in this study and Redware/*CPR*, we show that ceramics made in Peru were circulating within Ecuador during the 16th Century. Colonial trade between Panama and Peru during the 16th Century is well documented and it is likely that olive jars reached Ecuador through Panama or other trade points along the northcoast of the Viceroyalty of Peru, such as the port of Guayaquil (Borah, 1954; Ward, 1993). Primarily used as storage containers, the jars possibly contained Peruvian export products, such as oil or wine. The olive jars might also have been sent empty to Panama and other ports where they were used to transport products such as wine following disembarkation, or where they found other uses including architectural functions (Avery, 1997; Carruthers, 2003; Lister & Lister, 1981).

CONCLUSIONS

This study determined the U-Pb ages of 143 zircons extracted from five olive jar sherds from 16th Century sites in Solomon Islands. Based on the ages of the zircons in these sherds a Peruvian rather than a Panamanian origin is proposed. The similarity of chemical fingerprints of olive jar sherds in this study with those found in Ecuador and Panama suggests that the latter are also Peruvian in origin, evidence for the wide trade networks operating in the Viceroyalty of Peru during the late 16th Century. This paper further shows the advantages of using zircon ages to source archaeological ceramics, especially where other avenues have been exhausted as was the case in this study, where petrological and chemical analyses combined with historical and archaeological investigation were unable to determine source region beyond that of possibly Panama or Peru.

Samples were prepared at both the ARC National Key Centre for the Geochemical Evolution and Metallogeny of Continents (GEMOC), Department of Earth and Planetary Sciences, University of Macquarie (GEMOC), and the Arizona LaserChron Centre, University of Arizona. The authors wish to thank the reviewers and Peter White for their valuable comments and the Solomon Islands National Museum for the sample material. The authors also acknowledge NSF-EAR 1032156 for support of the Arizona LaserChron Centre, the Carlyle Greenwell Research Fund (University of Sydney) for providing analysis funds, the Australian Research Council Discovery Project grant #dp1093168 for transport of the ceramics to Sydney, and the National Science Foundation grant DBS-1110793 for supporting the instrumental neutron activation analyses.

REFERENCES

Acevedo, S. (2004). La Loza de la Tierra: Cerámica vidriada en el Perú. Lima: Universidad Ricardo Palma.

Allen, J. (1976). New light on the Spanish settlement of the Southeast Solomons: An archaeological approach. In R. C. Green & M. Cresswell (Eds.), Southeast solomon islands

cultural history: A preliminary survey (pp. 19–29). Bulletin 11. Wellington: The Royal Society of New Zealand.

Allen, J., & Green, R.C. (1972). Mendana 1595 and the Fate of the Lost 'Almiranta': An Archaeological Investigation. The Journal of Pacific History, 7, 73–91.

Astuhuamán Gonzáles, C.W. (2011). Proyecto de Investigación Arqueológica San Miguel de Piura – Temporada 2011. Lima: Universidad Politécnica de Madrid and Universidad de Piura (Udep).

Avery, G. (1997). Pots as packing: The spanish olive jar and andalusian transatlantic commercial activity, 16th-18th centuries. Florida: University of Florida.

Bedford, S., Dickinson, W.R., Green, R.C., & Ward, G.K. (2009). Detritus Of Empire: Seventeenth Century Spanish Pottery From Taumako, Southeast Solomon Islands, And Mota, Northern Vanuatu. Journal of the Polynesian Society, 118, 69–89.

Borah, W. (1954). Early Colonial Trade and Navigation Between Mexico and Peru. Berkeley and Los Angeles: Ibero-Americana.

Carruthers, C. (2003). Spanish *Botijas* or Olive Jars from the Santo Domingo Monastery, La Antigua Guatemala. Historical Archaeology, 37, 40–55.

Case, J.E. (1974). Oceanic Crust Forms Basement of Eastern Panamá. Geological Society of America Bulletin, 85, 645–652.

Castro, A., Corretgé, L.G., de la Rosa, J., Enrique, P., Martínez, F.J., Pascual, E., Lago, M., Arranz, E., Galé, C., Fernndez, C., Donaire, T., & López, S. (2002). Palaeozoic magmatism. In W. Gibbons & T. Moreno (Eds.), The geology of Spain (pp. 117–153). London: The Geological Society.

Chatfield, M. (2007). From Inca to Spanish Colonial: Transitions in Ceramic Technology. Doctoral Dissertation, Santa Barbara: Department of Anthropology, University of California.

Chatfield, M. (2008). Clay recipes and the spread of european kiln technology in Peru, Society for Historical Archaeology Annual Meeting. Albuquerque, New Mexico. Albuquerque.

Chatfield, M. (2010). Tracing firing technology through clay properties in Cuzco, Peru. Journal of Archaeological Science, 37, 727–736.

Cobbing, E.J., & Pitcher, W.S. (1972). The Coastal Batholith of Central Peru. Journal of the Geological Society of London, 128, 421–460.

Cobbing, E.J., Pitcher, W.S., & Taylor, W.F. (1977). Segments and Super-unit in the Coastal Batholith of Peru. Journal of Geology, 85, 625–631.

Cobbing, E.J., Pitcher, W.S., Wilson, J.J., Baldock, J.W., Taylor, W.P., McCourt, W.J., & Snelling, N.J. (1981). The geology of Western Cordillera of northern Peru. London: Her Majesty's Stationery Service.

Coffey, K.T., Schmitt, A.K., Ford, A., & Spera, F.J. (2012). Comparing zircon crystallization ages between volcanic ash in Maya Ceramics and Tierra Blanca Joven Pumice (Ilopango Volcano, Central American Volcanic Arc) Geological Society of America Annual Meeting and Exposition. Charlotte, North Carolina.

Davis, D.W., Williams, I.S., & Krogh, T.E. (2003). Historical Development of Zircon Geochronology. In J.M. Hanchar & P.W.O. Hoskin (Eds.), Zircon (pp. 145–182). Washington: Mineralogical Society of America.

Deagan, K. (1987). Artefacts of the Spanish Colonies of Florida and the Carribean, 1500–1800. Volume I: Ceramics, Glassware and Beads. Washington, D.C.: Smithsonian Institute Press.

Dickinson, W.R., & Green, R.C. (1973). Temper Sands in 1595 A.D.: Spanish Ware from the Solomon Islands. Journal of the Polynesian Society, 82, 293–300.

Elburg, M.A. (2011). Geochronological Dating. In F. Vanhaecke & P. Degryse (Eds.), Isotopic Analysis: Fundementals and Applications Using ICP-MS (pp. 235–274). Washington, D.C.: Wiley-VCH Verlag and Co.

Fournier, P., & Blackman, J.M. (2008). Production, exchange and consumption of glazed wares in New Spain: formation of a database of elemental composition through INAA. Research Report. Foundation for the Advancement of Mesoamerican Studies.

Gehrels, G.E. (2011). Detrital Zircon U-Pb Geochronology: Current Methods and New Opportunities. In C. Busby & A. Azor (Eds.), Tectonics of Sedimentary Basins: Recent Advances (pp. 47–62). John Wiley and Sons, Online.

Gehrels, G.E., Valencia, V.A., & Pullen, A. (2006). Detrital Zircon Geochronology by Laser-ablation Multicollector ICPMS at the Arizona Laserchron Center. In T. Olszewski (Ed.), Geochronology: Emerging Opportunities, Paleontological Society Short Course (Vol. 12). Philadelphia: The Paleontological Society.

Gehrels, G.E., Valencia, V.A., & Ruiz, J. (2008). Enhanced precision, accuracy, efficiency, and spatial resolution of U-Pb ages by laser ablation-multicollector-inductively coupled plasma mass spectrometry. Geochemistry Geophysics Geosystems, 9, 1–13.

Gibbs, M. (2011). Beyond the New World – the failed Spanish colonies of the Solomon Islands. In J. Schablitsky & M. Leone (Eds.), Historical Archaeology and the Importance of Material Things (pp. 121–142). Ann Arbor: Society for Historical Archaeology.

Goggin, J.S. (1960). The Spanish olive jar: an anthropological study. New Haven: Yale University Press.

Goggin, J.S. (1968). Spanish Majolica in the New World, Types of the Sixteenth to Eighteenth Centuries. New Haven: Yale University Press.

Green, R.C. (1973). The Conquest of the Conquistadors. World Archaeology, 5, 14–31.

Guynn, J., & Gehrels, G.E. (2010). Comparison of Detrital Zircon Age Distributions Using the K-S Test. Tucson: University of Arizona.

Iñañez, J.G., Bellucci, J.J., Rodríguez-Alegría, E., Ash, R., McDonough, W., & Speakman, R.J. (2010). Romita pottery

revisited: a reassessment of the provenance of ceramics from Colonial Mexico by LA-MC-ICP-MS. Journal of Archaeological Science, 37, 2698–2704.

Iñañez, J.G., & Speakman, R.J. (2011). Technological features of Colonial Glazed Pottery from el Convento de Santo Domingo (Antigua, Guatemala). Similarities and differences between Colonial and Spanish pottery. In I. Turbanti-Memmi (Ed.), Proceedings of the 37th International Symposium on Archaeometry, 13th – 16th May 2008, Siena, Italy (pp. 77–82). Berlin Heidelberg, Germany: Springer.

Iñañez, J.G., Speakman, R.J., Buxeda i Garrigós, J., & D., G.M. (2008). Chemical characterization of majolica from 14th to18th century production centers on the Iberian Peninsula: A preliminary neutron activation study. Journal of Archaeological Science, 35, 425–440.

Jailiard, E., Hérail, G., Monfret, T., Diaz-Martínez, E., Baby, P., Lavenu, A., & Dumon, J.F. (2000). Tectonic Evolution of the Andes of Ecuador, Peru, Bolivia and northernmost Chile. In U.G. Cordani, E.J. Milani, A. Thomaz Filho & D.A. Camps (Eds.), Tectonic Evolution of South America (pp. 481–560). Rio de Janeiro: Brazil, 31st International Geological Congress.

Jailiard, E., & Soler, P. (1996). Cretaceous to early Paleogene tectonic evolution of the northern Central Andes (0–18°S) and its relations to geodynamics. Tectonophysics, 259, 41–53.

Jamieson, R.W., & Hancock, R.G.V. (2004). Neutron Activation Analysis of Colonial Ceramics from Southern Highland Ecuador. Archaeometry, 46, 569–583.

Jamieson, R.W., Hancock, R.G.V., Beckwith, L.A., & Pidruczny, A.E. (2012). Neutron Activation Analysis of Inca and Colonial Ceramics from Central Highland Ecuador. Archaeometry, 55, 198–213.

Johnston, S., Gehrels, G., Valencia, V., & Ruiz, J. (2009). Small-volume U–Pb zircon geochronology by laser ablation-multicollector-ICP-MS. Chemical Geology, 259, 218–229.

Kaschko, M. (1979). Field Report: 1975 Excavations on site BB-2–15, Makira, S.E. Solomon. University of Hawaii, Department of Anthropology.

Kelloway, S.J., Gibbs, M., & Craven, S. (2013). The Sherds of Conquistadors: A petrological study of ceramics from Graciosa Bay and Pamua, Solomon Islands. Archaeology in Oceania, 48, 53–59.

Košler, J., & Sylvester, P.J. (2003). Present Trends and the Future of Zircons in Geochronology: Laser Ablation ICPMS. In J.M. Hanchar & P.W.O. Hoskin (Eds.), Zircon (pp. 243–276). Washington: Mineralogical Society of America.

Lister, F.C., & Lister, R.H. (1981). The Recycled Pots and Potsherds of Spain. Historical Archaeology, 15, 67–78.

Lister, F.C., & Lister, R.H. (1987). Andalusian Ceramics in Spain and New Spain: A Cultural Register from the Third Century B.C. to 1700. The Tuscon: University of Arizona Press.

Long, G.A. (1964). Excavations at Panama Vieja. Florida Anthropologist, 17, 104–109.

Ludwig, K.R. (2008). Isoplot 3.60. Berkeley: Berkeley Geochronology Center.

Maggetti, M., Westley, H., & Olin, J.S. (1984). Provenance and technical studies of Mexican Majolica using elemental and phase analysis. In J.B. Lambert (Ed.), Archaeological chemistry, (pp. 151–191), Vol. III. Washington, D.C.: American Chemical Society.

Marken, M.W. (1994). Pottery from Spanish Shipwrecks, 1500–1800. Gainesville: University Press of Florida.

McCourt, W.J. (1981). The geochemistry and petrography of the Coastal Batholith of Peru, Lima segment. Journal of the Geological Society of London, 138, 407–420.

Mogrovejo Rosales, J.D. (1996). Arqueología urbana de evidencias coloniales en la ciudad de Lima. Lima: Instituto Riva-Agüero.

Mukasa, S.B. (1986). Zircon U-Pb ages of super-units in the Coastal batholith, Peru: Implications for the magmatic and tectonic processes. Geological Society of America Bulletin, 97, 241–254.

Olin, J.S., & Blackman, M.J. (1989). Compositional classification of Mexican majolica ceramics of the Spanish Colonial period. In R.O. Allen (Ed.), Archaeological Chemistry (pp. 87–112), Vol. IV. Washington, DC: American Chemical Society.

Olin, J.S., Harbottle, G., & Sayre, E.V. (1978). Elemental Compositions of Spanish and Spanish-Colonial Majolica Ceramics in the Identification of Provenience. In G.F. Carter (Ed.), Archaeological Chemistry (pp. 200–229) Vol. II. Washington, DC: American Chemical Society.

Olin, J.S., & Sayre, E.V. (1975). Neutron Activation Analysis of Majolica from Spanish Colonial Sites in Meso-America. Bulletin of the American Institute for Conservation of Historic and Artistic Works, 15, 57–62.

Padilla, R., Schalm, O., Janssens, K., Arrazcaeta, R., & Van Espen, P. (2005). Microanalytical characterization of surface decoration in Majolica pottery. Analytica Chimica Acta, 535, 201–211.

Peacock, D.P.S., & Williams, D.F. (1986). Amphorae and the Roman Economy: An Introductory Guide. London: Longman.

Pitcher, W.S. (1974). The Mesozoic and Cenozoic Batholiths of Peru. Pacific Geology, 8, 51–62.

Ramos, V.A. (2009). Anatomy and global context of the Andes: Main geologic features and the Andean orogenic cycle. In S.M. Kay, V.A. Ramos & W.R. Dickinson (Eds.), Backbone of the Americas: Shallow Subduction, Plateau Uplift, and Ridge and Terrane Collision (pp. 57–65). Colorado: The Geological Society of America.

Rice, P.M. (1994). The Kilns of Moquegua, Peru: Technology, excavations, and functions. Journal of Field Archaeology, 21, 325–344.

Rice, P.M. (1996). The Archaeology of Wine: The Wine and Brandy Haciendas of Moquegua, Peru. Journal of Field Archaeology, 23, 187–204.

Rice, P.M. (1997a). Tin-Enameled Wares of Moquegua, Peru. In J. Gasco, G.C. Smith & P. Fournia-Garcia (Eds.), Approaches to the Historical Archaeology of Mexico, Central & South America (pp. 173–180). Los Angeles: The Institute of Archaeology, University of California.

Rice, P.M. (1997b). Wine and Brandy Production in Colonial Peru: A Historical and Archaeological Investigation. Journal of Interdisciplinary History, 27, 455–479.

Rice, P.M. (2012a). Andean Loza from Moquegua, Peru. 1st Global Pottery Conference. Barcelona, Spain.

Rice, P.M. (2012b). Vintage Moquegua: history, wine, and archaeology on a colonial Peruvian periphery. Austin: University of Texas.

Rice, P.M., & Van Beck, S.L. (1993). The Spanish Colonial Kiln Tradition of Moquegua, Peru. Historical Archaeology, 27, 65–81.

Rovira, B.E. (1997). Hecho en Panamá: la manufacura colonial de mayólicas. Revista Nacional de Cultura (Panama), 27, 67–85.

Rovira, B.E. (2001). Presencia de mayolicas panamenas en el mundo colonial: algunas consideraciones acerca de su distribucion y cronologia. Latin American Antiquity, 12, 291–303.

Rovira, B.E., Blackman, J.M., van Zelst, L., Bishop, R., Rodríguez, C.C., & Sánchez, D. (2006). Caracterización química de cerámicas coloniales del sitio de Panamá Viejo: Resultados preliminares de la aplicación de activación neutrónica instrumental. Canto Rodado, 1, 101–131.

Smith, G.C. (1991). Heard it through the Grapevine: Andean and European Contributions to Spanish Colonial Culture and Viticulture in Moquegua, Peru. Gainesville, Florida: University of Florida.

Smith, G.C. (1997). Andean and European Contributions to Spanish Colonial Culture and Viticulture in Moquegua, Peru. In J. Gasco, G.C. Smith & P. Fournia-Garcia (Eds.), Approaches to the Historical Archaeology of Mexico, Central & South America (pp. 165–172). Los Angeles: The Institute of Archaeology, University of California.

Stacey, J.S., & Kramers, J.D. (1975). Approximation of terrestrial lead isotope evolution by a two-stage model. Earth and Planetary Science Letters, 26, 207–221.

Tochilin, C., Dickinson, W.R., Felgate, M.W., Pecha, M., Sheppard, P., Damon, F.H., Bickler, S., et al. (2012). Sourcing temper sands in ancient ceramics with U–Pb ages of detrital zircons: A southwest Pacific test case. Journal of Archaeological Science, 39, 2583–2591.

VanValkenburgh, N.P. (2012). Building Subjects: Landscapes of Forced Resettlement in the Zaña and Chamán Valleys, Peru, 16th-17th centuries C.E., Cambridge, Massachusetts: Harvard University.

Vaz, J., & Cruxent, J.M. (1975). The Determination of the Provenience of Majolica Pottery Found in the Caribbean Area Using Gamma-Ray Induced Thermoluminiscence. American Antiquity, 40, 71–83.

Ward, C. (1993). Imperial Panama: Commerce and Conflict in Isthmian America 1550–1800. Albuquerque: University of New Mexico Press.

Wegner, W., Wörner, G., Harmon, R.S., & Jicha, B.R. (2011). Magmatic history and evolution of the Central American Land Bridge in Panama since Cretaceous times. Geological Society of America Bulletin, 123, 703–724.

Wörner, G., Harmon, R.S., & Wegner, W. (2009). Geochemical evolution of igneous rock and changing magma sources during the evolution and closure of the Central American Landbridge. In S.M. Kay, V.A. Ramos & W.R. Dickinson (Eds.), Backbone of the Americas: Shallow Subduction, Plateau Uplift, and Ridge and Terrane Collision (pp. 183–196), Memoir 204. Colorado: Geological Society of America.

Digital Appendix

DVD containing:

1) LA-ICPMS Trace Element Data
2) LA-ICPMS - Common Lead Corrected Uranium Lead Data
3) MC-LA-ICPMS Hafnium Data
4) Zircon EMP and LA-ICPMS Composition